IMAGE COMPRESSION FOR TELEMEDICINE

Ph.D. THESIS

by

EMJEE PUTHOORAN

DEPARTMENT OF ELECTRICAL ENGINEERING
INDIAN INSTITUTE OF TECHNOLOGY ROORKEE
ROORKEE-247667 (INDIA)

JUNE, 2013

IMAGE COMPRESSION FOR TELEMEDICINE

A THESIS

Submitted in partial fulfilment of the requirements for the award of the degree of

DOCTOR OF PHILOSOPHY
in
ELECTRICAL ENGINEERING

by

EMJEE PUTHOORAN

DEPARTMENT OF ELECTRICAL ENGINEERING
INDIAN INSTITUTE OF TECHNOLOGY ROORKEE
ROORKEE-247667 (INDIA)

JUNE, 2013

INDIAN INSTITUTE OF TECHNOLOGY ROORKEE, ROORKEE

CANDIDATE'S DECLARATION

I hereby certify that the work which is being presented in this thesis entitled **"IMAGE COMPRESSION FOR TELEMEDICINE"** in partial fulfilment of the requirements for the award of *the Degree of Doctor of Philosophy* and submitted in the Department of Electrical Engineering of Indian Institute of Technology Roorkee, Roorkee is an authentic record of my own work carried out during a period from July, 2007 to June, 2013 under the supervision of **Dr. R. S. Anand**, Professor, and **Dr. S. Mukherjee**, Professor, Department of Electrical Engineering, Indian Institute of Technology Roorkee, Roorkee.

The matter presented in this thesis has not been submitted by me for the award of any other degree of this or any other Institute.

(EMJEE PUTHOORAN)

This is to certify that the above statement made by the candidate is correct to the best of our knowledge.

(S. Mukherjee)
Supervisor

(R. S. Anand)
Supervisor

Date:

The Ph.D. Viva-Voce Examination of **Mr. Emjee Puthooran**, Research Scholar, has been held on ……

Supervisors | Chairman, SRC | External Examiner

Head of the Department/ Chairman, ODC

ABSTRACT

Telemedicine is a new practice of medicine over distance. One of the important aspects of telemedicine is medical image transmission between and among healthcare organizations. Most of the medical image modalities such as, CT, MR, PET etc. occupy large amount of binary data size as multiple slices are generated in single examination. Therefore, efficient image compression techniques are inevitable for telemedicine applications.

Lossless compression technique is generally preferred for medical images as it prevents the possibility of losing diagnostic information by preserving every relevant detail of the image. However, the compression ratio obtained by lossless image compression techniques are very less. Near lossless compression is a lossy compression technique, in which the maximum peak absolute error (PAE) of the reconstructed image can be set to a desired specific value. It produces higher compression ratio than the lossless technique, with the control over the maximum absolute error of each pixel in the image. Region of Interest (RoI) coding technique, takes the advantage of both lossy and lossless techniques. In this method, diagnostically important areas called Region of Interest are compressed in lossless way or with high quality, whereas the unimportant areas such as background are compressed in lossy way. The RoI coding achieves high compression ratio without loss of diagnostically important information. Resolution scalable image coding is useful in applications such as telebrowsing when several images of low resolution are displayed together for comparison at first and later magnified into a higher resolution. The image with a reduced resolution is transmitted at first, then the information required to obtain a higher resolution of the same image is transmitted progressively.

The present work is aimed at achieving four objectives. The first objective has been to develop a lossless image compression algorithm which can provide higher compression ratio than the state-of-the-art techniques. Lossless image compression is most generally performed in two stages. In the first stage, image data is decorrelated and in the second stage, the decorrelated data is entropy coded. The entropy coding algorithms developed over the past years such as arithmetic coding, have achieved compression performance very close to its theoretical bound. Thus, the research objective is more focused at the image data decorrelation stage. A novel dual level DPCM namely DL-DPCM is proposed for efficient decorrelation of

image data. The DL-DPCM consists of a linear DPCM cascaded by a neural network based non-linear DPCM namely, context adaptive switching neural network predictor (CAS-NNP).

A lossless compression technique namely 'DLD-LS' was developed using the DL-DPCM. In this scheme, the image is encoded sequentially, pixel by pixel, in a raster scan order. The inter-pixel redundancies present in the input image data are removed in two stages by two DPCMs which are cascaded. The '2D-LDPCM' produces a prediction error image, which is the difference between the original image and the predicted image based on a subset of previously encoded pixels called the causal template. The CAS-NNP, which is adaptive and nonlinear, further removes the redundancies present in the error image. In the predictor stage, the pixels in an image are divided into plain, gradient and edge regions. Three different NN predictors are used so that each predictor is optimized to predict pixels in different regions for achieving higher overall prediction accuracy. The prediction error image of CAS-NNP is entropy coded using context adaptive arithmetic coding after pre-processing to produce a binary output code-stream. Comparative analysis is done with standard lossless image compression techniques, 'CALIC' and 'LOCO-I'. The developed algorithm was tested on five different datasets consisting of CT, MR, PET and Angiogram.

It is observed from the experiments that the proposed DL-DPCM has provided an improvement in the first order entropy values of the prediction error, which has resulted in lower bits per pixel (bpp) value of the lossless encoder. From the comparative analysis with predictors, 'GAP' (used in CALIC) and 'MED' (used in LOCO-I), it is observed that DL-DPCM achieved an average improvement of 0.34 bpp and 1.20 bpp in first order entropy values for CT images, which are 12.9% and 32.7%, respectively. Similarly, for MR images the improvements were 0.64 bpp and 1.88 bpp, which are 17.7% and 38.2% improvement compared to GAP and MED. For PET images the improvements were 0.52 bpp and 0.97 bpp, which are 34.8% and 49.6% improvement compared to GAP and MED. Similarly, for angiogram sequences the improvements were 0.04 bpp and 1.40 bpp, which are 1.43% and 33.3% improvement compared to GAP and MED.

The bit rate per pixel improvement after entropy coding the prediction error were 0.07 bpp (4.3%) compared to CALIC and 0.16 bpp (9.0%) compared to LOCO-I for CT images. Similarly for MR images, the improvements were 0.21 bpp and 0.41 bpp which are 7.4% and 13.4% improvement compared to CALIC and LOCO-I. For PET images, the improvements were 0.17 bpp and 0.27 bpp which are 23.4% and 31.7% improvement compared to CALIC and LOCO-I. Similarly for angiogram sequences, the performance was slightly less than

CALIC with 0.01 bpp (0.5%) extra requirement but showed 0.06 bpp (2.6%) improvement over LOCO-I.

In the second stage, the DLD-LS was extended to perform near lossless compression. This is achieved by including a quantization stage after the 2D-LDPCM. The prediction error image produced by the 2D-LDPCM is quantized depending on the quality of the reconstructed image required. The developed algorithm was tested on CT, MR, PET and angiogram. The performance of the developed algorithm was compared with the near lossless compression performance of CALIC and LOCO-I in terms of PSNR values. The overall bit rate per pixel performance of the developed near lossless compression algorithm was better than CALIC, LOCO-I, JPEG and JPEG2000, for same maximum PAE. Further, for low PAE values, the developed near lossless compression algorithm showed better performance in terms of the parameters, PSNR, MSSIM and UQI.

In the third stage, the DLD-NLS was extended to perform region of interest coding. The region of interest were compressed without loss of information and the area other than the region of interest were compressed with near lossless compression technique. The algorithm is realized by quantizing the prediction error image only on the selected areas defined by an RoI mask. Region of interests with 5%, 10% and 25% of the image area with square shape at the middle were defined. The CT, MR, PET and angiogram were used to test the RoI coding capabilities of the developed algorithm. It was observed that by using the developed RoI coding, bit savings of 0.75 bpp, 0.61 bpp and 0.53 bpp were achieved when 5%, 10% and 25% of the image were marked as RoI respectively and PAE = 1 was allowed for background compared to lossless compression without RoI coding.

In the fourth and final stage, a resolution scalable image compression algorithm was developed using the DL-DPCM. To achieve resolution scalability, firstly the image was scaled down to the desired level by sub-sampling, which represents the lowest level of resolution. The image at the lowest resolution level is coded first using 2D-DPCM and context adaptive arithmetic coding. Similarly, the image at the next higher level is encoded. This procedure is followed progressively till the original resolution of the image. Near lossless compression and region of interest coding capabilities were incorporated by adding a quantization stage after the DPCM stage. The proposed algorithm, 'RDLD' was designed to perform lossless compression (RDLD-LS), near lossless compression (RDLD-NLS) and region of interest coding (RDLD-RoI). The compression performance of the RDLD-LS, RDLD-NLS and RDLD-RoI were compared with benchmark compression algorithms by testing on CT, MR, PET and angiogram.

The overall compression performance of the developed resolution scalable coding algorithm was better than JPEG2000 in lossless mode. An improvement of 0.09 bpp (4.05%) was achieved for CT images and a very slight improvement of 0.002 bpp (0.42%) was achieved for MR images. The average improvement on the total data set was 0.03, which is 1.47% improvement over JPEG2000. Further, the developed algorithm achieved lower maximum PAE compared to JPEG2000 for different compression ratios.

ACKNOWLEDGEMENTS

I express my deepest sense of gratitude towards my esteemed supervisors, Prof. R. S. Anand and Prof. S. Mukherjee, Professor, Electrical Engineering Department, Indian Institute of Technology Roorkee for their inspiring guidance, constant encouragement and moral support during this work. Their wide experience, dynamism, timely help and painstaking efforts made it possible for me to complete this work.

I wish to acknowledge most sincerely Dr. G. N. Pillai, Prof. M. V Kartikeyan, Prof. Indra Gupta, Prof. B. Das for their constructive discussions during the meetings of my research committee and Prof. Pramod Agarwal, Head of Department for extending the various facilities. I am thankful to the faculty members of the Department of Electrical Engineering for their invaluable encouragement and support.

I am thankful to Mr. Dinesh Sharma, the staff of Bio-Medical Instrumentation Lab of the Department of Electrical Engineering for his co-operation and assistance.

I am extremely thankful to my fellow researchers Dr. Jainy Sachdeva and Mr. Jithendra Virmani, for their every help rendered during my research work. They encouraged me and boosted my morale whenever I approached in trying times. I am highly thankful to my friends and fellow researchers Dr. Ramesh Kumar Sankaria and Dr. Narendra D. Londhe, for their every necessary help and invaluable support during this work. I am thankful to other fellow researchers Mr. Ashok Kumar Dhore, Mr. Mohan Poddar, Dr. Tirupathiraju Kanumuri, Mr. Mohammed Arif, Mr. Nagendra H, Ms. Padma Ganasala, Mr. Subrahmanya M. B for their kind support during this work.

I owe a debt of gratitude to my parents, sister, brother-in-law and niece for their consistent support and encouragement. Words can hardly explain the co-operation and company of many friends who stood by me at every moment and during my work.

Above all, I am thankful to the Lord Jesus who gave me wisdom and helped me through different people at the time of my need to complete my research work.

Emjee Puthooran

CONTENTS

LIST OF FIGURES

LIST OF TABLES

Chapter 1

Introduction

1.1 Motivation

Most of the medical images provide anatomical and pathological details of the human body parts by non-invasive means. With the advancement of various imaging technology in the medical field, physicians tend to use medical images more extensively for disease diagnosis. Geographical barriers often prevent patients living in rural and remote areas from accessing primary and speciality medical care, as most of the healthcare centres are located at urban and semi-urban areas. Casualties from natural disasters and battlefield are also deprived of urgent medical care, when the medical facilities are not located near the site of accident. Utilisation of information and communication technology (ICT) in medicine overcomes the geographical barriers in reaching the medical care to a distant place. Telemedicine is a medical practice, which utilises ICT to provide care and medical information to patients at a distance.

Transmission of medical images between healthcare organizations is an important part of telemedicine. Medical images such as MR and CT occupy a considerable amount of data space as multiple slices are acquired for diagnosis and interpretation by the radiologists. Moreover, these image modalities are increasingly being used for medical examination today. Medical images may needs to be stored for many years due to legal reasons. Thus, there is a high demand for digital storage space in a modern healthcare organization, as more number of images are produced every day. Moreover, the bandwidth requirement for the transmission of medical images between healthcare organizations is an important part of the ICT enabled e-Health practices such as telemedicine.

Large volume of image data needs to be transmitted and stored in telemedicine. Compressing the data before storage or transmission allows the data to be transmitted more economically and quickly. The task involved in any data compression technique is to reduce the amount of data required to represent the information. Image compression techniques therefore greatly help in reducing the total volume of data in many applications. With reduced data, the information can be communicated faster or with reduced bandwidth requirements and can be stored in a lesser storage space. Therefore, although numerous researches were carried out, medical image compression remains as an active field of study.

1.2 Telemedicine

The concept of telemedicine existed decades ago through the use of telephone, facsimile transmission, and slow-scan images. Computers and robot assist physicians in many areas [9], [5]. Through telesurgery a surgeon can perform surgery on a patient, even though they are not physically present in the same location. The term telemedicine, in short refers to the utilization of ICT for medical diagnosis, treatment and patient care. Telemedicine equips an expert medical practitioner to electronically communicate primary and specialty medical care to a patient in the most remote area, as well as to obtain diagnostic information from the patient. Thus, the patients who live far from advanced medical care, or even from basic medical services, can directly access high quality medical expertise without travelling long distance. Telemedicine is also very useful for providing care for casualty in the battle-field and in the areas affected by natural calamities.

1.3 Image Compression

With the development of digital communication and storage technology, the gross information content communicated and stored globally have increased at an unprecedented rate over the past two decades. An elaborate study by Hilbert and López [35] estimated that the volume of data communicated worldwide in the year 2007 was about 1.96×10^9 terabytes with an exponential growth rate over the past two decades. It is estimated that in the same year image data occupied about 32% of the internet web storage space [43].

The technological capacity to transmit the information through space (communication) and time (storage) has become the backbone of social, economic and political features of today's society – the network society – as described by the social scientists. The technological challenges in the frontiers of Information and Communication Technology (ICT) are to achieve higher bandwidth, storage space and computing power. Apart from innovation and usefulness of a specific technology, economic reasons such as capital investment and operating cost do play an important role in the wide spread utilization of it. For instance, AT&T introduced videophone trademarked as *Picturephone*to the public as early as 1964. The *Picturephone* required six wire loops against two wire loops in the case of normal phone, for connecting the service unit to the central office [53]. The service was expensive and discontinued by late 1970 because of few users. Hence, researchers are involved in developing economic means to transmit the information, alongside the efforts to increase the communication channel capacity.

Image compression techniques provide an economical and fast means of image data transmission by removing the redundant and less significant data.

Image compression techniques reduce the data size of an image by removing the irrelevant and redundant information. They are broadly classified into two – lossy and lossless. Lossy techniques [90], [72], [75], [77] achieve higher compression ratios than lossless techniques, but cause permanent loss of information and may degrade image quality. Lossless compression techniques [14], [65] preserve every detail in the original image.

1.4 Image Compression for Telemedicine

With the availability of less-expensive digital computing power and the advancement of technology, an increasing range of imaging systems are being employed in the medical field. The spectrum of medical imaging varies from 2-D X-Ray images to sophisticated techniques such as virtual reality [10]. Medical images acquired from various modalities, such as MR, CT, positron emission tomography (PET), Nuclear Medicine, angiogram, Single Photon Emission Computed Tomography (SPECT), and Computed Radiography (CR), require large amount of data storage capacity. The interest in telemedicine systems has created significant demand for improved compression and decompression algorithms and economic and reliable ways for sending and receiving, storing and retrieving multimedia data. Compressing the volume of data allows images to be sent more economically and quickly, followed by reconstruction of images at receiving end for viewing and interpretation [6].

Features desirable for medical image compression are, progressive fidelity encoding/decoding, progressive resolution decoding, Region-of-Interest encoding/decoding, and random access decoding. Progressive fidelity transmission allows visualization of a full size image even when only a small part of the full information has reached the receiver. This full size image is an approximate version of the original image. The greater the amount of data received the more similar the decompressed image is to the original image [42]. In progressive resolution an image of reduced resolution is transmitted first, then the information required to obtain a higher resolution version from the original image is transmitted. This is useful when several images are displayed together for comparison and later magnified into a larger area. Medical images also may required to be stored with encryption in many applications due to legal reasons. Encryption can be used while compression [15], [79], [13], [102] to secure medical image data.

The most commonly used digital modalities, generate multiple slices in a single examination as mentioned previously. One slice is normally a cross section of the body part. Its adjacent slices

are cross sections parallel to the slice under consideration. Multiple slices generated this way are normally anatomically or physiologically correlated to each other. Hence efficient compression can be achieved by exploring the correlation between slices. Methods to remove slice correlation for three-dimensional (3-D) compression include prediction methods and 3-D transformations [70], [63], [91].

1.5 Literature Review

A wide verity of image compression technique has been developed in the past years. There has been a continuous impetus for improving the compression ratio by developing a variety of lossless as well as lossy compression algorithms. A review of the relevant image compression algorithms are presented below.

1.5.1 Lossless Image Compression

The techniques for reversible compression using the elementary manipulation of pixel values which have been developed in the past are: differential pulse code modulation (DPCM), hierarchical interpolation (HINT), difference pyramid (DP), bit-plane encoding (BPE) and multiplicative autoregression (MAR) [55], [36].

In lossless compression method, either predictive techniques, transform techniques or vector quantization technique is used to decorrelate the image data. Entropy coding such as Huffman, arithmetic, run-length encoding (RLE) [66] and Lempel-Ziv-Welch (LZW) coding [39], further reduce the bit size of the decorrelated image data. The RLE is best suited for image areas with low variation in pixel values, such as soft tissue regions in CT images and Huffman coding is efficient in coding the image differences with highly peaked histograms [96]. The above primitive methods could not achieve appreciable compression ratios.

Many image compression schemes based on fractals [34], [44], [95] have been developed in the last few years. Fractals can describe natural scenes better than shapes of traditional geometry. There are several methods developed based on different characteristics of fractals. The most important fractal image compression method is based on Iterated Function System (IFS) promoted by Barnsley [8]. In this method, images are compressed into compact IFS codes at encoding stage, and fractal images are generated to approximate the original image at the decoding stage. Another image compression method is based on the fractal dimension. Fractal dimension is a good representation of roughness of image surfaces. Based on this, images can be segmented according to their roughness and these segments can be coded efficiently using the properties of the human visual system.

Most of the successful lossless coding schemes employ simple and efficient predictive coding techniques [14]. It involves pixel value prediction from causal neighboring pixels, modeling and entropy coding of the prediction error. Predictive coding technique is used by the two state-of-the-art lossless compression algorithms *viz*., the context-based adaptive lossless image coding (CALIC) [98] proposed by Wu and Memon and the low complexity context-based lossless image compression (LOCO-I) [94] proposed by Weinberger *et al*. Boolean and stack filters [62],[60],[61] were used in the prediction stage of lossless compression.

CALIC uses a nonlinear predictor called Gradient Adjusted Predictor (GAP) and uses a large number of modeling contexts to condition a nonlinear predictor and adapt the predictor to varying source statistics. The nonlinear predictor can correct itself via an error feedback mechanism by learning from its mistakes under a given context in the past. The LOCO-I is used at the core of the ISO/ITU standard for lossless and near-lossless compression of continuous-tone images, JPEG-LS. It is based on a simple fixed context model. The model is tuned for efficient performance in conjunction with an extended family of Golomb-type codes, which are adaptively chosen. The CALIC generally achieves a higher data reduction than the LOCO-I, with a higher computational complexity than LOCO-I. The JPEG-2000 [77] includes a lossless mode based on integer wavelet transform. However, the lossless mode is slower and often achieves lower compression ratios than JPEG-LS.

Image coders which use reversible integer wavelet transform [24] [12] facilitate decompression from low bit rates all the way up to lossless reconstruction. However, the energy compaction of integer wavelet transform is less, which results in higher bit rate. Memon *et al*. [49] proposed a context modeling techniques for lossless image compression with reversible integer wavelet transforms. The method achieved compression ratios within 1% of CALIC when tested on a set of natural images. However, the hierarchical nature of the wavelet coding is only up to the first level of decomposition.

Pan *et al*. [57] proposed a lossless embedded coding algorithm based on binary wavelet transform (BWT) called progressive partitioning binary wavelet-tree coder (PPBWC). Although the algorithm is fast, the compression performance is less than the benchmark lossless compression techniques.

Zhang and Adjeroh [100] introduced prediction by partial approximate matching (PPAM), technique for compression and context modeling. The algorithm needs to be trained offline

before encoding and an average improvement of 0.03 bits per pixel (bpp) and 0.151 bpp over the CALIC and the JPEG-LS is achieved for a set of ten natural images.

Zhao and He [101] proposed super-spatial structure prediction, in which the image area is partitioned into two regions: structure regions (SRs) and non-structure regions (NSRs). SRs are encoded with the super-spatial prediction, whereas NSRs are encoded with the CALIC. However, in this method only image with larger SRs achieves a higher compression ratio compared to CALIC.

Recently Taquet and Labit [82] proposed two variants of hierarchical oriented prediction (HOP) approaches using least square estimation (LSE) namely HOP-LSE and HOP-LSE$^+$. The HOPE-LSE and the HOP-LSE$^+$ had an average improvement of 0.14 bpp and 0.21 respectively over CALIC, when tested on MR images. However, the computationally intensive least square optimization needs to be performed at both the encoder side as well as the decoder side.

Many researchers used computational intelligence for pixel value prediction and context modeling. Marusic and Deng [47] presented two adaptive prediction schemes based on adaptive neural network (AdNN) and local area training recursive-least mean square (LAT-RLMS) algorithm. The adaptation of the respective predictor coefficients is based on training of the predictors in a local causal area adjacent to the pixel to be predicted. The AdNN had an average improvement of 0.06 bpp over the CALIC and 0.24 bpp over the LOCO-I. The LAT-RLMS had an average improvement of 0.04 bpp over the CALIC and 0.22 bpp over the LOCO-I. However, on-the-fly training of predictors is required during encoding as well as decoding, which is computationally complex. Aiazzi *et al*. [4] proposed a fuzzy matching pursuits (FMPs) encoder, which consists of a space-varying linear-regression predictor obtained through fuzzy-logic techniques. It achieved an average improvement of 0.108 bpp and 0.29 bpp over the CALIC and the JPEG-LS respectively, when tested on a set of 24 natural as well as medical images.

Neural networks has the capability to model nonlinear functional relationships existing between the causal neighboring pixels and the current pixel being predicted. It also has the ability of adapting to different types of input data. Since neural networks are parallel in architecture, they can also work efficiently in parallel computing environment, where the computation time can be reduced considerably. Many image compression schemes are reported in the literature, using neural networks as pixel value predictors [26], [37], [19].

Kau *et al*. [38] proposed the switching adaptive predictor (SWAP) with automatic fuzzy context modeling. The context of the coding pixel and the SWAP encoder switches between

two predictors: the adaptive neural predictor (ANP) and the texture context matching (TCM) predictor. The bit rate is improved by an average of 0.2 bpp compared with the CALIC for natural images. However, the online adaptive training used in ANP is computationally complex and both the encoder and the decoder need to perform the training.

Among the above techniques, the HOP-LSE^{+} and the SWAP had some significant improvement in bpp compared to the CALIC. However, for both the HOP-LSE^{+} and the SWAP, the predictor need to be optimized on-the-fly during encoding as well as decoding. This is a computationally intensive operation. In most of the medical imaging applications such as picture archiving and communication system (PACS) and telemedicine, an image is compressed only once but decompressed many times. Therefore, it is highly desirable to have a decoder with lesser computational complexity.

1.5.2 Lossy image compression

Lossy image compression methods are based on techniques such as, lossy predictive coding, transform coding, Wavelet coding, Embedded Zero-tree Wavelet (EZW) [75], Set Partitioning in Hierarchical Trees (SPIHT) [72], Set Partitioned Embedded Block Coder (SPECK), Embedded Block Coding with Optimized Truncation (EBCOT), Principal Component Analysis (PCA) [85] etc. The JPEG based on Discrete Cosine Transform (DCT) [3] [90] and JPEG2000 [46], [21], [111] based on wavelet transform are defined by the International Standard Organisation (ISO) and the Telecommunication Standardization Sector (ITU-T) of International Telecommunication Union (ITU) [110]. Miew et al [18] conducted a study on the acceptability of lossy compression of MR images among radiologists. It showed that if the imaging noise to compression ratio (ICR) is greater than 4, radiologists tend to prefer the compressed image than the original image.

Euclid Seeram [74] pointed out that lossless compression offers limited compression ratios generally between 1.5:1 and 3:1 but lossy compression algorithms can provide higher compression ratios from about 10:1 or greater. Further it noted that images such as digitized chest images, CT, MRI and ultrasound images have different ‘compression tolerance’ and therefore a single compression ratio cannot be assigned to a modality, even for a given organ system.

Recently, Fukatsu *et al*. [30] reported improved results with ANN for lossless compression of chest radiology, mammography and CT images. To achieve high bit rate reduction while maintaining the best quality, post-processing techniques provide one attractive solution [17], [76]. Oguzhan et al [87] proposed an optimal post-processing filter at the decoder to improve

warped discrete cosine transform (WDCT) encoding performance. The filter coefficients are determined at the encoder and used at the decoder to improve the quality of the decoded image.

Three-dimensional wavelet transform and transform coding are used for compressing volumetric images having multiple slices in a single examination [91], [103], [78]. The 3-D transform methods outperform 2-D transform applied to individual slices since they can better reduce the redundancy present within the adjacent slices. Methods to remove slice correlation for three-dimensional (3-D) compression include prediction methods and 3-D transformations [91], [63], [103].

Near lossless compression technique is a lossy compression technique in which each pixel in the reconstructed image is guaranteed to have error less than a fixed maximum value. The benchmark lossless compression algorithms CALIC [98] and LOCO-I [94] includes a near lossless compression mode also. Adjeroh *et al*. used a near lossless compression scheme to compress DNA micro array images [2].

1.5.3 Region of Interest Coding

Compression schemes available today, produces high compression rates if loss of quality is affordable. However, deficiency in diagnostically important regions of medical images, called regions of interest (RoIs), are not acceptable in most cases. RoI Compression is a compression technique where explicitly defined regions of interest (RoI) are compressed in a lossless way whereas image regions containing unimportant information are compressed in a lossy manner. This brings a high compression rate with good quality in the RoI [11].

The aim of the research focused on RoI coding is to allow the use of multiple and arbitrarily shaped RoIs within images, with arbitrary weights describing the degree of importance for each RoI including the background (i.e., image regions not belonging to RoI) so that the latter regions may be represented by different quality levels [27].

When an image is coded with an emphasis on RoI, it is necessary to identify the coefficients required for the reconstruction of the RoI. Thus, an RoI mask is introduced to indicate which coefficients have to be transmitted exactly in order for the receiver to reconstruct the RoI. The wavelet transform is commonly applied to the image at the encoder side. The mask in the wavelet domain is a map pointing out all the related coefficients for the reconstruction of the RoI. The corresponding locations of the coefficients in the next scale are calculated from the current scale.

Part 1 of the JPEG2000 standard defines the MAXSHIFT method [80]. Here the scaling value is computed in such a way that it makes possible to have arbitrarily shaped RoIs without the need for transmitting shape information to the decoder. Thus the decoder does not have to perform RoI mask generation. Part II of the JPEG2000 [111] Imaging Standard defines the principle of the general scaling method of coefficients so that the bits associated with the RoI are placed in higher bit planes than the bits associated with the background. During the embedded coding process, the most significant RoI bit planes are placed in the bit stream before any background bit planes of the image. Thus, the RoI will be decoded, or refined, before the rest of the image.

1.5.4 Resolution Scalable Coding

Hierarchical interpolation (HINT) [69], inter-leaved HINT (IHINT) [1], integer wavelet transform (IWT) used in the JPEG2000 standard [20] are resolution scalable lossless compression schemes. HIP use sub-sampling to produce a low-resolution image. Residual data compressed by a sub-band bit-plane coder such as EBCOT [84] or SPIHT [72] can achieve resolution scalability. Taquet and Labit [83] introduced a new hierarchical oriented prediction (HOP) that combines DPCM with HIP. It exploits already coded pixels of the same subband to improve decorrelation.

1.6 Objective of the Thesis

Lossless compression technique is generally preferred for medical images as it prevents the possibility of losing diagnostic information by preserving every relevant detail of the image. However, the compression ratio obtained by lossless image compression techniques are very less. Near lossless compression is a lossy compression technique, in which the maximum peak absolute error (PAE) of the reconstructed image can be set to a desired specific value. It produces higher compression ratio than the lossless technique, with the control over the maximum absolute error of each pixel in the image. Region of Interest (RoI) coding technique, takes the advantage of both lossy and lossless techniques. In this method, diagnostically important areas called Region of Interest are compressed in lossless way or with high quality, whereas the unimportant areas such as background are compressed in lossy way. RoI coding achieves high compression ratio without loss of diagnostically important information. Resolution scalable image coding is useful in applications such as telebrowsing when several images of low resolution are displayed together for comparison at first and later magnified into a higher resolution. The image with a reduced resolution is transmitted at first, then the

information required to obtain a higher resolution of the same image is transmitted progressively.

The first objective has been to develop a lossless image compression algorithm, which can provide higher compression ratio than the state-of-the-art techniques, and to test the same on volumetric medical images such as CT, MR, PET and Angiogram. Lossless image compression has two stages namely, image data decorrelation and entropy coding. The entropy coding algorithms developed over the past years have achieved compression performance very close to its theoretical bound. Thus, the research is more focused at the image data decorrelation stage.

The second objective has been to extend the lossless compression technique to perform near lossless compression. The comparative performance of the developed near lossless image compression algorithm with respect to bench mark algorithms has to be carried out by exhaustive testing on CT, MR, PET and angiogram considering different maximum PAE values.

The third objective has been to extend the lossless compression technique to perform region of interest coding. The region of interest is to be compressed without loss of information and the area other than the region of interest is to be compressed with near lossless compression technique. The compression ratio of CT, MR, PET and angiogram compressed with different percentage of region of interest and different quality of background were to be compared with that of the benchmark algorithms.

The fourth objective has been to develop a resolution scalable image compression algorithm. The algorithm is expected to perform lossless compression, near lossless compression and region of interest coding. The compression performance of the developed resolution scalable algorithm has to be compared with benchmark compression algorithms by testing on CT, MR, PET and Angiogram.

1.7 Organization of the Thesis

The work carried out in this thesis is broadly classified into four sections. The first section deals with the lossless compression of medical images. The second section deals with near lossless compression of medical images. Region-of-interest compression of medical image is dealt with in the third section. The fourth section deals with progressive resolution encoding of medical images.

Chapter 1: This chapter deals with the introduction of the thesis problem and literature survey of lossless and lossy image compression techniques applied to medical as well as general images.

Chapter 2: This chapter deals with the methodology and formulation of thesis problem. It details the medical image database used for testing the proposed algorithms and comparing it's compression performance with the benchmark image compression algorithms.

Chapter 3: This chapter deals with the lossless compression of medical images. It presents the image data decorrelation capabilities of NN predictor and proposes a dual level predictor for lossless compression.

Chapter 4: This chapter deals with the near lossless compression of medical images. It proposes a near lossless image compression technique by extending the dual level predictor based lossless compression algorithm.

Chapter 5: This chapter deals with the region of interest coding of medical images using the dual level predictor.

Chapter 6: This chapter proposes an image compression scheme with progressive resolution transmission of medical images for telemedicine applications using the dual level predictor.

Chapter 7: This final chapter concludes the work and presents the contributions. It also directions for the future work.

Chapter 2

Methodology

2.1 Introduction

Compression of medical images poses a challenge due to a number of reasons. The volume of medical image data produced continues to increase, as new and improved biomedical instruments provide images with higher resolution. The usage of lossy compression techniques on medical images to reduce the volume of data will result in loss of important diagnostic information. On the other hand, error free or lossless compression techniques achieve only less data reduction. Further, image reconstruction with progressive resolution feature is very much desirable for medical applications such as telemedicine and teleradiology. Therefore, this research is focused on developing image compression techniques which can produce low bit rate per pixel of the image, without losing diagnostically important information and which have the feature of progressive resolution reconstruction.

The research methodology is designed in four stages to meet the research objective. In the first stage, the main focus is to remove the interpixel redundancy present in the image data by developing a novel image data decorrelation technique. Compressed image without loss of information can be produced by entropy coding the decorrelated data. In the second stage, the lossless compression technique developed in the first stage is extended to near lossless compression technique, where the PAE of the reconstructed image can be specified during the compression. RoI coding capability is introduced in the third stage, in which the diagnostically important areas of the image can be compressed without loss of information and the areas other than RoI can be compressed with near lossless technique. In the final stage, the developed compression algorithm is extended to have progressive resolution reconstruction and RoI coding capability. The stepwise procedure of the methodology, as well the details of the medical image dataset used to test, validate and compare the developed compression techniques are explained in the following section.

2.2 Proposed Methods: An overview

The schematic diagram of the research methodology is presented in Fig.2.1. Among the lossless compression techniques developed over the past years, predictive coding techniques showed better performance. Predictive coding techniques generally have two stages namely, image data decorrelation stage and entropy coding stage. The coding efficiency of entropy coding

techniques which were developed in the past years have reached near to the theoretical limit. Therefore, the design methodology is more focused on the decorrelation stage. Non-linear correlation exists between the neighboring pixels of the image data. Therefore, a better nonlinear decorrelation technique is sought for in design methodology. A novel dual level DPCM (DL-DPCM) is proposed here to achieve higher image data decorrelation than the existing methods. The DL-DPCM consists of 2D linear DPCM (2D-LDPCM) predictor followed by a nonlinear context adaptive switching neural network predictor (CAS-NNP). The usage of linear predictor before the nonlinear predictor effectively reduces the range of input values to the nonlinear predictor. Further, three NNP were used in the proposed CAS-NNP, which switches between three image regions predicted from the context of the pixel being predicted. This results in improvement of the overall prediction accuracy. A context adaptive arithmetic coding is used in the proposed lossless compression algorithm to encode the prediction which takes the advantage of the correlation between the context and the prediction error. If the image contains areas with constant pixel values, run length encoding is more efficient than arithmetic coding. Therefore, the proposed lossless compression algorithm operates in run length mode, when it detects an area with constant pixel values.

2.2.1 Near lossless compression technique

In the second part of the design methodology, the developed lossless compression technique is extended to perform near lossless compression. This is attained by incorporating a quantization stage after the linear prediction stage. The prediction error of the 2D-LDPCM is quantized to the desired level. Here, the prediction is made from the neighboring pixels, which are reconstructed, rather than the original pixel values. This ensures that the same neighboring pixel values are available to the encoder as well as the decoder. Runlength encoding mode is not used in near lossless compression. This is because, the probability of zero value in the prediction error is more and the arithmetic coding can efficiently encode the prediction error.

2.2.2 Region of interest compression technique

In the third part, the near lossless compression algorithm is extended to perform RoI compression. The methodology is to use quantization value ‘0’ for RoI and the desired level of quantization for the regions other than the RoI. The RoI is determined by an RoI mask. Multiple RoI masks can be used if there are multiple RoIs in the image. If the shape of the RoI is simple geometry figures like square, polygon etc., it can be encoded by their vertices. If the RoI is arbitrary shaped, it can be encoded by using binary image compression techniques such as binary contour mapping.

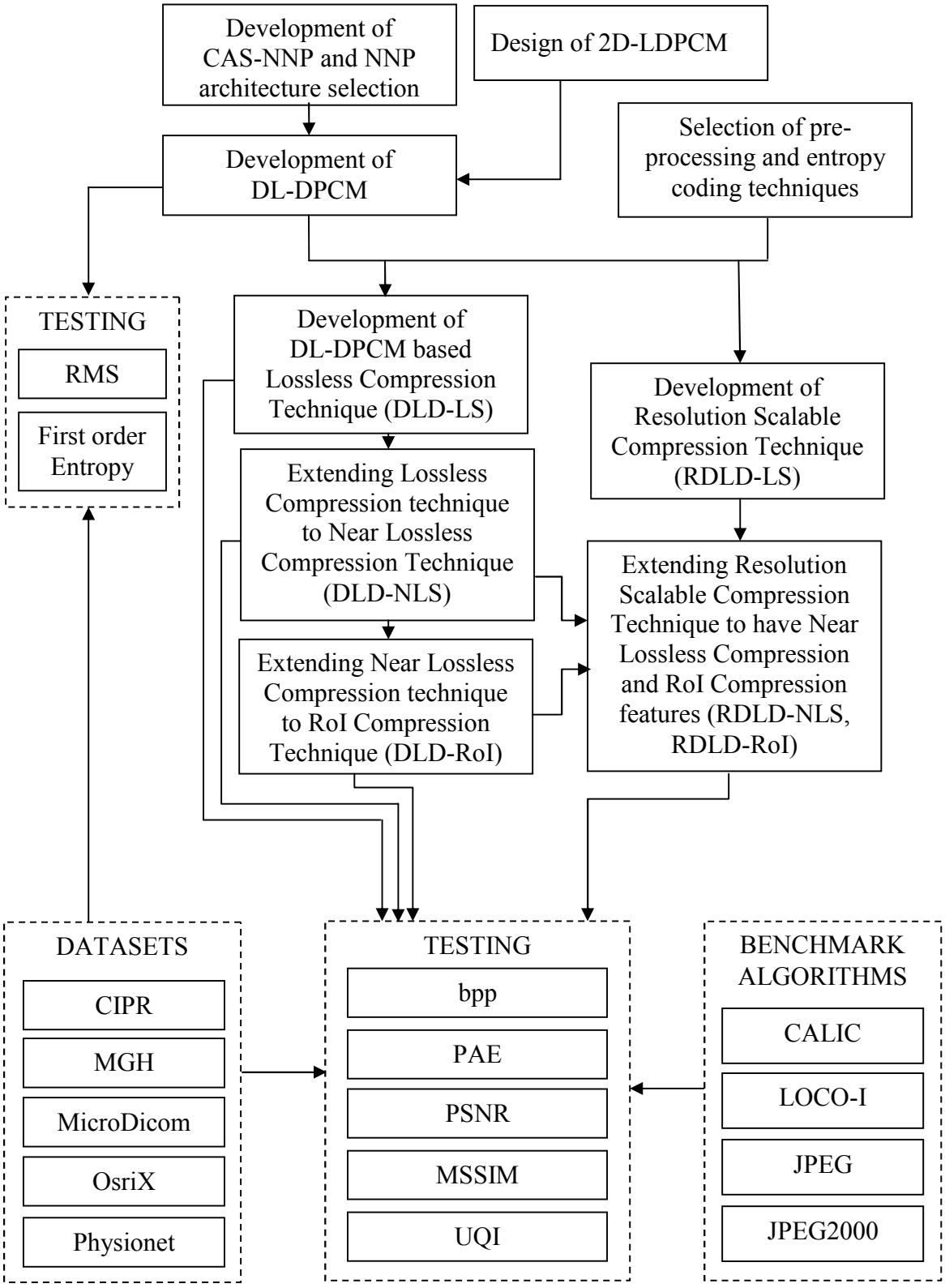

Fig.2.1 Schematic diagram of the research methodology

The proposed algorithm is tested with a single square shaped RoI at the center with three different percentage of areas, which are 5%, 10% and 25%. This is used to study the variation of bit rates when RoIs of different sizes are used.

2.2.3 Resolution scalable compression

Fourthly, a resolution scalable image coding algorithm is proposed using the DL-DPCM as its decorrelation stage. To achieve resolution scalability, the image was scaled down to the desired level by sub-sampling, which represents the lowest level of resolution. The image at the lowest resolution level is coded first using 2D-DPCM and context adaptive arithmetic coding. Similarly, the image at the next higher level is encoded. This procedure is followed progressively till the original resolution of the image. Near lossless compression and region of interest coding capabilities were incorporated by adding a quantization stage after the DPCM stage. The developed algorithm was tested using CT and MR images. The performance of the developed resolution scalable algorithm was compared with JPEG and JPEG2000.

2.3 Data Redundancy

The occurrence of data which does not provide any relevant information or is a repetition of the already presented data is called redundant data. In general, there is significant redundancy present in image data. This redundancy is proportional to the amount of correlation among the image data samples. For example, in a natural still image, there is usually a high degree of spatial correlation among neighboring image samples.

The compression algorithm examines the data for any redundancies in it, and tries to remove them [73]. Mathematically redundant data can be quantified only in terms of relative data redundancy, expressed in terms of compression ratio. When two data sets carries the same information with different quantity of data, n_1 and n_2, the relative data redundancy is defined as:

$$R_D = 1 - \frac{1}{C_R} \tag{2.1}$$

where, compression ratio,

$$C_R = \frac{n_1}{n_2} \tag{2.2}$$

The data redundancy present in digital image are categorized in to three different forms namely, (i) coding redundancy, (ii) interpixel redundancy and (iii) psychovisual redundancy

[66]. A practical image compression system, removes a combination of these redundancies. Coding and interpixel redundancies can be removed without loss of information. However, removing psychovisual redundancy results in permanent loss of information from the image.

2.3.1 Coding Redundancy

A code is a system of symbols (letters, numbers, bits, etc.) used to represent the body of an information or set of events. Each piece of information or event is assigned a sequence of code symbols, called a code word. The number of symbols in each code word is its length. Coding redundancy is associated with average length of the code word used to represent a data set. This can be better understood by examining the histogram of an image as shown in the

Fig.2.2. Consider a grey level image having n pixels, with the grey levels range from 0 to L-1 and n_k number of pixels with k grey levels. Then the probability of occurring grey level k is:

$$P(k) = \frac{n_k}{n} \tag{2.3}$$

If the number of bits used to represent the grey level k is $l(k)$, then the average number of bits required to represent each pixel is:

$$L_{avg} = \sum_{k=0}^{L-1} l(k).p(k) \tag{2.4}$$

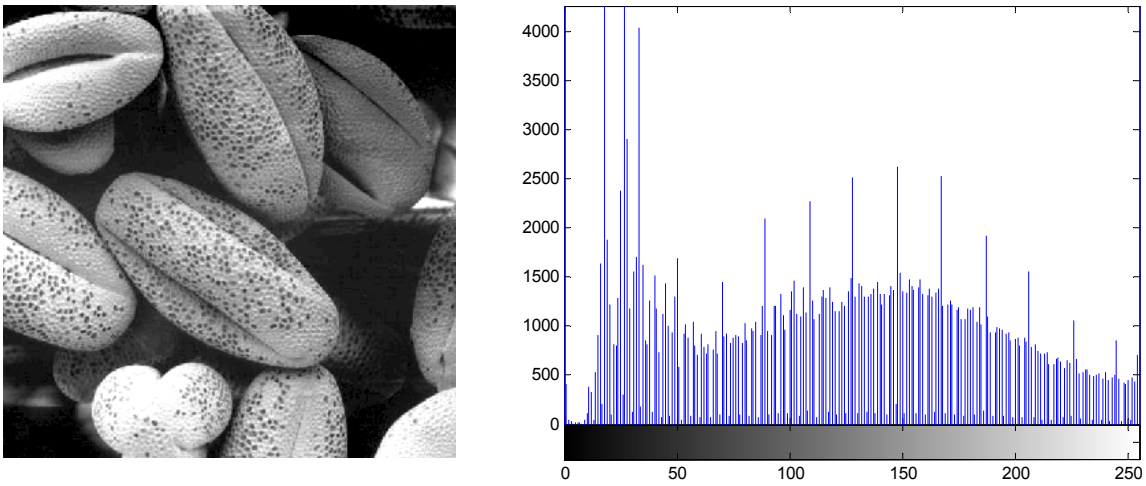

Fig.2.2(a) Grey scale Image (b) Image histogram

Hence, the number of bits required to represent the whole image is nxL_{avg}. Maximum compression ratio is achieved when L_{avg} is minimized. Coding the grey levels in such a way, that the L_{avg} is not minimized, results in an image containing coding redundancy. Generally coding redundancy occurs when the codes assigned grey levels do not take full advantage of the non-uniformity in the image histogram. Therefore, it is almost always present when grey levels of an image are represented with a natural binary code. Common methods of removing coding redundancy are by using variable length codes such as Huffman coding, Arithmetic coding etc.

2.3.2 Interpixel Redundancy

Interpixel redundancy is related to interpixel correlation within an image. This can be established by examining the autocorrelation coefficients computed along any line of an image. These correlations results from the structural or geometric relationships between the objects in the image. Usually the value of a certain pixel in the image can be reasonably predicted from the values of group of other pixels in the image. For example, the grey levels of neighboring pixels are roughly the same and gives a lot of information about grey levels of other neighborhood pixels. Fig.2.3 shows the grey level values of the pairs of adjacent pixels. Each dot represents a pixel in the image with the x coordinate being its grey level value and the y coordinate being the grey level value of its neighbor to the right. The strong diagonal relationship about the x = y line clearly shows the strong correlation between neighboring pixels [67].

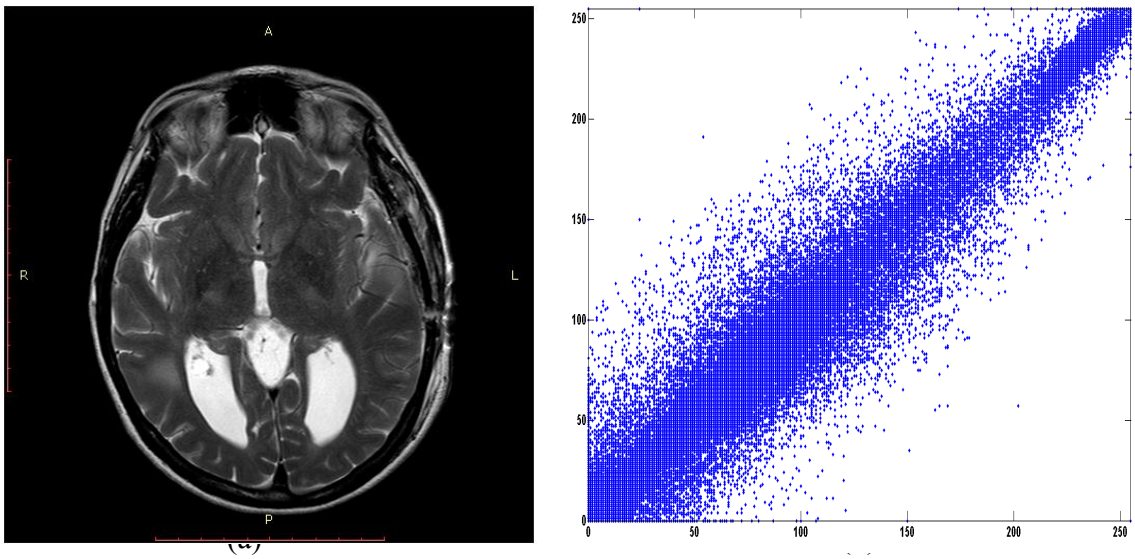

Fig.2.3 (a) Grey scale Image (b) Scatter plot of adjacent pixel value pairs

Thus, it can be said that the information carried by individual pixel is relatively small or the visual contribution of a single pixel to an image is redundant. Interpixel redundancy is also termed as spatial redundancy, geometric redundancy and inter-frame redundancy.

Interpixel redundancy can be removed first by applying a transformation on the image referred as mapping. Examples are, difference between the adjacent pixels, DCT, Wavelet transform etc. After the mapping, many of the data may become zero or very small value, which occurs due to the correlation between the pixels. These values then would require only smaller code length than the original image data set.

2.3.3 Psychovisual Redundancy

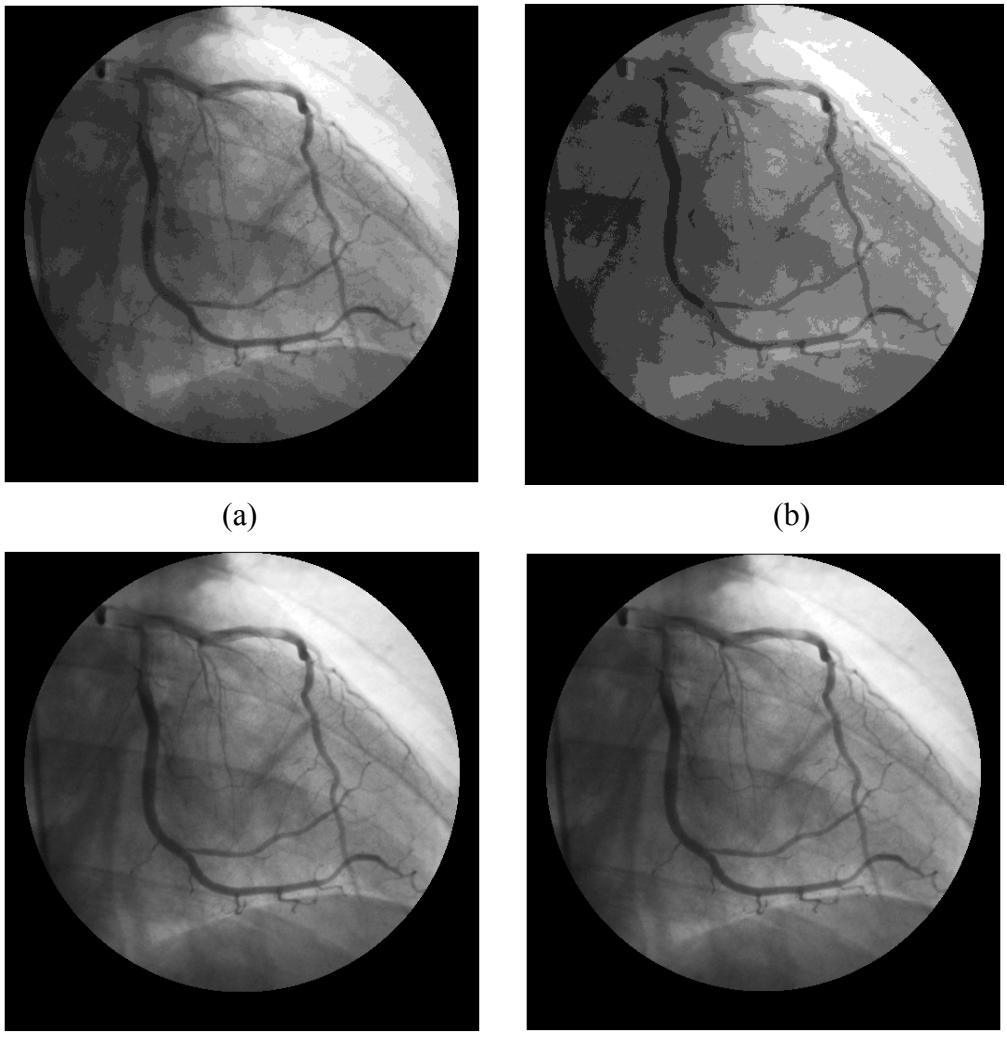

Fig. 2.4 Angiogram quantized into different levels. (a) Original image (b) Image quantized by a factor of 4. (c) Image quantized by a factor of 16 (d) Image quantized by a factor of 32

It is known that the human eye does not respond to all visual information with equal sensitivity. For example, in an image the regions such as edges are more sensitive whereas plane surface is of less sensitivity. Thus, certain information in an image is relatively less important for normal visual processing and thus they are psycho-visually redundant. Although, the removal of psychovisual redundancy from an image results in permanent loss of data and introduces error in the resulting image, it does not deteriorate the quality of image perception to human visual system.

Psychovisual redundancy can be removed by using the technique of quantization, which can be defined as mapping of a broad range of input values to a limited number of output values. Quantization results in the permanent loss of data and also results in the reduction of the image's spatial and/or grey scale resolution. The level and location of psychovisual redundancy can be determined only with feedback from a human operator and tends to be relatively subjective.

Figures 2.4 (a) – (d) shows the effect of different levels of quantization of an angiogram. Fig. 2.4 (a) is the original image, Fig. 2.4 (b) is quantized by a factor of 4, Fig. 2.4 (c) is quantized by a factor of 16 and Fig. 2.4 (d) is quantized by a factor of 32. It can be noted that although, Fig. 2.4 (b) is quantized by a factor of 4, there is no significant difference with the original image for a human observer.

2.4 Image Compression Model

The algorithm used in a practical image compression system, removes a combination of the above mentioned redundancies. A typical compression system consists of an encoder and a decoder as shown in Fig.2.5. The input image $f(x,y)$ is fed into encoder producing a set of symbols $g(f(x,y))$ describing the image. Then, this set of symbols is transmitted over a communication channel and is fed into decoder and it generates a reconstructed output image $\hat{f}(x,y)$. The encoder is responsible for reducing or eliminating any coding, interpixel or psychovisual redundancies presented in the image. In lossless compression $\hat{f}(x,y)$ is an exact replica of $f(x,y)$.

Fig.2.5 A general image compression system

If the channel between encoder and decoder is not immune to noise, additional measures are required to keep the symbols noise free or less susceptible to noise. This is done by further encoding of the symbols that are produced after compression, by channel encoder. Thus the encoder consists of source encoder, which is responsible for image compression and channel encoder, which is responsible for noise immunity. Similarly decoder also consists of source decoder and channel decoder. If the channel is noise free, the channel encoder and channel decoder can be eliminated. The structure of encoder is depicted in Fig.2.6(a) and the structure of corresponding decoder is depicted in Fig.2.6 (b).

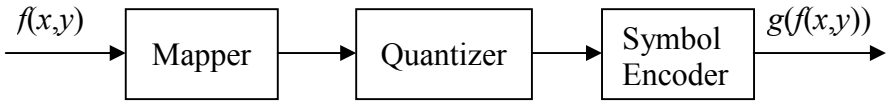

(a) Encoder

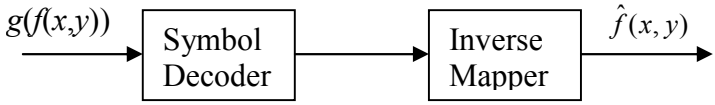

(b) Decoder

Fig.2.6(a) Encoder and (b) decoder model

In the first stage of source encoder, interpixel redundancies are reduced or eliminated by mapper. Psychovisual redundancies are reduced in the second stage by quantizer. The resulting data still contains coding redundancies, which are reduced or eliminated in the next stage by symbol encoder. However for error free compression, quantization stage is omitted. The decoder works in reverse order, applying firstly symbol decoding (inverse operation to symbol encoding) and then inverse mapper to get the original image $f(x,y)$.

2.4.1 Lossless Compression

In many applications, permanent loss of image data during compression is not simply acceptable. This may be due to legal reasons in the case of image archiving, loss of data is not affordable in case of rare and costly images and the loss of data in medical images may deteriorate the diagnostic accuracy. Lossless compression techniques operate by reducing the coding and interpixel redundancy present in the data. The common ways of doing this are by Huffman coding, Arithmetic coding, LZW coding etc. Lossless compression is also known as error free compression or reversible compression. Lossless or reversible compression, provide only low compression ratio. The compression ratios achieved by lossless compression for medical images is generally less than 3:1 [78].

2.4.2 Lossy Compression

Lossy compression techniques use the trade-off between the accuracy of the decoded image and the compression ratio to achieve a greater compression ratio. In most cases, the main difference between the structure of a lossy decoder and a lossless decoder is the presence of a quantizer. The function of the quantizer is to reduce the amount of psychovisual redundant data in the image. In most cases, the decoded images are not distinguishable by subjective evaluation of the human eye.

Lossy or irreversible compression involves at least three steps viz., image transformation, quantization, and encoding. No loss of information occurs in the transformation step whereas in the quantization step, less important coefficients are lost permanently, preserving the most important information [73], [67]. Further lossy encoding results in better compression ratios. Several image compression technique such as SPIHT, JPEG2000-LS, etc. can encode/decode an image from lossy to lossless form. Region of Interest coding technique [27], [11], [80] takes the advantage of both lossy and lossless techniques. In this method, diagnostically important areas called Region of Interest are compressed in lossless way or with high quality, whereas the unimportant areas such as background are compressed in lossy way, there by achieving high compression ratio without loss of important information.

2.5 Predictive Coding

Predictive coding operates by reducing the interpixel redundancy of near located pixels. This type of coding extracts and stores only the new information included in the new pixel. This information is defined by the difference of the pixel and the predicted value of that pixel. The prediction is based on the known values of the closely located pixels. The basic components of a lossless predictive coding system is shown in the Fig. 2.7 below.

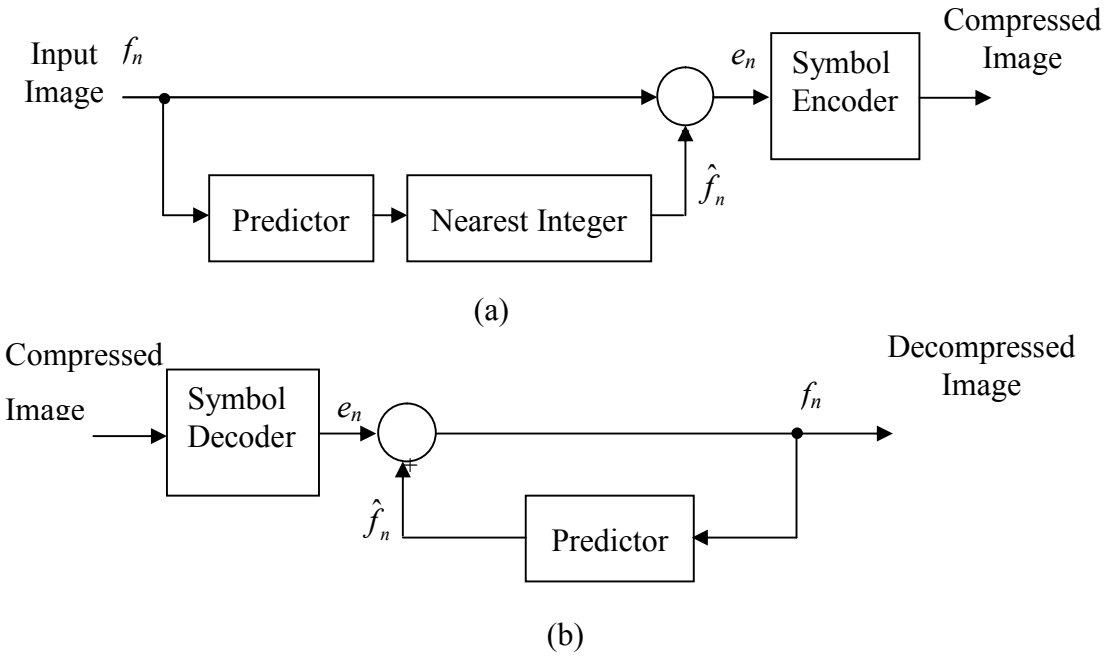

Fig. 2.7 (a) Lossless predictive encoding model (b) Lossless predictive decoding model

The system consists of an encoder and a decoder, each containing an identical predictor. As each successive pixel of the input image, denoted f_n, is introduced to the encoder, the predictor generates the anticipated value of that pixel based on some number of past inputs. The output of the predictor is then rounded to nearest integer, denoted $\hat{f}_n$ and used to form the difference or prediction error, $e_n = f_n - \hat{f}_n$. It is then coded using a variable-length code to generate the next element of the compressed data stream.

The decoder reconstructs e_n from the received variable length code words and performs the inverse operation.

$$f_n = e_n + \hat{f}_n \tag{2.5}$$

The prediction can be formed by a linear combination of 'm' previous pixels.

$$\hat{f}_n = \text{round}\left[\sum_{i=1}^{m} \alpha_i f_{n-i}\right] \tag{2.6}$$

Where m is the order of linear predictor and α_i for $i = 1,2,\ldots,m$ are prediction coefficients.

Conceptually, a lossless predictive coding scheme can be divided into modelling and coding phase [14]. In the modelling phase, information about the image data is collected as a probabilistic model to be used in the coding phase. The image data is processed in some fixed order, usually raster scan. A finite subset of the previously coded neighbouring pixel values

C^T, called a casual template, (e.g., $C^{12} = \{x_1, x_2, x_3, \ldots, x_{12}\}$, as shown in Fig.2.8 is chosen for making an inference of the current pixel value $x_{i,j}$, which is being predicted. The significance of causal template is that, the pixel values therein are coded previously and these values will be available with the decoder as well. The current pixel value can be estimated by assigning a conditional probability distribution $P(\cdot|C^T)$, conditioned on the causal template or the context. In the coding phase, the code assignment is carried out based on this conditional probability. The minimum code length that can be assigned to the pixel $x_{i,j}$, based on the given probabilistic model can be calculated as $-\log_2 P(x_{i,j}|C^T)$. The average of these values gives the entropy of the probabilistic model. Thus, the main pursuit of a lossless compression scheme is to model the context efficiently to obtain minimum entropy value.

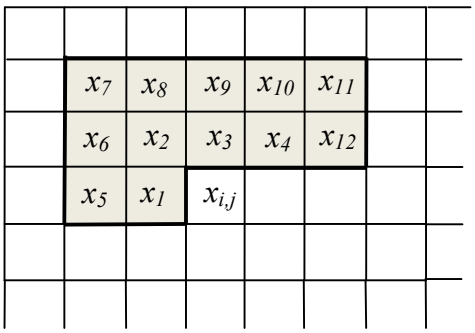

Fig.2.8 $x_{i,j}$ is the current pixel being predicted and $C^{12} = \{x_1, x_2, ..., x_{12}\}$ is a casual template (shaded region) with 12 neighboring pixels

2.5.1 Benchmark Algorithms

The basic structure in most of the lossless predictive coding scheme, as pioneered by the Sunset [86] algorithm, consists of pixel value prediction from causal neighbouring pixels, modelling of prediction errors and entropy coding. In this paradigm, the modelling phase is divided into prediction stage and error modelling stage. The two benchmark lossless compression techniques viz., LOCO-I [94] and CALIC [98], which follow this predictive coding scheme are briefly described below.

2.5.1.1 LOCO-I

LOCO-I is used at the core of the ISO standard for lossless image compression, JPEG-LS. It uses a predictor called Median Edge Detector (MED) for predicting the current pixel from its three neighboring pixels (N, NW, W), as shown in Fig.2.9. The predictor is able to accurately

predict horizontal, vertical and -45^o edge orientations. Context modeling is done to compensate for the error in prediction.

NW	N	NE
W	$x_{i,j}$	

Fig.2.9 $x_{i,j}$ – is the current pixel predicted from the neighboring pixels, W, N and NW

$$x_{i,j} = \begin{cases} \left.\begin{matrix} \min(W,N), \text{if } NW \geq \max(W,N) \\ \max(W,N), \text{if } NW \leq \min(W,N) \end{matrix}\right\} Edge \\ W + N - NW \quad \text{otherwise} \end{cases} \tag{2.7}$$

Contexts are determined by obtaining the local gradients G1, G2 and G3 of the neighboring pixels as shown below. The higher order structures like texture patterns and local activity of the image can be detected from the local gradients.

$$G1 = NE - N \tag{2.8}$$

$$G2 = N - NW \tag{2.9}$$

$$G3 = NW - W \tag{2.10}$$

The gradients G1, G2, and G3 are quantized into 9 regions and the regions are indexed from -4 to 4. With the assumption on the prediction error probability

$$P(e \mid [q1, q2, q3]) = P(-e \mid [-q1, -q2, -q3]) \tag{2.11}$$

There are a total of 365 contexts. Prediction bias for each context is calculated by dividing cumulative prediction error for each context by the number of occurrence of the respective contexts. Golomb-Rice coding [31]is used further to remove the coding redundancy .

2.5.1.2 CALIC

CALIC operates in two modes viz., binary mode and continuous-tone mode. If the local pixels contain only two different values, it operates in binary mode, or else it operates in continuous-tone mode. In continuous-tone mode, CALIC employs a prediction scheme called GAP (Gradient-Adjusted Predictor) which is a gradient based nonlinear prediction scheme. The current pixel is predicted from the neighboring pixels, by applying predetermined weights,

depending on the difference in the horizontal and the vertical gradient. Context modeling and error feedback is done to further improve the prediction accuracy. Finally, the error data is entropy coded using an adaptive arithmetic coder.

Context modeling and error feedback used in CALIC provides substantial compression gain, by further exploring the complex relationships such as texture patterns. Seven causal neighboring pixels (W, N, WW, NW, NE, NN, NNE), as shown in Fig.2.10 are used for context modeling.

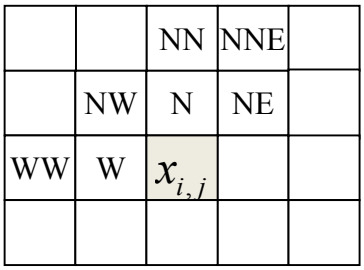

Fig.2.10 Seven Causal neighbours (W, N, WW, NW, NE, NN, NNE) used to calculate vertical and horizontal gradient of $x_{i,j}$.

The vertical gradient 'dv' and horizontal gradient 'dh' are calculated as the sum of absolute difference among the horizontal and vertical neighboring pixels. An energy estimator 'Δ' is calculated from the horizontal gradient, vertical gradient and the previous prediction error 'e_W'. The estimated energy is quantized into four regions, in order to reduce the model cost.

$$dv = |W - NW| + |N - NN| + |NE - NNE| \tag{2.12}$$

$$dh = |W - WW| + |N - NW| + |NE - N| \tag{2.13}$$

$$\Delta = dv + dh + 2.e_W \tag{2.14}$$

From a local neighborhood of eight pixel values (N, W, NW, NE, NN, WW, 2.N-NN, 2.W-WW), texture context 'C' is formed by using the predicted pixel value $x_{i,j}$ as the threshold. 'C' is quantized into an 8-bit binary number 'B' i.e.,

$$C = \{N,\ W,\ NW,\ NE,\ NN,\ WW,\ 2.N - NN,\ 2.W - WW\} \tag{2.15}$$

$$B = \{b_0,\ b_1,\ b2..b_i,..\ b_7\} \tag{2.16}$$

where,

$$b_i = \begin{cases} 0, \text{if } C_i \geq x_{i,j} \\ 1, \text{if } C_i < x_{i,j} \end{cases} \tag{2.17}$$

The quantized error energy Q(Δ) together with the quantized texture pattern B forms the final context model. The expected error is estimated for each of the contexts and is updated after each prediction step. The expected error is used to further improve the prediction accuracy. Sign flipping is yet another technique used to reduce the error entropy. Underlying concept is to predict the sign of the prediction error from the estimated expected error. If the expected error is negative, then prediction error is sign flipped, else it is not sign flipped. This results in the concentration of the prediction errors more over the positive axis, rather than spreading over both positive and negative axes.

2.6 Transform Coding

In the transform coding approach, a transformations that operate on an image to produce a set of coefficients is used. A subset of these coefficients is selected appropriately, quantized and entropy coded to produce the compressed image. The transformation is chosen in such a way that, a subset of coefficients is adequate to reconstruct the image with a minimum noticeable distortion. The optimal linear transformation with respect to minimizing the mean squared error (MSE) is the Karhunen-Loeve transformation (KLT). The KLT produces uncorrelated coefficients and results in the most efficient coding of the data. However, the computational complexity of KLT is high. Fixed-basis transforms such as the discrete cosine transform (DCT) [3], and discrete wavelet transform (DWT) has less computational complexity and are used in many compression algorithms [89], [88]. The Joint Photographics Expert Group (JPEG) [50] uses the DCT at for transformation stage.

2.6.1.1 The JPEG Standard

JPEG is a lossy/lossless compression method for colour or grayscale still images [90], [50]. The JPEG standard first transforms image data into the frequency domain using the discrete cosine transform (DCT). The data is then quantized and entropy coded. There are two main modes: lossy and lossless. In the JPEG image compression algorithm, the input image is divided into 8-by-8 blocks, and the two-dimensional DCT is computed for each block. The DCT coefficients are then quantized, coded and transmitted. The JPEG receiver decodes the quantized DCT coefficients, computes the inverse two-dimensional DCT of each block and then puts the blocks back together into a single image. For typical images, many of the DCT coefficients have

values close to zero; these coefficients can be discarded without seriously affecting the quality of the reconstructed image. A block diagram shown in Fig.2.11 illustrates the process involved in the JPEG compression scheme.

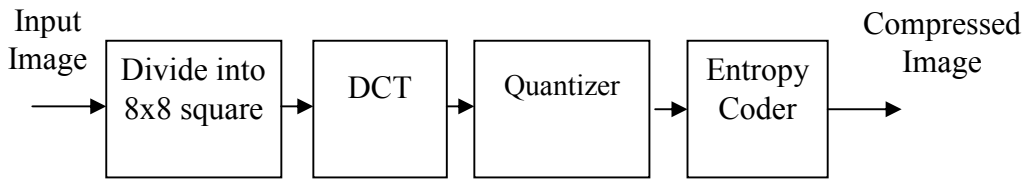

Fig.2.11 Block diagram of JPEG coding scheme

The DCT is performed by way of matrix multiplication. The resulting matrix is then processed in a quantization stage in which a user specified quality factor, usually between 1 and 100, is utilized to define quantum steps. It is in this stage that loss occurs as high frequency components of the matrix are in effect zeroed out. This stage is the significant component of this compression technique in that the user has the trade-off decision between file size and data loss. The greater the quality factor the greater the compression ratios and image degradation. Finally the quantized matrix is encoded. This encoding is a lossless procedure and utilizes any of the variable length encoding methods like Huffman coding.

2.6.1.2 The JPEG2000 Standard

JPEG2000 [21], [111] extends the initial JPEG standard. The standard is based on the Wavelet transform coding technique departing from the block based DCT coding used by existing JPEG. It delivers better quality than JPEG and allows scalability without having to store redundant data. Coefficient quantization is adapted to individual scales and sub-bands and the quantized coefficients are arithmetically coded on a bit-plane basis.

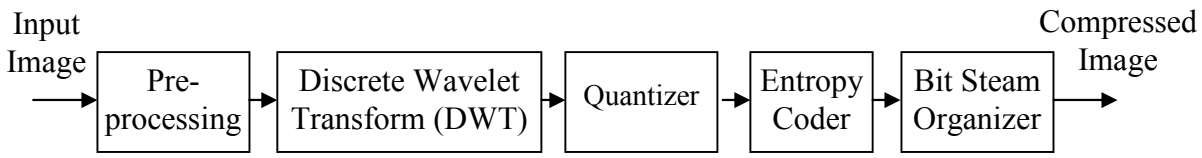

Fig.2.12 Block diagram of JPEG2000 coding scheme

Fig.2.12 illustrates the basic building blocks of JPEG2000. A pre-processing step which typically consists of tiling, dc level shifting and multi component transform, then a DWT is

applied. It is then followed by a quantizer, an entropy coder and, finally, a bit stream organization step to prepare the final codestream of the compressed image.

2.7 Vector Quantization

Vector quantization (VQ) employs a set of representation vectors (for the one-dimensional case) or matrices (for the two-dimensional case) [51], [41], [54], [52]. The set is referred to as the "codebook" and the entries as "code-words". The high degree of correlation between neighboring pixels can be exploited in vector quantization. In the coding phase, the image is subdivided into blocks, typically of a fixed size of n× n pixels. For each block, the nearest codebook entry under the distance metric is found and the ordinal number of the entry is transmitted. On reconstruction, the same codebook is used and a simple look-up operation is performed to produce the reconstructed image. The standard approach to calculate the codebook is by way of the Linde, Buzo and Gray (LBG) algorithm [41]. Initially, K codebook entries are set to random values. On each iteration, each block in the input space is classified, based on its nearest codeword. Each codeword is then replaced by the mean of its resulting class. The iterations continue until a minimum acceptable error is achieved. This algorithm minimizes the mean squared error over the training set.

2.8 Dataset Details

For validation, testing and comparative analysis of the proposed algorithms, medical image datasets are collected from five sources. The dataset details are given below:

2.8.1 Center for Image Processing Research (CIPR) Dataset

This dataset consists of CT and MR images, which are collected from CIPR [106], Rensselaer Polytechnic Institute. The dataset consists of the following images as shown in Table 2.1

Table 2.1 CIPR dataset details

TAG	Sequence Name	Modality	Plane	Image Size	Slices
CIPR-CT-01	CT_Aperts	CT	Axial	256x256	97
CIPR-CT-02	CT_carotid	CT	Axial	256x256	74
CIPR-CT-03	CT_skull	CT	Axial	256x256	203
CIPR-CT-04	CT_wrist	CT	Sagittal	256x256	183
CIPR-MR-01	MR_liver_t1	MR	Axial	256x256	77
CIPR-MR-02	MR_liver_t2e1	MR	Axial	256x256	58
CIPR-MR-03	MR_ped_chest	MR	Axial	256x256	58
CIPR-MR-04	MR_sag_head	MR	Sagittal	256x256	58

2.8.2 Massachusetts General Hospital (MGH) Dataset

This dataset is collected from MGH Dataset Center for Morphometric Analysis internet brain segmentation Repository (IBSR) [113]. All scans were acquired at the NMR Center of Massachusetts General Hospital with 1.5 T General Electric Signa. This dataset consists of following images as shown in Table 2.2:

Table 2.2 MGH dataset details

TAG	Sequence Name	Modality	Plane	Image Size	Slices
MGHD-MR-01	657_10	MR (PD)	Coronal	256x256	18
MGHD-MR-02	657_2	MR (T1)	Coronal	256x256	18
MGHD-MR-03	657_11	MR (T2)	Coronal	256x256	18

2.8.3 MicroDicom Dataset

This dataset consists of DICOM images of MR sequences-T1-weighted, T2-weighted, post contrast T1-weighted and Flair images of normal subjects in coronal, axial and sagittal plane. All scans were acquired at Toronto Tri-Hospital MR Centre with 1.5 T General Electric Genesis Signa [114]. The dataset consists of thefollowing image sequences as shown in Table 2.3.

Table 2.3MicroDicom dataset details

TAG	Sequence Name	Modality	Plane	Image Size	Slices
MIDI-MR-01	SAG-T1	MR	Sagittal	512x512	13
MIDI-MR-02	COR-T1	MR	Coronal	512x512	20
MIDI-MR-03	COR-FSE-T2	MR	Coronal	512x512	20
MIDI-MR-04	COR-FLAIR	MR	Coronal	512x512	12
MIDI-MR-05	AX-FSE-T2	MR	Axial	512x512	18
MIDI-MR-06	COR-T1-POST-GAD	MR	Coronal	512x512	15
MIDI-MR-07	SAG-T1-POST-GAD	MR	Sagittal	512x512	15

2.8.4 Physionet Dataset

This dataset consist of DICOM images of MR sequences as shown in Table 2.4. The scan was acquiredwith 1.5T General Electric (GE) Signa imaging system [116].

Table 2.4Physionet dataset details

TAG	Sequence Name	Modality	Plane	Image Size	Slices
PHNT-MR-01	E1154S7I	MR	Coronal	512x512	76

2.8.5 OsiriX Dataset

This dataset consists of DICOM images of CT, MR, PET and Angiogram sequences [115]. This dataset consists of following image sequences as shown in Table 2.5.

Table 2.5OsiriX dataset details

TAG	Sequence Name	Modality	Plane	Image Size	Slices
OSRX-CT-01	BREBIX_01	CT	Axial	512x512	244
OSRX-CT-02	MAGIX_01	CT	Axial	512x512	76
OSRX-MR-01	BRAINIX_01	MR	Axial	512x512	22
OSRX-MR-02	CEREBRIX_05	MR	Coronal	270x320	28
OSRX-MR-03	CEREBRIX_06	MR	Axial	364x448	24
OSRX-MR-04	CEREBRIX_08	MR	Axial	320x384	29
OSRX-PT-01	CEREBRIX_02	PET	Axial	336x336	82
OSRX-XA-01	GUSERAMBIX_11	Angiogram	Coronal	512x512	13
OSRX-XA-02	GUSERAMBIX_01	Angiogram	Coronal	512x512	75

2.9 Evaluation criteria

For quantitative analysis, the following parameters are used to evaluate the proposed methods. These parameters are described below:

2.9.1 Bits per pixel

Bits per pixel (bpp) represents the average number of bits required to represent each pixel of the image. The total number of bits in the image data is divided by the total number of pixels in the image to find the bpp value as given by:

$$bpp = \frac{n_b}{M \times N}. \tag{2.18}$$

where, n_b is the number bits of the output code-stream, $M \times N$ are the number of rows and columns in an image [32].

2.9.2 First order entropy

Entropy is the measure of average information content present in a data. The first order entropy [32] can be calculated from a frequency distribution of symbol sets as:

$$H(z) = -\sum_{i=1}^{L} P(a_i) \log P(a_i). \tag{2.19}$$

where, $P(a_i)$ is the probability of the symbol a_i in the data set containing L symbols.

2.9.3 Mean square error

Mean square error (MSE) [32], [56] measures the average of the squares of the prediction errors.

$$MSE = \frac{1}{M \times N} \sum_{i=1}^{M} \sum_{j=1}^{N} \left(x_{i,j} - \hat{x}_{i,j} \right)^2. \tag{2.20}$$

where, $x_{i,j}$ is the pixel value of the i^{th} row and j^{th} column of the original image and $\hat{x}_{i,j}$ is the i^{th} row and j^{th} column of the predicted image.

2.9.4 Peak absolute error

Peak absolute error (PAE) is the maximum absolute error of the reconstructed image. PAE is calculated as:

$$PAE = \left\{ \max(abs(x_{i,j} - \hat{x}_{i,j})) \mid i = 1,2,...M, j = 1,2,...N \right\})) \tag{2.21}$$

where, $x_{i,j}$ is the pixel value of the i^{th} row and j^{th} column of the original image and $\hat{x}_{i,j}$ is the i^{th} row and j^{th} column of the predicted image.

2.9.5 Peak signal to noise ratio

Peak signal to noise ratio (PSNR) [32] for an 8-bit image is:

$$PSNR = 10.\log_{10} \left[\frac{(255)^2}{MSE} \right] dB. \tag{2.22}$$

2.9.6 Universal quality index

Universal quality index (UQI) measures image quality based upon three factors namely, loss of correlation, luminance distortion and contrast distortion [92]. The UQI is reported to perform significantly better than MSE and PSNR in the measurement of images distortion. It is

formulated based on the assumption that the human visual system (HVS) is highly capable of extracting structural information from an image. If $x = \{x_i \mid i = 1, 2, ..., N\}$ is the original image signal and $y = \{y_i \mid i = 1, 2, ..., N\}$ is the test image signal, the UQI calculated over an image block BxB as:

$$Q(x, y) = \frac{4\sigma_{xy}\overline{x}\overline{y}}{(\sigma^2{}_x + \sigma^2{}_y)[(\overline{x})^2 + (\overline{y})^2]}. \tag{2.23}$$

where,

$$\overline{x} = \frac{1}{N}\sum_{i=1}^{N} x_i. \tag{2.24}$$

$$\overline{y} = \frac{1}{N}\sum_{i=1}^{N} y_i. \tag{2.25}$$

$$\sigma^2{}_x = \frac{1}{N-1}\sum_{i=1}^{N} (x_i - \overline{x})^2. \tag{2.26}$$

$$\sigma^2{}_y = \frac{1}{N-1}\sum_{i=1}^{N} (y_i - \overline{y})^2. \tag{2.27}$$

$$\sigma_{xy} = \frac{1}{N-1}\sum_{i=1}^{N} (x_i - \overline{x})(y_i - \overline{y}). \tag{2.28}$$

If there are M blocks, then the overall image quality index is given by:

$$Q(X, Y) = \frac{1}{M}\sum_{j=1}^{M} Q(x_i, y_j) \tag{2.29}$$

2.9.7 Mean structural similarity index

The mean structural similarity index (MSSIM) [93] is derived from UQI. It measures the structural distortion of the reconstructed image. The SSIM for a block of image is given by:

$$SSIM(x, y) = \frac{(2\overline{x}\overline{y} + C_1)(2\sigma_{xy} + C_2)}{[(\overline{x})^2 + (\overline{y})^2 + C_1](\sigma^2{}_x + \sigma^2{}_y + C_2)}. \tag{2.30}$$

where,

$$\bar{x} = \frac{1}{N}\sum_{i=1}^{N} w_i x_i. \tag{2.31}$$

$$\bar{y} = \frac{1}{N}\sum_{i=1}^{N} w_i y_i. \tag{2.32}$$

$$\sigma^2{}_x = \frac{1}{N-1}\sum_{i=1}^{N} w_i (x_i - \bar{x})^2. \tag{2.33}$$

$$\sigma^2{}_y = \frac{1}{N-1}\sum_{i=1}^{N} w_i (y_i - \bar{y})^2. \tag{2.34}$$

$$\sigma_{xy} = \frac{1}{N-1}\sum_{i=1}^{N} w_i (x_i - \bar{x})(y_i - \bar{y}). \tag{2.35}$$

$w = \{w_i \mid i = 1, 2, ..., N\}$ is a circular-symmetric Gaussian weighing function, C_1 and C_2 are constants added to avoid instability when $(\bar{x})^2 + (\bar{y})^2$ is closed to zero. The overall quality of the image is calculated as:

$$MSSIM(X, Y) = \frac{1}{M}\sum_{j=1}^{M} SSIM(x_i, y_j) \tag{2.36}$$

2.10 Summary

The design methodology to achieve the research objectives is presented in this chapter. The datasets used and the evaluation criteria for the proposed compression algorithm are also presented here. The detailed proposed algorithm for DL-DPCM, lossless image compression based on DL-DPCM, near lossless compression, RoI compression, resolution scalable compression are discussed in the subsequent chapters.

Chapter 3

Lossless Compression of Medical Images

3.1 Introduction

Non-degraded images are essential for radiologists to interpret disease and to extract related diagnostic information. However, lossy compression alters the texture parameters of an image. Therefore, it may affect the diagnostic accuracy when interpreted by a radiologist. The accuracy of a computer aided diagnosis (CAD) system is also affected when lossy compressed image is used. In addition, legal reasons may require the medical images to be preserved without any loss of information. Therefore, lossless compression techniques are used most often to store medical images. Among the lossless compression techniques developed in the past years, predictive coding techniques were more successful and generally achieved higher compression ratio than transform coding or vector quantization techniques.

A lossless compression technique using a dual level DPCM (DL-DPCM) namely DLD-LS is proposed in this chapter. The DLD-LS is described in the following sections.

3.2 Lossless compression using dual level DPCM

The block diagram of the proposed lossless image compression method, DLD-LS is shown in Fig. 3.1. In this scheme, the image is encoded sequentially, pixel by pixel, in a raster scan order. The DLD-LS operates in two modes – run mode and predictive mode. If the three adjacent neighboring pixels of the current pixel being predicted are equal, the DLD-LS operates in run mode. Run mode is efficient when the pixels values are constant. The DLD-LS switches to predictive mode when the run is broken.

In the predictive mode, the inter-pixel redundancies present in the input image data are removed in two stages by two DPCM which are cascaded *viz*., 2D-linear differential pulse code modulator (2D-LDPCM) followed by context adaptive switching neural network predictor (CAS-NNP). The 2D-LDPCM produces an error image, which is the difference between the original image and the predicted image based on a subset of previously encoded pixels called the causal template. The CAS-NNP, which is adaptive and nonlinear, further removes the redundancies present in the error image.

There are three NN predictors namely NNP1, NNP2 and NNP3; each optimized to predict a specific area in the image *viz*., plain-region, gradient-region and edge-region. The context

texture switch (CTS) identifies the different regions of the image by texture analysis of the causal template. Finally, the prediction error of CAS-NNP is entropy coded using context adaptive arithmetic coding after pre-processing to produce a binary output code-stream. The data size of the resulting binary code-stream will be less than the original image and the original image can be reconstructed from it without error.

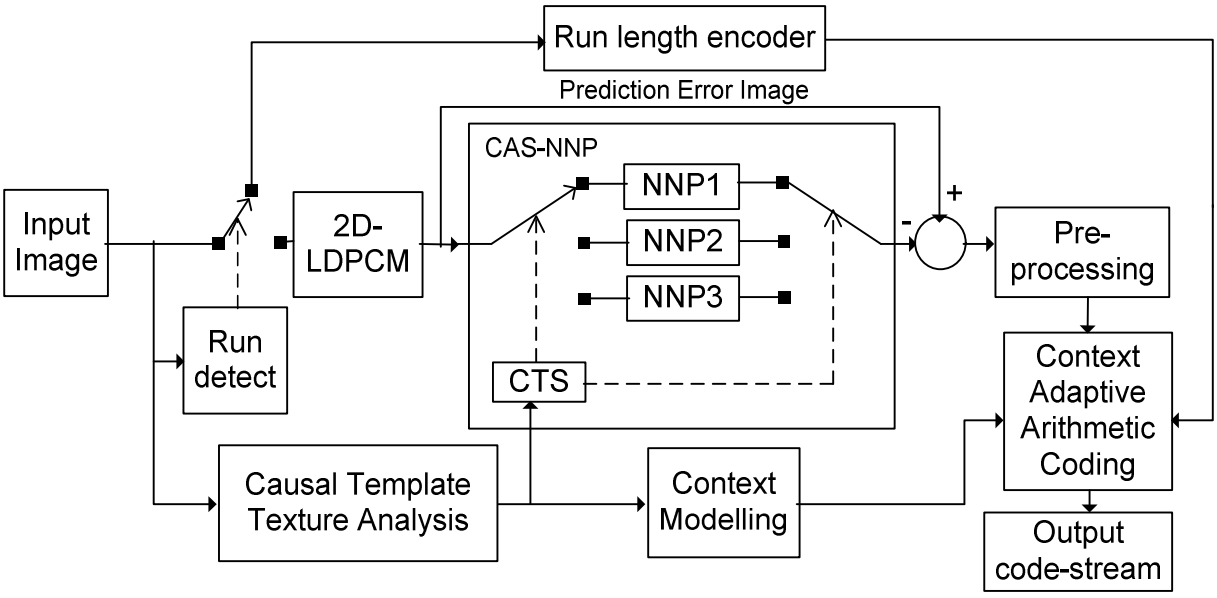

Fig. 3.1 Flow diagram of the proposed lossless image compression technique (DLD-LS) using the DL-DPCM.

3.2.1 Differential pulse code modulation

The differential pulse code modulation (DPCM) is a predictive decorrelation method. In DPCM, the current value of a signal is predicted from previously encoded values. The predicted value is subtracted from the original value to get the error signal. The error will be small when the predicted signal nears to the original signal. An error signal containing mostly small values will have a peaked histogram, which can be efficiently coded by a variable length coder.

A two-dimensional DPCM (2D-DPCM) is most suitable for decorrelation of images, which are essentially two-dimensional signals. The 2D-DPCM predicts the current pixel value in a raster scan order from a causal template of neighboring pixels.

Fig.3.2 shows a causal template of 12 neighboring pixels, $\{x_1, x_2, ..., x_{12}\}$ and the pixel to be predicted, $x_{i,j}$. The significance of the causal template is that, it contains only the pixels that are already predicted in the raster scan order. During decompression, the same will be available at the decoder side as well.

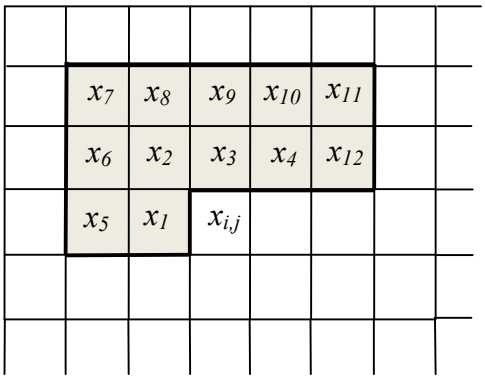

Fig.3.2 $x_{i,j}$ is the current pixel being predicted and $C^{12} = \{x_1, x_2, ..., x_{12}\}$ is a casual template (shaded region) with 12 neighboring pixels.

Consider an image, x having $M \times N$ rows and columns, with pixel values $x_{i,j}, i = 1,2,...,M, j = 1,2,...,N$. The causal template C^N, with N number of neighboring pixels is defined as:

$$C^N = \{x_k : k = 1,2,...,N\}. \tag{3.1}$$

The predicted pixel value $\hat{x}_{i,j}$, in a 2D linear DPCM (2D-LDPCM) scheme is given by:

$$\hat{x}_{i,j} = \sum_{k=1}^{N} \alpha_k x_k. \tag{3.2}$$

where, $\alpha_k, k = 1,2,...,N$ are predictor coefficients.

The prediction error is the difference between the original pixel value $x_{i,j}$ and the predicted value $\hat{x}_{i,j}$:

$$\varepsilon_{i,j} = x_{i,j} - \hat{x}_{i,j}. \tag{3.3}$$

3.2.1.1 2D-LDPCM

A causal template with four neighboring pixels is used in the 2D-LDPCM for pixel value prediction as shown in Fig.3.3..

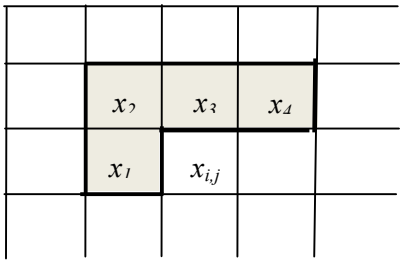

Fig.3.3 $C^4 = \{x_1, x_2, x_3, x_4\}$ is the casual template (shaded region) used by 2D-LDPCM to predict the pixels $x_{i,j}$

Firstly, an initial approximation of $x_{i,j}$ is obtained by taking the average of two nearest neighboring pixel values x_1 and x_3. Therefore, the value of coefficients corresponding to x_1 and x_3 (i.e. α_1 and α_3) is taken as ½.

$$\begin{aligned} x_{i,j}(\text{initial}) &= \alpha_1.x_1 + \alpha_3.x_3 \\ &= (½).x_1 + (½).x_3. \end{aligned} \tag{3.4}$$

However, further improvement in prediction of $x_{i,j}$ can be obtained by adding the difference between x_2 and x_4 to the initial prediction value. As the distance between x_2 and x_4 is double the distance between x_1 and $x_{i,j}$, magnitude of the coefficients of x_2 and x_4 (i.e. α_2 and α_4) are taken as half of α_1 and α_3.

$$\begin{aligned} x_{i,j}(\text{final}) &= x_{i,j}(\text{initial}) + \alpha_2.x_1 + \alpha_4.x_4 \\ &= (½).x_1 + (½).x_3 + (-¼).x_2 + (¼).x_4. \end{aligned} \tag{3.5}$$

Therefore, the set of coefficients used to predict $x_{i,j}$ from the causal template are:

$$\alpha = \{\tfrac{1}{2}, \tfrac{-1}{4}, \tfrac{1}{2}, \tfrac{1}{4}\}. \tag{3.6}$$

3.2.2 Artificial Neural Network

The structure of an artificial neural network with one input layer, one hidden layer and one output layer is shown in Fig.3.4. The neurons of the input layer are connected to the hidden layer by the weight matrix W^1 and that of hidden layer are connected to output layer by the weight matrix W^2. The number of layers and the number of neurons in each layer are chosen depending on the complexity of the problem by hit and trial method. The output of the individual neuron is the weighted sum of inputs and bias value, mapped by an activation

function as shown in Eq. (3.7), where w_i is the weight, x_i is the input to the neuron and b_i is the bias.

$$y = f(\sum w_i.x_i + b_i). \tag{3.7}$$

Activation function can be either linear or nonlinear. The two commonly used nonlinear activation functions are sigmoid as depicted in Eq. (3.8) and hyperbolic tangent sigmoid function as depicted in Eq. (3.9).

$$f(n) = \frac{1}{1+e^{-n}}. \tag{3.8}$$

$$f(n) = \frac{2}{1+e^{-2n}}. \tag{3.9}$$

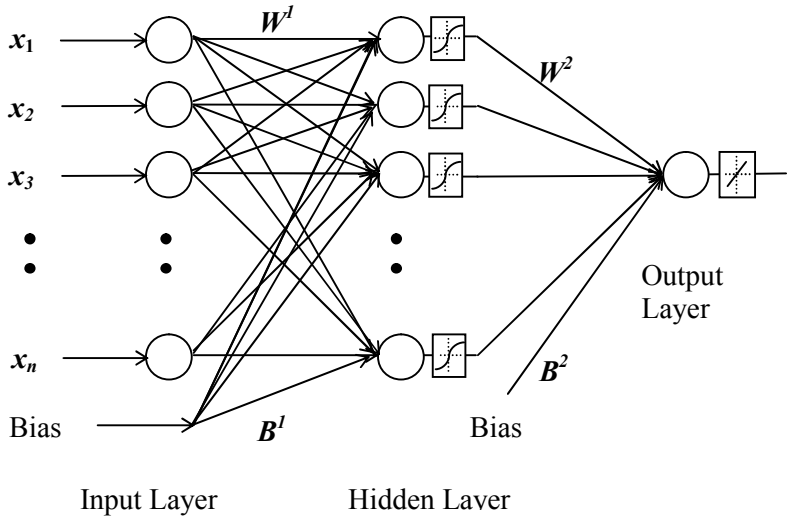

Fig.3.4 The structure of an artificial neural network

The network weights and bias can be optimized by back-propagation algorithm. The standard back-propagation is a gradient descent method, in which the network weights are moved along the negative gradient of the performance function, calculated as:

$$\mathbf{x}_{k+1} = \mathbf{x}_k - \alpha_k \mathbf{g}_k. \tag{3.10}$$

where $\mathbf{x}_k$ is a vector of current weights and biases, $\mathbf{g}_k$ is the current gradient, and α_k is the learning rate.

Improved learning performance are achieved by a variety of quasi-Newton algorithms and by using computational intelligence [16].

3.2.2.1 Levenberg-Marquardt algorithm

The Levenberg-Marquardt (LM) algorithm [33] is a nonlinear least square algorithm used to approach a second-order training speed. When the performance function is computed as the mean square error, the Hessian matrix **H** can be approximated from the Jacobian matrix as:

$$\mathbf{H} = \mathbf{J}^{\mathrm{T}}.\mathbf{J}. \tag{3.11}$$

where **J** is the Jacobian matrix.

The Jacobian matrix contains first derivatives of the network errors with respect to the weights and biases. It can be computed through a standard back-propagation technique, which is less complex than computing the Hessian matrix.

The gradient **g** is computed as:

$$\mathbf{g} = \mathbf{J}^{\mathrm{T}}.\mathbf{e}. \tag{3.12}$$

where **e** is a vector of neural network errors.

The Levenberg-Marquardt algorithm updates the network parameters as:

$$\mathbf{x}_{k+1} = \mathbf{x}_k - [\mathbf{J}^{\mathrm{T}}\mathbf{J} + \mu\mathbf{I}]^{-1}\mathbf{J}^{\mathrm{T}}\mathbf{e}. \tag{3.13}$$

where $\mathbf{x}_k$ is a vector of current weights and biases, μ is a scalar parameter.

Eq. (3.13) reduces to Newton's method, if μ is zero. If μ is large, it becomes a gradient descent method. Newton's method is faster and more accurate near an error minimum. Therefore, μ is decreased after a successful iteration and increased when an iteration would increase the performance function. This procedure ensures the reduction of performance function after each iteration.

3.2.2.2 Neural network predictor

Neural networks have the capability to model nonlinear functional relationships. They also have the ability of adapting to different classes of input data, by means of training. Since neural networks are parallel in architecture, they can also work efficiently with parallel computing hardware, where the computation time is reduced considerably.

A neural network (NN) architecture with I number of input neurons, H number of hidden layer neurons and O number of output layer neurons (I:H:O) is considered in the present work. The NN architecture (I:H:O)→(16:16:1) was decided empirically after repeated experimentation for different number of input layer neurons I $\in$ {4,6,8,...,16} and different number of hidden layer neurons H $\in$ {2,4,8,….,16}. It was observed that the NN architecture (I:H:O)→(16:16:1) yields the best performance in terms of prediction accuracy. The linear activation function gives a better accuracy, while nonlinear activation functions are used when the input – output relationship is nonlinear. Hence, hyperbolic tangent sigmoid activation function is used for the hidden layer and linear activation function is used for the output layer.

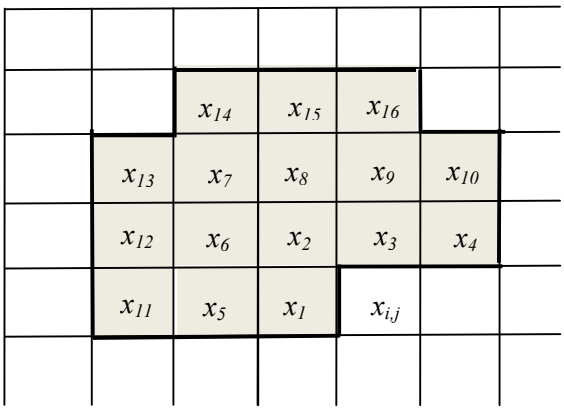

Fig.3.5 $C^{16} = \{x_1, x_2, ..., x_{16}\}$ is the casual template (shaded region) used by NNP to predict the pixels $x_{i,j}$

Levenberg-Marquardt algorithm is used for training as it is much faster than the gradient descent search methods. Training data is prepared with 16 causal neighbouring values (Fig.3.5) as input data set and the pixel to be predicted as the target. This is taken from the whole error image produced by the 2D-LDPCM.

During the learning process, the NN predictor forms a relationship model between the neighbouring pixel values and the pixel value to be predicted. The learning process can be viewed as encoding the global image characteristics into the neural network. Thus, it is required to transmit the weight and bias values of the NN predictor to the decoder as side information. For the present case, there are 256 elements in the weight matrix W^1, each element representing a connection from input layer neuron to hidden layer neuron, and 16 elements in the weight matrix W^2, connecting hidden layer to the output layer. Similarly, there are 16 bias values for each neuron in the hidden layer and one bias value at the output layer. Thus, a total of 289 elements are transmitted as header information to the decoder. Using 16-bit floating point

representation for each element, total of 4624 bits are sent as side information. This produces an overhead of 0.0176 bpp for a 512×512 gray scale image.

While predicting the pixels at the edges, some of the causal neighbouring pixel (or all of the neighbouring pixels in the case of the first pixel) are absent. This difficulty is overcome by padding the image with grey level value of 128. The use of other padding schemes, such as mirror padding will require transmitting the border pixel values to the decoder in advance, which will the overall bits per pixel (bpp) value.

3.2.3 Dual level DPCM

A linear predictor cannot accurately estimate a pixel from its causal template, since a nonlinear relationship exists between them. Different sub-images blocks in an image have different mean pixel values. Since superposition theorem does not hold good for a nonlinear predictor, same variations in the causal template with mean value will be presented to nonlinear predictor as different classes of inputs.

Improvements such as reduced complexity, higher accuracy and reduced learning time can be achieved if the mean value is subtracted from the causal template and only the variation is presented to the inputs of the nonlinear predictor. One method to realize this is to divide the image into many blocks of sub-images andsubtract the block mean value from each block. However, in this case the block mean value needs to be transmitted to the decoder, which will decrease the overall coding efficiency. Moreover, this will introduce sharp changes at the block edges, since the block mean values will be different for different blocks.

The error signal obtained by subtracting the linear predictor estimate of an image from the original image will be automatically normalized. In this case there is no need to transmit any value to the receiver end and the sharp changes due to mean value subtraction will not be introduced as in the former case. Therefore, in the proposed method a linear DPCM (2D-LDPCM) is cascaded with a nonlinear DPCM (CAS-NNP) to achieve a higher overall coding efficiency.

3.2.3.1 Context adaptive switching

Since the image contains different textures at different areas, a single NN is inefficient to learn the whole pattern. By using three different NN predictors, each NN can be optimized to predict a particular class of texture. This also reduces learning time, since now the input pattern used by the individual NN has less variation compared to the original overall input data.

The image is divided into three different regions: plain-region, gradient-region and edge-region. The different regions in the image are determined from the causal neighbouring pixels, so that the same steps can be carried out by the decoder. This avoids the overhead of sending the side information to detect different regions in the image.

A modified algorithm proposed by Kau *et al*. [38] is used, for detecting the different regions. The variance of data in the plain-region is small, and that of an area with gradient-region and edge-region is large. The histogram will be evenly distributed in the case of gradient-region but in the edge-region, histogram will have two peaks, representing the two sides of an edge. Ten causal neighbouring pixels $x_1, x_2, ..., x_{10}$ (similar to Fig.3.5) are defined as the causal context (C^T) for texture prediction.

In order to estimate the texture, mean μ and variance σ^2 of the context C^T are calculated. If the variance is less than a constant k_1, the texture is estimated as plain region. If the variance is greater than k_1, the texture is determined as gradient or edge region. The pixels in the context C^T are then divided into two sets: the pixels with grey level values less than μ are formed into one group C^{TL} and the other are formed into group C^{TH}.

$$C^{TL} = \{\forall x_i \in C_T : x_i \leq \mu\}. \tag{3.14}$$

$$C^{TH} = \{\forall x_i \in C_T : x_i > \mu\}. \tag{3.15}$$

The variances of C^{TL} and C^{TH} are computed as ${\sigma^2}_L$ and ${\sigma^2}_H$ respectively. The relative variance γ is calculated as:

$$\gamma = \frac{\sigma^2}{0.01 + {\sigma^2}_L + {\sigma^2}_H}. \tag{3.16}$$

A small value, 0.01 is added to the denominator of Eq. (3.16) so that it does not become zero when ${\sigma^2}_L$ and ${\sigma^2}_H$ are both zeros.

A region with an edge will have large variance (σ^2), and small $\sigma^2{}_L$ and $\sigma^2{}_H$ values. Hence, if the variance σ^2 is greater than or equal to k_1 and relative variance γ is greater than or equal to a constant k_2 then the context is estimated as an edge-region. If the variance σ^2 is greater than or equal to k_1 and the relative variance γ is less than k_2, then the context is estimated as gradient-region. In this work, k_1 and k_2 are chosen empirically as 25 and 2 respectively. The algorithm for the texture context estimation is listed below:

Calculate mean μ *and variance* σ^2 *of* C^T

if ($\sigma^2 < k_1$)

    assume: plain-region.

else,

    Group all pixels in C^T *less than* μ *into* C^{TL} *and group the rest to* C^{TH} .

    Calculate the variances $\sigma^2{}_L$ and $\sigma^2{}_H$ *of* C^{TL} *and* C^{TH} *respectively.*

    Calculate the relative variance, $\gamma = \dfrac{\sigma^2}{0.01 + \sigma^2{}_L + \sigma^2{}_H}$

    if ($\gamma < k_2$)

        assume: gradient-region.

    else

        assume: edge-region.

    end

end

3.2.4 Lossless image coding

The prediction error from CAS-NNP is entropy coded after pre-processing, as explained below.

3.2.4.1 Context Modelling and Entropy Coding

An adaptive arithmetic encoder [71] is used for entropy coding the prediction error. The advantages of adaptive arithmetic coding are that there is no need to transmit the symbol frequency table as side information to the decoder and it can encode efficiently when there is a variation in the symbol statistics during the encoding process. The adaptive arithmetic algorithm is inefficient while the frequency of the symbol table is being adapted to the source symbol statistics. Therefore, grouping the symbols into different sets is done which are having different frequency distribution. This improves the coding efficiency. However, for each symbol set, the symbol table is initialized to the same frequency at the beginning of the encoding process. Hence, increasing the number of symbol sets decreases the overall coding efficiency.

In order to improve the coding efficiency, error symbols are divided into different sets based on the contexts of the predicted pixel. The prediction errors are more at the top and left edge of the image and they form a separate set of symbols. A total of 13 different contexts were defined empirically based on the variance σ^2 and the relative variance γ as defined in Eq.(3.16). Contexts with variance up to the value of 121 are classified into 11 classes on a logarithmic scale. Another class is formed with contexts having $\sigma^2 \leq 400$ and $\gamma \leq 64$. The rest of the error symbols are grouped into another class. The following pre-processing is also done to improve the coding efficiency of the arithmetic encoder.

3.2.4.2 Error Remapping

When the image data has a dynamic range [0, L], the prediction error takes values in the range [$-L$, $+L$]. This increases the total number of symbols in the error histogram, and reduces the coding efficiency of the entropy coder. However, for a predicted value $\hat{x}_{i,j}$ of the pixel $x_{i,j}$, this can be mapped into the range [$-L/2$, $L/2-1$] since the error $\varepsilon = x_{i,j} - \hat{x}_{i,j}$ can takes values only in the range [$-\hat{x}_{i,j}$, $L-\hat{x}_{i,j}$].

3.2.4.3 Histogram Tail Truncation

In the error histogram, large error occurs with very less frequency. Coding the values with very small frequency decreases the coding efficiency. The error symbols whose absolute values are larger than four times the standard deviation is replaced with an escape sequence. The corresponding error values are grouped into a separate symbol set and are entropy coded separately.

3.3 Software Implementation

The binary executable of CALIC is provided by X. Wu [105], and that of LOCO-I is provided by HP Labs [112].The algorithm is implemented in MATLAB 9.0 on a PC having Intel® CORE™2 Duo, 2.0 GHz using Neural Network Toolbox. The publically available MATLAB implementation of the arithmetic coder developed by Karl Skretting [104] is used in this work for entropy coding.

3.4 Experimentation Details

In the first part of this work, experiments were carried out with six different datasets for determining the suitable architecture of the NN predictor. Experiments are performed with different casual neighborhood templates used as input to the NNP for predicting pixel values. The eight different causal templates are shown in Fig. 3.6.

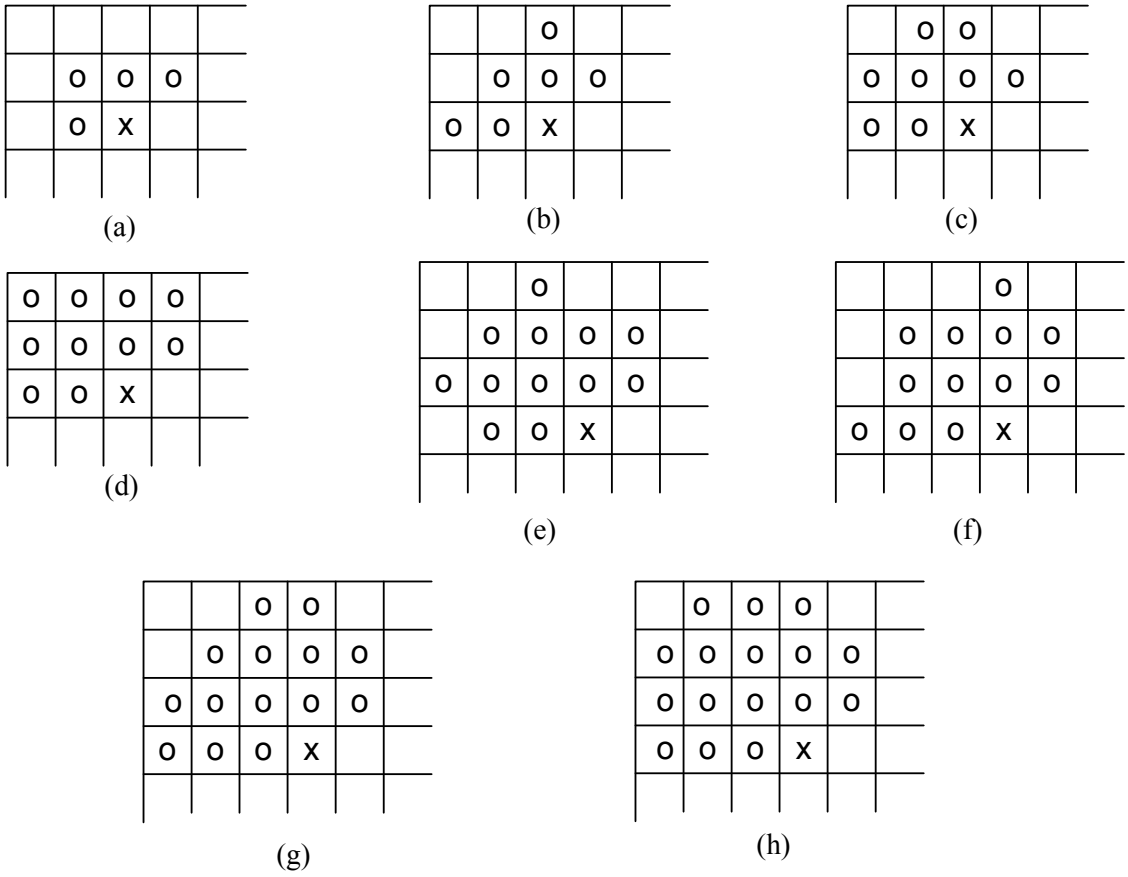

Fig. 3.6 Eight different causal template used to evaluate the performance of NNP. 'O' – represents the neighboring pixel values, 'X' – represents the pixel being predicted. (a) CX1, (b) CX2, (c) CX3, (d) CX4, (e) CX5, (f) CX6, (g) CX7, (h) CX8.

Four different NN architecture, with different activation functions at the hidden layer and output layer were tested for their prediction capabilities.

Table 3.1 Four different NN architecture used to test the prediction performance of the NNP

NN Architecture	Hidden layer activation function	Output layer activation function
AR1	linear	linear
AR2	linear	tangent-sigmoid
AR3	tangent-sigmoid	linear
AR4	tangent-sigmoid	tangent-sigmoid

In the second part of this work, Medical image datasets consisting of CT, MR, PET and angiogram were used to test the performance of the proposed lossless compression. For quantitative analysis, RMS and first order entropy values of the prediction error were used for evaluating the image data decorrelation capabilities of the proposed DL-DPCM method. These parameters were also used for comparing the performance the DL-DPCM with the predictors such as, MED and GAP. For evaluating and comparing the lossless compression performance of DLD-LS, bpp values of the compressed image were calculated. Theses evaluation criteria are defined in chapter 2.

3.5 Results and Discussions

In this section, first the experimental results obtained for different NNP architecture are presented. Results obtained for the proposed dual level predictor and the proposed lossless image compression algorithm is presented afterwards.

3.5.1 NNP architecture

Table 3.2 shows the first order entropy values of the prediction error obtained for six medical image datasets (MIDI-MR-01, MIDI-MR-02, OSRX-MR-01, MGH-MR-01, MGH-MR-02, MGH-MR-03) with the four different architecture (AR1, AR2, AR3) of NNP. Similarly, Table 3.3 shows the MSE values of the prediction error obtained for the same datasets with the four different architecture of NNP. The average first order entropy values of the six datasets are shown in Fig. 3.7 and the average MSE values obtained for the same six datasets are shown in Fig. 3.8.

Table 3.2 First order entropy values of NN prediction error obtained for eight different causal templates (CX1,CX2,CX3,CX4,CX5,CX6,CX7,CX8) and four different NN architecture (AR1, AR2, AR3, AR4). Lowest values for each dataset are shown in boldface and lowest average value is shaded gray.

	Image dataset	First order entropy (bpp)							
		CX1	**CX2**	**CX3**	**CX4**	**CX5**	**CX6**	**CX7**	**CX8**
AR1 (LIN-LIN)	MIDI-MR-01	2.85	2.68	2.65	2.65	2.65	2.64	2.64	**2.63**
	MIDI-MR-02	3.03	2.87	2.85	2.85	2.85	2.84	2.84	**2.83**
	OSRX-MR-01	2.46	2.32	2.31	2.30	2.30	**2.18**	**2.18**	**2.18**
	MGH-MR-01	4.36	4.32	4.31	4.32	4.31	4.29	4.29	**4.28**
	MGH-MR-02	3.87	3.80	3.80	3.80	3.80	3.74	3.74	**3.75**
	MGH-MR-03	4.74	4.70	4.69	4.69	4.68	**4.66**	**4.66**	**4.66**
	AVERAGE	3.55	3.45	3.43	3.43	3.43	**3.39**	**3.39**	**3.39**
AR2 (LIN-NLIN)	MIDI-MR-01	2.86	2.68	2.65	2.65	2.65	2.64	2.64	**2.63**
	MIDI-MR-02	3.03	2.87	2.86	2.85	2.85	2.84	2.84	**2.83**
	OSRX-MR-01	2.46	2.32	2.31	2.30	2.30	2.19	2.19	**2.18**
	MGH-MR-01	4.36	4.32	4.32	4.32	4.31	**4.29**	**4.29**	**4.29**
	MGH-MR-02	3.88	3.80	3.80	3.80	3.80	**3.74**	**3.74**	3.75
	MGH-MR-03	4.74	4.70	4.69	4.69	4.68	**4.66**	**4.66**	**4.66**
	AVERAGE	3.55	3.45	3.44	3.44	3.43	**3.39**	**3.39**	**3.39**
AR3 (NLIN-LIN)	MIDI-MR-01	2.83	2.62	2.59	2.57	2.58	2.56	2.56	**2.53**
	MIDI-MR-02	2.99	2.79	2.74	2.73	2.73	2.73	**2.71**	**2.71**
	OSRX-MR-01	2.44	2.29	2.26	2.25	2.25	2.13	2.13	**2.12**
	MGH-MR-01	4.29	4.20	4.17	4.17	4.16	4.14	**4.12**	**4.12**
	MGH-MR-02	3.81	3.70	3.66	3.66	3.65	**3.59**	**3.59**	**3.59**
	MGH-MR-03	4.70	4.62	4.59	4.59	4.58	4.56	4.54	**4.53**
	AVERAGE	3.51	3.37	3.33	3.33	3.32	3.29	**3.27**	**3.27**
AR4 (NLIN-NLIN)	MIDI-MR-01	2.83	2.80	2.64	2.59	2.59	2.61	2.57	**2.56**
	MIDI-MR-02	2.99	2.80	2.76	2.76	2.75	2.77	2.75	**2.74**
	OSRX-MR-01	2.45	2.32	2.28	2.28	2.25	2.14	2.15	**2.13**
	MGH-MR-01	4.29	4.21	4.19	4.21	4.17	4.16	4.14	**4.13**
	MGH-MR-02	3.82	3.72	3.70	3.68	3.69	3.65	**3.62**	3.64
	MGH-MR-03	4.71	4.63	4.60	4.61	4.60	4.57	4.56	**4.55**
	AVERAGE	3.52	3.41	3.36	3.35	3.34	3.32	3.30	**3.29**

It can be noted from Table 3.2 that for all datasets and for all NN architecture, there is an improvement in the performance of the predictor in terms of lower first order entropy values, as the causal template used for prediction is changed from CX1 to CX8. While comparing the average values of the six image datasets, the prediction performance of the NN architectures AR1 and AR2 are quite similar. This implies that the change in transfer function of the output layer from linear to nonlinear does not change prediction accuracy noticeably. However, it can be noted that, a linear activation function at the output layer gives better results than nonlinear activation function. It can also be noted that, there is a marginal improvement in prediction performance when the activation function of the hidden layer is changed from linear to nonlinear (AR3 and AR4). In this case also a linear activation function at the output layer gives better results, which can be evidently seen from the lower average entropy values produced by the NN architecture AR3, which is having a nonlinear hidden layer activation function and linear output layer activation function.

Table 3.3 MSE values obtained for eight different causal templates (CX1, CX2, CX3, CX4, CX5, CX6, CX7, CX8) and four different NN architecture (AR1, AR2, AR3, AR4). Lowest values for each dataset are shown in boldface and lowest average value is shaded gray.

	Image dataset	MSE							
		CX1	**CX2**	**CX3**	**CX4**	**CX5**	**CX6**	**CX7**	**CX8**
AR1 (LIN-LIN)	MIDI-MR-01	3.9	3.0	2.9	2.8	2.8	2.8	2.8	**2.7**
	MIDI-MR-02	6.2	5.1	4.9	4.9	4.9	**4.8**	4.9	**4.8**
	OSRX-MR-01	15.0	9.4	9.0	8.7	8.6	6.6	6.6	**6.4**
	MGH-MR-01	38.5	33.7	33.1	32.8	32.5	31.1	31.0	**30.6**
	MGH-MR-02	23.3	19.7	18.9	18.6	18.3	16.5	16.3	**16.1**
	MGH-MR-03	60.8	54.1	53.2	53.0	52.2	50.5	50.2	**49.9**
	AVERAGE	24.6	20.8	20.3	20.1	19.9	18.7	18.6	**18.4**
AR2 (LIN-NLIN)	MIDI-MR-01	3.9	3.0	2.9	2.8	2.8	2.8	2.8	**2.7**
	MIDI-MR-02	6.2	5.1	5.0	5.0	5.0	4.9	4.9	4.8
	OSRX-MR-01	15.0	9.4	9.0	8.7	8.7	6.7	6.6	**6.5**
	MGH-MR-01	38.2	34.0	33.1	32.9	32.6	30.8	31.0	**30.8**
	MGH-MR-02	23.3	19.6	18.5	18.4	18.3	16.6	16.5	**16.2**
	MGH-MR-03	60.5	54.7	53.3	53.1	51.8	50.3	**50.1**	**50.1**
	AVERAGE	24.5	21.0	20.3	20.2	19.9	18.7	18.7	**18.5**
AR3 (NLIN-LIN)	MIDI-MR-01	3.5	2.5	2.3	2.2	2.3	2.2	2.2	**2.1**
	MIDI-MR-02	5.6	4.1	3.7	3.6	3.6	3.6	**3.4**	**3.4**
	OSRX-MR-01	13.6	7.8	7.0	6.6	6.4	4.8	4.8	**4.5**
	MGH-MR-01	33.8	27.4	25.4	24.5	23.6	22.7	21.8	**21.6**
	MGH-MR-02	20.1	15.1	13.4	12.8	12.6	11.4	**10.9**	**10.9**
	MGH-MR-03	55.6	46.3	42.6	41.8	39.7	38.9	37.3	**37.1**
	AVERAGE	22.0	17.2	15.7	15.3	14.7	13.9	13.4	**13.3**
AR4 (NLIN-NLIN)	MIDI-MR-01	3.5	2.6	2.6	2.5	2.4	2.4	2.3	**2.2**
	MIDI-MR-02	5.7	4.2	3.9	3.8	3.8	3.6	3.7	**3.6**
	OSRX-MR-01	13.8	8.0	7.0	6.9	6.6	5.0	5.1	**4.6**
	MGH-MR-01	34.0	27.4	25.7	25.4	24.0	24.4	22.3	**21.5**
	MGH-MR-02	20.5	15.4	14.3	12.9	13.5	12.0	**11.3**	11.6
	MGH-MR-03	56.1	46.8	42.9	40.6	41.5	39.3	38.9	**37.0**
	AVERAGE	22.3	17.4	16.1	15.4	15.3	14.5	13.9	**13.4**

Similar to the first order entropy values, the NN architecture AR3 has better performance in terms of lower MSE values, as shown in Table 3.3. While considering different causal templates, CX8 has best performance in terms of lower RMS value. The AR3 NN architecture is having nonlinerar tangent-sigmoid function at the hidden layer and liner activation function at the output layer. Considering different causal templates, there is an increase in performance while moving from CX1 to CX8. Context CX8 has best performance in terms of lowest MSE value.

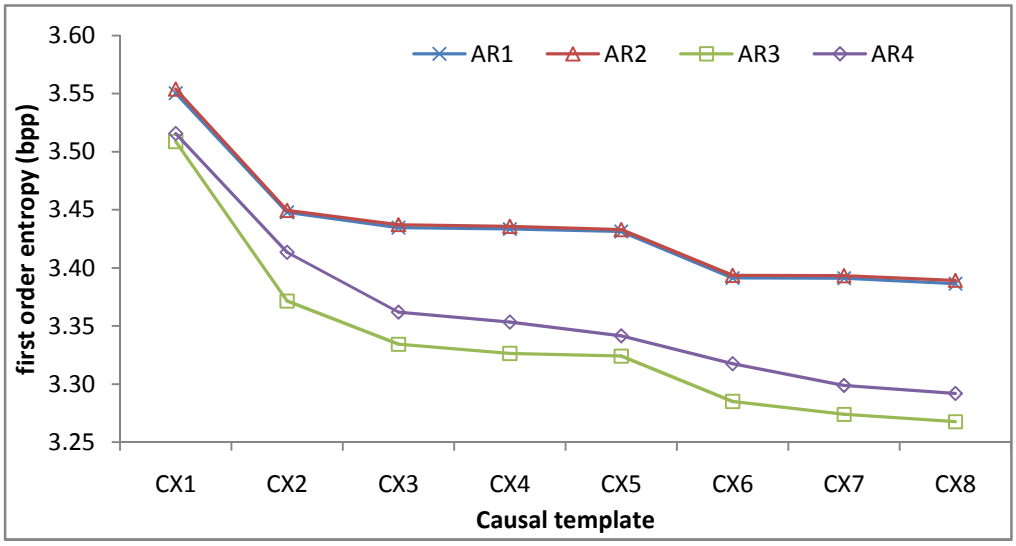

Fig. 3.7 Comparison of average first order entropy values obtained for eight different causal templates (CX1, CX2, CX3, CX4, CX5, CX6, CX7, CX8) and four different NN architecture (AR1,AR2,AR3,AR4)

It can be noted from Fig. 3.7 that the for all the four NN architectures, there is a marginal improvement in prediction performance when the causal template is changed from CX1 to CX2. The improvement is less as the causal template is changed further from CX2 to CX8. Moreover, prediction with CX8 achieves best performance among all the four NN architecture.

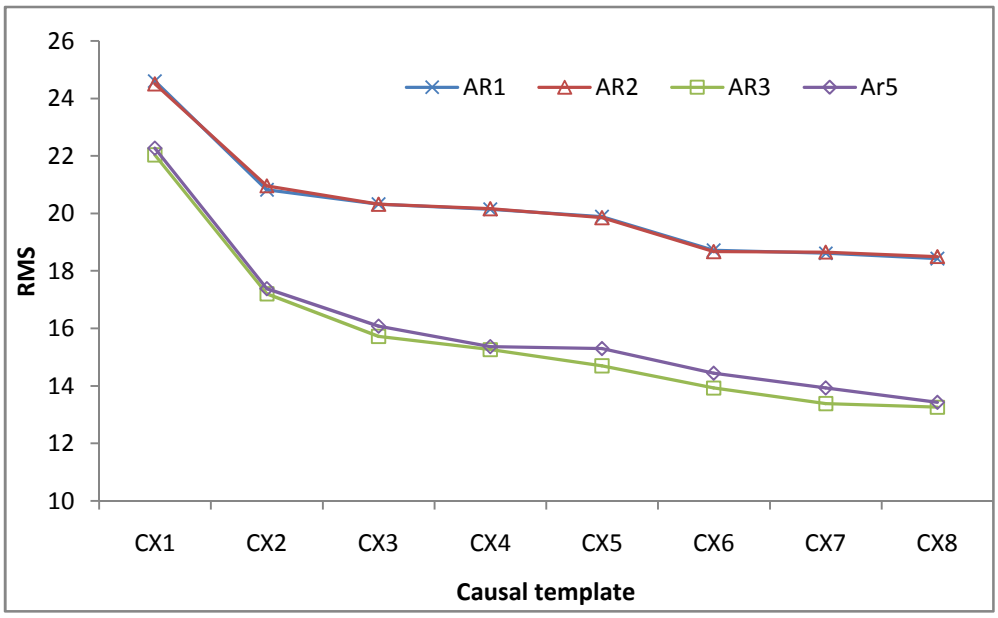

Fig. 3.8 Comparison of average RMS values obtained for eight different causal templates (CX1, CX2, CX3, CX4, CX5 ,CX6, CX7, CX8) and four different NN architecture (AR1, AR2, AR3, AR4)

Similar to the observation of the first order entropy values in Fig. 3.7,

Fig. 3.8 shows that the best result is obtained by the NN architecture AR3, which is having the lowest RMS values of the prediction error. Further, as in the case of first order entropy values, AR3 with causal template CX8 showed the best performance in terms of lower RMS value of the prediction error.

3.5.2 Lossless compression

Compression results obtained with the DLD-LS on CIPR, MGH, MicroDicom OsiriX and Physionet datasets are discussed in this section. The dataset details are given in chapater 2. These results are compared with the results obtained with CALIC and LOCO-I.

Table 3.4 First order entropy values obtained with the predictors MED, GAP and DL-DPCM. Lowest values for each dataset are shown in boldface

Image Dataset	GAP	MED	DL-DPCM (proposed)	% improvement over	
				GAP	MED
CIPR-CT-01	1.74	2.39	**1.40**	19.4	41.4
CIPR-CT-02	2.57	3.69	**2.12**	17.3	42.5
CIPR-CT-03	3.52	4.66	**3.20**	9.12	31.4
CIPR-CT-04	2.55	3.66	**1.82**	28.6	50.3
CIPR-MR-01	3.27	4.37	**2.73**	16.7	37.5
CIPR-MR-02	3.64	5.14	**2.98**	18.3	42.1
CIPR-MR-03	3.33	4.45	**2.53**	24.0	43.2
CIPR-MR-04	3.31	4.13	**3.17**	4.4	23.2
MGH-MR-01	4.41	5.72	**4.13**	6.5	27.9
MGH-MR-02	4.03	5.33	**3.55**	11.9	33.3
MGH-MR-03	4.79	5.96	**4.53**	5.3	24.0
MIDI-MR-01	3.32	4.83	**2.53**	23.9	47.7
MIDI-MR-02	3.50	4.81	**2.66**	24.0	44.8
MIDI-MR-03	4.19	5.48	**3.31**	20.9	39.5
MIDI-MR-04	4.11	5.73	**2.98**	27.5	48.0
MIDI-MR-05	4.06	5.51	**3.17**	21.9	42.4
MIDI-MR-06	3.52	4.88	**2.60**	26.2	46.7
MIDI-MR-07	3.38	4.96	**2.44**	27.8	50.8
OSRX-CT-01	2.83	3.48	**2.76**	2.4	20.7
OSRX-PT-01	1.51	1.95	**0.98**	34.8	49.6
OSRX-CT-02	2.65	3.78	**1.75**	33.8	53.5
OSRX-MR-01	2.64	3.32	**2.11**	20.0	36.5
OSRX-MR-02	5.19	6.30	**4.89**	5.9	22.5
OSRX-MR-03	4.82	6.06	**4.43**	8.1	26.9
OSRX-MR-04	4.36	5.67	**3.98**	8.6	29.7
OSRX-XA-01	2.77	4.10	**2.67**	3.6	34.8
OSRX-XA-02	2.87	4.24	**2.84**	1.1	33.0
PHNT-MR-01	3.62	4.85	**3.06**	15.3	36.8
CT	2.78	3.63	**2.44**	12.9	32.7
MR	3.71	4.96	**3.07**	17.7	38.2
XA	2.86	4.22	**2.81**	1.4	33.3
PET	1.51	1.95	**0.98**	34.8	49.6
AVERAGE	3.08	4.11	**2.65**	14.4	35.4

Table 3.4 gives the average first order entropy values of prediction errors obtained for MED, GAP and DL-DPCM when tested on the medical image dataset sequences used in this work. The GAP and MED are the predictors used in CALIC [98] and LOCO-I [94] respectively. The results are again grouped into CT, MR, XA and PT according to the respective modality of the image. Average values of the whole dataset are also calculated. The grouping was performed by weighted averaging – weighed according to the number of pixels in each dataset sequence.

It is observed from the Table 3.4 that, the first order entropy values were the least for the proposed DL-DPCM in all the cases. In the case of CT, the DL-DPCM achieved 12.% improvement compared to GAP and 32.7% compared to MED. Similarly, for MR, the DL-DPCM achieved 17.7% improvement compared to GAP and 38.2% compared to MED. For angiogram, the improvement were only 1.4% compared to GAP and 33.3% compared MED. In the case of PET, substantial improvements of 34.8% and 49.6% compared to GAP and MED respectively. The average improvements were 14.4% and 35.4% compared to GAP and the MED respectively. The proposed method showed very good image data decorrelation capabilities for CT, MR and PET, as evident from the lower first order entropy values obtained for DL-DPCM compared to GAP and MED. The improvement in data decorrelaton for angiogram was very small, which is 1.4% compared to GAP and 33.3% compared to MED. This is because the angiogram contains texture pattern and the NNP is not very good at decorrelating texture patterns.

Similarly, Table 3.5 compares the average RMS values of the prediction error obtained for each dataset sequence. As with the case of first order entropy values, the RMS values of the prediction error produced by the DL-DPCM was the least compared to that of GAP and MED. An average, improvement of 42.9% and 88.3% were achieved by the DL-DPCM while considering the RMS values. It is evident from the results that the proposed DL-DPCM is able to remove the statistical redundancies efficiently as compared to GAP and MED predictors. The DL-DPCM gives lower entropies and RMS values for each dataset. A low average RMS value (3.53) is obtained by the proposed method whereas the average RMS value is quite high for the GAP and MED the i.e. 6.36 and 30.62, respectively. Better results are achieved by the DL-DPCM as the CAS-NNP is used, in which each NN predictor is tuned for a particular area in the image (plain, gradient and edge). The 2D-LDPCM contributes to the performance of the CAS-NNP by presenting only the variation in the context template to the CAS-NNP rather than the original pixel values.

Table 3.5 RMS values obtained with the predictors MED, GAP and DL-DPCM. Lowest values for each dataset are shown in boldface

Image Dataset	GAP	MED	DL-DPCM (proposed)	% improvement over	
				GAP	MED
CIPR-CT-01	3.72	21.06	**1.00**	73.1	95.2
CIPR-CT-02	4.06	34.91	**1.77**	56.4	94.9
CIPR-CT-03	6.93	41.94	**3.87**	44.1	90.8
CIPR-CT-04	4.36	27.48	**1.68**	61.4	93.9
CIPR-MR-01	3.56	13.17	**1.83**	48.6	86.1
CIPR-MR-02	5.92	28.96	**2.18**	63.2	92.5
CIPR-MR-03	6.87	39.06	**2.28**	66.8	94.2
CIPR-MR-04	4.62	16.40	**4.07**	12.0	75.2
MGH-MR-01	7.02	39.37	**5.19**	26.1	86.8
MGH-MR-02	6.56	30.96	**3.89**	40.8	87.4
MGH-MR-03	8.40	29.74	**6.67**	20.5	77.6
MIDI-MR-01	2.83	14.28	**1.57**	44.5	89.0
MIDI-MR-02	3.78	25.35	**1.90**	49.8	92.5
MIDI-MR-03	6.07	34.31	**3.05**	49.8	91.1
MIDI-MR-04	4.47	28.76	**2.01**	55.0	93.0
MIDI-MR-05	4.84	34.46	**2.34**	51.6	93.2
MIDI-MR-06	3.86	26.90	**1.75**	54.6	93.5
MIDI-MR-07	3.09	17.90	**1.37**	55.6	92.3
OSRX-CT-01	7.14	33.08	**5.57**	22.0	83.2
OSRX-PT-01	2.38	17.03	**0.93**	61.0	94.5
OSRX-CT-02	13.10	38.50	**1.71**	87.0	95.6
OSRX-MR-01	5.40	28.29	**2.23**	58.7	92.1
OSRX-MR-02	12.11	35.46	**7.95**	34.4	77.6
OSRX-MR-03	8.69	36.83	**6.18**	28.9	83.2
OSRX-MR-04	6.52	37.37	**4.61**	29.3	87.7
OSRX-XA-01	4.53	34.67	**2.47**	45.5	92.9
OSRX-XA-02	7.64	43.38	**6.04**	20.8	86.1
PHNT-MR-01	3.50	13.74	**2.27**	35.2	83.5
CT	7.54	33.87	**3.89**	44.2	88.5
MR	4.97	24.60	**2.81**	44.1	87.8
XA	7.18	42.09	**5.52**	24.5	87.1
PET	2.38	17.03	**0.93**	61.0	94.5
AVERAGE	6.36	30.62	**3.53**	42.9	88.3

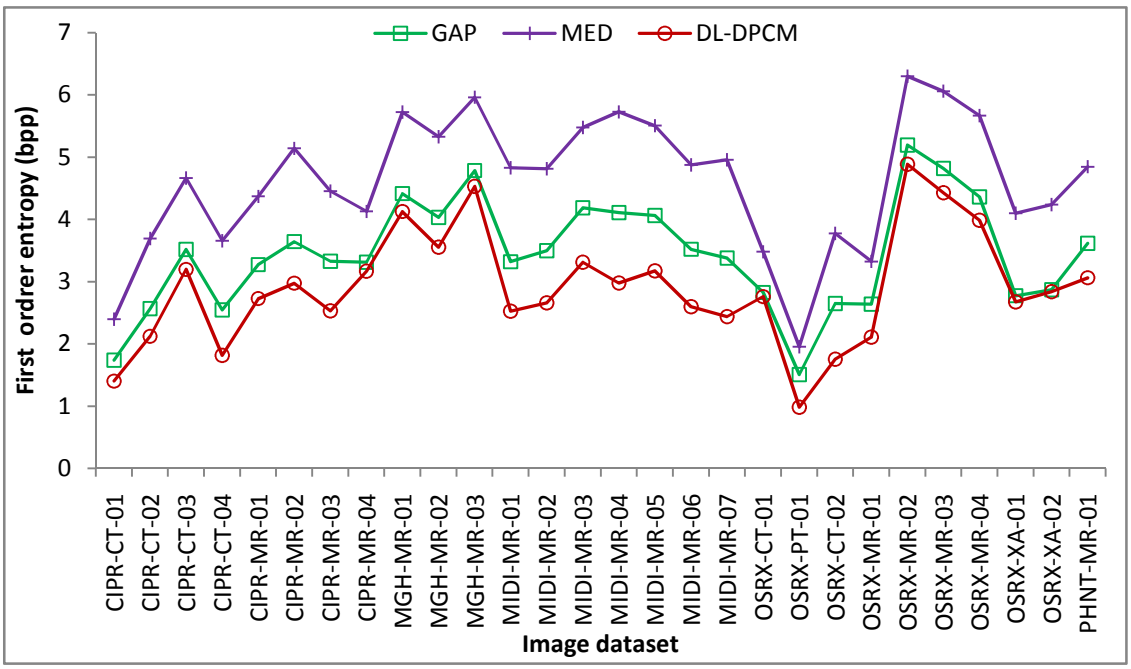

Fig. 3.9 Comparison of first order entropy values obtained for the predictors, GAP, MED and the proposed DL-DPCM

It can be noted from Fig. 3.9 that the first order entropy value of the prediction error produced by the proposed DL-DPCM is the lowest for every dataset, compared to the first order entropy value of the prediction errors produced by GAP and MED.

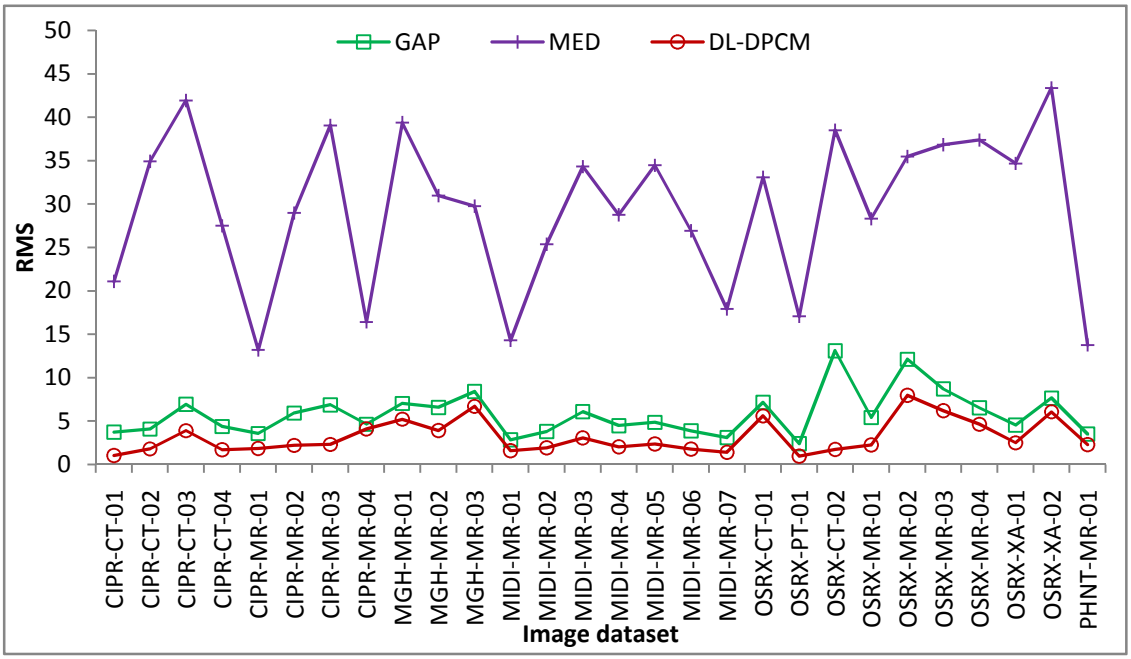

Fig. 3.10 Comparison of RMS values obtained for the predictors, GAP, MED and the proposed DL-DPCM

It can be noted from Fig. 3.10 that the RMS value of the prediction error produced by the proposed DL-DPCM is the lowest for every dataset, compared to the RMS value of the prediction errors produced by GAP and MED.

Table 3.6 Comparison of lossless compression performance the proposed DLD-LS method with the CALIC and the LOCO-I. Lowest values for each dataset are shown in boldface

Image Dataset	CALIC	LOCO-I	DLD-LS (proposed)	% improvement over	
				CALIC	LOCO-I
CIPR-CT-01	1.00	1.06	**0.98**	2.2	7.7
CIPR-CT-02	1.68	1.78	**1.51**	10.1	14.8
CIPR-CT-03	2.63	2.76	**2.53**	3.9	8.5
CIPR-CT-04	1.55	1.63	**1.38**	11.3	15.4
CIPR-MR-01	2.79	2.94	**2.66**	4.7	9.5
CIPR-MR-02	3.02	3.16	**2.90**	4.1	8.3
CIPR-MR-03	2.27	2.42	**1.86**	18.1	23.1
CIPR-MR-04	**2.52**	2.58	2.57	-2.0	0.5
MGH-MR-01	3.96	4.13	**3.93**	0.8	4.8
MGH-MR-02	3.41	3.61	**3.33**	2.2	7.6
MGH-MR-03	4.42	4.57	**4.34**	1.7	5.0
MIDI-MR-01	2.70	2.98	**2.51**	7.2	16.0
MIDI-MR-02	2.51	2.75	**2.27**	9.4	17.3
MIDI-MR-03	3.20	3.47	**2.83**	11.7	18.4
MIDI-MR-04	3.51	3.85	**2.96**	15.7	23.1
MIDI-MR-05	3.44	3.72	**3.09**	10.2	17.1
MIDI-MR-06	2.51	2.76	**2.21**	11.9	19.8
MIDI-MR-07	2.68	2.96	**2.41**	10.3	18.8
OSRX-CT-01	1.90	1.96	**1.89**	0.3	3.5
OSRX-PT-01	0.75	0.84	**0.57**	23.4	31.7
OSRX-CT-02	1.45	1.62	**1.28**	11.6	20.8
OSRX-MR-01	1.64	1.79	**1.39**	14.9	22.0
OSRX-MR-02	5.28	4.96	**4.79**	9.3	3.4
OSRX-MR-03	4.14	4.32	**4.07**	1.8	5.9
OSRX-MR-04	3.78	3.95	**3.72**	1.5	5.9
OSRX-XA-01	2.15	2.23	**2.15**	0.4	3.9
OSRX-XA-02	**2.24**	2.31	2.26	-0.7	2.4
PHNT-MR-01	3.05	3.29	**2.92**	4.3	11.4
CT	1.81	1.90	**1.74**	4.3	9.0
MR	3.02	3.22	**2.81**	7.4	13.4
XA	**2.23**	2.30	2.24	-0.5	2.6
PET	0.75	0.84	**0.57**	23.4	31.7
AVERAGE	2.25	2.38	**2.13**	5.7	10.9

Table 3.6 presents the comparative bpp values of the compressed images obtained by the proposed method DLD-LS and the existing methods. It can be noted that the proposed method achieved lower bpp values for all the datasets except CIPR-MR-03 and OSRX-XA-02. The average bpp value of the complete dataset when it is compressed using CALIC, LOCO-I and DLD-LS are 2.27 bpp, 2.38 bpp and 2.13 bpp respectively. An improvement of 0.12 bpp compared to the CALIC and 0.25 bpp compared to the LOCO-I are achieved by the proposed

DLD-LS lossless compression technique. The percentage improvement over the CALIC and the LOCO-I are 5.7% and 10.9% respectively. The improvement in bpp values is due to higher image data decorrelation capability of the proposed DL-DPCM .

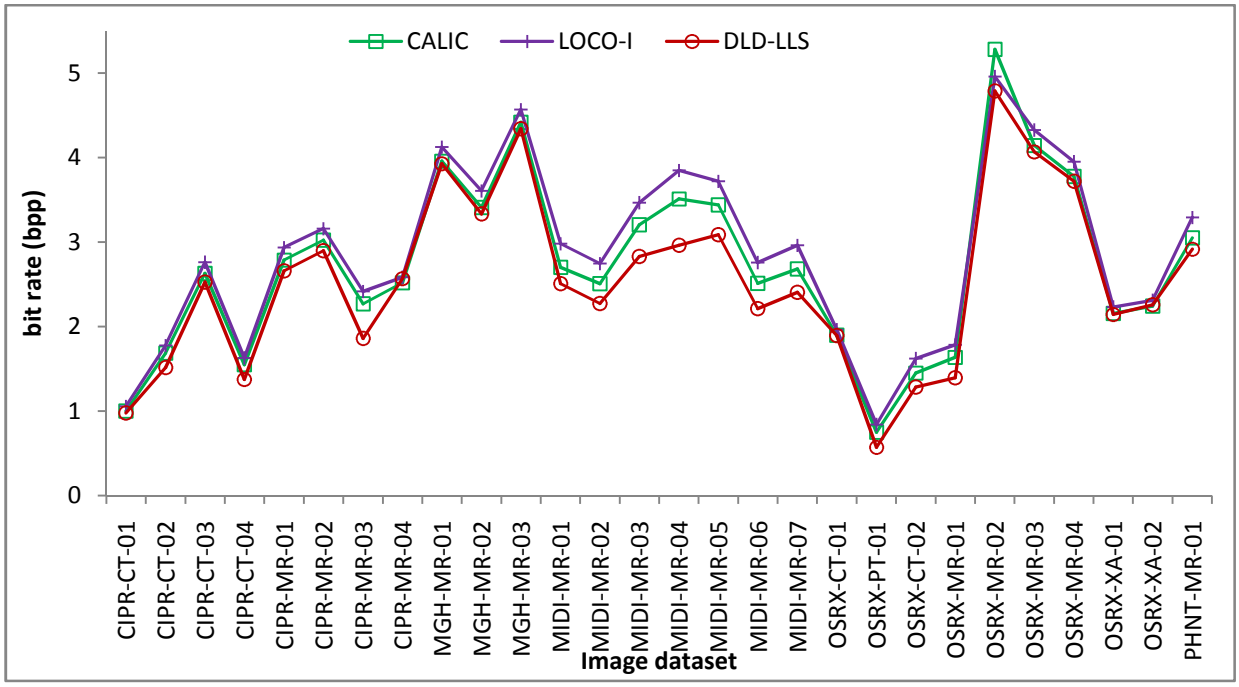

Fig. 3.11 Comparison of bit rate for the lossless compression algorithms, CALIC, LOCO-I and the proposed DLD-LS

It can be noted from Fig. 3.11 that the bit rate of the compressed image produced by the proposed lossless compression method, DLD-LS is comparable or less than the bit rate obtained for the state-of-the-art lossless compression techniques, CALIC and LOCO-I.

3.6 Summary

A lossless compression scheme, with a dual level DPCM has been implemented. The dual level DPCM is realized by cascading the 2D-DPCM (linear DPCM) and the CAS-NNP (nonlinear DPCM). It is observed that the cascaded architecture of linear and nonlinear DPCM achieved higher decorrelation for CT, MR, PET and angiogram with varying intensity and texture patterns. The CAS-NNP switches between three different NN predictorsbased on the causal context information. The comparative analysis with the MED and the GAP shows that lower first order entropy and RMS values are obtained with DL-DPCM. It is also observed that the lossless coding using the DLD-LS achieved lower bpp values compared to the state-of-the-art methods such as CALIC and LOCO-I. The improvement achieved using CAS-NNP, which is a nonlinear predictor, shows that the functional relationship between the pixels is considerably nonlinear in nature.

Chapter 4

Near Lossless Compression

4.1 Introduction

The bit rate per pixel for lossless compression is generally high. Reduction in bit rate can be obtained by near lossless (NLS) compression, which allows a maximum predefined error in reconstructed image. Therefore, NLS is a lossy compression technique, in which every pixel value in the reconstructed image is guaranteed to differ by a maximum preset value 'δ'. If 'δ' is set to zero, the algorithm operates in lossless mode. The NLS compression is generally achieved by quantizing the prediction residuals at the desired level. In transform coding techniques such as JPEG and JPEG2000, quantization is performed on the transform coefficients. The reconstructed image is obtained by the inverse transform of the quantized transform coefficient. Hence, in the case of transform coding, the maximum quantization error introduced in the reconstructed image cannot be guaranteed. Therefore, NLS compression is a good choice if a guaranteed maximum error in the reconstructed image can be allowed. It is also useful in applications with legal restrictions such as medical image archiving.

Bench mark lossless compression algorithms such as CALIC [98] and LOCO-I [94] operate in NLS mode also. For small PAE values, rate distortion performance is better than the transform coding standards, JPEG and JPEG2000. The lossless compression technique proposed in chapter 3 is extended to perform near lossless compression. The following sections details the proposed DL-DPCM based NLS compression technique (DLD-NLS). The performance of the proposed DLD-NLS technique is compared with benchmark compression techniques, namely CALIC, LOCO-I, JPEG and JPEG2000.

4.2 Near Lossless Compression with DL-DPCM

The proposed DLD-NLS compression method is an extension of the DLD-LS lossless compression algorithm proposed in chapter 2. The block diagram of the proposed scheme is shown in Fig.4.1. A linear quantizer is used to quantize the prediction error produced by the 2D-LDPCM. Quantization is performed by dividing the prediction error by a constant value and truncating the decimal places as shown below in Eq.(4.1). It may be noted that the run mode is not used in this scheme. This is because, context adaptive arithmetic coding is more efficient as the frequency of zeros in the error image produced by the 2D-LDPCM is large due to quantization. The quantized error is in turn used by the 2D-LDPCM to reconstruct the

predicted pixel. Instead of true values of neighboring pixels, here the 2D-LDPCM uses the reconstructed pixel values of the neighboring pixels for prediction. The reconstructed pixel thus may contain a maximum error which is defined by the quantization value 'δ'. This method of prediction is followed at the encoder stage so that the decoder can mimic the behavior of the encoder. The quantized error is de-quantized by multiplying with a constant value as shown below in Eq.(4.2).

$$Q(e) = sign(e)\left\lfloor \frac{|e| + \delta}{2\delta + 1} \right\rfloor \tag{4.1}$$

$$\hat{e} = Q(e).(2\delta + 1) \tag{4.2}$$

where, 'e' is the prediction error, and 'δ' is the amount of quantization.

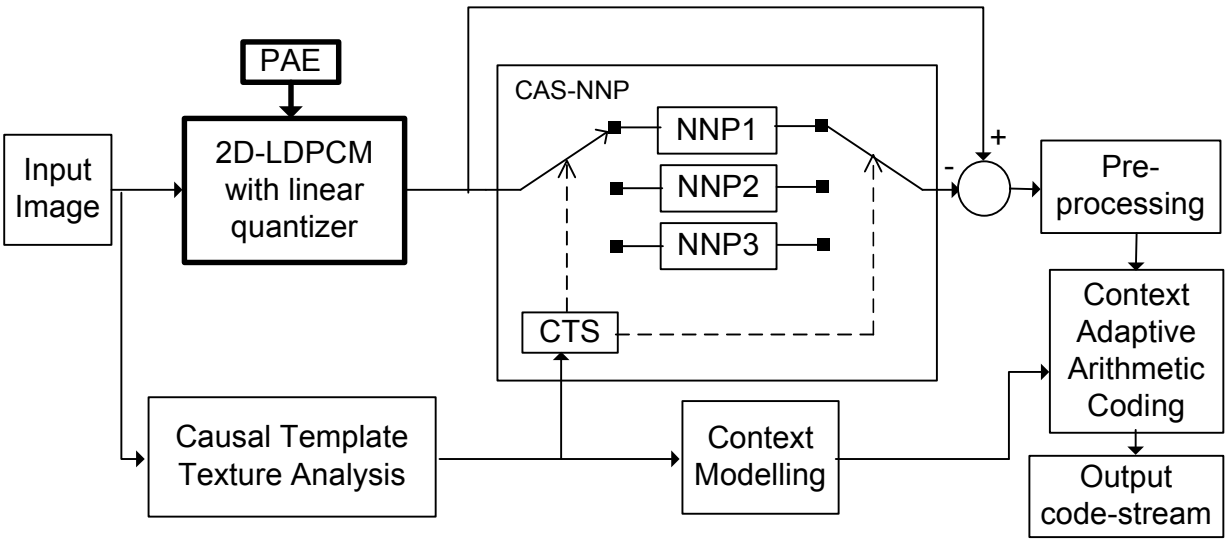

Fig.4.1 The proposed DLD-NLS compression scheme. A linear quantizer is added to the proposed DLD-LS compression scheme to perform near lossless compression.

The quantized error output from the 2D-LDPCM is further decorrelated by the CAS-NNP as described in the chapter 3. The preprocessing and context adaptive arithmetic coding of the final error output is performed in same manner as used in the proposed DLD-LS compression technique, which are described in chapter 3.

4.3 Software Implementation

The binary executable of CALIC is provided by X. Wu [105], and that of LOCO-I is provided by HP Labs [112]. The JPEG and JPEG2000 are tested using publically available image processing software package Image Magic [108]. The algorithm is implemented in MATLAB 9.0 on a PC having Intel® CORE™2 Duo, 2.0 GHz using Neural Network Toolbox. The

publically available MATLAB implementation of the arithmetic coder developed by Karl Skretting [104] is used in this work for entropy coding.

4.4 Experimentation Details

The experiments are performed for NLS compression of medical image data consisting of CT, MR, PET and angiogram images. The images were compressed with different PAE criteria, ie, PAE = 1, 2, 3, 4, 6, 8, 10, 12, 16. For evaluating and comparing the NLS compression performance, bpp, PAE, PSNR, MSSIM and UQI values were calculated. Theses evaluation criteria are defined in chapter 2. The performance measurement of the 28 datasets are made into 12 groups namely, CIPR-CT, OSRX-CT, CIPR-MR, MGH-MR, MIDI-MR, OSRX-MR, PHNT-MR, OSRX-XA, OSRX-PT, CT, MR, AVERAGE for brevity.

Table 4.1 The grouping of dataset

Image datasets	Voxels	Group	Group	Group
CIPR-CT-01	6356992	CIPR-CT	CT	AVERAGE
CIPR-CT-02	4849664			
CIPR-CT-03	13303808			
CIPR-CT-04	11993088			
OSRX-CT-01	58720256	OSRX-CT		
OSRX-CT-02	19922944			
CIPR-MR-01	5046272	CIPR-MR	MR	
CIPR-MR-02	3801088			
CIPR-MR-03	3801088			
CIPR-MR-04	3801088			
MGH-MR-01	1179648	MGH-MR		
MGH-MR-02	1179648			
MGH-MR-03	1179648			
MIDI-MR-01	3407872	MIDI-MR		
MIDI-MR-02	5242880			
MIDI-MR-03	5242880			
MIDI-MR-04	3145728			
MIDI-MR-05	4718592			
MIDI-MR-06	3932160			
MIDI-MR-07	3932160			
OSRX-MR-01	5767168	OSRX-MR		
OSRX-MR-02	2419200			
OSRX-MR-03	3913728			
OSRX-MR-04	3563520			
PHNT-MR-01	19922944	PHNT-MR		
OSRX-XA-01	3407872	OSRX-XA	XA	
OSRX-XA-02	19660800			
OSRX-PT-01	19922944	OSRX-PT	PT	

CIPR-CT-01, CIPR-CT-02, CIPR-CT-02 and CIPR-CT-04 are grouped to form CIPR-CT;
OSRX-CT-01 and OSRX-CT-02 is grouped to form OSRX-CT;
CIPR-MR-01, CIPR-MR-02, CIPR-MR-02 and CIPR-MR-04 is grouped to form CIPR-MR;
MGH-MR-01, MGH-MR-02 and MGH-MR-03 is grouped to form MGH-MR;
MIDI-MR-01 MIDI-MR-02, MIDI-MR-03, MIDI-MR-04, MIDI-MR-05, MIDI-MR-06 and MIDI-MR-07 is grouped to form MIDI-MR;
OSRX-MR-01, OSRX-MR-02, OSRX-MR-03 and OSRX-MR-04 forms OSRX-MR;
PHNT-MR-01 alone form PHNT-MR;
OSRX-XA-01 and OSRX-XA-02 forms OSRX-XA;
OSRX-PT-01 alone form OSRX-PT.

All the measurements for the group are calculated as weighted average taking into account of the voxels or the total number of pixels in each dataset.

4.5 Results and Discussions

In this section, NLS compression results obtained with the proposed DLD-NLS compression method on CIPR, MGH, MicroDicom, OsiriX and Physionet datasets are discussed. The dataset details are given in chapter 2. The performance of the proposed method is compared with NLS compression performance of the CALIC and the LOCO-I, as well as with the lossy compression performance of JPEG and JPEG2000.

The original and the reconstructed image from the compressed images produced by the proposed DLD-NLS method is shown in Fig. 4.2. Fig. 4.2 (a) shows a single original slice from the MGHD-MR-01 dataset. Fig. 4.2 (b)-(j) show the reconstructed image of the same slice, which is compressed by the proposed DLD-NLS method with different image quality as specified: (b) PAE=1, (c) PAE=2, (d) PAE=3, (e) PAE=4, (f) PAE=6, (g) PAE=8, (h) PAE=10, (i) PAE=12, (j) PAE=16. It can be noted that the images Fig. 4.2 (b) (PAE=1) and Fig. 4.2 (c) (PAE=2) are almost visually identical to the original image. Fig. 4.2 (d) (PAE=3) to Fig. 4.2 (h) (PAE=10) are fairly similar to the original image. In Fig. 4.2 (i) (PAE=12) and Fig. 4.2 (j) (PAE=16) there is noticeable difference from the original image. However, the image quality determination is a subjective matter and depends from one radiologist to another. Therefore, in this work, objective image quality indices such as PAE, PSNR, MSSIM and UQI are measured for the reconstructed images.

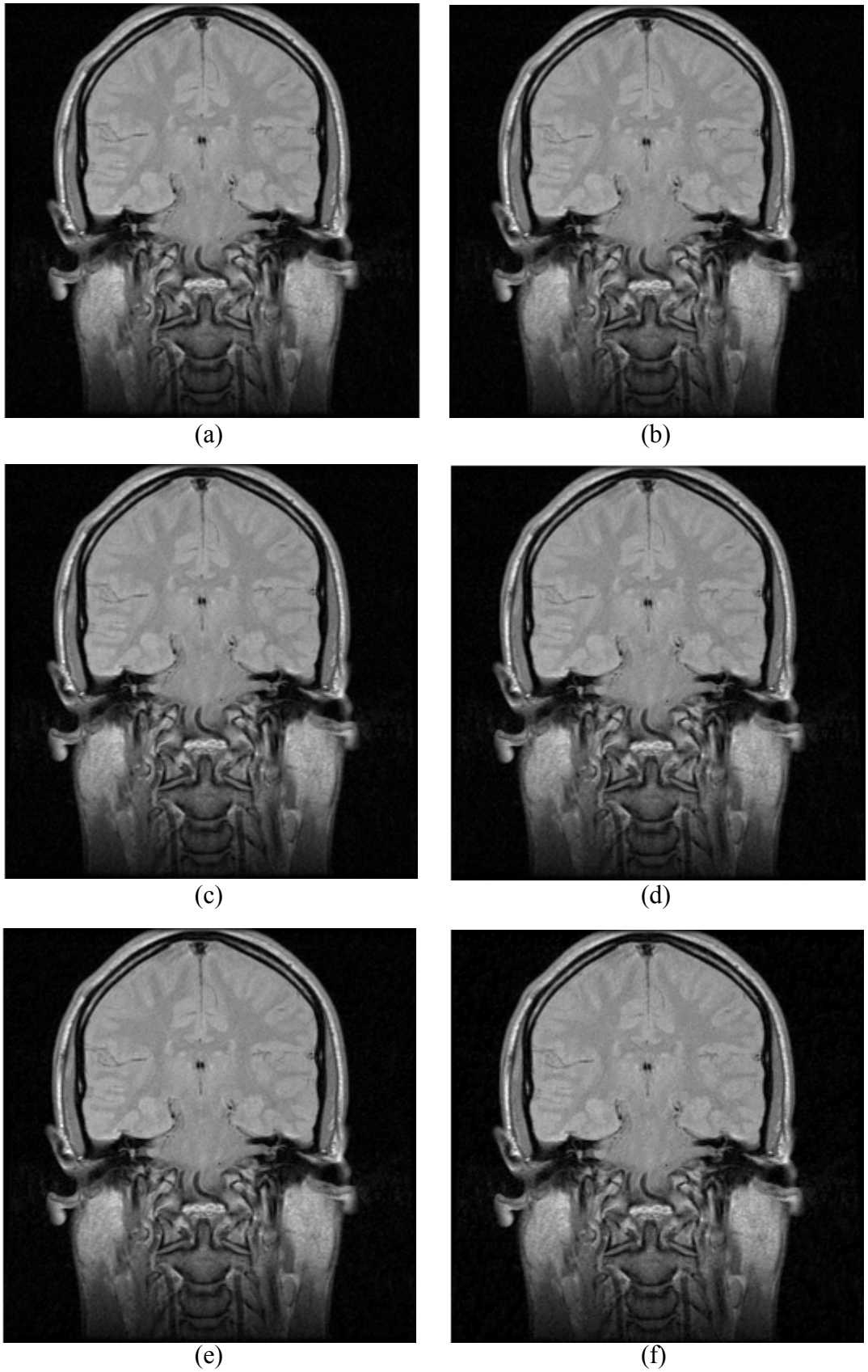

Fig. 4.2 (a) A single slice of the original image from the dataset MGH-MR-01. (b)-(f) a single slice of the reconstructed image which is compressed by the proposed DLD-NLS method with different image quality. (b) PAE=1, (c) PAE=2, (d) PAE=3, (e) PAE=4, (f) PAE=6, (g) PAE=8, (h) PAE=10, (i) PAE=12, (j) PAE=16.

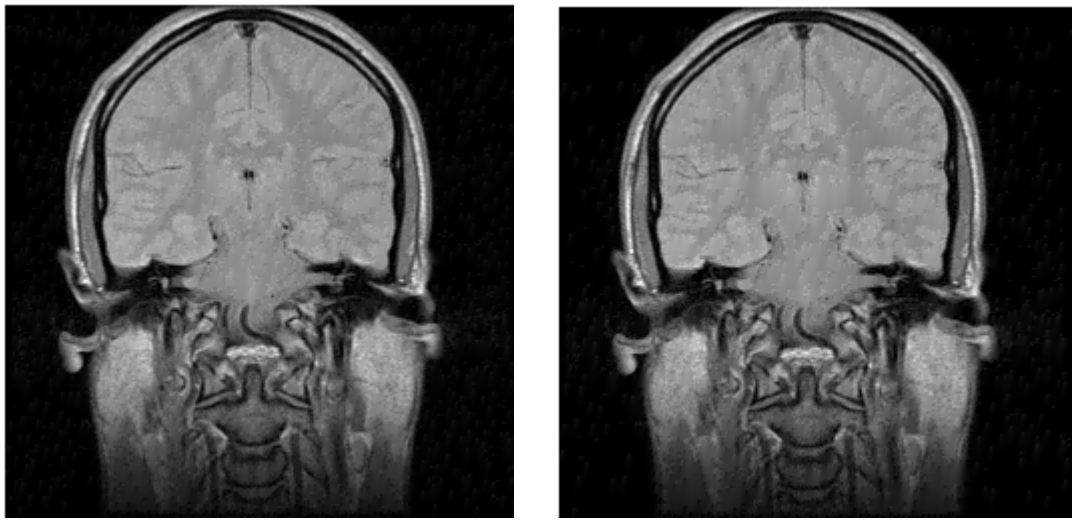

(g) (h)

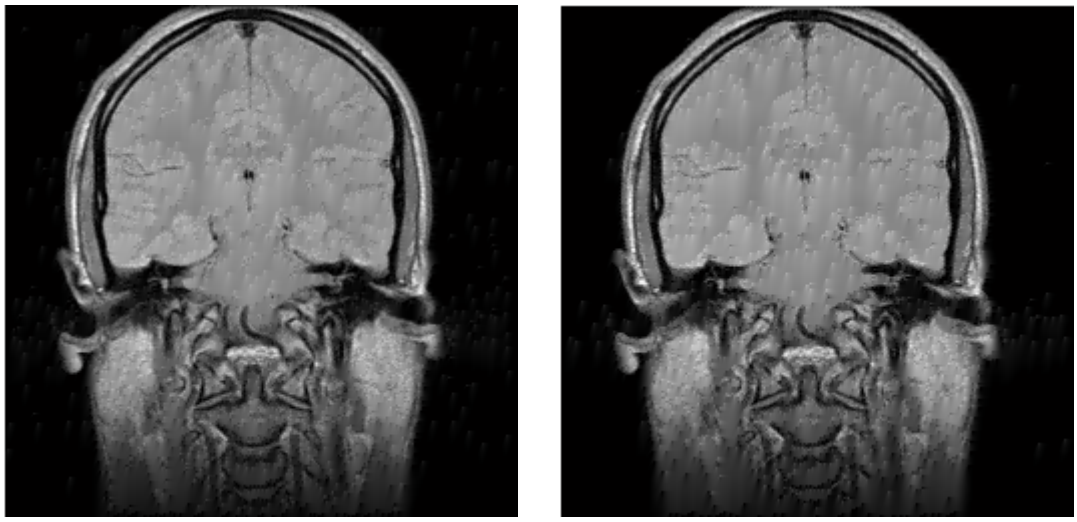

(i) (j)

Fig. 4.2 (g)-(j) a single slice of the reconstructed image which is compressed by the proposed DLD-NLS method with different image quality. (g) PAE=8, (h) PAE=10, (i) PAE=12, (j) PAE=16.

Table 4.2 shows the PSNR, MSSIM, UQI, bpp values obtained with different image qualities (PAE=1,2,3,4,6,8,10,12,16) for each group of the dataset as shown in Table 4.1.

Table 4.2 NLS compression performance comparison of CALIC, LOCO-I and the proposed DLD-NLS compression method for different image quality (PAE = 1,2,3,4,6,8,10,12,16). Results are shown for the dataset groups, CIPR-CT, OSRX-CT, CIPR-MR and MGH-MR. Lowest bpp values for each set is shown in bold face.

	PAE	CALIC				LOCO-I				DLD-NLS (Proposed)			
		PSNR	MSSIM	UQI	bpp	PSNR	MSSIM	UQI	bpp	PSNR	MSSIM	UQI	bpp
CIPR-CT	1	52.7	1.00	0.95	**1.17**	52.3	0.99	0.90	1.24	52.6	1.00	0.95	1.21
	2	48.1	0.99	0.90	**0.91**	47.7	0.98	0.85	0.99	48.0	0.99	0.92	**0.91**
	3	45.3	0.98	0.86	**0.75**	44.8	0.97	0.81	0.84	45.2	0.98	0.88	**0.75**
	4	43.3	0.97	0.81	0.66	42.7	0.95	0.78	0.72	43.2	0.97	0.85	**0.63**
	6	40.4	0.94	0.71	0.54	39.8	0.92	0.71	0.56	40.2	0.95	0.79	**0.47**
	8	38.0	0.89	0.62	0.48	37.6	0.89	0.66	0.48	38.1	0.94	0.74	**0.38**
	10	36.6	0.88	0.59	0.42	35.8	0.85	0.63	0.42	36.3	0.92	0.71	**0.32**
	12	35.3	0.86	0.56	0.37	34.5	0.83	0.60	0.38	34.9	0.90	0.68	**0.28**
	16	32.9	0.81	0.49	0.33	32.3	0.78	0.56	0.32	32.4	0.87	0.63	**0.25**
OSRX-CT	1	53.9	1.00	0.99	**1.22**	53.2	1.00	0.88	1.30	53.8	1.00	0.99	1.25
	2	49.1	1.00	0.98	**0.97**	48.4	0.99	0.86	1.08	49.0	1.00	0.98	0.99
	3	46.1	0.99	0.96	**0.82**	45.4	0.97	0.85	0.93	46.0	0.99	0.97	0.84
	4	43.8	0.98	0.94	0.73	43.2	0.96	0.84	0.83	43.8	0.99	0.96	**0.72**
	6	40.7	0.97	0.92	0.59	39.9	0.93	0.80	0.70	40.7	0.98	0.94	**0.58**
	8	38.3	0.94	0.86	0.51	37.6	0.89	0.78	0.62	38.5	0.96	0.92	**0.49**
	10	36.4	0.90	0.80	0.45	35.8	0.86	0.75	0.55	36.8	0.95	0.90	**0.42**
	12	34.9	0.87	0.75	0.41	34.4	0.83	0.73	0.49	35.4	0.94	0.88	**0.36**
	16	32.7	0.84	0.72	0.36	32.0	0.78	0.69	0.41	33.2	0.91	0.84	**0.28**
CIPR-MR	1	51.2	0.99	0.88	1.55	50.5	0.99	0.84	1.67	51.1	0.99	0.89	**1.49**
	2	46.9	0.99	0.79	1.15	46.0	0.97	0.76	1.28	46.5	0.98	0.79	**1.09**
	3	44.2	0.98	0.73	0.93	43.4	0.95	0.70	1.06	43.8	0.96	0.73	**0.85**
	4	42.4	0.97	0.69	0.80	41.3	0.93	0.65	0.91	41.9	0.94	0.68	**0.71**
	6	39.7	0.94	0.62	0.64	38.5	0.89	0.58	0.72	39.1	0.90	0.62	**0.53**
	8	37.6	0.91	0.55	0.55	36.3	0.85	0.53	0.61	37.0	0.86	0.56	**0.42**
	10	35.9	0.89	0.50	0.48	34.7	0.80	0.48	0.52	35.4	0.82	0.52	**0.35**
	12	34.4	0.86	0.47	0.44	33.3	0.76	0.45	0.46	34.1	0.79	0.48	**0.30**
	16	32.3	0.81	0.42	0.37	31.1	0.69	0.40	0.38	32.0	0.74	0.43	**0.23**
MGH-MR	1	50.0	0.99	0.95	2.50	50.0	0.99	0.95	2.63	50.0	0.99	0.96	**2.42**
	2	45.6	0.99	0.89	1.92	45.4	0.98	0.88	2.01	45.4	0.98	0.90	**1.83**
	3	42.8	0.97	0.83	1.58	42.6	0.97	0.81	1.66	42.5	0.96	0.84	**1.48**
	4	40.9	0.96	0.78	1.36	40.5	0.95	0.76	1.43	40.6	0.94	0.78	**1.24**
	6	38.2	0.93	0.70	1.07	37.6	0.91	0.68	1.14	37.8	0.89	0.70	**0.94**
	8	36.2	0.90	0.65	0.91	35.5	0.86	0.62	0.97	35.9	0.84	0.64	**0.74**
	10	34.8	0.88	0.60	0.78	33.9	0.81	0.57	0.86	34.4	0.79	0.59	**0.60**
	12	33.6	0.86	0.57	0.70	32.5	0.77	0.53	0.77	33.2	0.75	0.55	**0.51**
	16	31.5	0.81	0.51	0.57	30.4	0.69	0.47	0.66	31.3	0.70	0.49	**0.38**

It is observed from Table 4.2 that, for dataset groups CIPR-MR and MGH-MR, the proposed DLD-NLS has the lowest bpp values for each PAE criteria. For dataset groups, CIPR-CT and OSRX-CT, the bpp values are comparable or lesser than the bpp values obtained for CALIC.

Table 4.3 NLS compression performance comparison of CALIC, LOCO-I and the proposed DLD-NLS compression method for different image quality (PAE = 1,2,3,4,6,8,10,12,16). Results are shown for the dataset groups, MIDI-MR, OSRX-MR, PHNT-MR and OSRX-XA.

	PAE	CALIC				LOCO-I				DLD-NLS (Proposed)			
		PSNR	MSSIM	UQI	bpp	PSNR	MSSIM	UQI	bpp	PSNR	MSSIM	UQI	bpp
MIDI-MR	1	50.6	0.99	0.97	1.77	50.4	0.99	0.92	1.99	50.5	0.99	0.97	**1.67**
	2	45.9	0.98	0.93	1.34	45.7	0.98	0.87	1.55	45.9	0.98	0.93	**1.31**
	3	43.1	0.97	0.88	1.09	42.8	0.96	0.83	1.29	43.0	0.97	0.88	**1.08**
	4	41.0	0.95	0.83	0.92	40.7	0.94	0.78	1.12	40.9	0.95	0.84	**0.91**
	6	38.2	0.92	0.74	0.72	37.8	0.89	0.69	0.89	38.1	0.91	0.75	**0.68**
	8	36.2	0.87	0.67	0.61	35.7	0.84	0.61	0.74	36.1	0.86	0.68	**0.52**
	10	34.8	0.84	0.61	0.50	34.1	0.79	0.55	0.64	34.5	0.81	0.62	**0.42**
	12	33.7	0.82	0.55	0.42	32.7	0.74	0.50	0.56	33.3	0.77	0.57	**0.34**
	16	31.7	0.77	0.47	0.32	30.7	0.65	0.42	0.46	31.3	0.70	0.49	**0.24**
OSRX-MR	1	51.7	1.00	0.97	2.14	51.2	0.99	0.90	2.28	51.6	1.00	0.96	**2.08**
	2	47.0	0.99	0.93	1.68	46.5	0.98	0.86	1.79	46.9	0.99	0.93	**1.63**
	3	44.2	0.98	0.89	1.40	43.6	0.97	0.82	1.50	43.9	0.98	0.90	**1.36**
	4	42.1	0.98	0.86	1.20	41.4	0.95	0.79	1.30	41.8	0.97	0.87	**1.17**
	6	39.1	0.96	0.81	0.94	38.4	0.92	0.73	1.05	38.7	0.94	0.82	**0.92**
	8	37.0	0.93	0.76	0.78	36.1	0.88	0.69	0.90	36.5	0.91	0.78	**0.75**
	10	35.4	0.91	0.73	0.66	34.4	0.84	0.66	0.80	34.8	0.87	0.74	**0.63**
	12	34.2	0.89	0.70	0.57	33.0	0.81	0.63	0.72	33.4	0.84	0.71	**0.53**
	16	31.8	0.84	0.65	0.46	30.7	0.74	0.58	0.61	31.4	0.78	0.66	**0.40**
PHNT-MR	1	50.1	0.99	0.97	1.78	50.0	0.99	0.96	1.97	50.2	0.99	0.98	**1.76**
	2	45.4	0.98	0.93	**1.31**	45.3	0.98	0.91	1.53	45.4	0.98	0.93	1.34
	3	42.6	0.96	0.88	**1.05**	42.4	0.96	0.87	1.30	42.5	0.96	0.89	1.07
	4	40.6	0.95	0.83	**0.86**	40.3	0.94	0.81	1.14	40.5	0.94	0.84	0.88
	6	37.9	0.90	0.72	0.63	37.4	0.89	0.70	0.88	37.8	0.90	0.75	**0.62**
	8	36.1	0.86	0.61	0.48	35.4	0.83	0.59	0.69	35.8	0.85	0.65	**0.45**
	10	34.8	0.83	0.51	0.40	33.8	0.78	0.49	0.55	34.2	0.80	0.57	**0.34**
	12	33.7	0.80	0.42	0.34	32.5	0.74	0.41	0.45	32.9	0.74	0.49	**0.26**
	16	32.1	0.75	0.30	0.28	30.5	0.65	0.30	0.32	30.9	0.63	0.38	**0.18**
OSRX-XA	1	51.6	0.99	0.97	**1.28**	51.4	0.99	0.89	1.36	51.7	0.99	0.97	1.31
	2	47.0	0.98	0.92	**0.92**	46.8	0.98	0.85	1.05	47.0	0.99	0.93	**0.92**
	3	44.3	0.97	0.88	**0.70**	43.9	0.96	0.80	0.88	44.2	0.97	0.89	**0.70**
	4	42.2	0.96	0.82	0.60	41.9	0.94	0.76	0.74	42.3	0.96	0.85	**0.55**
	6	39.5	0.92	0.73	0.45	39.0	0.90	0.68	0.56	39.6	0.93	0.78	**0.36**
	8	37.4	0.88	0.63	0.39	36.9	0.87	0.62	0.45	37.5	0.91	0.73	**0.26**
	10	35.8	0.85	0.57	0.33	35.2	0.83	0.56	0.37	35.8	0.89	0.68	**0.21**
	12	34.6	0.83	0.52	0.28	33.7	0.79	0.51	0.32	34.3	0.87	0.64	**0.17**
	16	32.2	0.80	0.47	0.26	31.3	0.72	0.45	0.25	31.7	0.84	0.58	**0.13**

It is observed from Table 4.3 that, for dataset groups MIDI-MR and OSRX-MR, the proposed DLD-NLS has the lowest bpp values for each PAE criteria. For dataset groups, PHNT-MR and OSRX-XA, the bpp values are comparable or lesser than the bpp values obtained for CALIC.

Table 4.4 NLS compression performance comparison of CALIC, LOCO-I and the proposed DLD-NLS compression method for different image quality (PAE = 1,2,3,4,6,8,10,12,16). Results are shown for the dataset groups, OSRX-PT, average of CT, average of MR and average of the whole dataset.

	PAE	CALIC				LOCO-I				DLD-NLS (Proposed)			
		PSNR	MSSIM	UQI	bpp	PSNR	MSSIM	UQI	bpp	PSNR	MSSIM	UQI	bpp
OSRX-PT	1	57.2	1.00	1.00	0.48	55.6	1.00	0.85	0.55	57.2	1.00	0.99	**0.44**
	2	52.4	1.00	0.99	0.38	50.7	0.99	0.83	0.45	52.4	1.00	0.99	**0.36**
	3	49.4	1.00	0.99	0.33	47.6	0.97	0.81	0.41	49.4	1.00	0.99	**0.32**
	4	47.2	0.99	0.98	0.30	45.2	0.95	0.80	0.38	47.2	1.00	0.98	**0.28**
	6	44.0	0.99	0.97	0.25	41.8	0.91	0.79	0.36	44.0	0.99	0.98	**0.24**
	8	41.7	0.98	0.96	0.23	39.4	0.88	0.78	0.33	41.8	0.99	0.97	**0.20**
	10	40.0	0.97	0.95	0.20	37.5	0.85	0.78	0.31	40.1	0.98	0.96	**0.17**
	12	38.5	0.96	0.94	0.18	36.1	0.83	0.77	0.29	38.7	0.97	0.96	**0.15**
	16	36.3	0.95	0.92	0.16	33.8	0.80	0.76	0.26	36.5	0.96	0.94	**0.12**
CT	1	53.8	1.00	0.99	**1.21**	53.2	1.00	0.88	1.30	53.7	1.00	0.99	1.25
	2	49.0	1.00	0.97	**0.97**	48.4	0.99	0.86	1.07	49.0	1.00	0.98	0.99
	3	46.0	0.99	0.96	**0.82**	45.4	0.97	0.85	0.93	46.0	0.99	0.97	0.83
	4	43.8	0.98	0.94	**0.72**	43.2	0.96	0.83	0.83	43.8	0.99	0.96	**0.72**
	6	40.7	0.97	0.91	0.59	39.9	0.93	0.80	0.70	40.7	0.98	0.94	**0.57**
	8	38.3	0.94	0.85	0.51	37.6	0.89	0.77	0.61	38.5	0.96	0.91	**0.48**
	10	36.5	0.90	0.79	0.45	35.8	0.86	0.75	0.54	36.7	0.95	0.89	**0.41**
	12	34.9	0.87	0.74	0.41	34.4	0.83	0.73	0.49	35.3	0.94	0.87	**0.36**
	16	32.7	0.84	0.71	0.36	32.1	0.78	0.68	0.41	33.2	0.91	0.83	**0.28**
MR	1	50.8	0.99	0.95	1.83	50.5	0.99	0.91	2.00	50.7	0.99	0.95	**1.77**
	2	46.2	0.99	0.90	1.38	45.8	0.98	0.86	1.56	46.0	0.98	0.90	**1.35**
	3	43.4	0.97	0.85	1.13	42.9	0.96	0.81	1.30	43.2	0.97	0.85	**1.10**
	4	41.4	0.96	0.81	0.95	40.9	0.94	0.76	1.13	41.2	0.95	0.81	**0.93**
	6	38.6	0.93	0.72	0.74	37.9	0.90	0.68	0.90	38.3	0.91	0.73	**0.69**
	8	36.6	0.89	0.65	0.61	35.8	0.85	0.61	0.74	36.3	0.87	0.67	**0.54**
	10	35.1	0.86	0.59	0.51	34.2	0.80	0.54	0.64	34.7	0.82	0.61	**0.43**
	12	33.9	0.84	0.53	0.44	32.8	0.76	0.49	0.56	33.4	0.78	0.56	**0.36**
	16	31.9	0.79	0.46	0.35	30.7	0.68	0.42	0.45	31.3	0.71	0.48	**0.26**
AVERAGE	1	52.7	1.00	0.97	1.41	52.2	0.99	0.89	1.52	52.6	1.00	0.97	**1.40**
	2	48.0	0.99	0.94	1.09	47.4	0.98	0.86	1.21	47.9	0.99	0.95	**1.08**
	3	45.1	0.98	0.91	0.90	44.5	0.97	0.83	1.03	45.0	0.98	0.92	**0.89**
	4	43.0	0.97	0.88	0.77	42.3	0.95	0.80	0.91	42.9	0.97	0.90	**0.76**
	6	40.0	0.95	0.83	0.61	39.2	0.91	0.75	0.74	39.9	0.95	0.85	**0.58**
	8	37.8	0.92	0.76	0.52	37.0	0.87	0.70	0.63	37.7	0.93	0.81	**0.47**
	10	36.1	0.89	0.70	0.45	35.2	0.84	0.66	0.55	36.1	0.90	0.78	**0.39**
	12	34.7	0.86	0.66	0.40	33.8	0.80	0.63	0.49	34.7	0.88	0.75	**0.33**
	16	32.5	0.82	0.61	0.34	31.6	0.74	0.57	0.40	32.5	0.83	0.69	**0.25**

It is obsereved from Table 4.4 that, for dataset groups, OSRX-PT, MR and AVERAGE, the proposed DLD-NLS has the lowest bpp values for each PAE criteria. For dataset groups, CT the bpp values are comparable or lesser than the bpp values obtained for CALIC. Therefore, on an average and for MR images, DLD-NLS has the lowest bpp values for each PAE criteria.

(a)

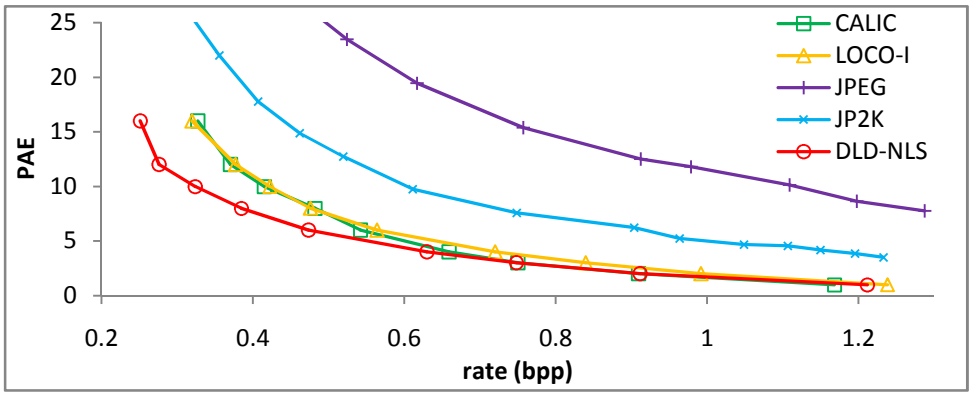

(b)

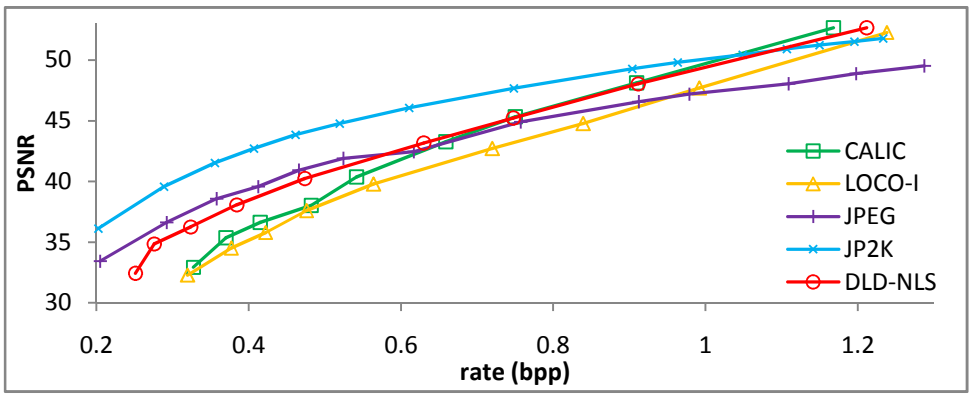

(c)

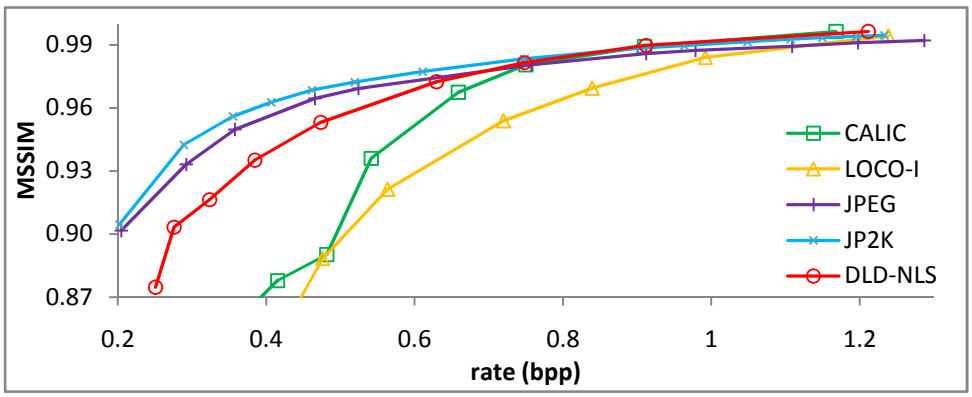

(d)

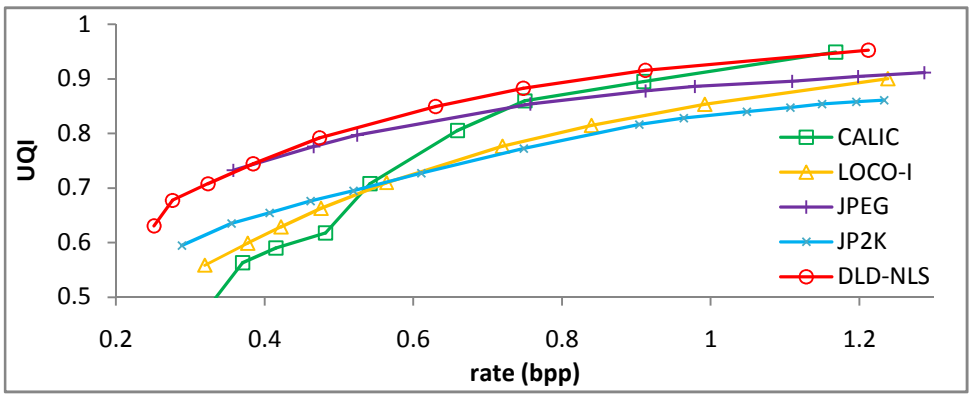

Fig.4.3 Comparison of NLS compression performance when tested with CIPR-CT dataset group. (a) PAE vs. bit rate (b) PSNR vs. bit rate (c) MSSIM vs. bit rate (d) UQI vs. bit rate

It is obsereved from Fig.4.3(a) that the proposed DLD-NLS provides comparable or lower bit rate for every PAE values, compared to all the other algorithms. Further, in terms of PSNR, MSSIM and UQI, the proposed DLD-NLS has comparable performance with CALIC and better performance than JPEG2000, JPEG and LOCO-I when the image is compressed at high quality with low PAE criteria.

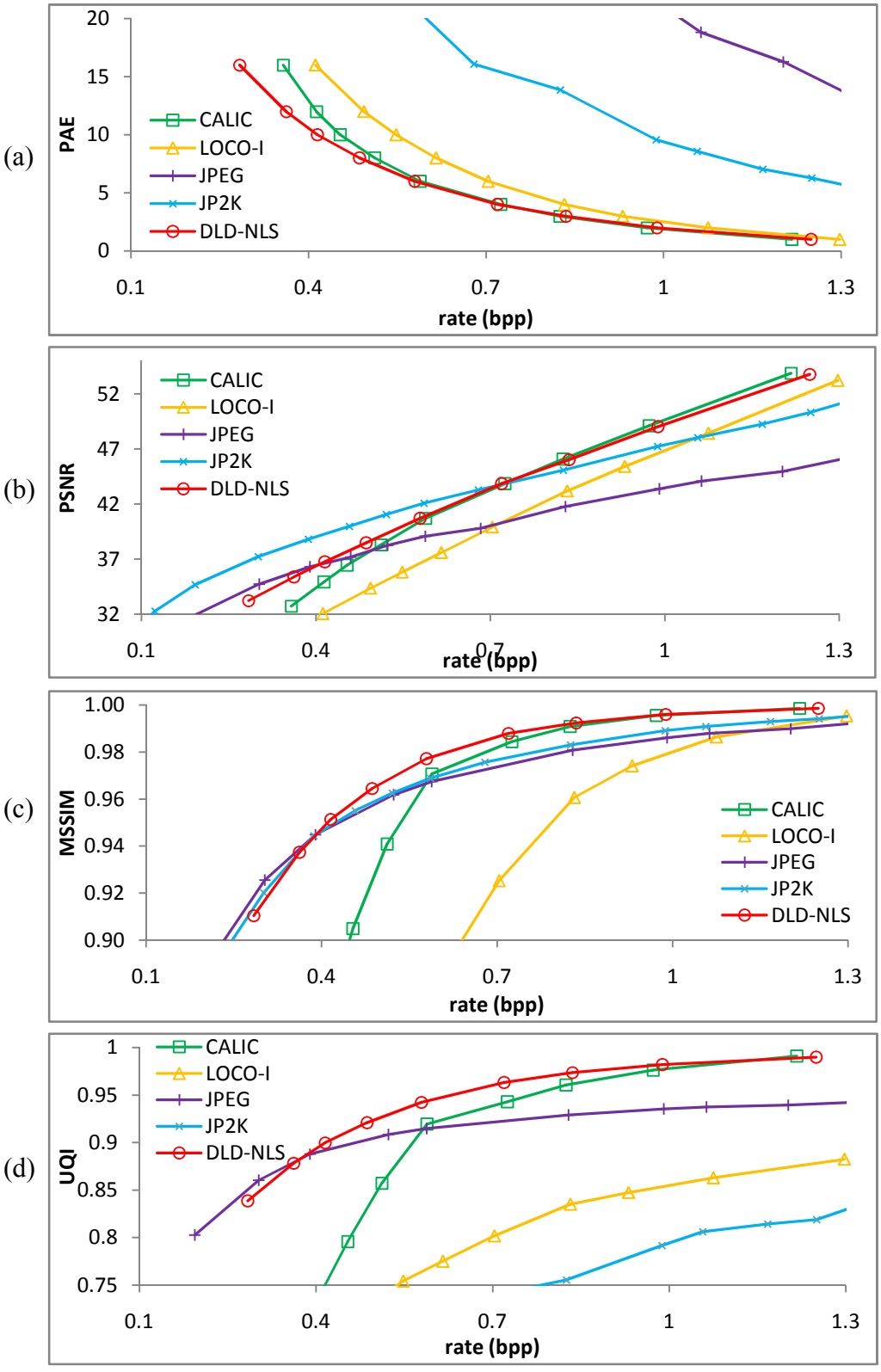

Fig.4.4 Comparison of NLS compression performance when tested with OSRX-CT dataset group. (a) PAE vs. bit rate (b) PSNR vs. bit rate (c) MSSIM vs. bit rate (d) UQI vs. bit rate

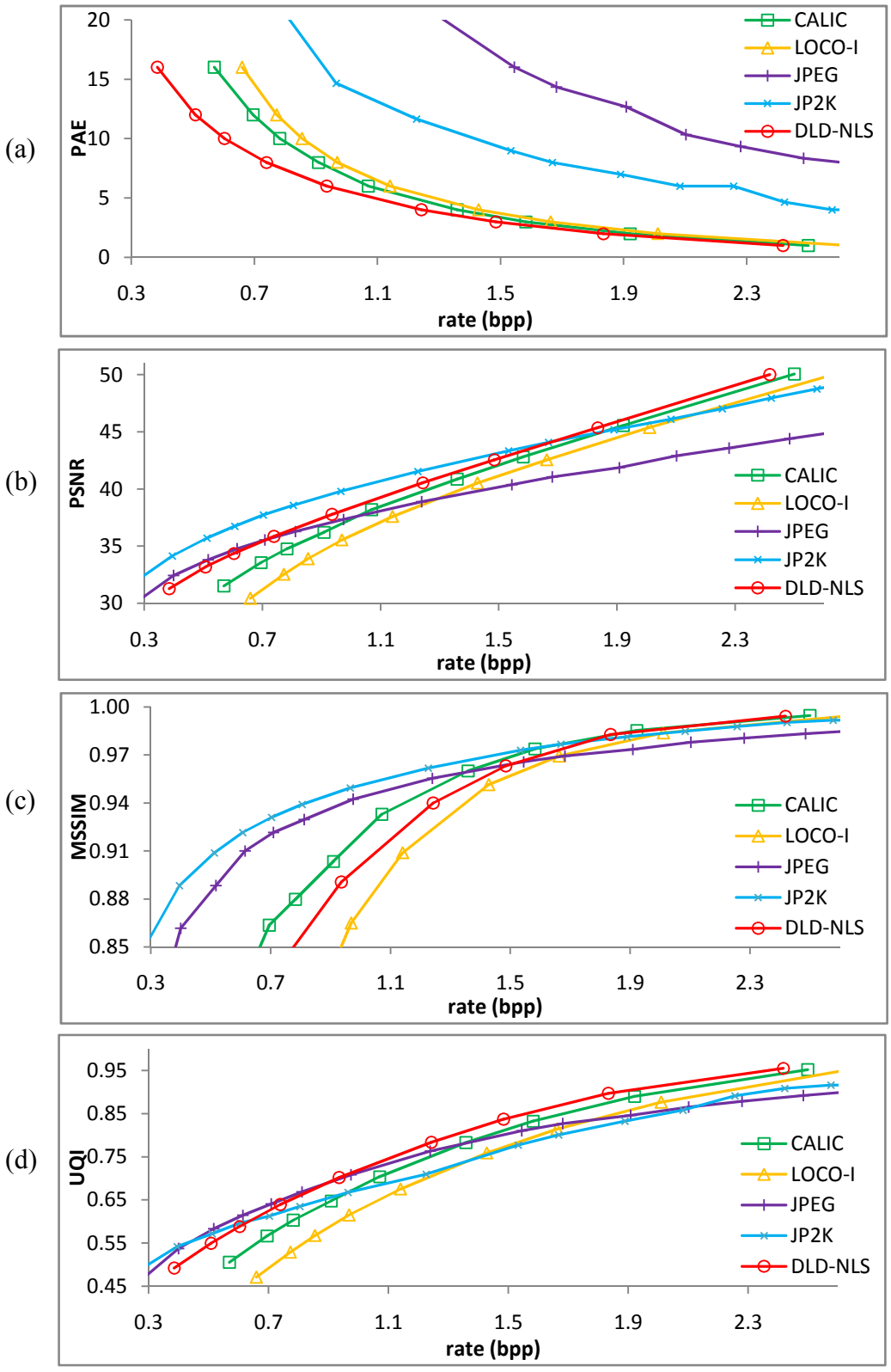

Fig.4.5 Comparison of NLS compression performance when tested with MGH-MR dataset group. (a) PAE vs. bit rate (b) PSNR vs. bit rate (c) MSSIM vs. bit rate (d) UQI vs. bit rate

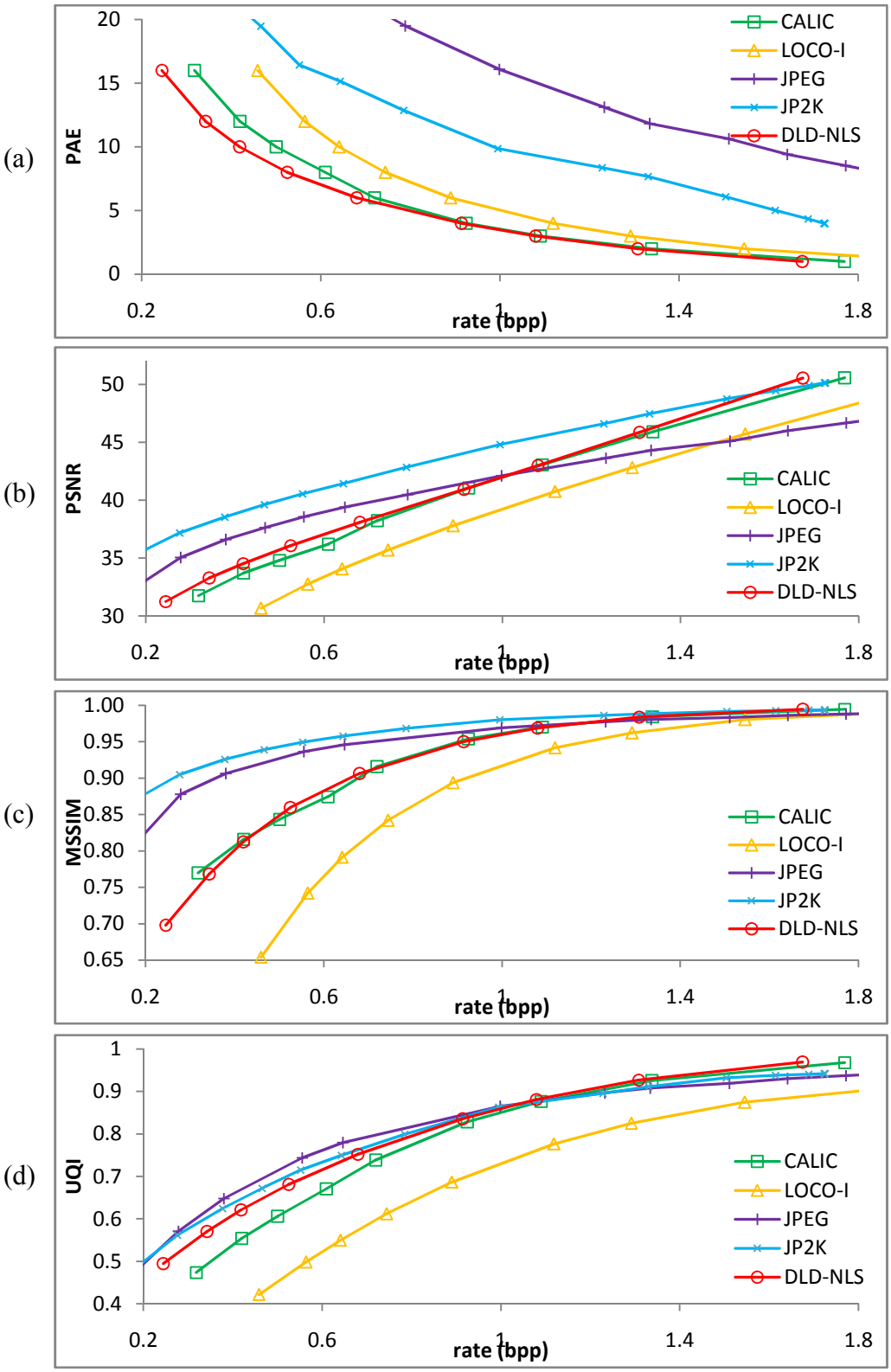

Fig.4.6 Comparison of NLS compression performance when tested with MIDI-MR dataset group. (a) PAE vs. bit rate (b) PSNR vs. bit rate (c) MSSIM vs. bit rate (d) UQI vs. bit rate

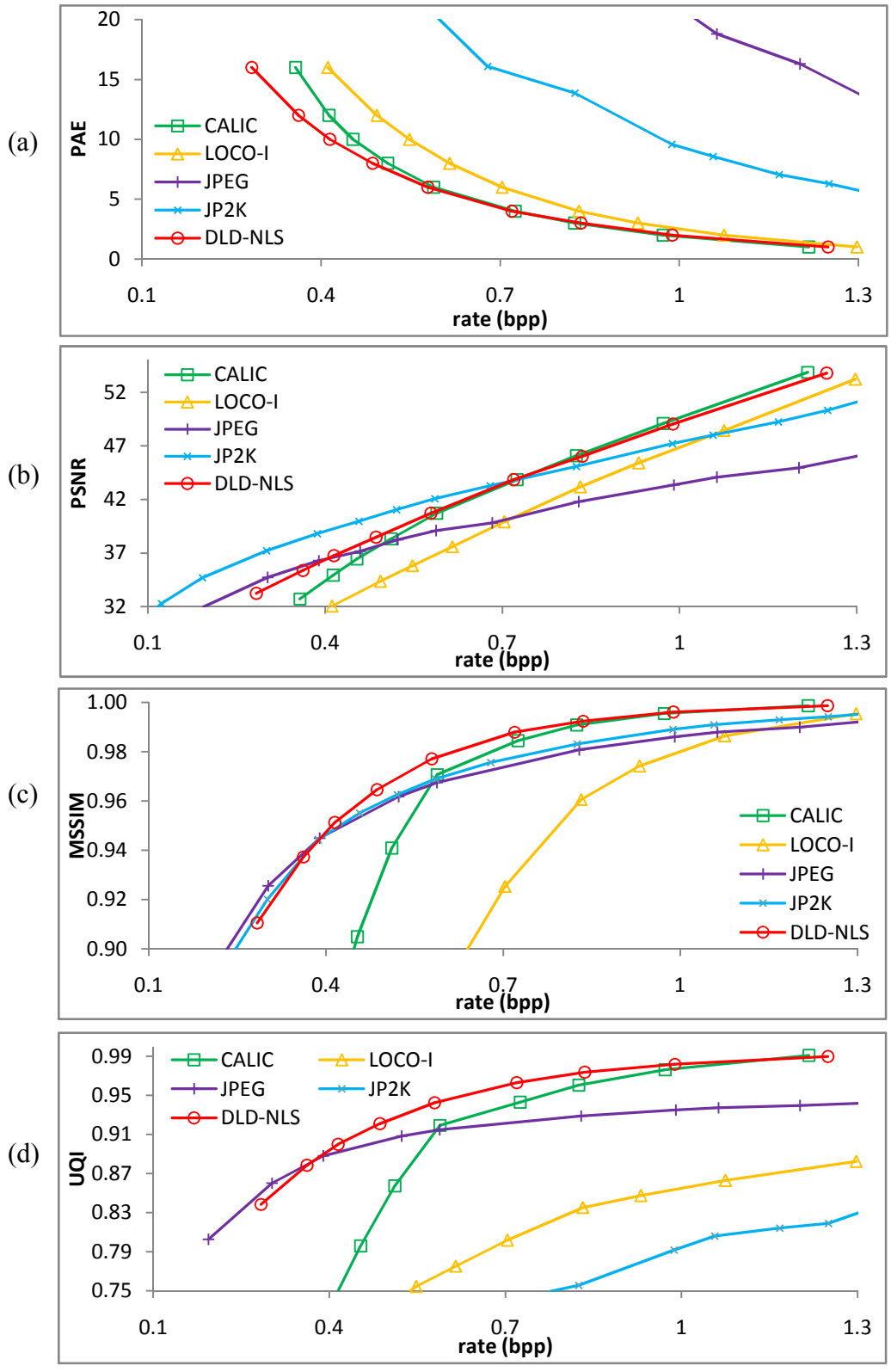

Fig.4.7 Comparison of NLS compression performance when tested with OSRX-CT dataset group. (a) PAE vs. bit rate (b) PSNR vs. bit rate (c) MSSIM vs. bit rate (d) UQI vs. bit rate

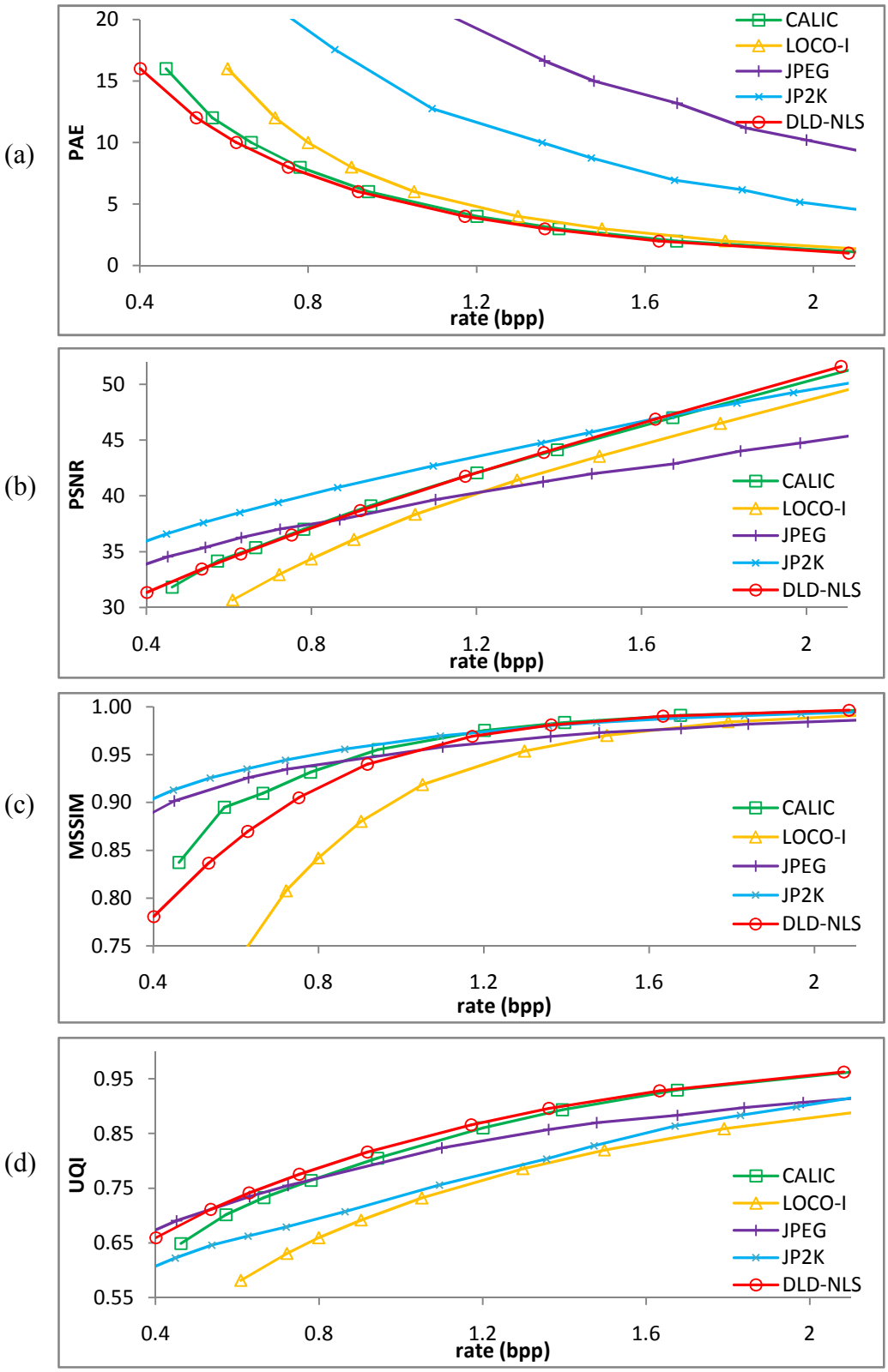

Fig.4.8 Comparison of NLS compression performance when tested with OSRX-MR dataset dataset group. (a) PAE vs. bit rate (b) PSNR vs. bit rate (c) MSSIM vs. bit rate (d) UQI vs. bit rate

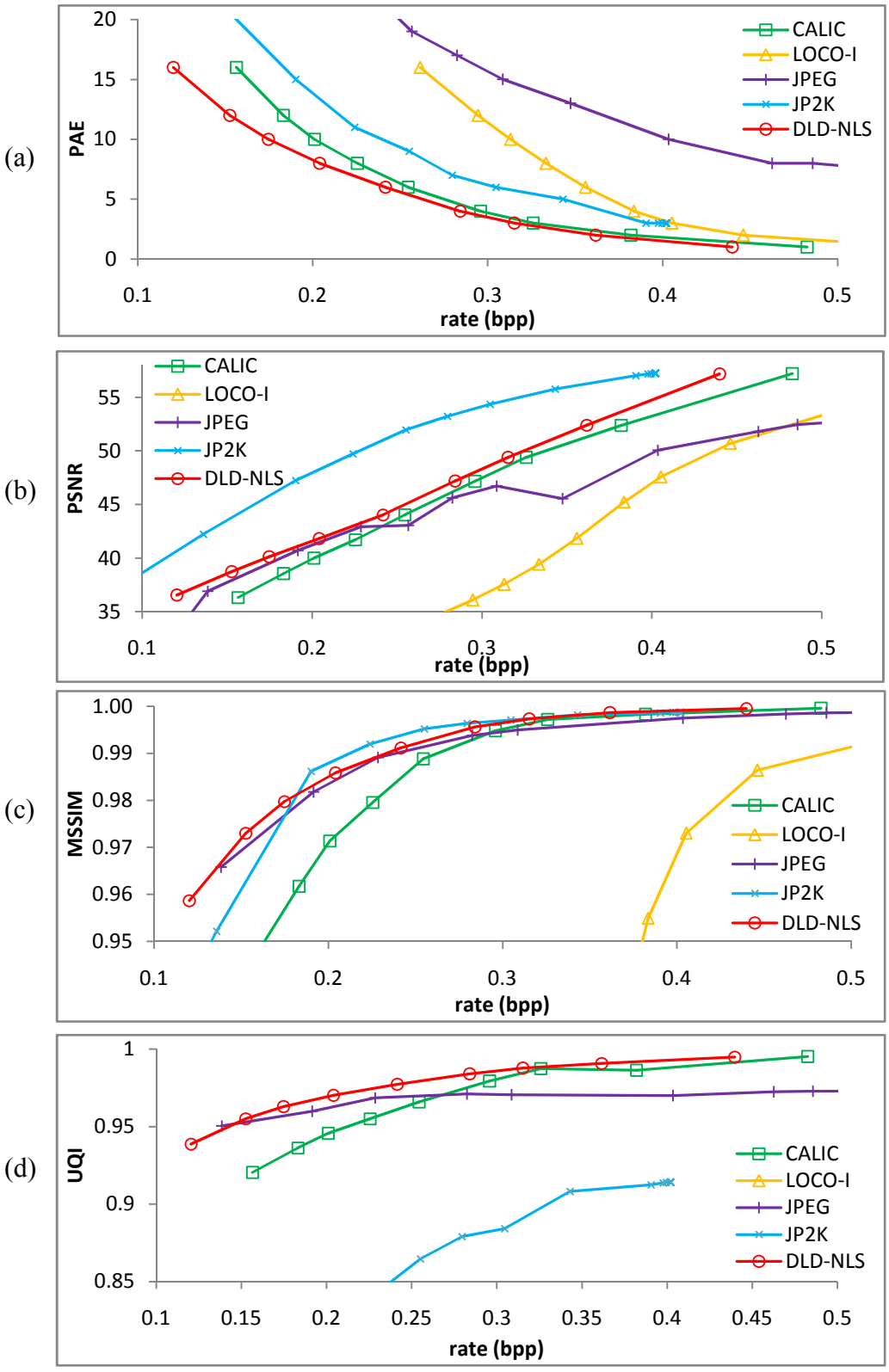

Fig.4.9 Comparison of NLS compression performance when tested with OSRX-PT dataset group.
(a) PAE vs. bit rate (b) PSNR vs. bit rate (c) MSSIM vs. bit rate (d) UQI vs. bit rate

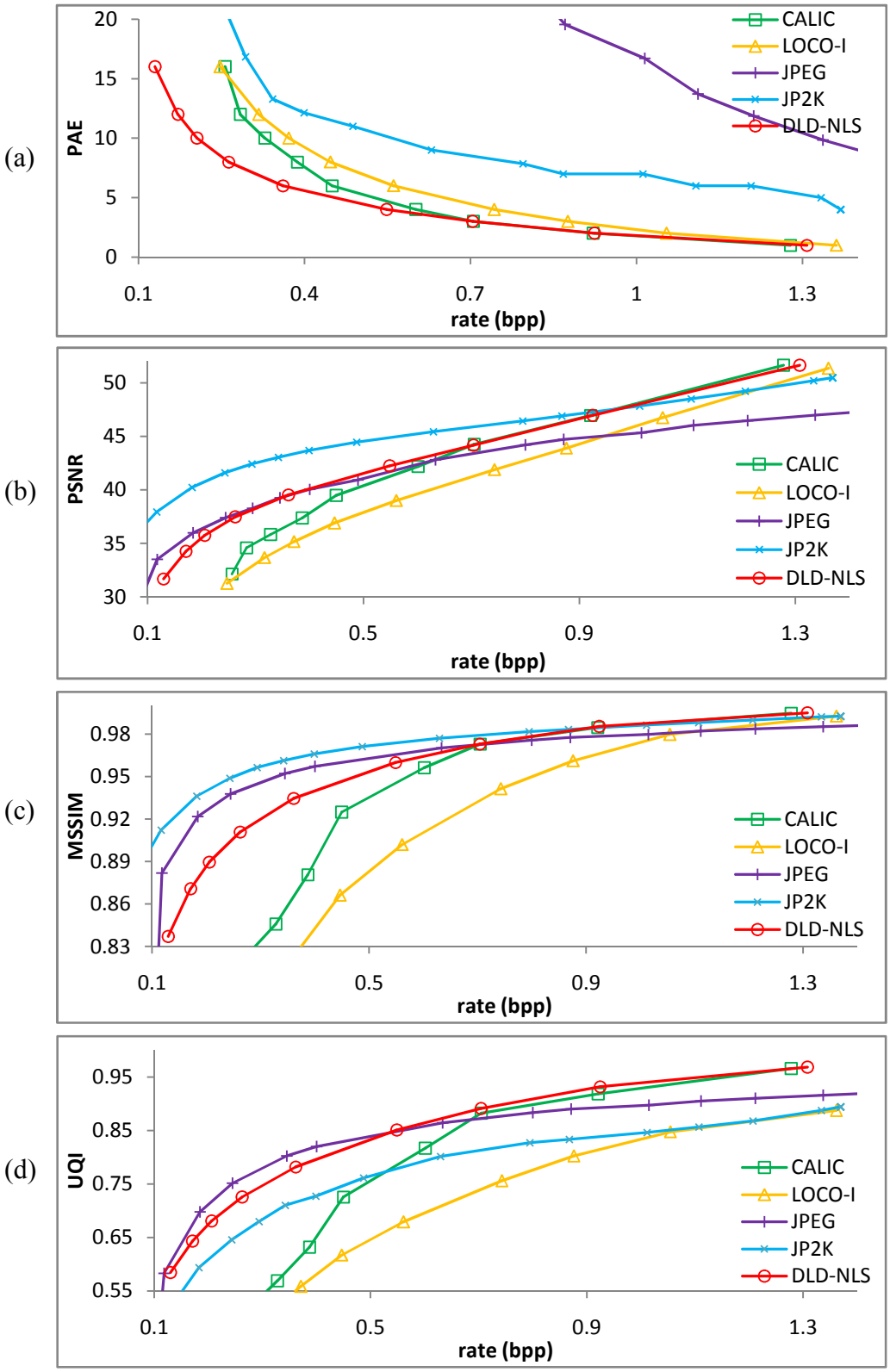

Fig.4.10 Comparison of NLS compression performance when tested with OSRX-XA dataset group. (a) PAE vs. bit rate (b) PSNR vs. bit rate (c) MSSIM vs. bit rate (d) UQI vs. bit rate

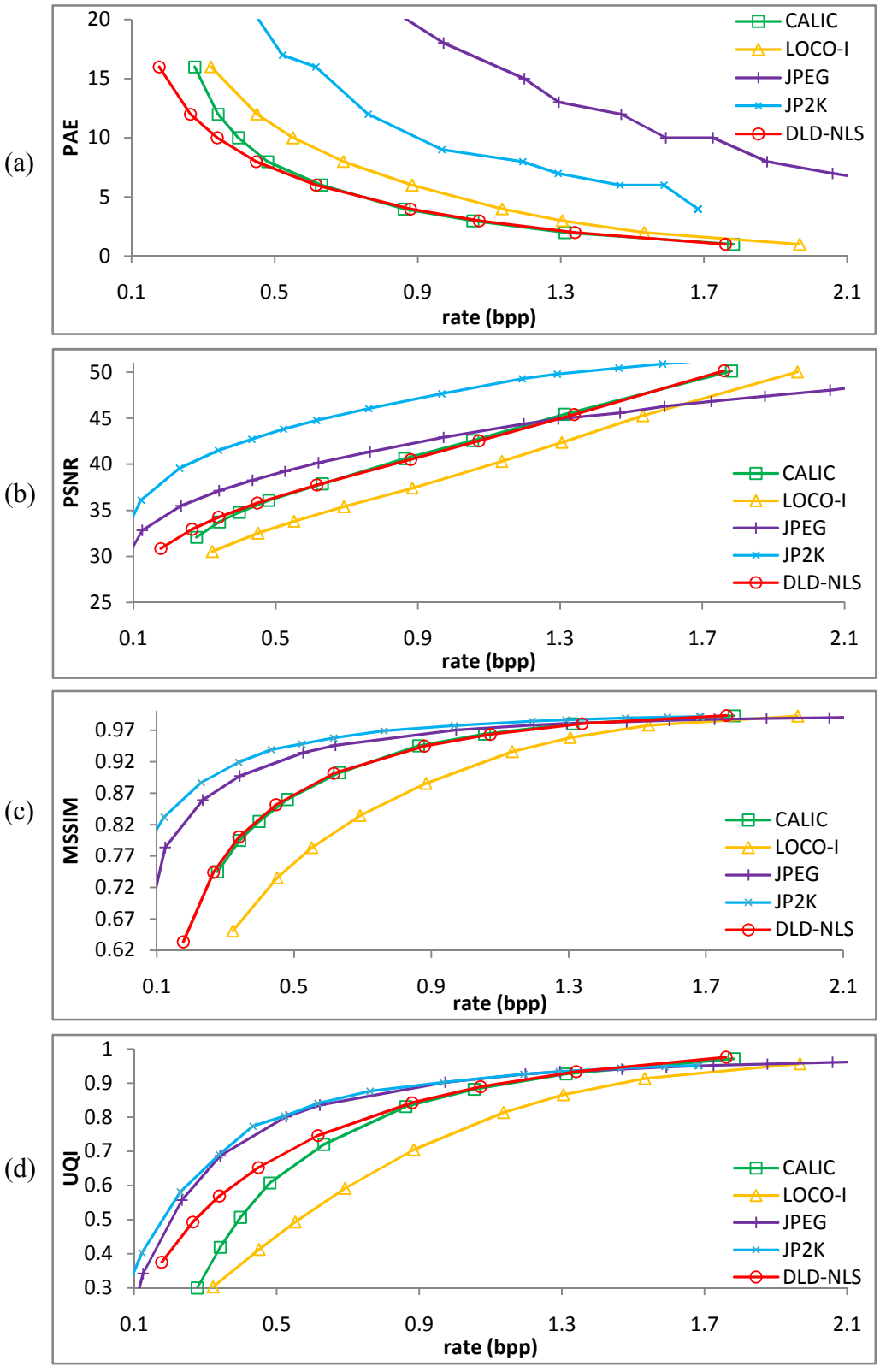

Fig.4.11 Comparison of NLS compression performance when tested with PHNT-MR dataset group. (a) PAE vs. bit rate (b) PSNR vs. bit rate (c) MSSIM vs. bit rate (d) UQI vs. bit rate

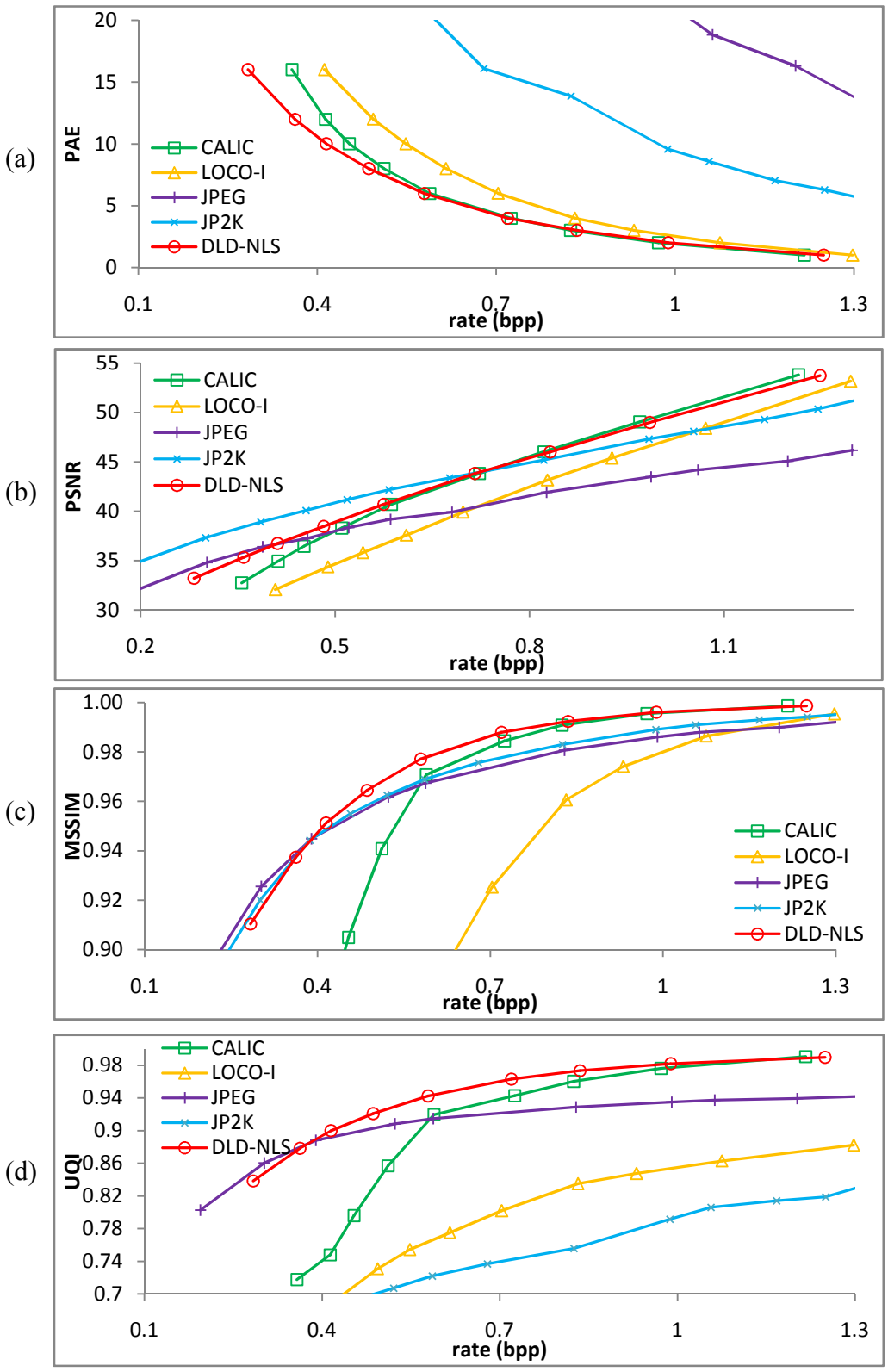

Fig.4.12 Comparison of NLS compression performance when tested with CT images in the whole dataset. (a) PAE vs. bit rate (b) PSNR vs. bit rate (c) MSSIM vs. bit rate (d) UQI vs. bit rate

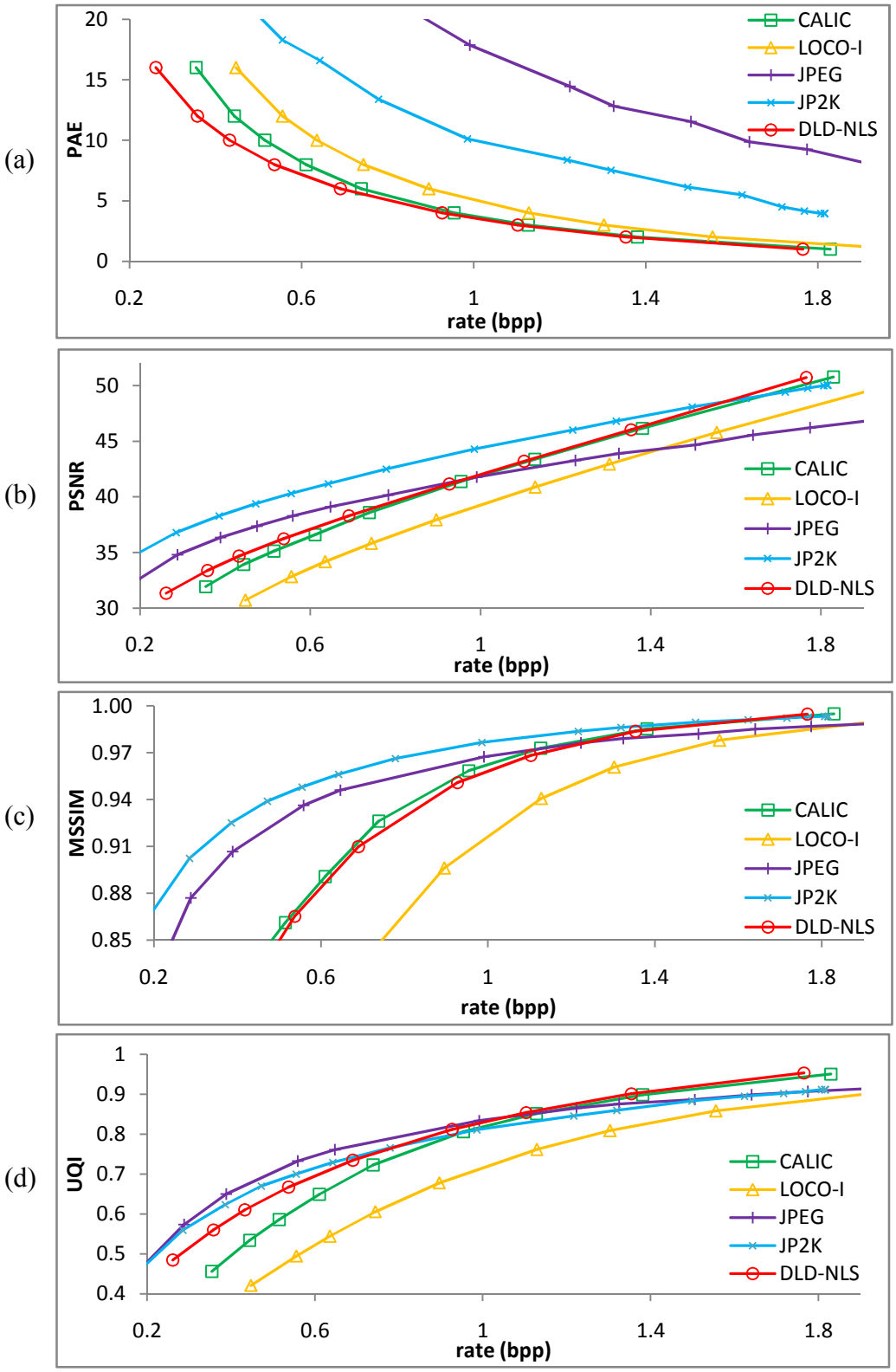

Fig.4.13 Comparison of NLS compression performance when tested with MR images in whole dataset. (a) PAE vs. bit rate (b) PSNR vs. bit rate (c) MSSIM vs. bit rate (d) UQI vs. bit rate

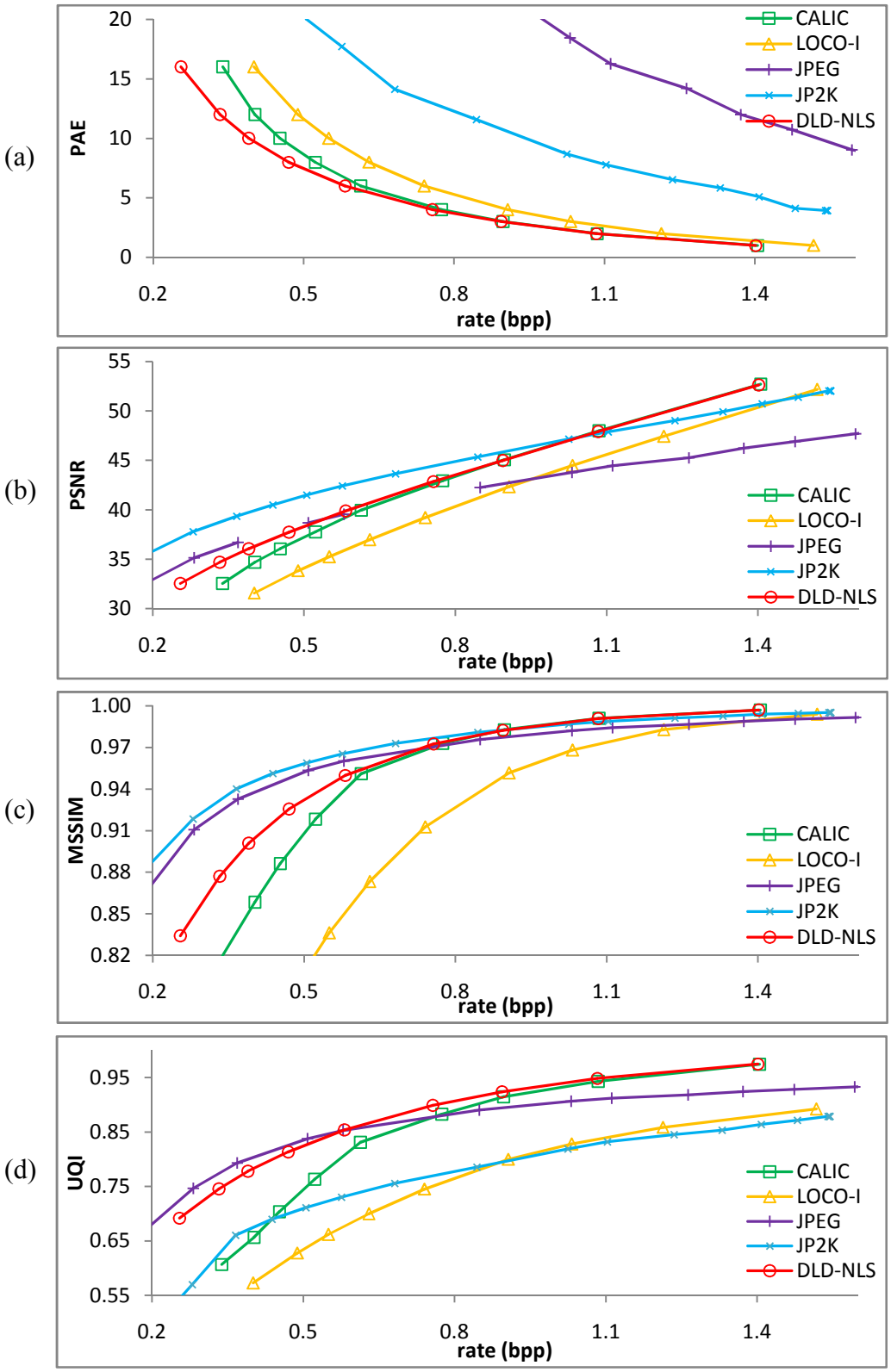

Fig.4.14 Comparison average NLS compression performance when tested with the complete dataset. (a) PAE vs. bit rate (b) PSNR vs. bit rate (c) MSSIM vs. bit rate (d) UQI vs. bit rate

Figures 4.3 to 4.14 shows the PAE, PSNR, MSSIM and UQI values for different bit rate per pixel. The individual values of each series are given in the appendix. It is observed that the proposed NLS compression technique based on DL-DPCM showed lowest bpp for each PAE. PSNR values of the proposed method is comparable with that of the CALIC for high quality images (image with low PAE values) and greater than LOCO-I, JPEG and JPEG2000. However, for low quality images, JPEG2000 shows superior performance with respect to PSNR values. The proposed algorithm showed better performance for high quality images in terms of quantitative values MSSIM and UQI. Therefore, it can be noted that the proposed method shows superior rate distortion performance for high quality images.

4.6 Summary

This chapter explained the proposed NLS compression technique based on the DL-DPCM predictor. The proposed NLS compression was evaluated with metric parameters, PAE, PSNR, MSSIM and UQI. The performance of the proposed algorithm was also compared with the NLS compression performance of CALIC and LOCO-I as well as the lossy compression performance of JPEG and JPEG2000. It can be concluded from the observations that, the proposed NLS compression technique has better performance for high quality images in terms of PAE, PSNR, MSSIM and UQI. Since the quality of medical images arevery important, the proposed method is highly suitable for medical image compression. Further, from the PAE measurement, it can be confirmed that the proposed compression technique can guarantee the maximum value of PAE.

Chapter 5

Region of Interest Compression

5.1 Introduction

Lossy compression techniques can achieve low bit per pixel rate with the loss of image quality. However, degradation in the image quality of the diagnostically important regions of medical image called region of interest (RoI) is not generally accepted in most cases. This may be due to legal reasons as well, when the medical images need to be archived for a certain number of years as a record. The accuracy of computer aided diagnostic (CAD) system may also be affected by lossy compression, since lossy compression alters the texture parameters of the image. RoI compression techniques takes the advantage of both lossless and lossy compression techniques. In RoI compression technique, explicitly defined RoIs are marked in the image and compressed in lossless manner. The non-RoIs are compressed in lossy manner to achieve bit rate reduction. This results in low bit rate with high quality of RoI.

An RoI compression scheme using DL-DPCM, namely DLD-RoI is proposed in this chapter. The following sections details the proposed method.

5.2 RoI Compression with DL-DPCM

In the proposed scheme, DLD-NLS encoder is modified to perform RoI compression. The block diagram of the proposed RoI scheme is showed in Fig.5.1. The linear quantizer performs quantization depending on the information given by the RoI mask. Quantization of the prediction error is not performed on the areas marked in the mask as RoI. Quantization of the prediction error is performed on the areas other than RoI depending on the quality of the background required. The RoI mask used during compression needs to be transmitted to the decoder to reconstruct the compressed image. If the RoIs are of regular shapes such as circle, rectangular, polygon etc., their geometric coordinates can be transmitted. If the RoI mask is of irregular shape, it can be transmitted as a binary image, compressed using binary image compression algorithms such as contour mapping.

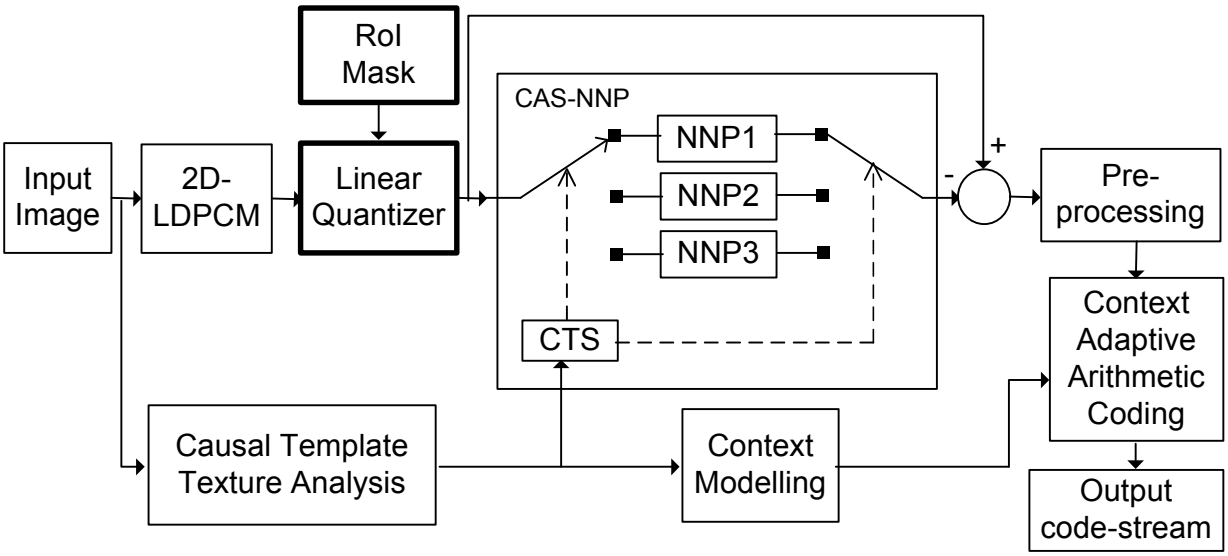

Fig.5.1 The proposed RoI compression Scheme. A linear quantizer quantizes the prediction error depending on the RoI mask.

5.3 Software Implementation

The algorithm is implemented in MATLAB 9.0 on a PC having Intel® CORE™2 Duo, 2.0 GHz using Neural Network Toolbox.

5.4 Experimentation Details

The experiments are performed for RoI compression of medical image data consisting of CT, MR,PET and Angiogram images. The images were compressed with 5%, 10% and 25% of square shaped RoIs at the center of the image. The RoI is compressed losslessly and the regions other than RoI are compressed with different PAE criteria (PAE= 1, 2, 3, 4, 6, 8, 10, 12, 16). The evaluation criteria and results and discussions are included in the following sub-sections.

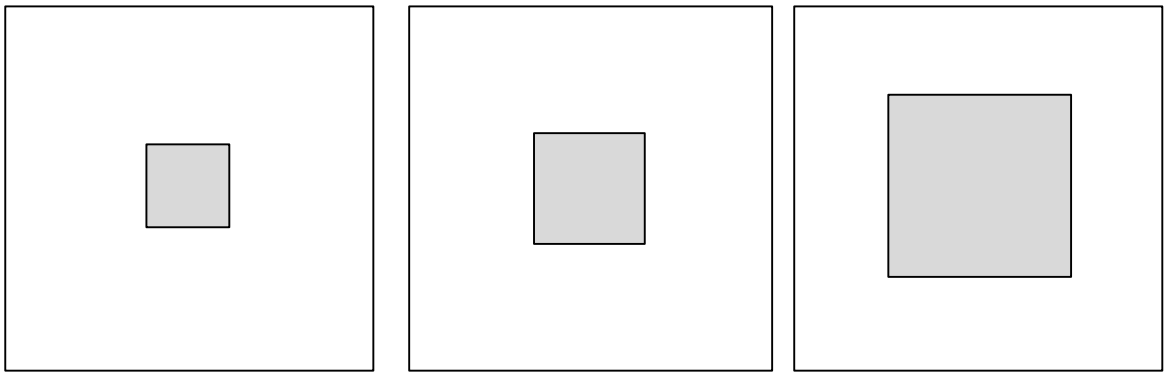

(a) 5% RoI (b) 10% RoI (c) 25% RoI

Fig. 5.2 Three different RoI masks used for testing the proposed DLD-RoI compression algorithm. Square shaped RoI (dark region) is select at the centre of the image (a) 5% of the image area is marked as RoI (b) 10% of the image area is marked as RoI (c) 25% of the image area is marked as RoI

Fig. 5.2 shows the three different RoIs used for the experiment. The central dark region represents the RoI.

For evaluating and comparing the RoI compression performance, bpp values were calculated as defined in chapter 2.

5.5 Results and Discussions

In this section, RoI compression results obtained with the DLD-RoI on CIPR, MGH, MicroDicom, OsiriX and Physionet datasets are discussed. The dataset details are given in chapater 2. The performance of the proposed DLD-RoI is compared with the performance of the proposed DLD-NLS compression technique proposed in chapter 4.

The original and the reconstructed image from the compressed images produced by the proposed DLD-NLS method is shown in Fig. 5.3. Fig. 5.3 (a) shows a single original slice from the MGHD-MR-02 dataset with a square shaped RoI mask of 10% of the image size. Fig. 5.3 (b)-(j) show the reconstructed image of the same slice, which is compressed by the proposed DLD-RoI method with different image quality for the non-RoI as specified: (b) PAE=1, (c) PAE=2, (d) PAE=3, (e) PAE=4, (f) PAE=6, (g) PAE=8, (h) PAE=10, (i) PAE=12, (j) PAE=16.

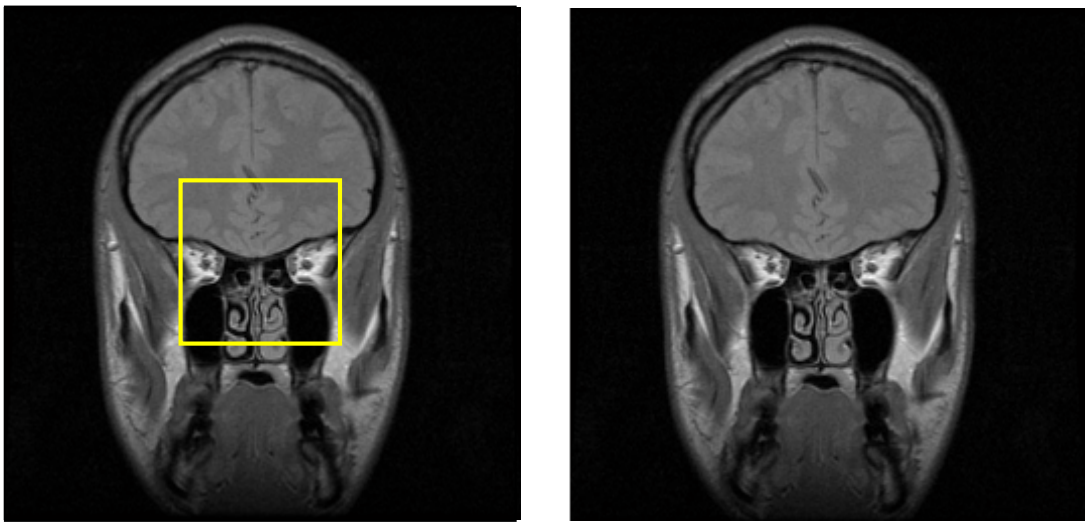

(a) (b)

Fig. 5.3 (a) A single slice from the original image dataset MGHD-02 with 10% of central area of the image marked as RoI (yellow square). (b)The reconstructed images after (a) is compressed using the proposed method, DLD-RoI with different non-RoI image qualities, PAE=1.

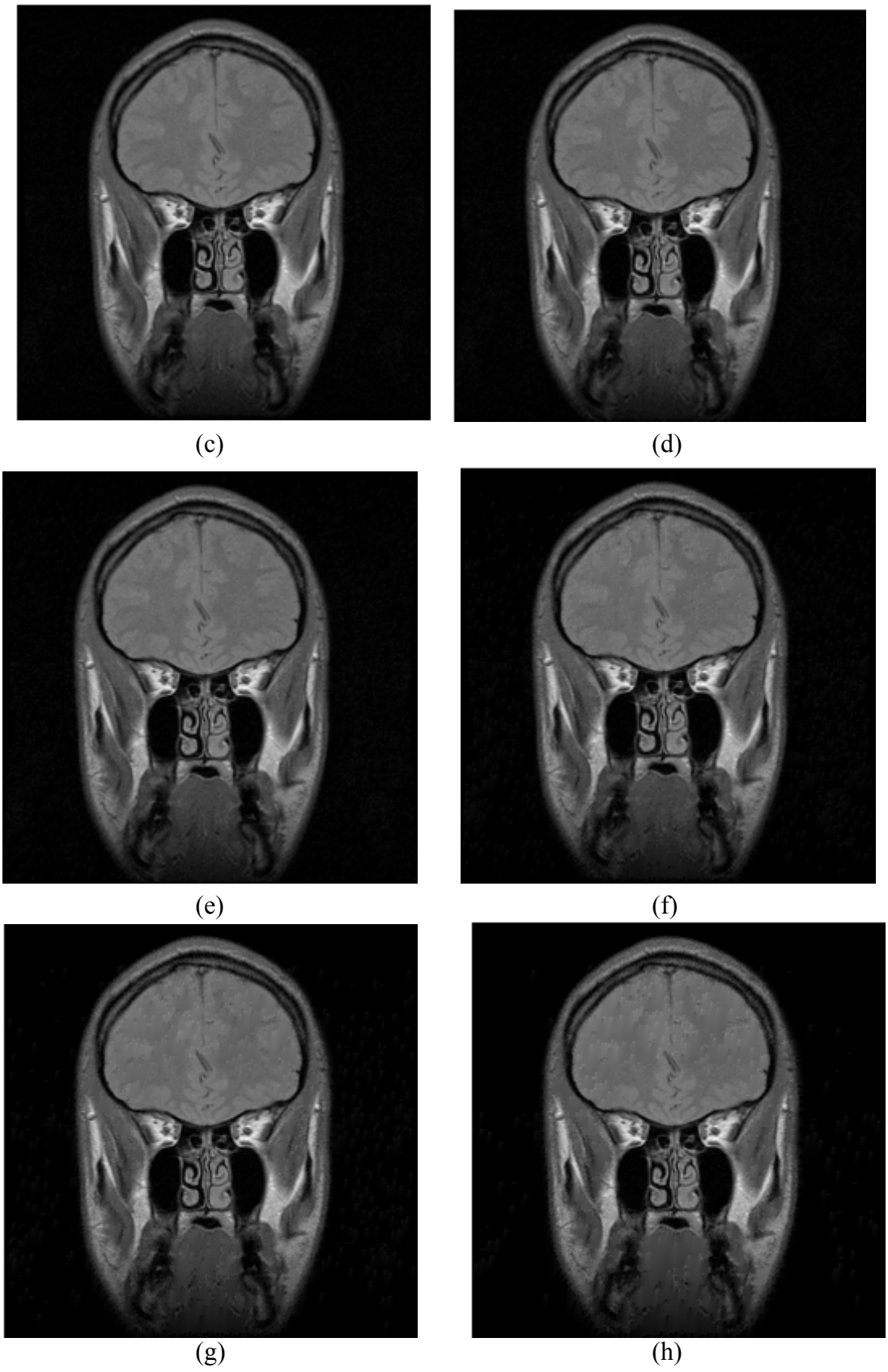

Fig. 5.3 (c)-(h) The reconstructed images after image in Fig. 5.3 (a) is compressed using the proposed method, DLD-RoI with different non-RoI image qualities ((c) PAE=2, (d) PAE=3, (e) PAE=4, (f) PAE=6, (g) PAE=8, (h) PAE=10.

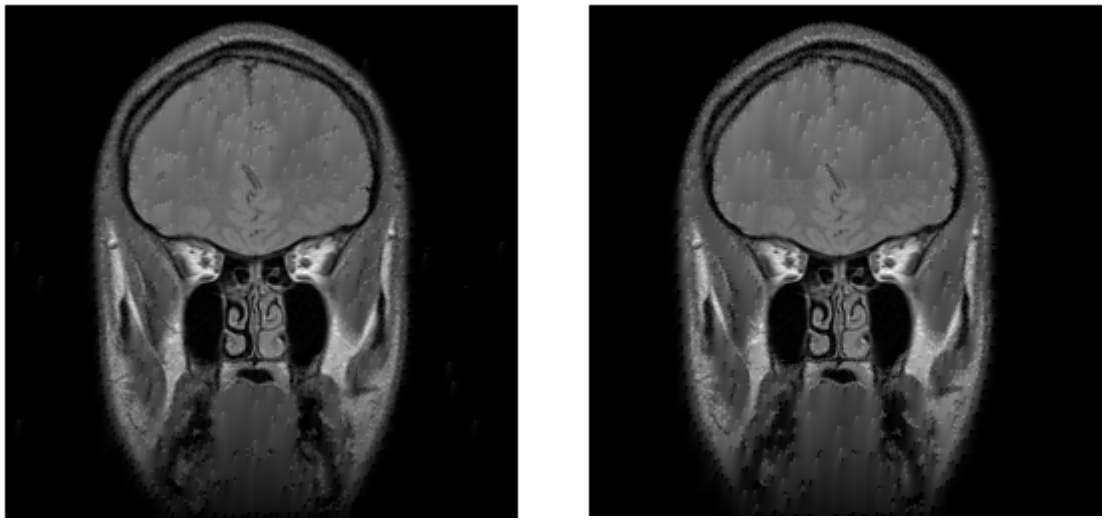

(i) (j)

Fig. 5.3 (i),(j) are the reconstructed images after (a) is compressed using the proposed method, DLD-RoI with different non-RoI image qualities (i) PAE=12, (j) PAE=16.

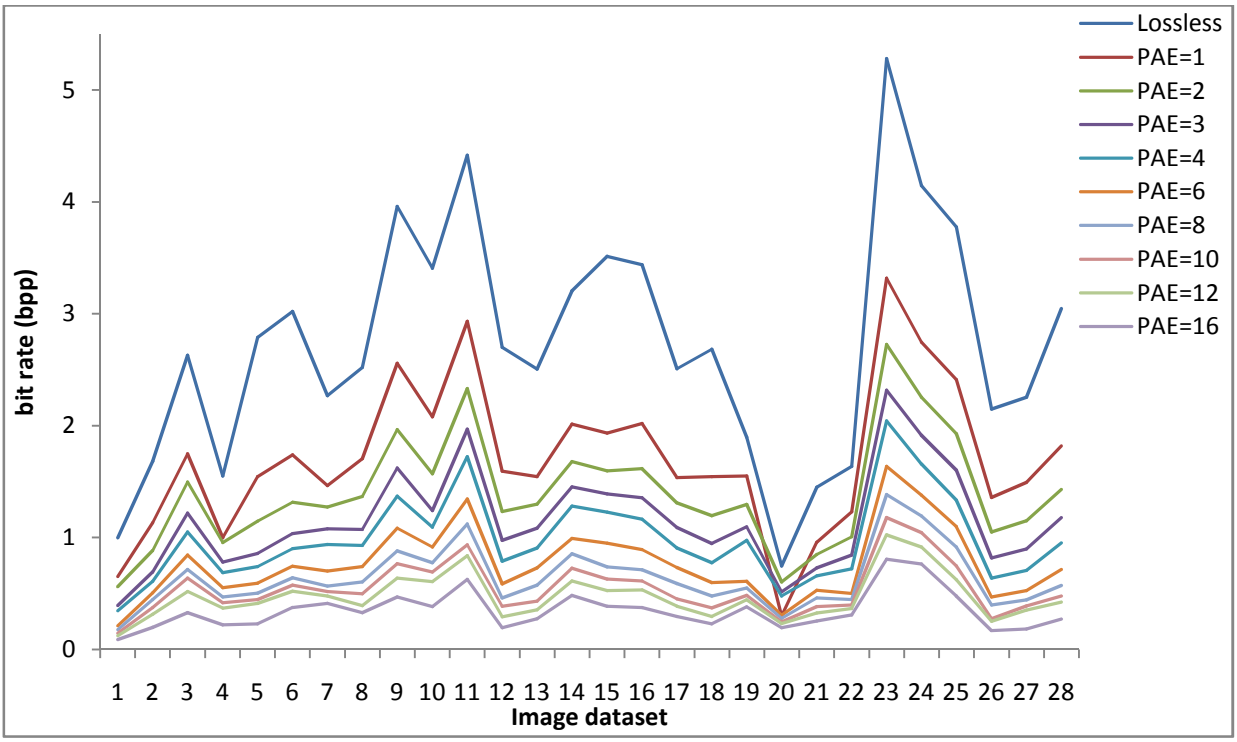

Fig. 5.4 Comparative compression performance of the proposed RoI compression method with 5% RoI for different non-RoI image quality (PAE1= 1,2,3,4,6 8,10,12,16)

It is observed that the there is substantial bit gain as the back ground is compressed with less image quality, ie. with PAE criteria increasing from PAE=1 to PAE=16.

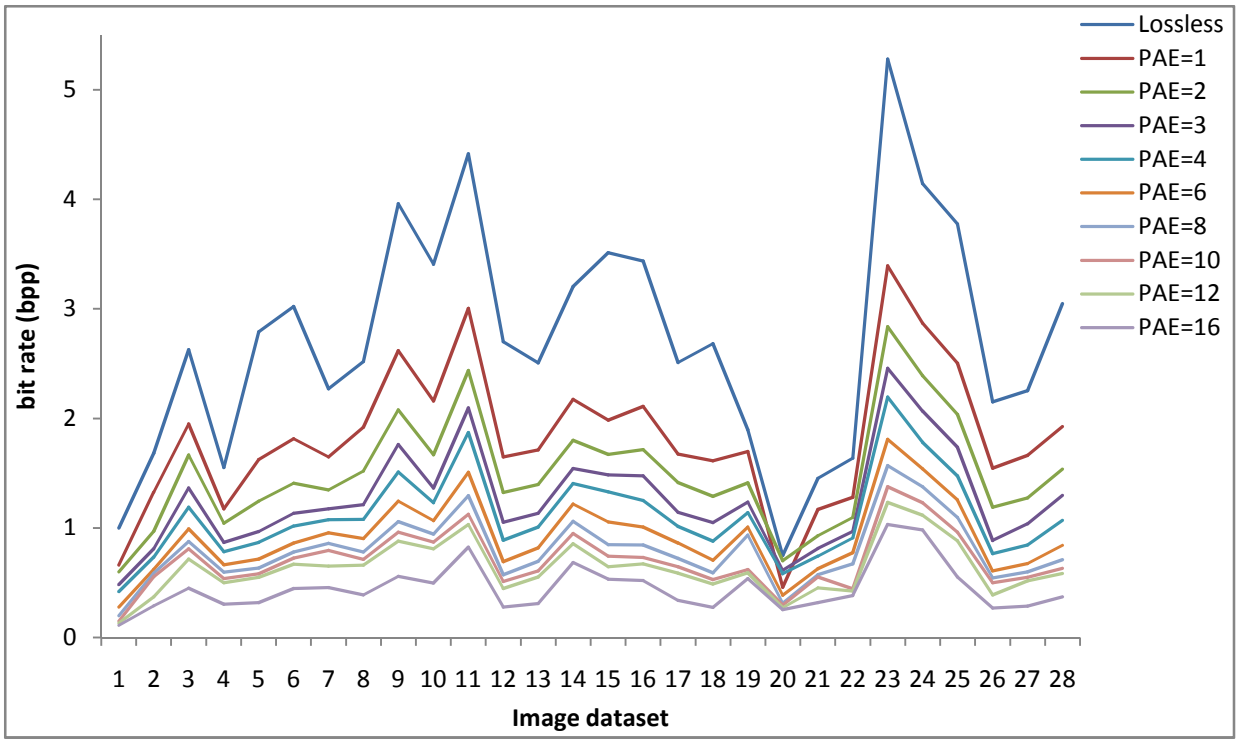

Fig. 5.5 Comparative compression performance of the proposed RoI compression method with 10% RoI for different non-RoI image quality (PAE1= 1,2,3,4,6 8,10,12,16)

Similar to the 5% RoI, it is observed that the there is substantial bit gain as the back ground is compressed with less image quality, ie. with PAE criteria increasing from PAE=1 to PAE=16, for 10% RoI and 25% RoI.

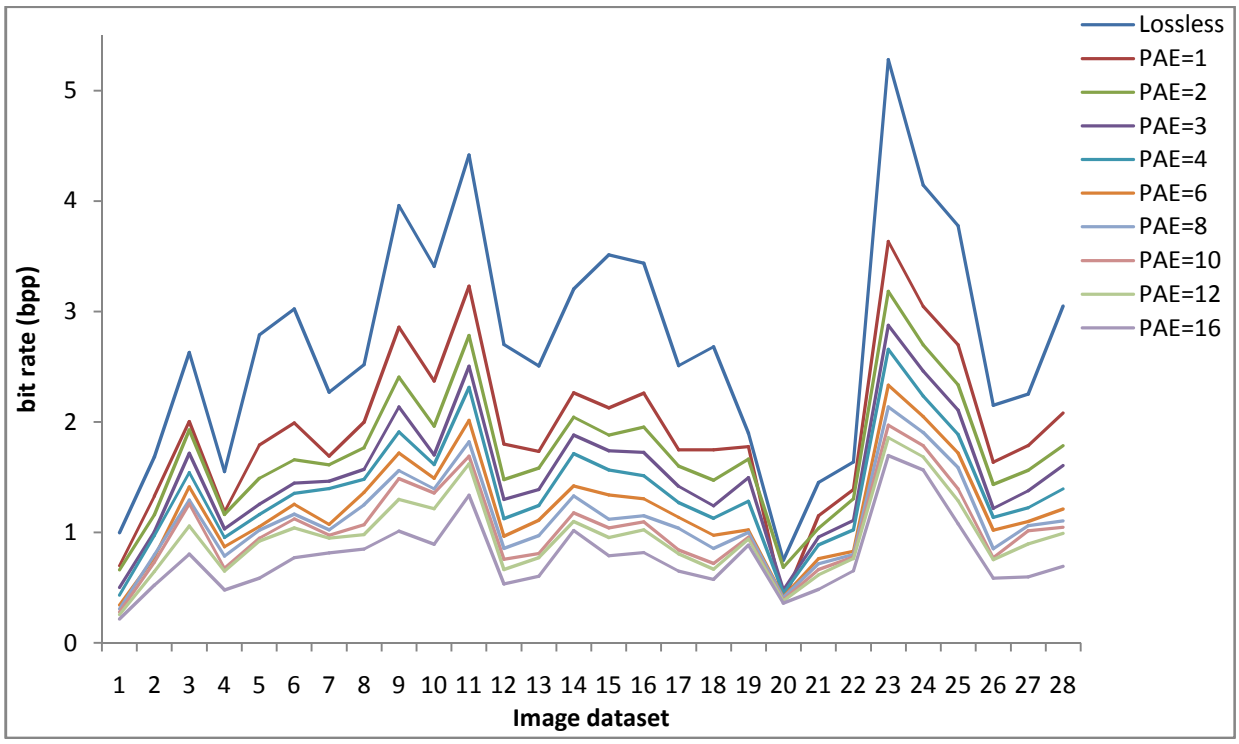

Fig. 5.6 Comparative compression performance of the proposed RoI compression method with 5% RoI for different non-RoI image quality (PAE1= 1,2,3,4,6 8,10,12,16)

Table 5.1 Comparison of bit rate per pixel of the proposed DL-DPCM based lossless method and the proposed RoI compression method with PAE=1 for non-RoI.

Dataset Group	Proposed DLD-LS (bpp)	Proposed DLD-RoI								
		RoI-5%			RoI-10%			RoI-25%		
		bpp	bit gain	% bit gain	bpp	bit gain	% bit gain	bpp	bit gain	% bit gain
CIPR-CT	1.86	1.23	0.64	34.1	1.39	0.48	25.6	1.42	0.45	24.0
OSRX-CT	1.78	1.40	0.38	21.5	1.08	0.71	39.6	1.11	0.68	37.9
CIPR-MR	2.66	1.61	1.05	39.5	1.74	0.92	34.5	1.86	0.80	30.0
MGH-MR	3.93	2.52	1.40	35.8	2.59	1.33	34.0	2.82	1.11	28.2
MIDI-MR	2.93	1.75	1.18	40.3	1.86	1.07	36.5	1.97	0.97	33.0
OSRX-MR	3.31	2.20	1.11	33.6	2.28	1.03	31.1	2.45	0.87	26.1
PHNT-MR	3.05	1.82	1.23	40.3	1.93	1.12	36.8	2.08	0.97	31.7
OSRX-XA	2.24	1.47	0.76	34.1	1.65	0.59	26.4	1.76	0.48	21.2
OSRX-PT	0.75	0.30	0.45	60.0	0.46	0.29	38.5	0.38	0.37	49.6
CT	1.81	1.35	0.46	31.4	1.51	0.30	22.6	1.55	0.26	20.9
MR	3.02	1.85	1.16	37.8	1.96	1.06	34.3	2.10	0.92	29.8
AVERAGE	2.25	1.50	0.75	37.1	1.65	0.61	32.6	1.73	0.53	28.6

It is observed from Table 5.1 that for every dataset, there is good measure of bit gain for the proposed DLD-RoI compression method compared to the proposed lossless method DLD-LS. Average bit gains of 0.75bpp (37.1%), 0.61bpp (32.6%) and 0.53 bpp (28.6%) , for 5% RoI, 10 % RoI and 25% RoI are observed when the background is compressed at low quality with PAE criteria PAE=1.

Table 5.2 Comparison of bit rate per pixel of the proposed DL-DPCM based lossless method and the proposed RoI compression method with PAE=4 for non-RoI.

Dataset Group	Proposed DLD-LS (bpp)	Proposed DLD-RoI								
		RoI-5%			RoI-10%			RoI-25%		
		bpp	bit gain	% bit gain	bpp	bit gain	% bit gain	bpp	bit gain	% bit gain
CIPR-CT	1.86	0.75	1.11	59.8	0.86	1.00	53.9	1.08	0.79	42.1
OSRX-CT	1.78	0.89	0.89	49.9	0.74	1.05	58.6	0.82	0.96	53.9
CIPR-MR	2.66	0.87	1.79	67.3	1.00	1.66	62.4	1.34	1.32	49.8
MGH-MR	3.93	1.40	2.53	64.5	1.54	2.39	60.9	1.95	1.98	50.4
MIDI-MR	2.93	1.02	1.91	65.3	1.12	1.81	61.8	1.38	1.55	53.0
OSRX-MR	3.31	1.30	2.01	60.8	1.45	1.86	56.1	1.78	1.54	46.4
PHNT-MR	3.05	0.95	2.10	68.8	1.07	1.98	64.9	1.39	1.65	54.2
OSRX-XA	2.24	0.70	1.54	68.8	0.83	1.40	62.8	1.21	1.03	45.8
OSRX-PT	0.75	0.48	0.27	35.9	0.58	0.17	22.4	0.45	0.30	39.6
CT	1.81	0.85	0.96	58.0	0.98	0.83	51.3	1.15	0.66	41.7
MR	3.02	1.04	1.98	64.8	1.16	1.85	60.5	1.47	1.55	50.3
AVERAGE	2.25	0.89	1.36	63.7	1.02	1.23	59.3	1.25	1.01	49.0

It is observed from Table 5.2 similar to the results in Table 5.1, for every dataset, there is good measure of bit gain for the proposed DLD-RoI compression method compared to the proposed lossless method DLD-LS. Average bit gains of 1.36 bpp (63.7%), 1.23 bpp (59.3%) and 1.01 bpp (49.0%) , for 5% RoI, 10 % RoI and 25% RoI are observed when the background is compressed at low quality with PAE criteria PAE=4. It is also observed that with higher value of PAE for background, there is improvement in bit gain.

Table 5.3 Comparison of bit rate per pixel of the proposed DL-DPCM based lossless method and the proposed RoI compression method with PAE=16 for non-RoI.

Dataset Group	Proposed DLD-LS (bpp)	Proposed DLD-RoI								
		RoI-5%			RoI-10%			RoI-25%		
		bpp	bit gain	% bit gain	bpp	bit gain	% bit gain	bpp	bit gain	% bit gain
CIPR-CT	1.86	0.23	1.63	87.4	0.32	1.54	82.7	0.56	1.31	70.1
OSRX-CT	1.78	0.35	1.43	80.4	0.34	1.44	80.9	0.55	1.23	69.1
CIPR-MR	2.66	0.33	2.33	87.6	0.40	2.26	85.1	0.74	1.92	72.0
MGH-MR	3.93	0.49	3.43	87.4	0.63	3.30	84.1	1.08	2.85	72.5
MIDI-MR	2.93	0.33	2.60	88.8	0.43	2.50	85.4	0.72	2.21	75.3
OSRX-MR	3.31	0.54	2.77	83.7	0.67	2.64	79.8	1.14	2.17	65.6
PHNT-MR	3.05	0.27	2.78	91.1	0.37	2.68	87.8	0.69	2.35	77.2
OSRX-XA	2.24	0.18	2.06	91.8	0.28	1.96	87.4	0.60	1.64	73.4
OSRX-PT	0.75	0.19	0.55	74.0	0.25	0.49	66.0	0.36	0.39	51.8
CT	1.81	0.31	1.50	85.8	0.43	1.38	80.8	0.71	1.10	67.7
MR	3.02	0.36	2.66	87.4	0.46	2.56	84.2	0.81	2.21	72.2
AVERAGE	2.25	0.31	1.94	87.2	0.42	1.83	83.5	0.72	1.53	71.3

It is observed from Table 5.3 that average bit gains of 1.94 bpp (87.2%), 1.83 bpp (83.5%) and 1.53 bpp (71.3%) , for 5% RoI, 10 % RoI and 25% RoI are observed when the background is compressed at low quality with PAE criteria PAE=16. It is also observed that with higher value of PAE for background, there is improvement in bit gain. It is also observed from Tables 5.1 – Table 5.3 that as the area of the RoI is decreasing, there is improvement in the bit rate.

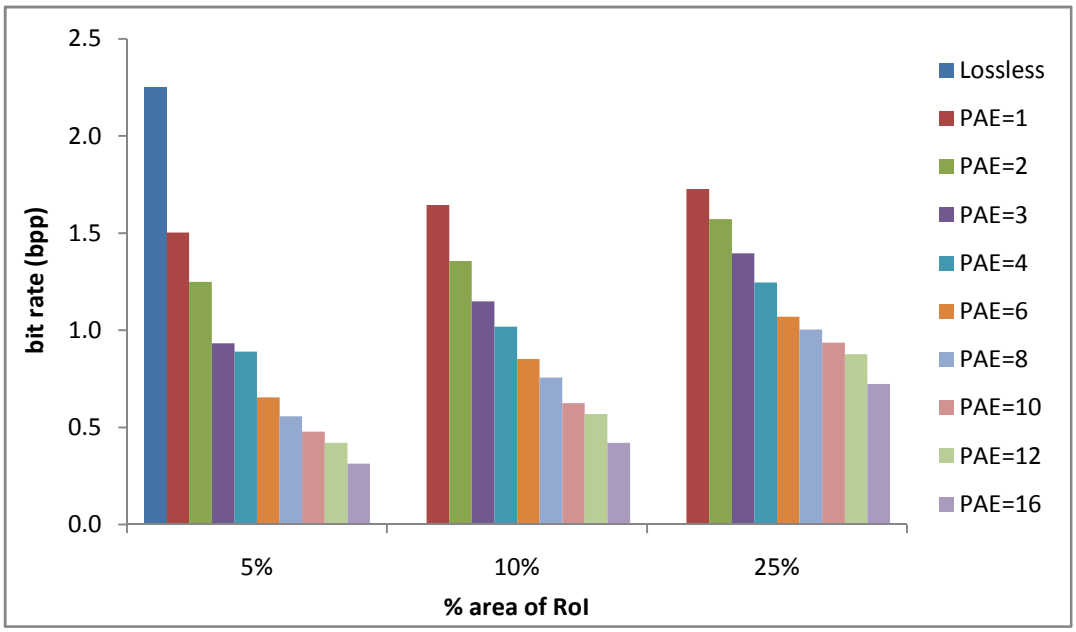

Fig. 5.7 Average bit rates obtained for the whole dataset with the proposed lossless compression as well as with the proposed RoI compression of different RoI (5%, 10%, 25%) and with different non-RoI image qualitative (PAE = 1,2,3,4,6,8,10,12,16)

It is observed from the Fig. 5.7 that when background image is compressed at low quality, substantial bit gain is achieved. The change in bit rate with respect to the change in the percentage of RoI is rather less.

5.6 Summary

The proposed NLS compression algorithm, DLD-NLS compression algorithm was modified to perform region of interest (RoI) coding. The algorithm is realized by quantizing the prediction error image only on the selected areas defined by an RoI mask. RoI with 5%, 10% and 25% of the image area with square shape at the center of the image were defined. The CT, MR, PET and angiogram were used to test the RoI coding capabilities of the developed algorithm. It was observed that the proposed RoI compression algorithm, DLD-RoI could achieve bit gain over the proposed lossless compression DLD-LS.

Chapter 6

Resolution Scalable Image Compression

6.1 Introduction

In applications such as telemedicine and teleradiology, several images of low resolution are displayed together at first and later the required image is magnified into a higher resolution. Images with low resolution is transmitted at first, then the information required to obtain a higher resolution of the same image is transmitted progressively in an interactive environment. The transmission can also be stopped at the required level of resolution. Bit saving can be achieved in this way if only low resolution is required for a part of image series being transmitted.

A resolution scalable image compression technique, using the DL-DPCM namely RDLD is proposed in this chapter. The proposed RDLD has capabilities of lossless compression, near lossless compression and region of interest compression, which are referred here as RDLD-LS, RDLD-NLS and RDLD-RoI, respectively. The following sections details the RDLD and the experimentation results when it is tested with medical image datasets such as CT, MR, PET and angiogram.

6.2 Resolution scalable image compression using DL-DPCM

The flow diagram of the proposed resolution scalable image compression technique, RDLD is depicted in Fig. 6.1. In order to facilitate resolution scalable image compression, the original image is first sub-sampled into the desired coarse resolution required. Fig. 6.2 shows image decomposition into two levels by sub-sampling. Fig. 6.2 (a) shows the original image, Fig. 6.2 (b) shows the coarse image obtained by sub-sampling the original image, Fig. 6.2 (c) shows the second level of decomposed image obtained by sub-sampling the image shown in Fig. 6.2 (b). The RDLD operates in two modes, namely run mode and predictive mode, if the image is compressed in lossless manner (RDLD-LS). When the values of three adjacent neighboring pixels of the pixel being predicted are equal, the RDLD-LS switches to run mode as in the case of DLD-LS described in chapter 3. When the run breaks, it operates in predictive mode.

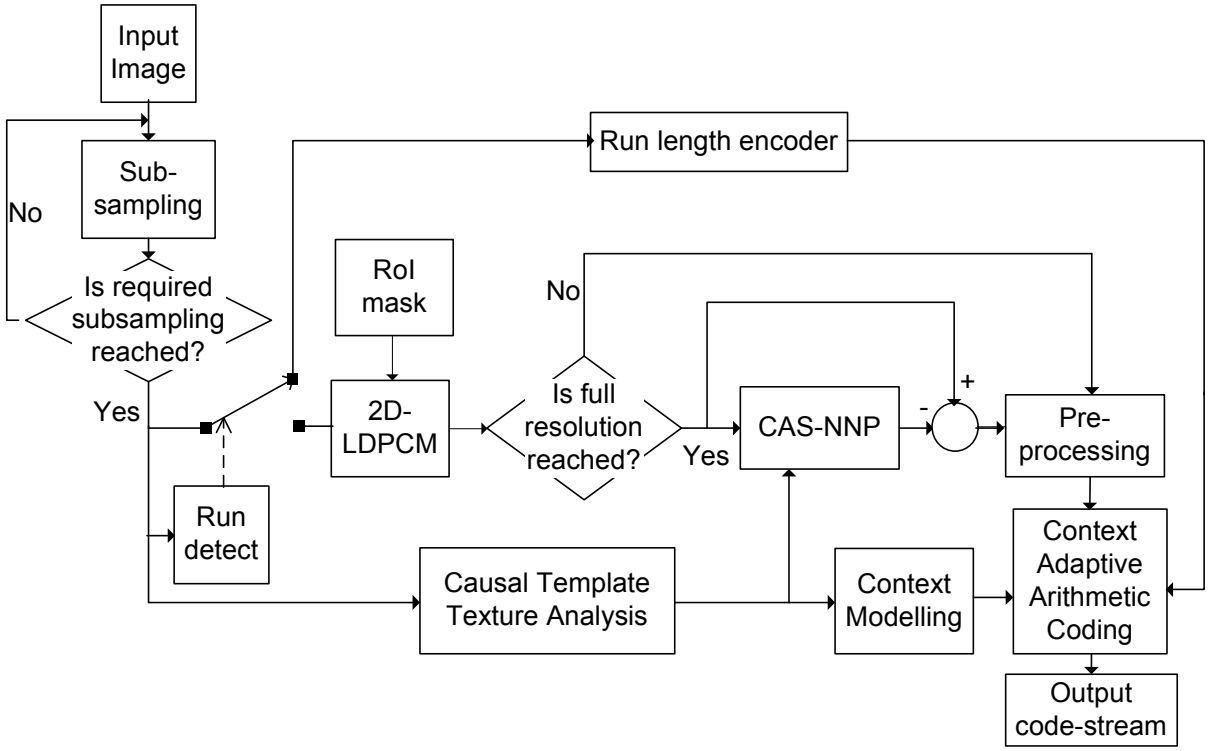

Fig. 6.1 The flow diagram of the proposed resolution scalable image compression technique (RDLD) using the DL-DPCM

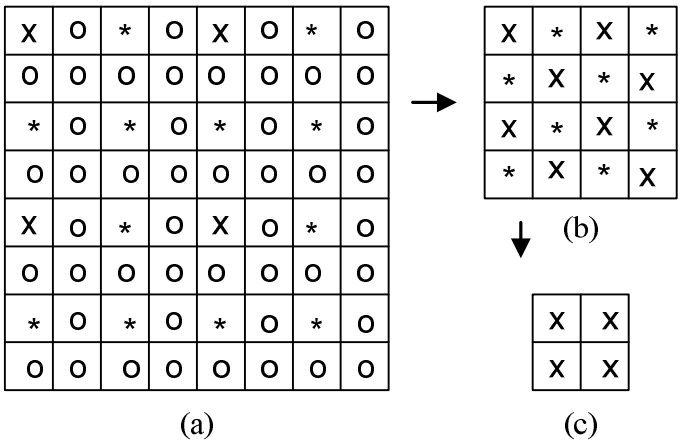

Fig. 6.2 Decomposition of image into two levels by sub-sampling. (a) is the original image (b) is the first level of coarse image obtained by sub-sampling the original image (c) is the second level of coarse image obtained by sub-sampling the image (b).

In predictive mode, 2D-LDPCM is used to deorrelate the image at the low-resolution levels. The error image produced by the 2D-LDPCM is entropy coded using adaptive arithmetic encoder after pre-processing. The pre-processing stage, context modeling and context adaptive arithmetic coding stage have same function as described in chapter 3.

The CAS-NNP is used to decorrelate the error image produced by 2D-LDPCM when the image is being encoded at the original resolution at the final stage. The CAS-NNP is not used at the coarse resolution levels because, sharp changes in pixel values become prominent due to sub-sampling and the CAS-NNP is less effective in further decorrelation.

6.3 Software Implementation

The algorithm is implemented in MATLAB 9.0 on a PC having Intel® CORE™2 Duo, 2.0 GHz using Neural Network Toolbox.

6.4 Experimentation Details

The experiments are performed on RDLD for evaluating compression performance using medical image datasets consisting of CT, MR, PET and angiogram. Three sets of experiments were conducted. Firstly, lossless compression is performed using the proposed RDLD-LS method. In the second step NLS compression is performed using the proposed RDLD-NLS method. For NLS compression, the PAE criteria used are (PAE=1,2,3,4,6,8,10,12,16). Finally, the images were compressed with 5%, 10% and 25% of square shaped RoIs at the center of the image using the proposed RDLD-RoI method. The RoI is compressed losslessly and the regions other than RoI are compressed with different PAE criteria (PAE=1,2,3,4,6,8,10,12,16). The evaluation criteria, results and discussions are included in the following sub-sections.

For evaluating and comparing the RoI compression performance, PAE, PSNR, MSSIM, UQI and bpp values were calculated. These evaluation criteria are defined in chapter 2.

6.5 Results and Discussions

In this section, the result obtained for the proposed resolution scalable lossless compression algorithm, RDLD-LS is presented first. Secondly, the near lossless compression performance of the proposed algorithm, RDLD-NLS is presented. Finally, the result obtained with the proposed algorithm, RDLD-RoI is presented.

6.5.1 RDLD-LS

The lossless compression performance of the proposed RDLD-LS compression technique is presented in Table 6.1

Table 6.1 Comparison of bit rates of lossless compression methods, JPEG2000, LOCO-I and the proposed method RDLD-LS

Image Dataset group	Bit rate (bpp)			% improvement over	
	JPEG2000	LOCO-I	RDLD-LS (Proposed)	JPEG2000	LOCO-I
CIPR-CT	2.17	1.96	2.11	2.72	-8.77
OSRX-CT	2.07	1.87	1.98	4.67	-5.56
CIPR-MR	2.96	2.79	2.91	2.11	-4.23
MGH-MR	4.16	4.10	4.23	-1.59	-3.12
MIDI-MR	3.14	3.20	3.08	1.86	3.57
OSRX-MR	3.31	3.402	3.397	-0.88	1.29
PHNT-MR	3.30	3.29	3.36	-1.72	-2.01
OSRX-XA	2.25	2.30	2.42	-7.98	-5.49
OSRX-PT	0.81	0.84	0.79	2.56	6.33
CT	2.11	1.90	2.02	4.05	-6.58
MR	3.218	3.218	3.220	0.42	0.06
AVERAGE	2.48	2.38	2.45	1.47	-3.53

It is observed that the RDLD-LS showed improvement in bit rate for the dataset groups, CIPR-CT, OSRX-CT, CIPR-MR, MIDI-MR and OSRX-PT compared to the resolution scalable image compression standard JPEG2000. However, compared to the non-resolution scalable image compression algorithm LOCO-I, the RDLD-LS showed improvement only for the dataset groups MIDI-MR, OSRX-MR and OSRX-PT. The RDLD-LS showed improvement over JPEG2000 for CT, MR and PET images. However, for angiogram, JPEG2000 showed better compression performance. RDLD-LS achieved an average improvement of 1.47% compared to the resolution scalable JPEG2000. However, the average bit rate of non-resolution scalable LOCO-I is lower than the RDLD-LS.

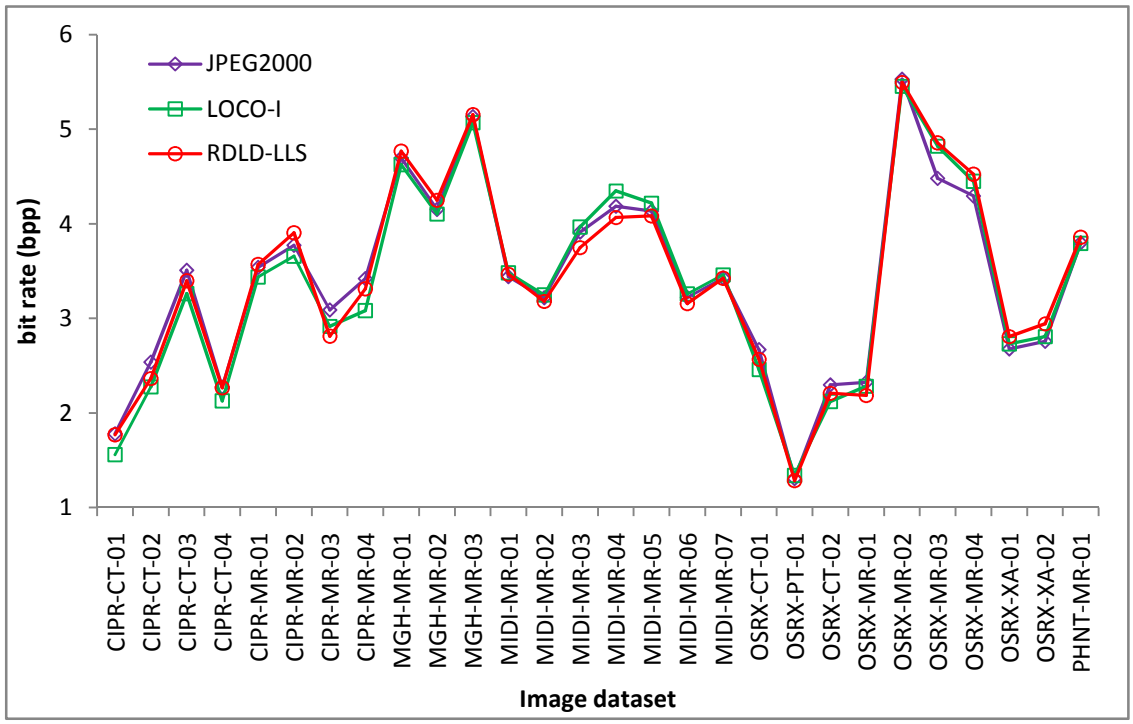

Fig. 6.3 Comparison of bit rates of JPEG2000, LOCO-I and the proposed RDLD-LS compression methods.

Fig 6.3 shows the comparative bit rate performance of the JPEG2000, LOCO-I and RDLD-LS when tested with the whole dataset. It is observed that the bit rate of RDLD-LS is slightly higher than the LOCO-I but comparable to the JPEG2000.

6.5.2 RDLD-NLS

Figures 6.4 – 6.15 shows the near lossless performance of the proposed RDLD-NLS compression technique. Near lossless compression performance of the standard compression algorithm LOCO-I and the lossy performance of the standard compression algorithm JPEG2000 are also shown. It is observed that the proposed method RDLD-NLS showed comparative performance to LOCO-I in terms of PAE for different bit rates. The PAE versus bit rate performance is better for the RDLD-NLS compared to the JPEG2000. PSNR and MSSIM values obtained for the RDLD-NLS is comparable to that of JPEG2000 for high quality images, ie., images compressed with low values of PAE. Moreover UQI values of the RDLD-NLS is better than the two standard methods, LOCO-I and JPEG-2000. Therefore it is observed that the near compression performance of the proposed RDLD-NLS is comparable or better to the LOCO-I and JPEG2000.

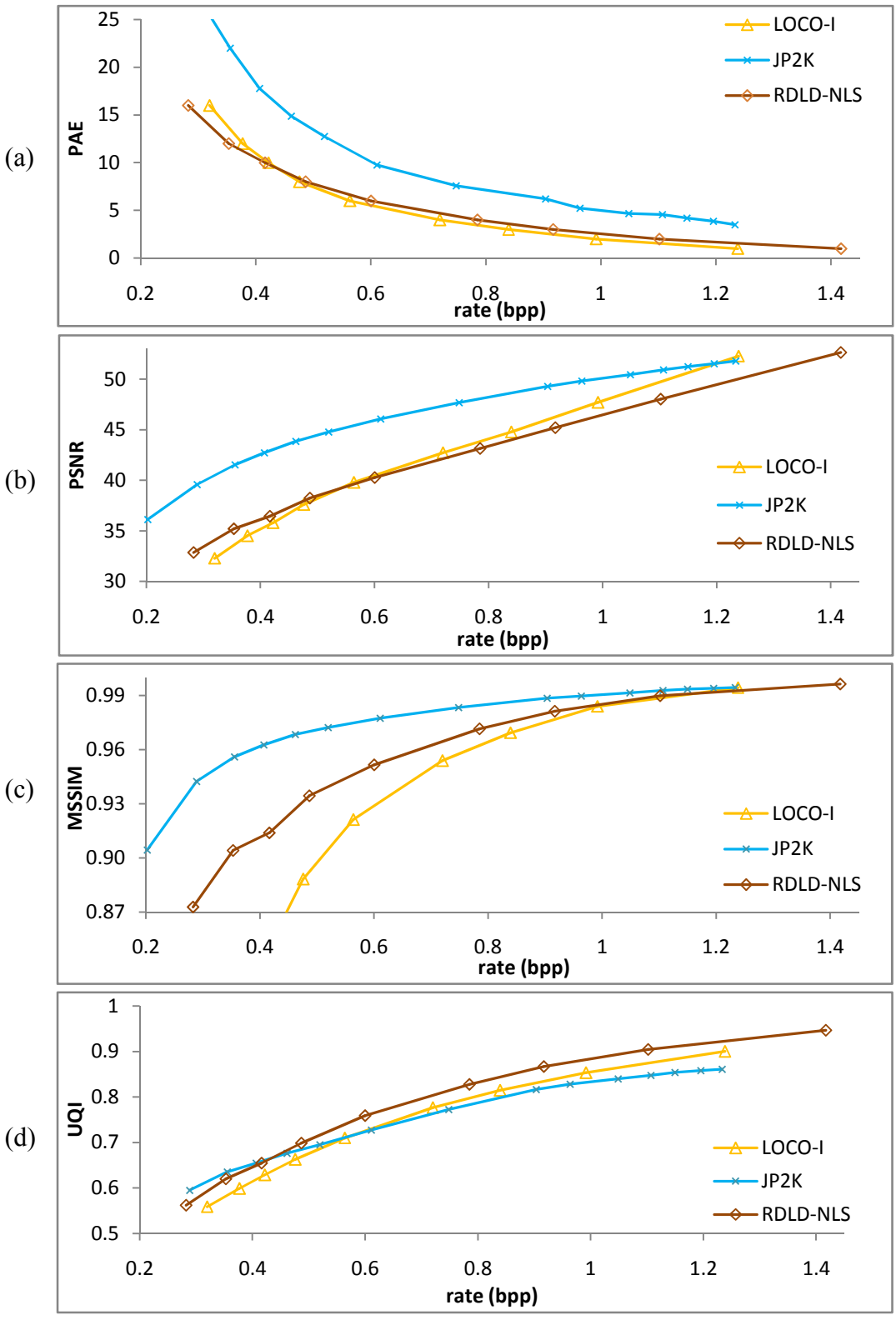

Fig. 6.4 Comparison of NLS compression performance of the proposed method when tested with CIPR-CT dataset group. (a) PAE vs. bit rate (b) PSNR vs. bit rate (c) MSSIM vs. bit rate (d) UQI vs. bit rate

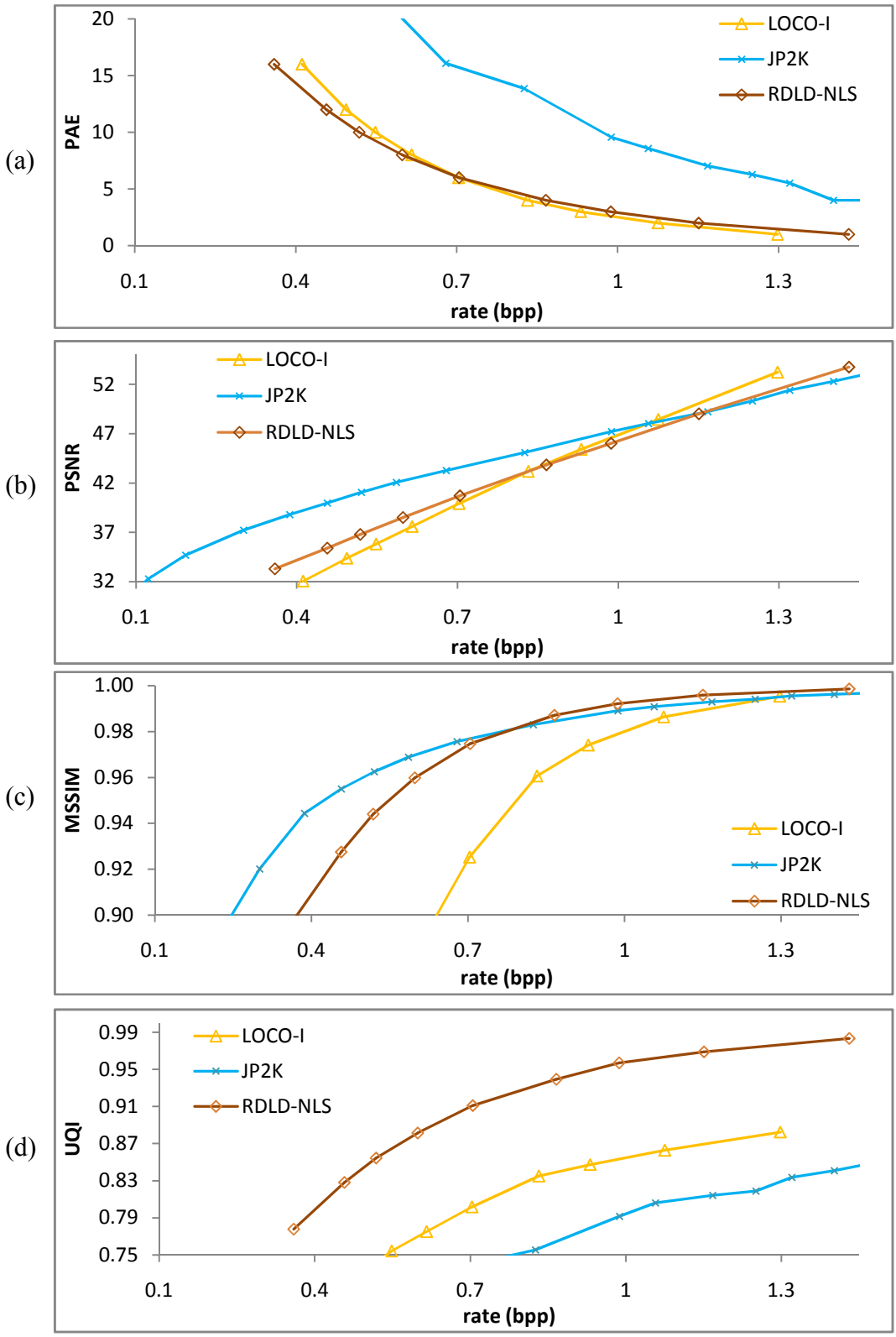

Fig. 6.5 Comparison of NLS compression performance when tested with OSRX-CT dataset group. (a) PAE vs. bit rate (b) PSNR vs. bit rate (c) MSSIM vs. bit rate (d) UQI vs. bit rate

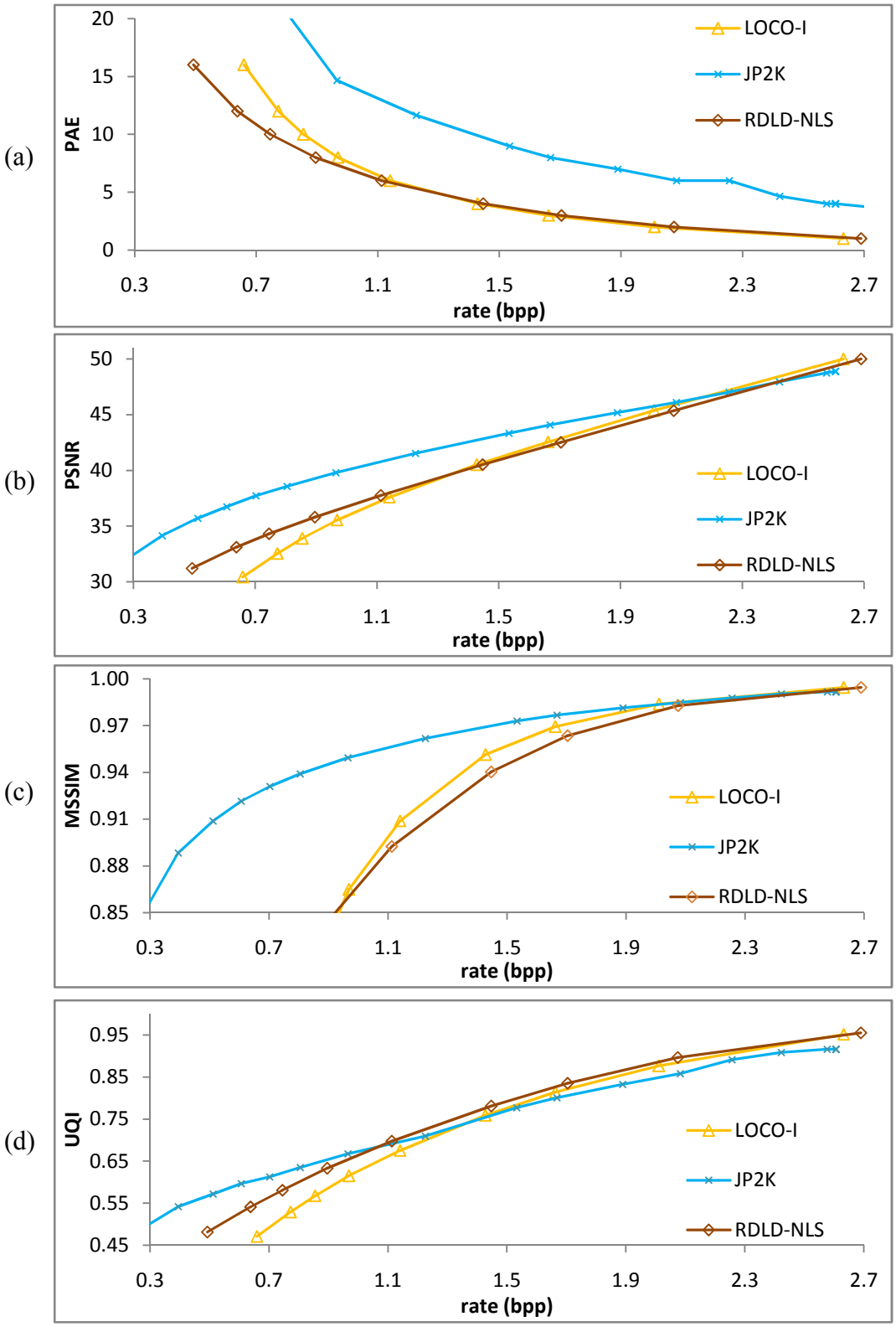

Fig.6.6 Comparison of NLS compression performance when tested with MGH-MR dataset group. (a) PAE vs. bit rate (b) PSNR vs. bit rate (c) MSSIM vs. bit rate (d) UQI vs. bit rate

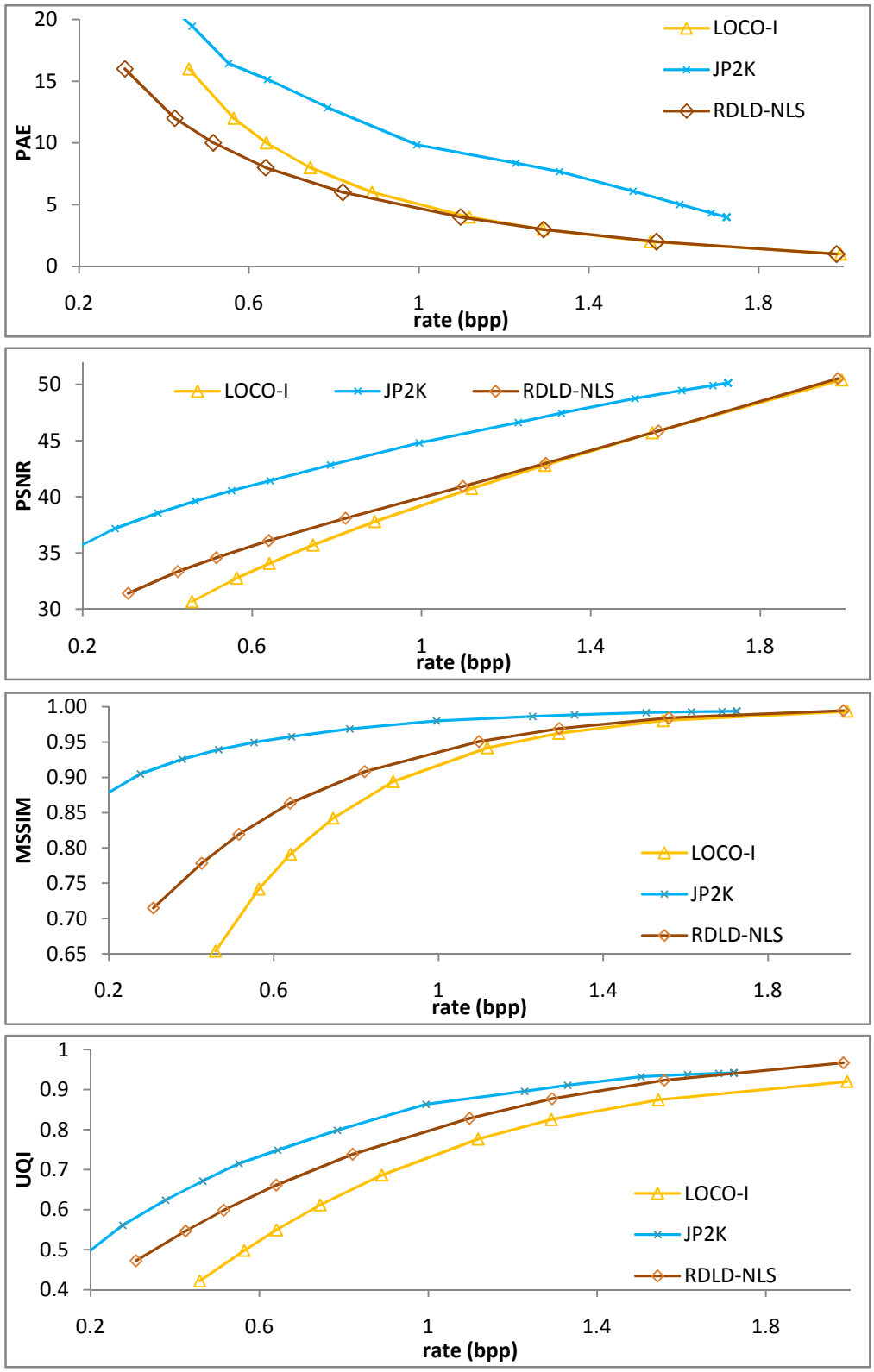

Fig.6.7 Comparison of NLS compression performance when tested with MIDI-MR dataset group. (a) PAE vs. bit rate (b) PSNR vs. bit rate (c) MSSIM vs. bit rate (d) UQI vs. bit rate

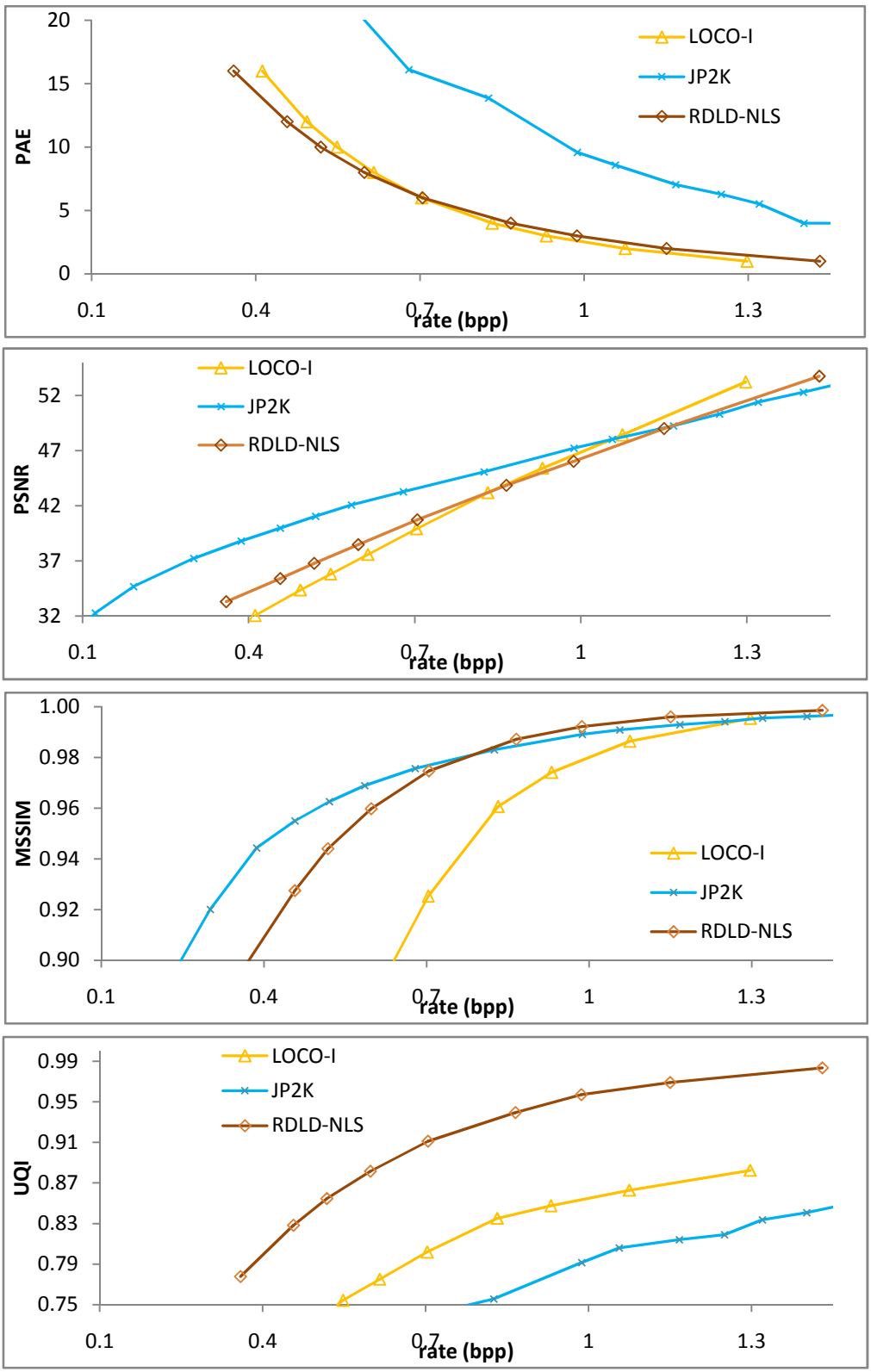

Fig.6.8 Comparison of NLS compression performance when tested with OSRX-CT dataset group. (a) PAE vs. bit rate (b) PSNR vs. bit rate (c) MSSIM vs. bit rate (d) UQI vs. bit rate

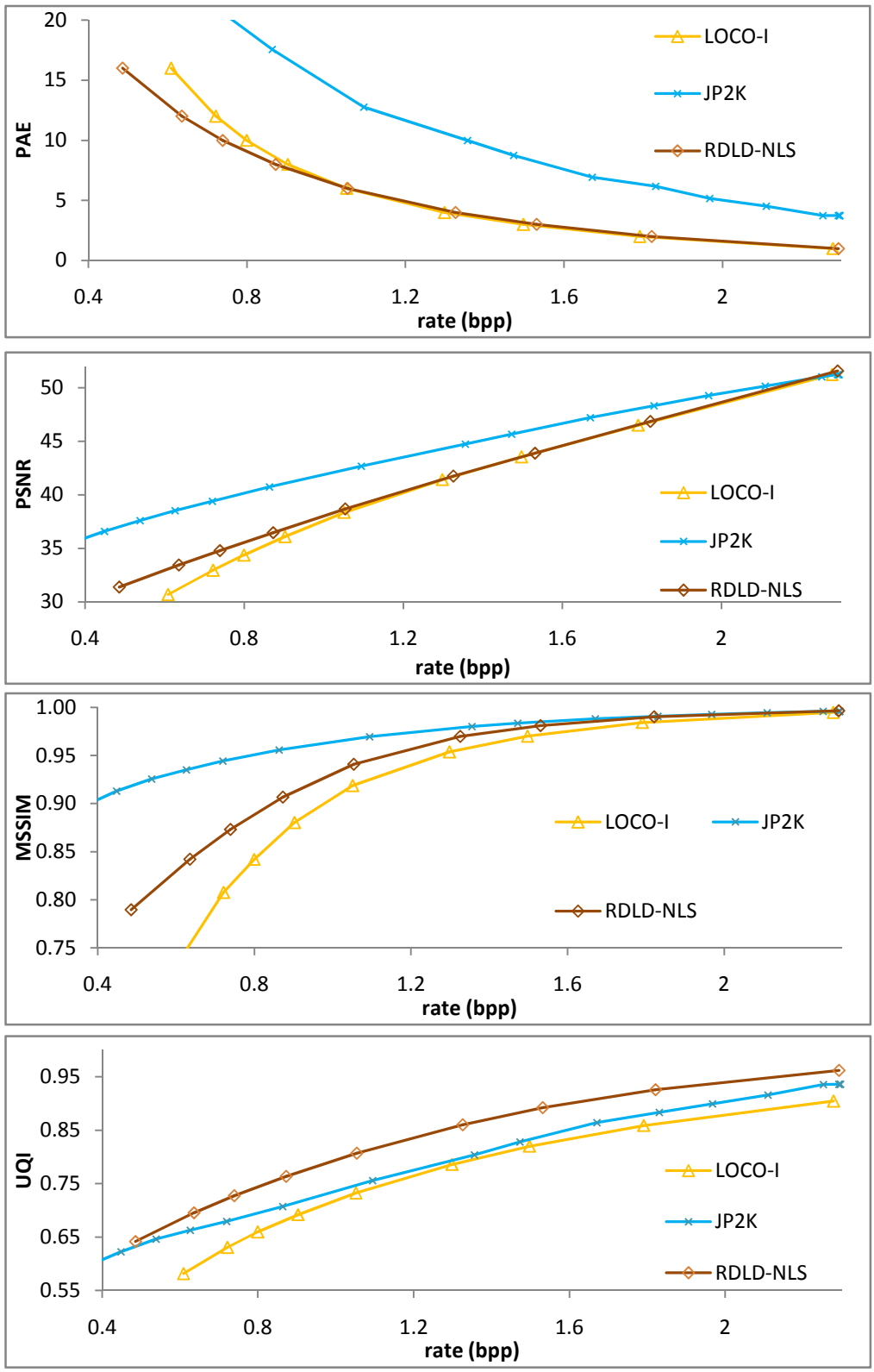

Fig.6.9 Comparison of NLS compression performance when tested with OSRX-MR dataset dataset group. (a) PAE vs. bit rate (b) PSNR vs. bit rate (c) MSSIM vs. bit rate (d) UQI vs. bit rate

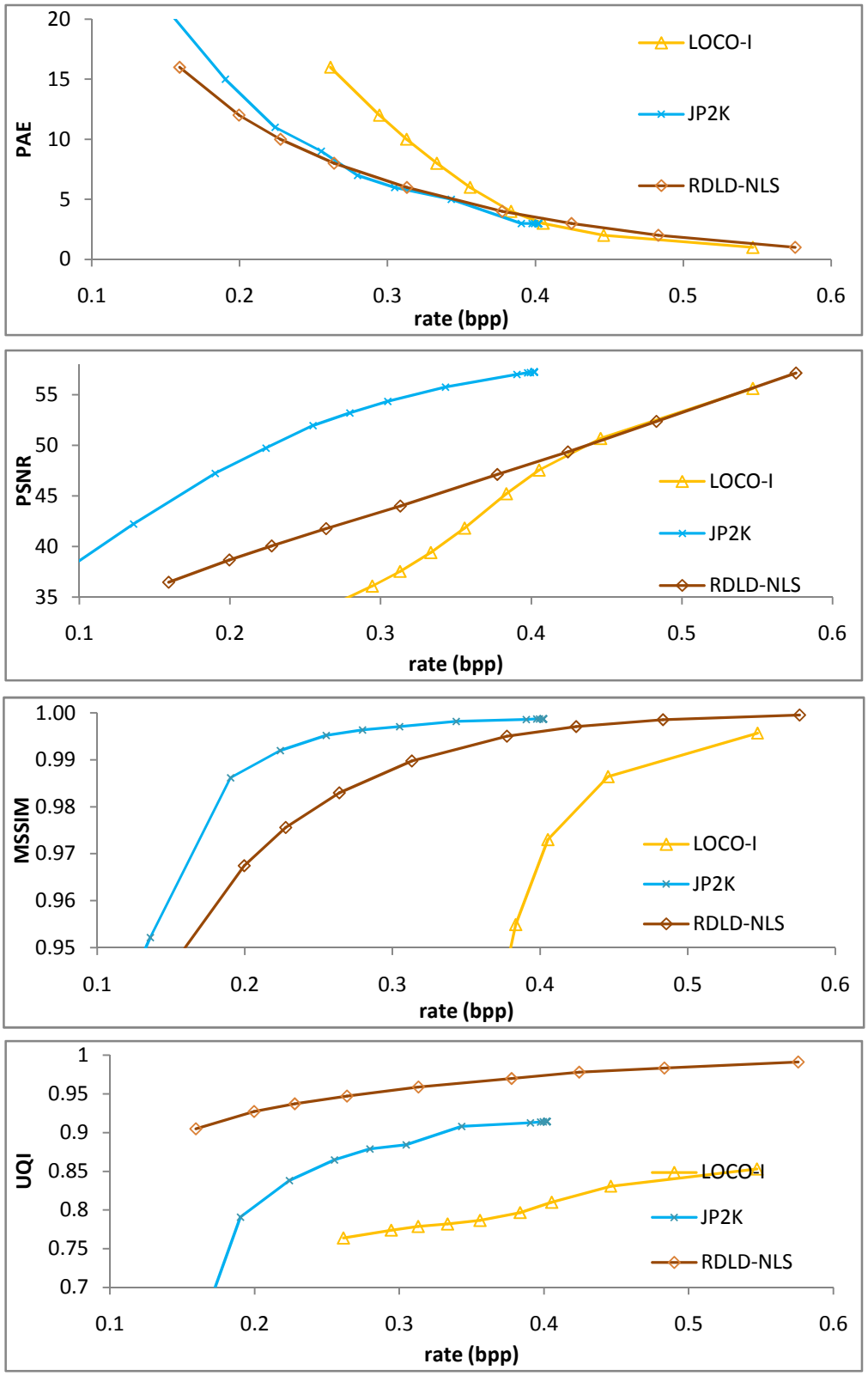

Fig.6.10 Comparison of NLS compression performance when tested with OSRX-PT dataset group. (a) PAE vs. bit rate (b) PSNR vs. bit rate (c) MSSIM vs. bit rate (d) UQI vs. bit rate

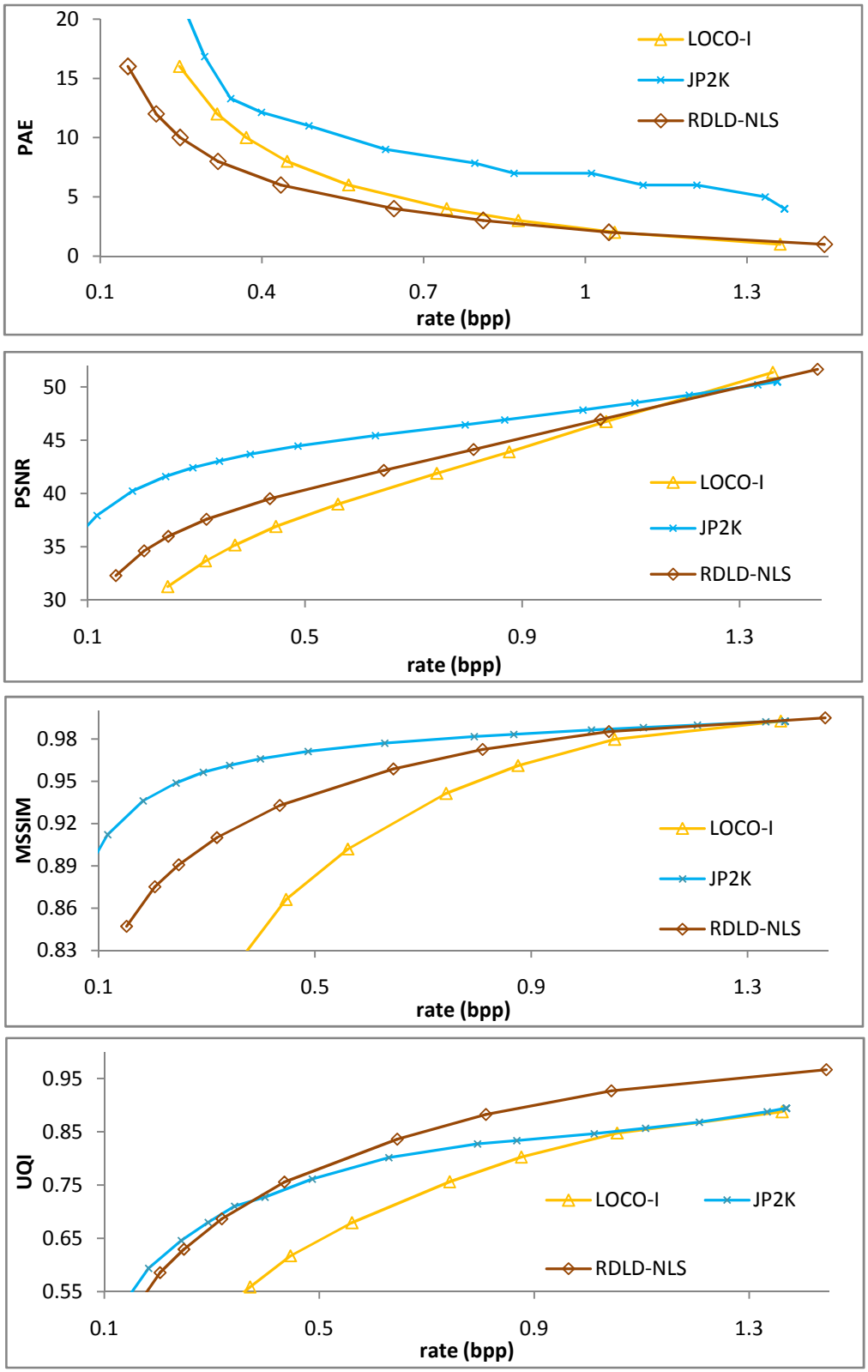

Fig.6.11 Comparison of NLS compression performance when tested with OSRX-XA dataset group. (a) PAE vs. bit rate (b) PSNR vs. bit rate (c) MSSIM vs. bit rate (d) UQI vs. bit rate

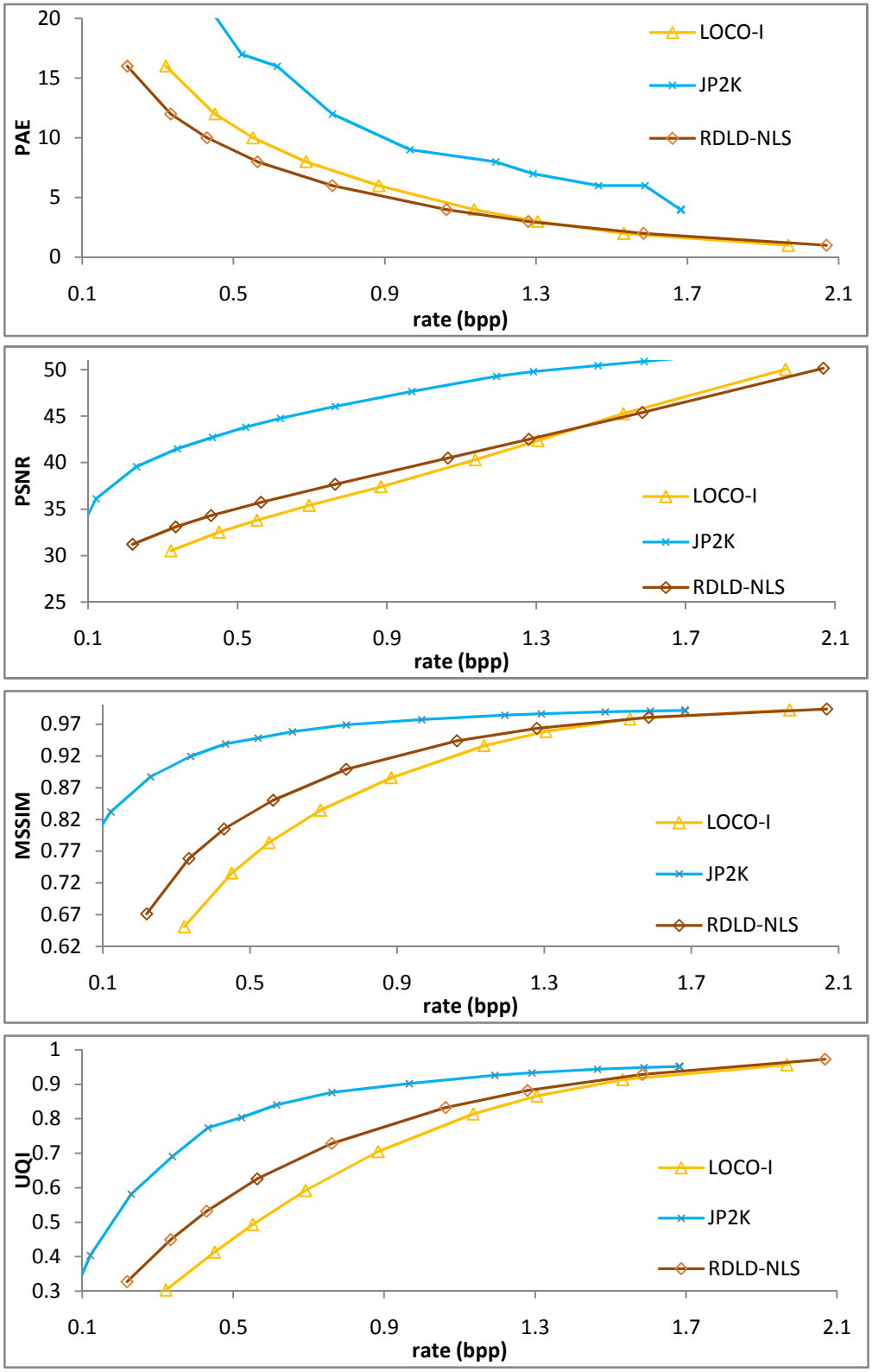

Fig.6.12 Comparison of NLS compression performance when tested with PHNT-MR dataset group. (a) PAE vs. bit rate (b) PSNR vs. bit rate (c) MSSIM vs. bit rate (d) UQI vs. bit rate

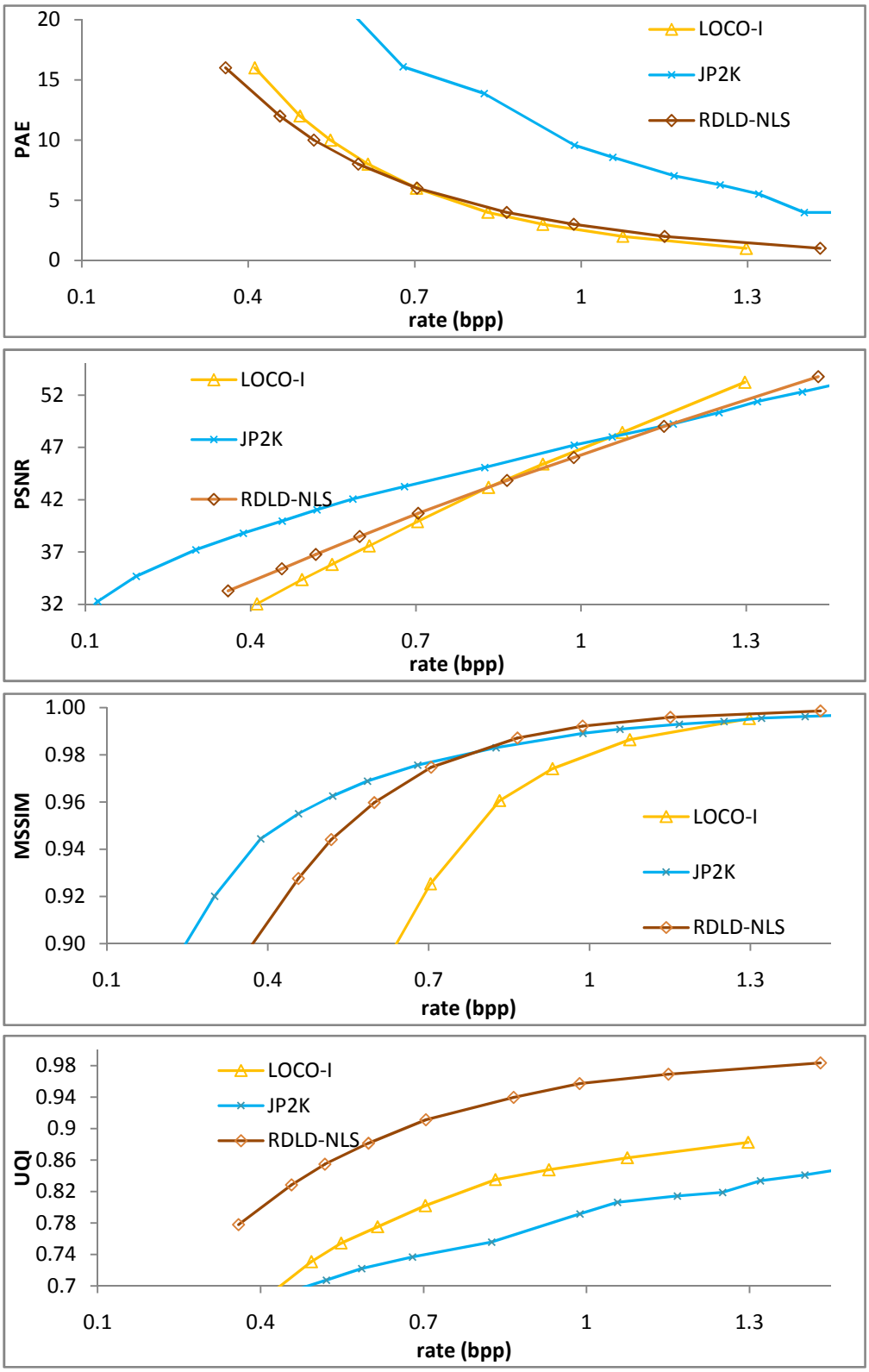

Fig.6.13 Comparison of NLS compression performance when tested with CT images in whole dataset. (a) PAE vs. bit rate (b) PSNR vs. bit rate (c) MSSIM vs. bit rate (d) UQI vs. bit rate

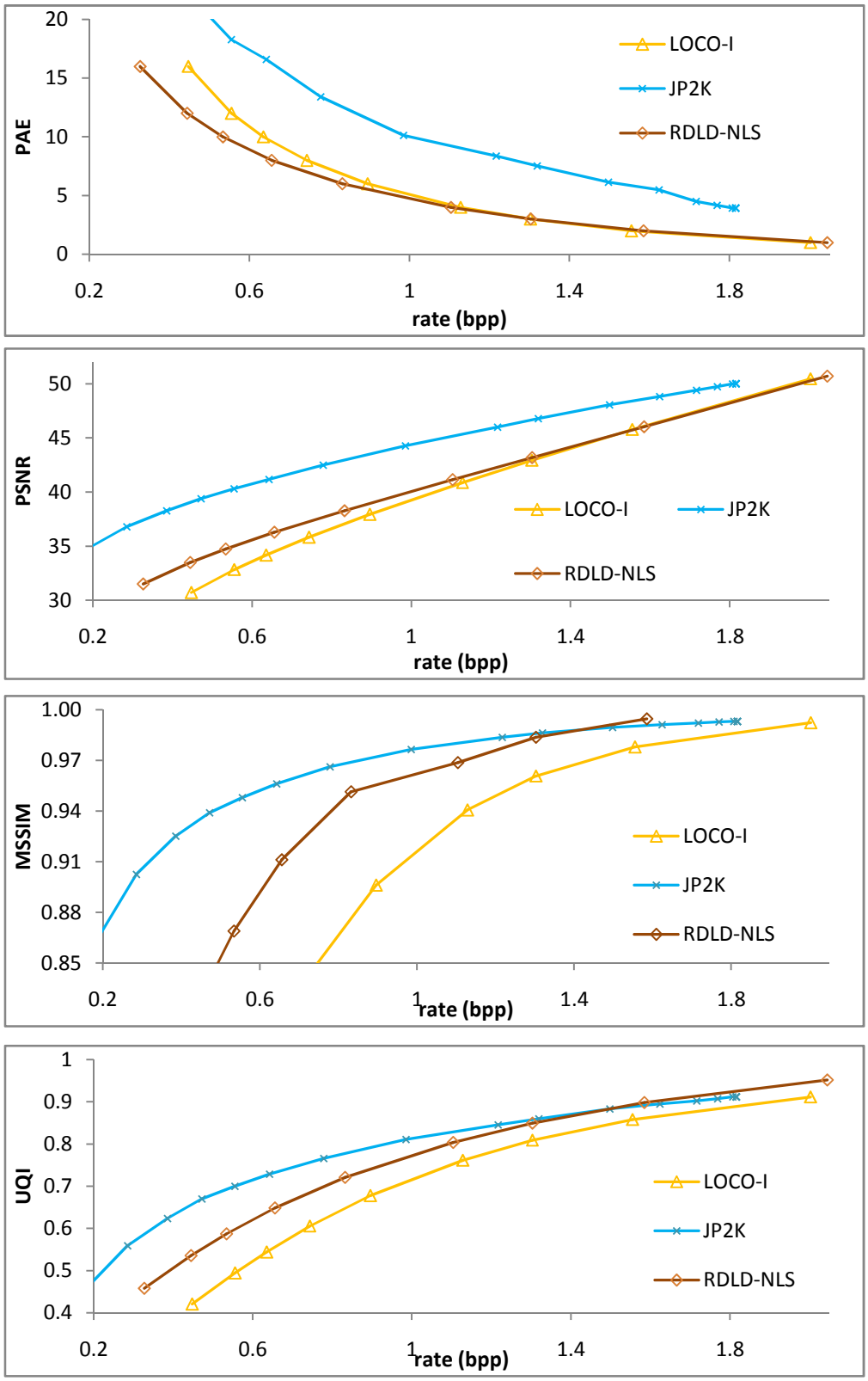

Fig.6.14 Comparison of NLS compression performance when tested with MR images in whole dataset. (a) PAE vs. bit rate (b) PSNR vs. bit rate (c) MSSIM vs. bit rate (d) UQI vs. bit rate

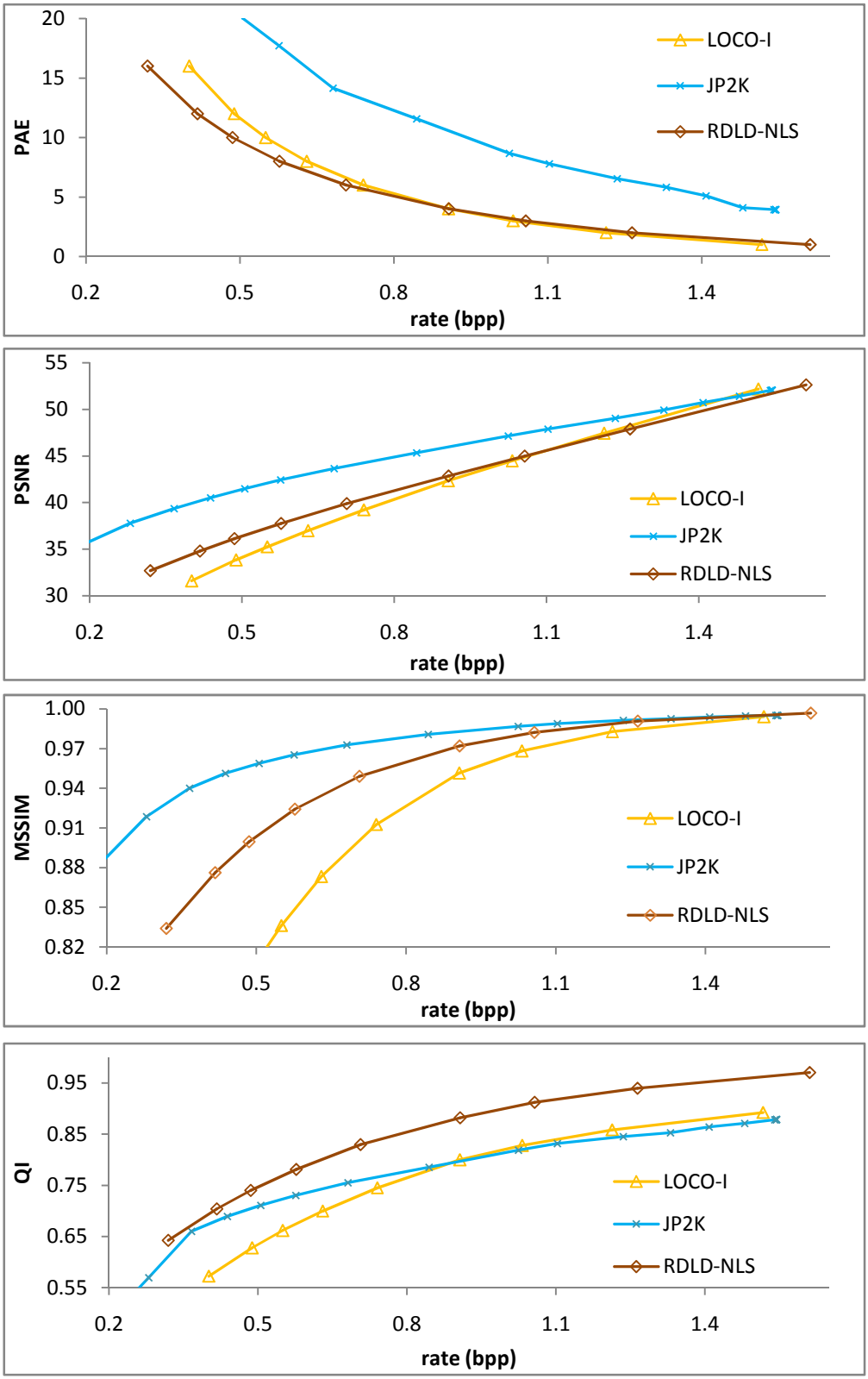

Fig.6.15 Comparison of NLS compression performance when tested with the whole dataset. (a) PAE vs. bit rate (b) PSNR vs. bit rate (c) MSSIM vs. bit rate (d) UQI vs. bit rate

6.5.3 RDLD-RoI

Table 6.2 shows the comparative compression performance of the proposed resolution scalable lossless compression method RDLD-LS and the resolution scalable region of interest compression method RDLD-RoI.

Table 6.2 Comparison of bit rate per pixel of the proposed DL-DPCM based lossless method and the proposed RoI compression method with PAE=1 for non-RoI.

Dataset Group	Proposed RDLD-LS bit rate (bpp)	Proposed RDLD-RoI Compression								
		RoI-5%			RoI-10%			RoI-25%		
		bpp	bit gain	% bit gain	bpp	bit gain	% bit gain	bpp	bit gain	% bit gain
CIPR-CT	2.11	1.53	0.57	27.2	1.73	0.38	18.1	0.38	1.73	82.1
OSRX-CT	1.98	1.60	0.38	19.1	1.30	0.68	34.5	1.30	0.68	34.3
CIPR-MR	2.91	1.90	1.01	34.8	2.08	0.83	28.6	2.20	0.71	24.5
MGH-MR	4.23	2.82	1.41	33.4	2.94	1.28	30.3	3.15	1.08	25.5
MIDI-MR	3.08	2.08	1.00	32.5	2.23	0.85	27.6	2.36	0.72	23.4
OSRX-MR	3.40	2.41	0.99	29.2	2.59	0.81	23.8	2.73	0.66	19.5
PHNT-MR	3.36	2.16	1.20	35.8	2.28	1.08	32.1	2.47	0.89	26.6
OSRX-XA	2.42	1.60	0.82	34.0	1.87	0.56	23.0	1.92	0.50	20.8
CT	2.02	1.58	0.44	24.9	1.80	0.22	15.6	1.38	0.64	42.9
MR	3.22	2.15	1.07	32.2	2.31	0.91	27.1	2.46	0.76	22.7
AVERAGE	2.45	1.76	0.69	31.3	1.96	0.49	25.5	1.81	0.64	21.0

It is observed from Table 6.2 that average bit gains of 0.69 bpp (31.3%), 0.49 bpp (25.5%) and 0.64 bpp (21.0%) , for 5% RoI, 10 % RoI and 25% RoI are observed when the background is compressed at low quality with PAE criteria PAE=1. It is also observed that with higher value of PAE for background, there is improvement in bit gain. Further, it is observed that as the area of the percentage RoI is increased there is increase in bit rate.

6.6 Summary

A resolution scalable image compression technique using DL-DPCM, was proposed in this chapter. The proposed technique, RDLD was designed to have the capabilities of resolution scalable lossless compression, resolution scalable near lossless compression and resolution scalable region of interest compression. The proposed technique was tested for compression performance using the medical image datasets from five different sources containing four modalities as described in chapter 2.

The overall compression performance of the proposed lossless resolution scalable coding algorithm, RDLD-LS was better than that of JPEG2000 in lossless mode. The average improvement on the total data set was 0.062 bpp, which is 2.9% improvement over JPEG2000. However, resolution scalability was achieved with increase in bit rate compared to non-resolution scalable benchmark algorithm LOCO-I. Further, the developed algorithm achieved lower PAE compared to JPEG2000 for all bit rates.

Chapter 7

Conclusions and Future Scope

Medical image compression pause a technological challenge due to many reasons. The gross binary data sizes of medical images are high since most of the modalities produce multiple image slices in a single examination. Legal reasons may necessitate the storage of the original medical images for a number of years. Radiologists who examine the medical images require them at high quality. Therefore, lossless compression is generally preferred for medical images. However, in spite of rigorous research in the past years, lossless compression techniques could not achieve high compression ratios. The ICT enabled medical practices such as telemedicine require extensive transmission of good quality medical images within and among healthcare organizations for its effective use. Therefore, use of efficient medical image compression technique is very important for the success of telemedicine.

Image data decorrelation is the important primary stage in any image compression technique. Successful lossless image compression techniques use predictive methods for image data decorrealtion. Therefore, the first approach for solving the thesis problem was to develop a novel image data decorrelation technique and to design a lossless compression algorithm based on it. The second approach was to extend the proposed lossless compression algorithm to near lossless compression algorithm. Subsequently, the third approach was to extend the proposed near lossless compression technique to region of interest compression technique. Fourth and final approach was to develop a resolution scalable image compression technique using the proposed image data decorrelation technique. The conclusions drawn from the experiential results obtained after testing the proposed image compression techniques with 28 medical image dataset series of four modalities (CT, MR, PET, angiogram) obtained from five different sources are stated in the following section.

7.1 Conclusions

7.1.1 Lossless image compression

In the first approach, a novel image data decorrealtion technique, namely dual level DPCM (DL-DPCM) was developed. The DL-DPCM was realized by cascading a linear DPCM cascaded by a nonlinear DPCM. The linear DPCM produces an error image after decorrealtion of the image data. The nonlinear DPCM uses context adaptive neural network predictor (CAS-

NNP) for further decorrelation of the data presented by the linear DPCM. Experiments were conducted on the proposed DL-DPCM using medical image datasets consisting of modalities CT, MR, PET and angiogram. It showed that the proposed DL-DPCM has superior image data decorrelation capabilities measured in terms of lower first order entropy values and lower values of RMS prediction error than the GAP and MED which are used as pixel value predictors in the bench mark algorithms CALIC and LOCO-I, respectively.

The DL-DPCM was used to develop a lossless image compression algorithm namely DLD-LS. Context adaptive arithmetic encoder was used in the DLD-LS method to entropy code the prediction error produced by the DL-DPCM. Experimental results on the 28 medical image dataset sequences showed that the DLD-LS has lower bit rate in all cases compared to the lossless standard LOCO-I and has lower bit rate for 26 out of the 28 cases compared to the benchmark algorithm CALIC. The bit rate of these two cases were comparable to that of the CALIC and within 2% difference. An average bit rate improvement of 10.7% was achieved compared to the LOCO-I. Similarly, compared to CALIC, the DLD-LS achieved an average improvement of 5.7%. This can be interpreted as 5.7% savings in the image storage while medical image archival and 5.7% less time of transmission when the images are transmitted in telemedicine applications. Therefore, it can be concluded from the above results that the proposed DLD-LS showed superior lossless compression performance on medical images. The lower bit rate achieved by the DLD-LS is mainly due to the higher image data decorrelation performance of the DL-DPCM.

7.1.2 Near lossless image compression

In the second approach, the proposed DLD-LS was extended to perform near lossless compression by introducing a linear quantization stage in the 2D-LDPCM. The proposed near lossless compression algorithm, DLD-NLS was tested with the same 28 medical image dataset sequences for different PAE criteria (PAE=1,2,3,4,6,8,10,12,16). It was observed that the proposed DLD-NLS method achieved lower bit rate compared to the LOCO-I for each PAE criteria. The bit rate of DLD-NLS was comparable to that of CALIC for each PAE criteria. The JPEG and JPEG2000 compressed with different quality index showed substantially higher mean PAE values for each of the 28 medical image dataset. Therefore, it can be concluded that the proposed near lossless compression algorithm DLD-NLS has lower bit rate when maximum tolerable error limit is specified in terms of PAE criteria for the reconstructed image.

The PSNR values obtained for the DLD-NLS was better than the JPEG, JPEG2000 and LOCO-I for high quality compressed images which are compressed with low PAE criteria. The PSNR

values of DLD-NLS was comparable to that of CALIC for the same high quality compressed images. The index for structural similarity, MSSIM for the DLD-NLS was higher or comparable to that of CALIC. The MSSIM values of the DLD-NLS was higher than that of JPEG and JPEG2000 for high quality compressed images. Whereas, UQI values, which is also an index used for the structural similarity measurement, showed higher or comparable values for the proposed DLD-NLS compared to all other methods. Therefore, it can be stated that the proposed near lossless compression method, DLD-NLS achieved better compression performance in terms of objective image quality and lower bit rate compared to the benchmark algorithms when the image is compressed at high quality with low PAE criteria. Since the medical images needs to be compressed at high quality, the proposed DLD-NLS is a very good candidate for medical image compression. Similarly, if maximum tolerable PAE criteria is defined, the DLD-NLS can be used for medical image archive as well.

7.1.3 Region of interest image compression

In the third approach, the proposed near lossless compression algorithm, DLD-NLS was modified to perform region of interest compression. This is realized by using an explicitly defined RoI mask. The areas defined as RoI are compressed in lossless manner and the areas other than RoI are compressed with near lossless compression method. Experiments were conducted on the proposed DLD-RoI with 28 medical image datasets sequences. Three different square shaped RoI masks were explicitly defined with 5%, 10% and 25% of the image area. Experimental results showed that, on an average 37.1% to 87.2% bit gain could be achieved over the proposed lossless compression DLD-LS, for 5% RoI, when the PAE criteria of the non-RoI was varied from 1 to 16. Similarly for 10% RoI, 32.6% to 83.5% bit gain could be achieved and for 25% RoI, 28.6% to 71.3% bit gain could be achieved compared to the DLD-LS. It can be noted that the proposed DLD-RoI compression technique gives substantial bit gain over lossless compression techniques. Therefore, the DLD-RoI is suitable for medical image compression, when the RoI can be explicitly defined.

7.1.4 Resolution scalable image compression

In the fourth and final approach, a resolution scalable image compression technique was developed using the DL-DPCM. The proposed resolution scalable method was designed to perform lossless compression, near lossless compression and region of interest compression. Experimental results showed that the bit rate values of the proposed lossless resolution scalable algorithm, RDLD-LS was better or comparable to the resolution scalable lossless standard JPEG2000. The resolution scalability is achieved at the cost of higher bit rate compared to the

proposed non resolution scalable image compression technique, DLD-LS. The performance of the proposed resolution scalable near lossless compression technique, RDLD-NLS was comparable to that of JPEG2000 in terms of PSNR values and MSSIM values for images compressed with high quality. Moreover, the performance of the RDLD-NLS was better in terms of lower PAE values and higher UQI values compared to JPEG2000. The proposed resolution scalable region of interest coding algorithm, RDLD-RoI achieved substantial bit gain over the proposed RDLD-LS. The proposed resolution scalable algorithm is suitable for telemedicine applications, where the medical images may required to be transmitted with progressive resolution.

7.2 Future Scope

The work presented here may be expended in the following directions, which are applicable to medical imaging.

1. The proposed image data decorrelation technique, DL-DPCM was developed for two dimensional image data. Volumetric medical image slices have inter-slice correlation. Therefore, this method can be extended and can be used to remove inter-slice redundancies.
2. The application of the proposed dual level predictor for compressed sensing of medical image modalities such as CT, MR etc. can be studied.
3. The proposed compression methods may be expanded to include authentication using digital watermarking.

Author's Research Contributions

Referred International Journal

[1] E. Puthooran, R. S. Anand, and S. Mukherjee, "Lossless Compression of Medical Images Using a Dual Level DPCM with Context Adaptive Switching Neural Network Predictor," *International Journal of Computational Intelligence Systems*, vol. 6, no. 6, pp. 1082–1093, Dec. 2013.

International Conferences

[1] E. Puthooran, R. S. Anand, and S. Mukherjee, "Lossless image compression using BPNN predictor with contextual error feedback," in *2011 International Conference on Multimedia, Signal Processing and Communication Technologies, AMU, Aligarh*, 2011, pp. 145–148.

[2] E. Puthooran, R. S. Anand, and S. Mukherjee, "Image Compression for Telemedicine and Teleradiology Applications," in *Proc. Int. Conf. Intelligent Healthcare, Bhubaneswar*, 2011, pp. 6–12.

References

[1] A. Abrardo, L. Alparone, and F. Bartolini, "Encoding-interleaved hierarchical interpolation for lossless image compression," *Signal Processing*, vol. 56, no. 3, pp. 321–328, Feb. 1997.

[2] D. A. Adjeroh, Y. Zhang, and R. Parthe, "On denoising and compression of DNA microarray images," *Pattern Recognition*, vol. 39, no. 12, pp. 2478–2493, Dec. 2006.

[3] N. Ahmed, T. Natarajan, and K. Rao, "Discrete cosine transform," *IEEE Trans. Computers*, vol. C–23, no. 1, pp. 90–93, 1974.

[4] B. Aiazzi, L. Alparone, and S. Baronti, "Fuzzy logic-based matching pursuits for lossless predictive coding of still images," *IEEE Trans. Fuzzy Systems*, vol. 10, no. 4, pp. 473–483, 2002.

[5] S. Anand and S. K. Guha, "Computer aided rehabilitation for the handicapped," in *Proceedings of the First Regional Conference, IEEE Engineering in Medicine and Biology Society and 14th Conference of the Biomedical Engineering Society of India. An International Meet*, 1995, vol. 2, pp. 2/119–2/120.

[6] I. N. Bankman, *Handbook of Medical Image Processing and Analysis*, 2nd ed. Academic Press, 2008, pp. 20–21.

[7] I. N. Bankman, *Handbook of medical imaging: processing and analysis*. San Diego Academic Press, 2000.

[8] M. F. Barnsley, "Fractal Image Compression," *Notices of the AMS*, vol. 43, no. 6, pp. 657–662, 1996.

[9] B. Bose, A. K. Kalra, S. Thukral, A. Sood, S. K. Guha, and S. Anand, "Tremor compensation for robotics assisted microsurgery," in *Proceedings of the Annual International Conference of the IEEE Engineering in Medicine and Biology Society*, 1992, vol. 3, pp. 1067–1068.

[10] J. D. Bronzino, Ed., *The Biomedical Engineering Handbook*, 2nd ed., vol. I. A CRC Handbook Published in Cooperation with IEEE Press, 2000.

[11] A. Bruckmann and A. Uhl, "Selective medical image compression techniques for telemedical and archiving applications.," *Computers in Biology and Medicine*, vol. 30, no. 3, pp. 153–69, May 2000.

[12] A. R. Calderbank, I. Daubechies, W. Sweldens, and B.-L. Yeo, "Wavelet Transforms That Map Integers to Integers," *Applied and Computational Harmonic Analysis*, vol. 5, no. 3, pp. 332–369, Jul. 1998.

[13] P. Campisi, D. Kundur, D. Hatzinakos, and A. Neri, "Compressive Data Hiding: An Unconventional Approach for Improved Color Image Coding," *EURASIP Journal on Advances in Signal Processing*, vol. 2002, no. 2, pp. 152–163, 2002.

[14] B. Carpentieri, M. J. Weinberger, and G. Seroussi, “Lossless compression of continuous-tone images,” *Proc. IEEE*, vol. 88, no. 11, pp. 1797–1809, Nov. 2000.

[15] E.-C. Chang, M. S. Kankanhalli, X. Guan, Z. Huang, and Y. Wu, “Robust image authentication using content based compression,” *Multimedia Systems*, vol. 9, no. 2, pp. 121–130, Aug. 2003.

[16] P. Chen, Y. Lu, and Y. Chen, “Extremal Optimization Combined with LM Gradient Search for MLP Network Learning,” *International Journal of Computational Intelligence Systems*, vol. 3, no. 5, pp. 622–631, 2010.

[17] S. Chen, Z. He, and B. L. Luk, “A Generic Postprocessing Technique for Image Compression,” *IEEE Trans. Circuits Syst. Video Technol.*, vol. 11, no. 4, pp. 546–553, 2001.

[18] M. K. Choong, R. Logeswaran, and M. Bister, “Cost-effective handling of digital medical images in the telemedicine environment.,” *Int. J. of Medical Informatics*, vol. 76, no. 9, pp. 646–54, Sep. 2007.

[19] Christopher Cramer, “Neural networks for image and video compression - A review,” *European J. of Operational Research*, vol. 108, no. 2, pp. 266–282, Jul. 1998.

[20] C. Christopoulos, A. Skodras, and T. Ebrahimi, “JPEG2000: The Upcoming Still Image Compression Standard,” *IEEE Trans. Consumer Electronics*, vol. 46, no. 4, pp. 1103–1127, 2000.

[21] E. B. Christopoulou, A. N. Skodras, T. R. Reed, and C. A. Christopoulos, “The JPEG2000 still image coding system: an overview,” *IEEE Trans. Consumer Electronics*, vol. 46, no. 4, pp. 1103–1127, Nov. 2000.

[22] D. A. Clunie, “Lossless Compression of Grayscale Medical Images - Effectiveness of Traditional and State of the Art Approaches,” in *Proc. SPIE, Medical Imaging 2000 - PACS Design and Evaluation: Engineering and Clinical Issues*, 2000, vol. 3980, pp. 74–84.

[23] G. Deng, H. Ye, and L. W. Cahill, “Adaptive combination of linear predictors for lossless image compression,” *IEE Proc.-Sci. Meas. Technol.*, vol. 147, no. 6, p. 414, 2000.

[24] S. Dewitte and J. Cornelis, “Lossless integer wavelet transform,” *IEEE Signal Proc. Letters*, vol. 4, no. 6, pp. 158–160, Jun. 1997.

[25] S. Dianat, N. Nasrabadi, and S. Venkataraman, “A non-linear predictor for differential pulse-code encoder (DPCM) using artificial neural networks,” in *Int. Conf. Acoustics, Speech, and Signal Processing, 1991. ICASSP-91*, 1991, pp. 2793–2796.

[26] R. D. Dony and S. Haykin, “Neural network approaches to image compression,” *Proc. IEEE*, vol. 83, no. 2, pp. 288–303, Feb. 1995.

[27] C. Doukas and I. Maglogiannis, “Region of Interest Coding Techniques for Medical Image Compression,” *IEEE Engineering in Medicine and Biology Magazine*, vol. 26, no. 5, pp. 29–35, Sep. 2007.

[28] A. Ebrahimi-moghadam, S. Shirani, and S. Member, “Progressive Scalable Interactive Region-of-Interest Image Coding Using Vector Quantization,” *IEEE Trans. Multimedia*, vol. 7, no. 4, pp. 680–687, 2005.

[29] D. D. Estrakh, H. B. Mitchell, P. A. Schaefer, Y. Mann, and Y. Peretz, “‘Soft’ median adaptive predictor for lossless picture compression,” *Signal Processing*, vol. 81, no. 9, pp. 1985–1989, 2001.

[30] H. Fukatsu, S. Naganawa, and S. Yumura, “Development and evaluation of a novel lossless image compression method (AIC: artificial intelligence compression method) using neural networks as artificial intelligence,” *Radiation Medicine*, vol. 26, no. 3, pp. 120–128, Apr. 2008.

[31] S. Golomb, “Run-length encodings (Corresp.),” *IEEE Transactions on Information Theory*, vol. 12, no. 3, pp. 399–401, Jul. 1966.

[32] R. C. Gonzalez and R. E. Woods, *Digital Image Processing*. Pearson Education, 2002.

[33] M. T. Hagan and M. B. Menhaj, “Training Feedforward Networks with the Marquardt Algorithm,” *IEEE Trans. Neural Networks*, vol. 5, no. 6, pp. 989–993, 1994.

[34] J. C. Hart, “Fractal image compression and recurrent iterated function systems,” *IEEE Computer Graphics and Applications*, vol. 16, no. 4, pp. 25–33, 1996.

[35] M. Hilbert and P. López, “The world’s technological capacity to store, communicate, and compute information.,” *Science*, vol. 332, no. 60, pp. 60–65, Apr. 2011.

[36] A. K. Jain, “Image data compression: A review,” *Proc. IEEE*, vol. 69, no. 3, pp. 349–389, Mar. 1981.

[37] J. Jiang, “Image compression with neural networks – A survey,” *Signal Processing: Image Communication*, vol. 14, no. 9, pp. 737–760, Jul. 1999.

[38] L. J. Kau, Y. P. Lin, and C. T. Lin, “Lossless image coding using adaptive, switching algorithm with automatic fuzzy context modelling,” *IEE Proc.-Vis. Image Signal Process.*, vol. 153, no. 5, pp. 684–694, Oct. 2006.

[39] A. Lempel and J. Ziv, “Compression of Two-Dimensional Data,” *IEEE Transactions on information theory*, vol. IT-32, no. 1, pp. 2–8, 1986.

[40] X. Li and M. T. Orchard, “Edge-Directed Prediction for Lossless Compression of Natural Images,” *IEEE Trans. Image Process.*, vol. 10, no. 6, pp. 813–817, 2001.

[41] Y. Linde, a. Buzo, and R. Gray, “An Algorithm for Vector Quantizer Design,” *IEEE Transactions on Communications*, vol. 28, no. 1, pp. 84–95, Jan. 1980.

[42] M. F. López, V. G. Ruiz, J. J. Fernández, and I. Garcıa, “Progressive-fidelity image transmission for telebrowsing: an efficient implementation,” in *Proceedings of the IASTED International Conference on Visualization, Imaging and Image Processing Acta Press*, 2001, pp. 334–339.

[43] P. López and M. Hilbert, “Methodological and Statistical Background on The World’s Technological Capacity to Store, Communicate and Compute Information,” 2012. [Online]. Available: http://www.martinhilbert.net/WorldInfoCapacity.html.

[44] G. Lu, “Fractal image compression,” *Signal Processing: Image Communication*, vol. 5, no. 4, pp. 327–343, 1993.

[45] C. N. N. Manikopoulos, “Neural network approach to DPCM system design for image coding,” *IEE Proceedings I, Communications, Speech and Vision*, vol. 139, no. 5, pp. 501–507, Oct. 1992.

[46] M. W. Marcellin, M. J. Gormish, A. Bilgin, and M. P. Boliek, “An overview of JPEG-2000,” in *Proc. of IEEE Data Compression Conference*, 2000, pp. 523–541.

[47] S. Marusic and G. Deng, “Adaptive prediction for lossless image compression,” *Signal Processing: Image Communication*, vol. 17, no. 5, pp. 363–372, 2002.

[48] N. Memon and X. Wu, “Recent developments in context-based predictive techniques for lossless image compression,” *The Computer Journal*, vol. 40, no. 2/3, pp. 127–136, 1997.

[49] N. Memon, X. Wu, and B. L. Yeo, “Improved techniques for lossless image compression with reversible integer wavelet transforms,” in *Proceedings 1998 International Conference on Image Processing. ICIP98 (Cat. No.98CB36269)*, 1998, vol. 3, pp. 891–895.

[50] N. Memon and C. Guillemot, “The JPEG Lossless Image Compression Standards,” in in *Handbook of Digital Image and Video Processing*, 2nd ed., no. March, A. C. Bovik, Ed. Elsevier Academic Press, 2005.

[51] S.-G. Miaou and S.-T. Chen, “Automatic Quality Control for Wavelet-Based Compression of Volumetric Medical Images Using Distortion-Constrained Adaptive Vector Quantization,” *IEEE Trans. Med. Imag.*, vol. 23, no. 11, pp. 1417–1429, Nov. 2004.

[52] A. A. Mohammed, R. Minhas, and Q. M. J. Wu, “An efficient fingerprint image compression technique based on wave atoms decomposition and multistage vector quantization,” *Integrated Computer-Aided Engineering*, vol. 17, no. 1, pp. 29–40, 2010.

[53] J. P. Molnar, “Picturephone service - a new way of communicating,” *Bell Laboratories*, vol. 47, no. 5, Bell Laboratories, pp. 134–135, 1969.

[54] N. M. Nasrabadi and R. a. King, “Image coding using vector quantization: a review,” *IEEE Trans. Commun.*, vol. 36, no. 8, pp. 957–971, 1988.

[55] A. N. Netravali and J. O. Limb, “Picture coding: A review,” *Proc. IEEE*, vol. 68, no. 3, pp. 366–406, Mar. 1980.

[56] S. R. Nirmala, S. Dandapat, and P. K. Bora, “Image Quality Assessment in Retinal Image Compression Systems,” in *Proc. IET-UK Int. Conf. on Information and Communication Technology in Electrical Sciences (ICTES 2007)*, 2007, pp. 737–742.

[57] H. Pan, W. Siu, and N. F. Law, “Lossless image compression using binary wavelet transform,” *IET Image Process.*, vol. 1, no. 4, pp. 353–362, Dec. 2007.

[58] N. G. Panagiotidis, D. Kalogeras, S. D. Kollias, and A. Stafylopatis, “Neural network-assisted effective lossy compression of medical images,” *Proc. IEEE*, vol. 84, no. 10, pp. 1474–1487, 1996.

[59] K. Park, H. Park, and S. Member, “Region-of-Interest Coding Based on Set Partitioning in Hierarchical Trees,” *IEEE Trans. Circuits Syst. Video Technol.*, vol. 12, no. 2, pp. 106–113, 2002.

[60] D. Petrescu and M. Gabbouj, “Prediction Based on Boolean, FIR-Boolean Hybrid And Stack Filters for Lossless Image Coding,” in *Proc. Int. Conf. on Acoustics, Speech and Signal Processing, ICASSP*, 1997, pp. 2965–2968.

[61] D. Petrescu and M. Gabbouj, “Adaptive Boolean Filters for the Prediction Stage in Lossless Image Compression,” in *Proc. IEEE Nonlinear Signal and Image Processing Workshop, NSIP 1997, Mackinac Island, Michigan, USA, 7-10 Sept.*, 1997.

[62] D. Petrescu, I. Tabus, and M. Gabbouj, “Prediction capabilities of Boolean and stack filters for lossless image compression,” *Multidimensional Systems and Signal Processing*, vol. 10, no. 2, pp. 161–187, 1999.

[63] W. Philips, S. Van Assche, D. De Rycke, and K. Denecker, “State-of-the-art techniques for lossless compression of 3D medical image sets,” *Computerized Medical Imaging and Graphics*, vol. 25, no. 2, pp. 173–85, 2001.

[64] P. L. Poehler and J. Chol, “Linear predictive coding of imagery for data compression applications,” in *IEEE Int. Conf. Acoustics, Speech Signal Processing (ICASSP ’83), Apr*, 1983, vol. 8, pp. 1240–1243.

[65] A. Przelaskowski, “Experimental Comparison of Lossless Image Coders for Medical Applications,” *Computer Vision and Graphics*, vol. 32, pp. 216–221, 2006.

[66] R. E. W. Rafael C. Gonzalez, *Digital Image Processing*, 2nd ed. Pearson Education, 2002.

[67] K. R. Rao and P. C. Yip, Eds., *The Transform And Data Compression Handbook*. CRC Press, 2001.

[68] J. A. Robinson, “Efficient general-purpose image compression with binary tree predictive coding.,” *IEEE Trans. Image Process.*, vol. 6, no. 4, pp. 601–8, Jan. 1997.

[69] P. Roos and M. A. Viergever, “Reversible interframe compression of medical images: a comparisonof decorrelation methods,” *IEEE Trans. Med. Imag.*, vol. 10, no. 4, pp. 538–547, 1991.

[70] P. Roos, M. A. Viergever, M. C. A. Van Dijke, and J. H. Peters, “Reversible intraframe compression of medical images,” *IEEE Trans. Med. Imag.*, vol. 7, no. 4, pp. 328–336, 1988.

[71] A. Said, “Arithmetic Coding,” in in *Lossless Compression Handbook*, Elsevier Science (USA)., 2003, pp. 101–152.

[72] A. Said and W. A. Pearlman, “A new, fast, and efficient image codec based on set partitioning in hierarchical trees,” *IEEE Trans. Circuits Syst. Video Technol.*, vol. 6, no. 3, pp. 243–250, 1996.

[73] D. Salomon, *Data Compression-The Complete Reference*, 3e ed. Springer-Verlag New York, Inc., 2004.

[74] E. Seeram, “Irreversible compression in digital radiology. A literature review,” *Radiography*, vol. 12, no. 1, pp. 45–59, 2006.

[75] J. M. Shapiro, “Embedded Image Coding Using Zerotrees of Wavelet Coefficients,” *IEEE Trans. Signal Processing*, vol. 41, no. 12, pp. 3445–3462, 1993.

[76] M.-Y. Shen and C.-C. J. Kuo, “Review of Postprocessing Techniques for Compression Artifact Removal,” *Journal of Visual Communication and Image Representation*, vol. 9, no. 1, pp. 2–14, Mar. 1998.

[77] A. Skodras, C. Christopoulos, and T. Ebrahimi, “The JPEG 2000 still image compression standard,” *IEEE Signal Proc. Mag.*, vol. 18, no. 5, pp. 36–58, 2001.

[78] M. G. Strintzis, “A review of compression methods for medical images in PACS,” *Int. J. of Medical Informatics*, vol. 52, no. 1–3, pp. 159–165, 1998.

[79] A. V Subramanyam, S. Emmanuel, and M. S. Kankanhalli, “Compressed-Encrypted Domain JPEG2000 Image Watermarking,” in *Proc. IEEE Int. Conf. on Multimedia and Expo (ICME), Singapore, July 2010*, 2010, pp. 1315–1320.

[80] P. G. Tahoces, J. R. Varela, M. J. Lado, and M. Souto, “Image compression: Maxshift ROI encoding options in JPEG2000,” *Computer Vision and Image Understanding*, vol. 109, no. 2, pp. 139–145, Feb. 2008.

[81] K. Takaya, C. G. Tannous, and L. Yuan, “Information preserved guided scan pixel difference coding for medical images,” in *IEEE Wescanex Proceedings*, 1995, vol. I, no. 95, pp. 238–243.

[82] J. Taquet and C. Labit, “Hierarchical oriented predictions for resolution scalable lossless and near-lossless compression of CT and MRI biomedical images,” *IEEE Trans. Image Process.*, vol. 21, no. 5, pp. 2641–52, May 2012.

[83] J. Taquet and C. Labit, “Near-lossless and scalable compression for medical imaging using a new adaptive hierarchical oriented prediction,” in *Proc. IEEE 17th Int. Conf. on Image Processing*, 2010, pp. 481–484.

[84] D. Taubman, “High performance scalable image compression with EBCOT,” *IEEE Trans. Image Process.*, vol. 9, no. 7, pp. 1158–1170, 2000.

[85] J. Taur and C. W. Tao, “Medical image compression using principal component analysis,” in *Proc. Int. Conf. Image Processing*, 1996, pp. 903–906.

[86] S. Todd, G. G. Langdon, and J. Rissanen, “Parameter reduction and context selection for compression of gray-scale images,” *IBM Journal of Research and Development*, vol. 29, no. 2, pp. 188–193, Mar. 1985.

[87] O. Urhan and S. Erturk, “Parameter Embedding Mode and Optimal Post-Process Filtering for Improved WDCT Image Compression,” *IEEE Transactions on Circuits and Systems for Video Technology*, vol. 18, no. 4, pp. 528–532, 2008.

[88] K. Viswanath, J. Mukherjee, and P. K. Biswas, “Wavelet transcoding in the block discrete cosine transform space,” *IET Image Processing*, vol. 4, no. 3, p. 143, 2010.

[89] K. Viswanath, J. Mukhopadhyay, and P. K. Biswas, “Transcoding in the Block DCT Space,” in *Proc.16th IEEE Int. Conf. on Image Processing (ICIP)*, 2009, pp. 3685–3688.

[90] G. K. Wallace, “The JPEG still picture compression standard,” *IEEE Trans. Consumer Electronics*, vol. 38, no. 1, pp. 18–34, 1992.

[91] J. Wang and K. Huang, “Medical image compression by using three-dimensional wavelettransformation,” *IEEE Trans. Med. Imag.*, vol. 15, no. 4, pp. 547–554, 1996.

[92] Z. Wang and A. C. Bovik, “A Universal Image Quality Index,” *IEEE Signal Proc. Letters*, vol. 9, no. 3, pp. 81–84, 2002.

[93] Z. Wang, A. C. Bovik, H. R. Sheikh, and E. P. Simoncelli, “Image quality assessment: from error visibility to structural similarity.,” *IEEE transactions on image processing*, vol. 13, no. 4, pp. 600–12, Apr. 2004.

[94] M. J. Weinberger, G. Seroussi, and G. Sapiro, “The LOCO-I lossless image compression algorithm: Principles and standardization into JPEG-LS,” *IEEE Trans. Image Process.*, vol. 9, no. 8, pp. 1309–1324, Aug. 2000.

[95] B. Wohlberg and G. De Jager, “A review of the fractal image coding literature,” *IEEE Trans. Image Process.*, vol. 8, no. 12, pp. 1716–1729, 1999.

[96] S. Wong, L. Zaremba, D. Gooden, and H. K. Huang, “Radiologic image compression-a review,” *Proc. IEEE*, vol. 83, no. 2, pp. 194–219, 1995.

[97] X. Wu, “Lossless compression of continuous-tone images via contextselection, quantization, and modeling,” *IEEE Trans. Image Process.*, vol. 6, no. 5, pp. 656–664, May 1997.

[98] X. Wu and N. Memon, “Context-Based, Adaptive, Lossless Image Coding,” *IEEE Trans. Commun.*, vol. 45, no. 4, pp. 437–444, Apr. 1997.

[99] H. Yang, M. Long, and H. Tai, “Region-of-interest image coding based on EBCOT,” *IEE Proc.-Vis. Image Signal Process.*, vol. 152, no. 5, 2005.

[100] Y. Zhang and D. A. Adjeroh, “Prediction by partial approximate matching for lossless image compression.,” *IEEE Trans. Image Process.*, vol. 17, no. 6, pp. 924–35, Jun. 2008.

[101] X. Zhao and Z. He, “Lossless Image Compression Using Super-Spatial Structure Prediction,” *IEEE Signal Proc. Letters*, vol. 17, no. 4, pp. 383–386, Apr. 2010.

[102] Y. Zhao, P. Campisi, and D. Kundur, “Dual domain watermarking for authentication and compression of cultural heritage images.,” *IEEE Trans. Image Process.*, vol. 13, no. 3, pp. 430–48, Mar. 2004.

[103] Zixiang Xiong, X. Wu, S. Cheng, and Jianping Hua, “Lossy-to-lossless compression of medical volumetric data using three-dimensional integer wavelet transforms,” *IEEE Trans. Med. Imag.*, vol. 22, no. 3, pp. 459–470, Mar. 2003.

[104] “Arithmetic Coding.” [Online]. Available: http://www.ux.uis.no/~karlsk/proj99/index.html.

[105] “CALIC Executable.” [Online]. Available: http://www.ece.mcmaster.ca/~xwu/calicexe/.

[106] “CIPR.” [Online]. Available: http://www.cipr.rpi.edu/resource/sequences/sequence01.html.

[107] “DICOM Standards.” [Online]. Available: ftp://medical.nema.org/medical/dicom.

[108] “Image Magic.” [Online]. Available: http://www.imagemagick.org/script/index.php.

[109] “ImajeJ.” [Online]. Available: http://rsbweb.nih.gov/ij/.

[110] “ITU.” [Online]. Available: http://www.itu.int/ITU-T/index.html.

[111] “JPEG2000 Standard.” [Online]. Available: http://www.jpeg.org/jpeg2000/.

[112] “LOCO-I Executable.” [Online]. Available: http://www.hpl.hp.com/loco/jlsrefV100.zip.

[113] “MGH Dataset.” [Online]. Available: http://www.cma.mgh.harvard.edu.ibsr.

[114] “MicroDicom Datatset.” [Online]. Available: http://www.microdicom.com/downloads.html.

[115] “OsiriX Dataset.” [Online]. Available: http://pubimage.hcuge.ch:8080/.

[116] “Physionet.” [Online]. Available: http://www.physionet.org/physiobank/database/images/.

Appendix - A: Image Datasets

The central slice of the medical image datasets used test the performance of image compression algorithms proposed in this work is shown in Fig. A.1 below.

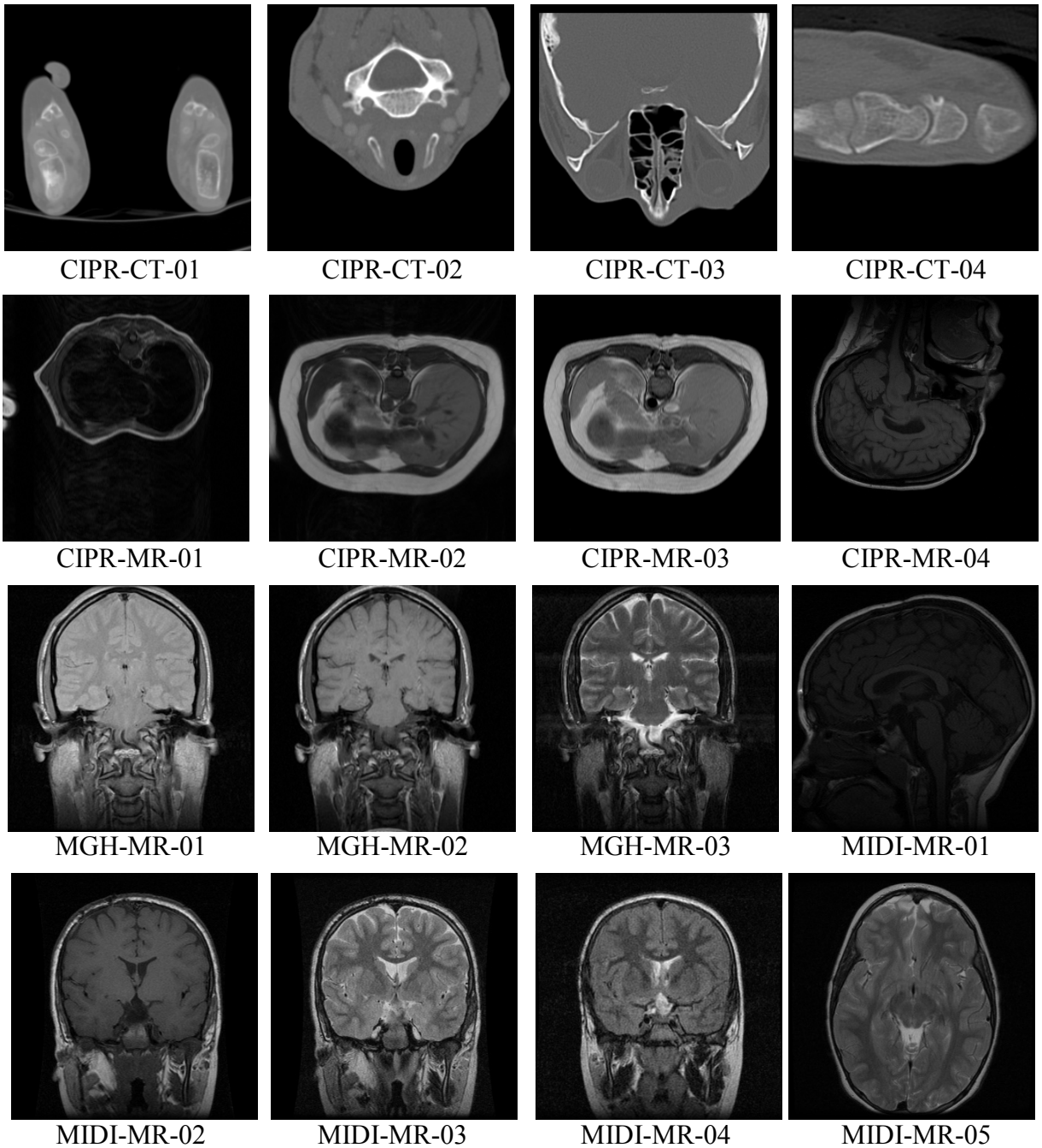

Fig. A.1 (a) The central slice of the medical image datasets

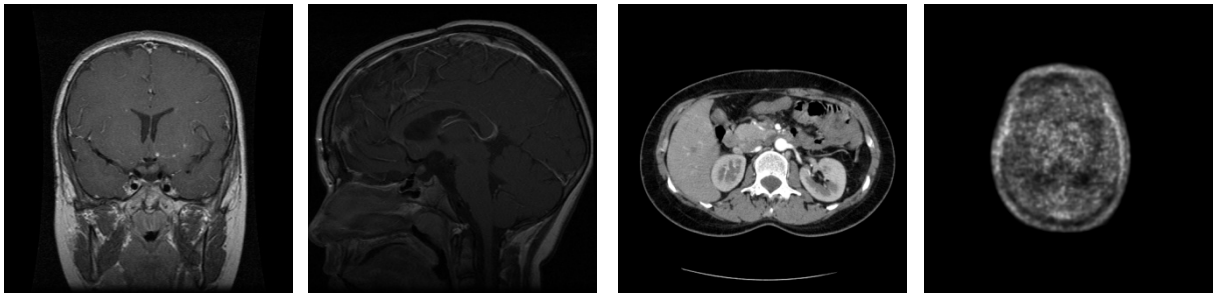

MIDI-MR-06 MIDI-MR-07 OSRX-CT-01 OSRX-PT-01

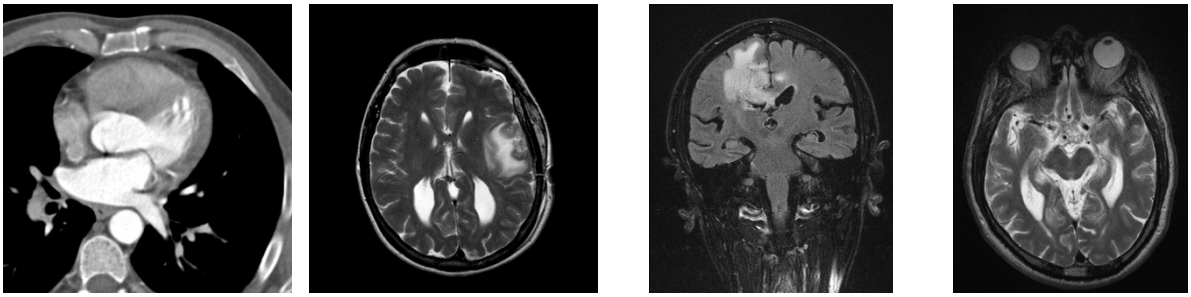

OSRX-CT-02 OSRX-MR-01 OSRX-MR-02 OSRX-MR-03

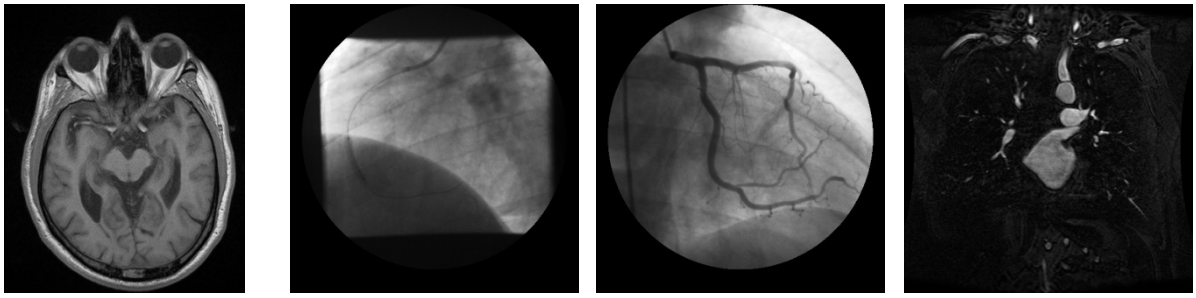

OSRX-MR-04 OSRX-XA-01 OSRX-XA-02 PHNT-MR-01

Fig. A.2 (b) The central slice of the medical image datasets (continuation of Fig. A.1(a))

Appendix - B: Lossless and NLS Compression

Table B.1 Comparison of lossless and near lossless compression performance of the proposed method DLD and lossless benchmark algorithms, CALIC and LOCO-I while tested with medical image datasets, CIPR-CT-01, CIPR-CT-02, CIPR-CT-03 and CIPR-CT-04.

Dataset	PAE	CALIC				LOCO-I				DLD			
		PSNR	MSSIM	UQI	BPP	PSNR	MSSIM	UQI	BPP	PSNR	MSSIM	UQI	BPP
CIPR-CT-01	0	Inf	1.000	1.000	0.998	Inf	1.000	1.000	1.058	Inf	1.000	1.000	0.970
	1	54.947	0.997	0.896	0.558	53.174	0.989	0.716	0.614	54.910	0.997	0.898	0.637
	2	50.889	0.994	0.863	0.419	48.940	0.971	0.673	0.499	50.746	0.993	0.859	0.460
	3	48.219	0.990	0.844	0.357	45.724	0.941	0.647	0.436	48.047	0.989	0.844	0.381
	4	46.114	0.984	0.827	0.328	43.540	0.915	0.631	0.393	46.015	0.985	0.830	0.324
	6	43.187	0.974	0.803	0.273	40.555	0.865	0.605	0.334	42.975	0.975	0.808	0.256
	8	40.791	0.956	0.775	0.249	38.173	0.821	0.587	0.294	40.710	0.965	0.788	0.214
	10	38.996	0.939	0.758	0.227	36.254	0.782	0.570	0.266	38.950	0.954	0.771	0.180
	12	37.442	0.920	0.733	0.208	35.077	0.759	0.559	0.245	37.465	0.943	0.756	0.158
	16	34.916	0.884	0.707	0.189	32.602	0.705	0.539	0.212	35.035	0.922	0.732	0.130
CIPR-CT-02	0	Inf	1.000	1.000	1.684	Inf	1.000	1.000	1.778	Inf	1.000	1.000	1.514
	1	52.794	0.997	0.976	1.058	52.701	0.996	0.962	1.154	52.777	0.997	0.977	0.970
	2	48.081	0.989	0.924	0.829	48.028	0.989	0.918	0.939	48.160	0.991	0.946	0.695
	3	45.373	0.981	0.885	0.674	45.212	0.980	0.871	0.795	45.401	0.983	0.914	0.550
	4	43.248	0.968	0.811	0.613	43.188	0.969	0.826	0.692	43.418	0.976	0.883	0.456
	6	40.505	0.942	0.720	0.505	40.269	0.945	0.759	0.559	40.494	0.960	0.832	0.342
	8	38.113	0.889	0.620	0.449	38.064	0.916	0.717	0.477	38.222	0.944	0.794	0.282
	10	36.545	0.864	0.589	0.393	36.286	0.888	0.687	0.423	36.350	0.929	0.761	0.248
	12	35.377	0.857	0.591	0.344	34.867	0.858	0.661	0.380	34.826	0.915	0.734	0.212
	16	32.663	0.774	0.489	0.336	32.494	0.798	0.619	0.320	32.310	0.891	0.684	0.178
CIPR-CT-03	0	Inf	1.000	1.000	2.628	Inf	1.000	1.000	2.761	Inf	1.000	1.000	2.526
	1	51.586	0.996	0.945	1.687	51.576	0.996	0.939	1.783	51.576	0.996	0.954	1.756
	2	46.977	0.987	0.867	1.313	46.944	0.987	0.878	1.420	46.836	0.988	0.910	1.359
	3	44.244	0.978	0.846	1.075	44.047	0.976	0.828	1.201	43.899	0.978	0.867	1.125
	4	42.257	0.965	0.793	0.930	42.021	0.963	0.777	1.016	41.805	0.966	0.823	0.958
	6	39.254	0.920	0.637	0.778	39.210	0.933	0.681	0.772	38.928	0.943	0.749	0.716
	8	36.944	0.874	0.555	0.682	37.097	0.903	0.620	0.650	36.850	0.923	0.690	0.571
	10	35.729	0.860	0.515	0.597	35.385	0.871	0.581	0.577	35.008	0.903	0.652	0.484
	12	34.680	0.850	0.496	0.536	33.959	0.841	0.557	0.524	33.721	0.896	0.620	0.411
	16	32.349	0.803	0.451	0.474	31.605	0.782	0.523	0.458	31.266	0.868	0.577	0.406
CIPR-CT-04	0	Inf	1.000	1.000	1.550	Inf	1.000	1.000	1.627	Inf	1.000	1.000	1.375
	1	52.556	0.996	0.970	0.960	52.377	0.995	0.929	1.000	52.580	0.996	0.970	1.011
	2	47.897	0.989	0.931	0.755	47.707	0.985	0.895	0.801	47.907	0.990	0.938	0.743
	3	44.972	0.978	0.874	0.629	44.862	0.973	0.865	0.671	45.075	0.981	0.906	0.604
	4	42.849	0.961	0.805	0.553	42.812	0.959	0.833	0.576	43.039	0.971	0.874	0.498
	6	40.024	0.931	0.731	0.437	39.809	0.929	0.778	0.457	40.116	0.950	0.814	0.373
	8	37.686	0.874	0.601	0.397	37.635	0.897	0.727	0.379	37.983	0.929	0.761	0.310
	10	36.350	0.871	0.585	0.322	35.782	0.861	0.688	0.334	36.190	0.907	0.716	0.254
	12	34.958	0.846	0.536	0.283	34.671	0.843	0.641	0.283	34.744	0.886	0.677	0.216
	16	32.648	0.786	0.409	0.235	32.743	0.806	0.584	0.224	32.360	0.851	0.615	0.172

Table B.2 Comparison of lossless and near lossless compression performance of the proposed method DLD and lossless benchmark algorithms, CALIC and LOCO-I while tested with medical image datasets, CIPR-MR-01, CIPR-MR-02, CIPR-MR-03 and CIPR-MR-04.

Dataset	PAE	CALIC				LOCO-I				DLD			
		PSNR	MSSIM	UQI	BPP	PSNR	MSSIM	UQI	BPP	PSNR	MSSIM	UQI	BPP
CIPR-MR-01	0	Inf	1.000	1.000	2.789	Inf	1.000	1.000	2.937	Inf	1.000	1.000	2.655
	1	50.294	0.992	0.850	1.485	50.134	0.991	0.864	1.677	49.979	0.990	0.884	1.499
	2	46.314	0.981	0.731	1.053	45.688	0.974	0.721	1.249	45.640	0.966	0.747	1.008
	3	43.951	0.970	0.658	0.835	43.021	0.950	0.625	1.005	43.156	0.936	0.648	0.745
	4	42.272	0.956	0.600	0.707	41.035	0.923	0.552	0.837	41.390	0.910	0.585	0.584
	6	39.839	0.931	0.503	0.569	38.030	0.859	0.441	0.624	38.734	0.841	0.482	0.412
	8	38.096	0.908	0.430	0.478	35.895	0.796	0.367	0.498	36.824	0.774	0.405	0.308
	10	36.582	0.879	0.373	0.424	34.207	0.733	0.312	0.414	35.306	0.709	0.344	0.246
	12	35.277	0.856	0.335	0.386	32.909	0.679	0.271	0.354	34.122	0.659	0.299	0.206
	16	33.411	0.804	0.274	0.324	30.715	0.588	0.217	0.278	32.310	0.583	0.237	0.154
CIPR-MR-02	0	Inf	1.000	1.000	3.022	Inf	1.000	1.000	3.160	Inf	1.000	1.000	2.898
	1	50.141	0.994	0.937	1.730	49.998	0.994	0.928	1.890	49.934	0.993	0.936	1.697
	2	45.815	0.985	0.861	1.263	45.483	0.982	0.845	1.450	45.340	0.979	0.867	1.218
	3	43.216	0.974	0.802	1.020	42.677	0.965	0.777	1.200	42.533	0.954	0.804	0.955
	4	41.308	0.961	0.752	0.871	40.615	0.944	0.721	1.034	40.566	0.925	0.751	0.790
	6	38.536	0.935	0.672	0.697	37.659	0.898	0.637	0.823	37.727	0.865	0.665	0.593
	8	36.496	0.906	0.609	0.582	35.481	0.848	0.575	0.695	35.685	0.813	0.601	0.478
	10	34.838	0.879	0.558	0.507	33.830	0.802	0.525	0.604	34.093	0.769	0.550	0.398
	12	33.067	0.855	0.516	0.458	32.439	0.757	0.486	0.536	32.768	0.733	0.508	0.343
	16	31.052	0.771	0.451	0.379	30.384	0.677	0.429	0.445	30.670	0.681	0.448	0.270
CIPR-MR-03	0	Inf	1.000	1.000	2.269	Inf	1.000	1.000	2.418	Inf	1.000	1.000	1.858
	1	52.523	0.998	0.987	1.506	52.363	0.996	0.957	1.610	52.555	0.998	0.989	1.297
	2	47.781	0.994	0.976	1.190	47.438	0.985	0.934	1.291	47.788	0.994	0.977	1.063
	3	44.830	0.988	0.962	1.007	44.499	0.975	0.918	1.114	44.819	0.988	0.963	0.897
	4	42.683	0.981	0.944	0.890	42.204	0.956	0.875	0.993	42.688	0.982	0.948	0.790
	6	39.760	0.968	0.914	0.709	39.285	0.937	0.851	0.826	39.673	0.967	0.917	0.631
	8	37.154	0.915	0.793	0.656	36.979	0.906	0.821	0.715	37.519	0.951	0.888	0.526
	10	35.423	0.882	0.746	0.589	35.256	0.878	0.782	0.633	35.832	0.934	0.861	0.449
	12	34.057	0.856	0.716	0.532	33.898	0.861	0.758	0.571	34.434	0.919	0.835	0.397
	16	31.943	0.827	0.695	0.454	31.463	0.796	0.712	0.480	32.134	0.888	0.789	0.321
CIPR-MR-04	0	Inf	1.000	1.000	2.519	Inf	1.000	1.000	2.582	Inf	1.000	1.000	2.571
	1	52.245	0.996	0.764	1.505	49.817	0.966	0.602	1.486	52.109	0.996	0.756	1.471
	2	47.748	0.989	0.598	1.108	45.455	0.922	0.539	1.137	47.719	0.989	0.596	1.082
	3	45.080	0.980	0.527	0.888	43.378	0.910	0.504	0.938	45.011	0.981	0.524	0.848
	4	43.208	0.971	0.493	0.749	41.648	0.896	0.477	0.806	43.055	0.972	0.488	0.700
	6	40.410	0.948	0.448	0.592	39.125	0.870	0.432	0.644	40.243	0.952	0.444	0.519
	8	38.383	0.932	0.411	0.486	37.172	0.848	0.396	0.549	38.158	0.931	0.409	0.403
	10	36.617	0.910	0.377	0.424	35.533	0.814	0.364	0.481	36.475	0.909	0.379	0.330
	12	35.033	0.884	0.347	0.381	34.124	0.778	0.337	0.431	35.061	0.887	0.352	0.280
	16	32.532	0.835	0.295	0.318	31.896	0.723	0.291	0.357	32.756	0.846	0.305	0.212

Table B.3 Comparison of lossless and near lossless compression performance of the proposed method DLD and lossless benchmark algorithms, CALIC and LOCO-I while tested with medical image datasets, MGHD-MR-01, MGHD-MR-02, MGHD-MR-03 and MIDI-MR-01.

Datasets	PAE	CALIC				LOCO-I				DLD			
		PSNR	MSSIM	UQI	BPP	PSNR	MSSIM	UQI	BPP	PSNR	MSSIM	UQI	BPP
MGHD-MR-01	0	Inf	1.000	1.000	3.960	Inf	1.000	1.000	4.126	Inf	1.000	1.000	3.928
	1	49.986	0.994	0.968	2.523	49.958	0.994	0.968	2.640	50.019	0.994	0.968	2.436
	2	45.354	0.984	0.917	1.931	45.319	0.984	0.913	2.031	45.332	0.984	0.919	1.856
	3	42.546	0.971	0.857	1.587	42.474	0.970	0.841	1.656	42.457	0.969	0.864	1.494
	4	40.656	0.956	0.795	1.359	40.438	0.954	0.771	1.401	40.429	0.949	0.811	1.247
	6	38.094	0.925	0.692	1.058	37.571	0.912	0.673	1.107	37.574	0.885	0.711	0.920
	8	36.170	0.890	0.630	0.903	35.529	0.857	0.604	0.933	35.679	0.807	0.628	0.709
	10	34.838	0.863	0.585	0.755	33.930	0.795	0.554	0.819	34.283	0.743	0.568	0.566
	12	33.677	0.858	0.554	0.684	32.678	0.747	0.515	0.737	33.177	0.705	0.529	0.477
	16	31.694	0.798	0.493	0.562	30.605	0.674	0.454	0.625	31.370	0.662	0.475	0.366
MGHD -MR-02	0	Inf	1.000	1.000	3.408	Inf	1.000	1.000	3.607	Inf	1.000	1.000	3.329
	1	50.208	0.994	0.904	2.039	50.104	0.993	0.903	2.205	50.014	0.993	0.914	1.967
	2	46.079	0.985	0.798	1.532	45.651	0.981	0.762	1.613	45.532	0.978	0.816	1.433
	3	43.599	0.976	0.723	1.250	42.924	0.963	0.684	1.337	42.870	0.947	0.727	1.122
	4	41.729	0.964	0.677	1.074	40.959	0.941	0.635	1.168	41.049	0.912	0.657	0.920
	6	39.044	0.944	0.635	0.869	38.015	0.888	0.582	0.967	38.546	0.865	0.588	0.692
	8	37.020	0.923	0.601	0.745	35.970	0.849	0.548	0.848	36.707	0.845	0.557	0.568
	10	35.435	0.906	0.573	0.662	34.258	0.808	0.518	0.768	35.189	0.827	0.532	0.483
	12	34.102	0.887	0.544	0.593	32.818	0.768	0.491	0.707	33.911	0.811	0.508	0.418
	16	31.819	0.845	0.489	0.506	30.587	0.700	0.443	0.617	31.805	0.780	0.466	0.327
MGHD -MR-03	0	Inf	1.000	1.000	4.416	Inf	1.000	1.000	4.569	Inf	1.000	1.000	4.340
	1	49.952	0.995	0.984	2.938	49.939	0.995	0.984	3.052	49.991	0.995	0.984	2.850
	2	45.218	0.987	0.956	2.301	45.195	0.987	0.955	2.389	45.254	0.987	0.956	2.215
	3	42.303	0.975	0.920	1.911	42.268	0.974	0.917	1.994	42.304	0.974	0.921	1.837
	4	40.200	0.960	0.877	1.644	40.174	0.960	0.871	1.715	40.187	0.959	0.883	1.562
	6	37.420	0.930	0.787	1.284	37.207	0.926	0.772	1.348	37.228	0.922	0.807	1.194
	8	35.484	0.897	0.713	1.078	35.137	0.889	0.694	1.126	35.173	0.871	0.734	0.941
	10	34.067	0.870	0.652	0.931	33.492	0.842	0.632	0.978	33.640	0.806	0.667	0.759
	12	32.938	0.845	0.604	0.809	32.129	0.788	0.582	0.875	32.434	0.745	0.611	0.628
	16	31.052	0.783	0.536	0.642	30.108	0.699	0.517	0.737	30.635	0.660	0.536	0.461
MGHD -MR-01	0	Inf	1.000	1.000	2.700	Inf	1.000	1.000	2.983	Inf	1.000	1.000	2.503
	1	50.061	0.992	0.940	1.535	50.019	0.992	0.938	1.726	50.014	0.992	0.941	1.535
	2	45.524	0.977	0.864	1.145	45.442	0.978	0.855	1.316	45.437	0.976	0.864	1.144
	3	42.851	0.958	0.780	0.910	42.660	0.958	0.767	1.066	42.706	0.953	0.783	0.887
	4	40.960	0.937	0.700	0.762	40.719	0.936	0.685	0.888	40.802	0.927	0.706	0.711
	6	38.474	0.899	0.565	0.564	37.963	0.885	0.546	0.655	38.149	0.868	0.577	0.476
	8	36.659	0.862	0.481	0.486	35.950	0.830	0.442	0.515	36.198	0.816	0.483	0.344
	10	35.452	0.841	0.400	0.382	34.391	0.778	0.366	0.424	34.590	0.770	0.415	0.265
	12	34.400	0.825	0.343	0.322	33.013	0.729	0.311	0.360	33.200	0.726	0.358	0.211
	16	31.973	0.780	0.237	0.219	31.055	0.650	0.231	0.275	30.880	0.647	0.280	0.150

Table B.4 Comparison of lossless and near lossless compression performance of the proposed method DLD and lossless benchmark algorithms, CALIC and LOCO-I while tested with medical image datasets, MIDI-MR-02, MIDI-MR-03, MIDI-MR-04 and MIDI-MR-05.

Datasets	PAE	CALIC				LOCO-I				DLD			
		PSNR	MSSIM	UQI	BPP	PSNR	MSSIM	UQI	BPP	PSNR	MSSIM	UQI	BPP
MIDI-MR-02	0	Inf	1.000	1.000	2.507	Inf	1.000	1.000	2.747	Inf	1.000	1.000	2.271
	1	51.174	0.996	0.974	1.507	50.845	0.993	0.874	1.713	51.154	0.995	0.976	1.469
	2	46.536	0.987	0.939	1.137	46.111	0.977	0.836	1.333	46.468	0.986	0.942	1.142
	3	43.671	0.975	0.899	0.932	43.158	0.955	0.794	1.116	43.576	0.973	0.905	0.941
	4	41.599	0.957	0.859	0.796	41.035	0.929	0.752	0.967	41.531	0.957	0.866	0.791
	6	38.735	0.916	0.779	0.621	38.030	0.873	0.678	0.770	38.723	0.917	0.791	0.579
	8	36.685	0.877	0.720	0.542	35.948	0.819	0.611	0.641	36.804	0.874	0.722	0.435
	10	35.413	0.851	0.662	0.426	34.347	0.767	0.555	0.553	35.348	0.835	0.667	0.339
	12	34.303	0.830	0.617	0.359	33.087	0.721	0.510	0.489	34.140	0.804	0.625	0.275
	16	32.471	0.802	0.548	0.267	30.992	0.648	0.445	0.404	32.149	0.762	0.564	0.197
MIDI-MR-03	0	Inf	1.000	1.000	3.204	Inf	1.000	1.000	3.465	Inf	1.000	1.000	2.829
	1	51.029	0.997	0.986	2.068	50.739	0.994	0.894	2.310	51.033	0.997	0.989	1.895
	2	46.310	0.991	0.973	1.613	45.960	0.983	0.878	1.839	46.294	0.991	0.975	1.519
	3	43.320	0.983	0.954	1.347	42.970	0.966	0.861	1.557	43.322	0.983	0.959	1.305
	4	41.154	0.972	0.935	1.163	40.822	0.949	0.843	1.376	41.153	0.972	0.939	1.151
	6	38.047	0.944	0.888	0.939	37.714	0.908	0.799	1.138	38.073	0.946	0.897	0.930
	8	35.746	0.909	0.846	0.796	35.483	0.863	0.754	0.981	35.931	0.917	0.853	0.760
	10	34.050	0.872	0.801	0.687	33.737	0.816	0.713	0.867	34.323	0.884	0.811	0.631
	12	32.812	0.835	0.755	0.584	32.312	0.772	0.672	0.775	33.042	0.850	0.771	0.531
	16	31.016	0.771	0.675	0.440	30.095	0.689	0.595	0.635	31.079	0.777	0.695	0.384
MIDI-MR-04	0	Inf	1.000	1.000	3.513	Inf	1.000	1.000	3.850	Inf	1.000	1.000	2.961
	1	49.928	0.995	0.988	2.106	49.924	0.995	0.988	2.418	49.932	0.995	0.988	1.892
	2	45.193	0.986	0.968	1.590	45.188	0.986	0.967	1.851	45.188	0.986	0.968	1.522
	3	42.242	0.973	0.940	1.310	42.236	0.973	0.940	1.589	42.223	0.973	0.941	1.301
	4	40.148	0.958	0.909	1.111	40.102	0.958	0.907	1.423	40.090	0.957	0.910	1.126
	6	37.256	0.922	0.837	0.845	37.122	0.920	0.837	1.187	37.177	0.918	0.843	0.849
	8	35.300	0.883	0.760	0.666	34.990	0.875	0.759	1.004	35.190	0.874	0.772	0.656
	10	33.851	0.843	0.682	0.551	33.353	0.827	0.680	0.853	33.692	0.829	0.704	0.518
	12	32.678	0.801	0.606	0.474	32.051	0.780	0.604	0.734	32.482	0.783	0.639	0.419
	16	30.940	0.732	0.486	0.379	30.040	0.691	0.486	0.577	30.546	0.687	0.524	0.289
MIDI-MR-05	0	Inf	1.000	1.000	3.437	Inf	1.000	1.000	3.721	Inf	1.000	1.000	3.087
	1	50.058	0.994	0.969	2.074	50.046	0.994	0.967	2.294	50.060	0.994	0.969	1.944
	2	45.368	0.982	0.921	1.559	45.356	0.982	0.919	1.763	45.348	0.982	0.921	1.523
	3	42.537	0.966	0.867	1.258	42.488	0.967	0.864	1.469	42.458	0.964	0.866	1.256
	4	40.550	0.948	0.809	1.055	40.466	0.948	0.805	1.253	40.428	0.945	0.813	1.056
	6	37.717	0.905	0.699	0.822	37.576	0.905	0.689	0.967	37.619	0.898	0.716	0.774
	8	35.711	0.852	0.608	0.694	35.517	0.857	0.601	0.802	35.610	0.836	0.631	0.593
	10	34.460	0.812	0.522	0.558	33.932	0.805	0.524	0.686	34.046	0.753	0.551	0.467
	12	33.441	0.771	0.467	0.451	32.632	0.745	0.463	0.604	32.816	0.668	0.483	0.374
	16	31.675	0.716	0.405	0.358	30.648	0.622	0.386	0.499	31.089	0.559	0.399	0.259

Table B.5 Comparison of lossless and near lossless compression performance of the proposed method DLD and lossless benchmark algorithms, CALIC and LOCO-I while tested with medical image datasets, MIDI-MR-06, MIDI-MR-07, OSRX-CT-01and OSRX-PT-01.

Datasets	PAE	CALIC				LOCO-I				DLD			
		PSNR	MSSIM	UQI	BPP	PSNR	MSSIM	UQI	BPP	PSNR	MSSIM	UQI	BPP
MIDI-MR-06	0	Inf	1.000	1.000	2.509	Inf	1.000	1.000	2.758	Inf	1.000	1.000	2.211
	1	51.139	0.996	0.975	1.518	50.839	0.993	0.876	1.730	51.105	0.996	0.976	1.459
	2	46.453	0.987	0.939	1.153	46.118	0.979	0.837	1.353	46.399	0.987	0.942	1.151
	3	43.587	0.975	0.900	0.941	43.187	0.958	0.796	1.134	43.501	0.974	0.904	0.946
	4	41.506	0.959	0.859	0.803	41.108	0.936	0.755	0.984	41.443	0.958	0.865	0.805
	6	38.586	0.917	0.780	0.626	38.046	0.881	0.684	0.793	38.577	0.918	0.794	0.595
	8	36.501	0.869	0.720	0.538	35.875	0.823	0.618	0.667	36.585	0.870	0.728	0.454
	10	35.156	0.838	0.664	0.443	34.212	0.769	0.561	0.576	35.071	0.823	0.673	0.359
	12	34.176	0.819	0.617	0.362	32.939	0.719	0.517	0.512	33.865	0.786	0.631	0.292
	16	32.360	0.788	0.554	0.274	30.898	0.636	0.453	0.426	31.929	0.738	0.571	0.211
MIDI-MR-07	0	Inf	1.000	1.000	2.682	Inf	1.000	1.000	2.964	Inf	1.000	1.000	2.405
	1	50.013	0.992	0.937	1.534	50.011	0.993	0.935	1.733	49.970	0.992	0.936	1.496
	2	45.508	0.978	0.854	1.123	45.464	0.979	0.849	1.322	45.400	0.977	0.857	1.117
	3	42.865	0.958	0.767	0.888	42.691	0.961	0.762	1.076	42.644	0.954	0.780	0.875
	4	41.070	0.939	0.686	0.735	40.748	0.940	0.683	0.906	40.702	0.926	0.709	0.707
	6	38.511	0.899	0.560	0.564	37.977	0.890	0.550	0.690	37.952	0.862	0.590	0.496
	8	36.624	0.862	0.488	0.482	35.981	0.832	0.461	0.565	35.979	0.809	0.507	0.373
	10	35.302	0.840	0.431	0.401	34.410	0.778	0.398	0.484	34.376	0.770	0.448	0.298
	12	34.238	0.825	0.384	0.341	33.105	0.731	0.352	0.426	33.023	0.738	0.402	0.247
	16	31.669	0.793	0.305	0.256	30.904	0.645	0.285	0.344	30.709	0.687	0.334	0.185
OSRX-CT-01	0	Inf	1.000	1.000	1.898	Inf	1.000	1.000	1.960	Inf	1.000	1.000	1.894
	1	54.197	0.999	0.992	1.317	53.648	0.997	0.915	1.368	54.094	0.999	0.992	1.362
	2	49.396	0.997	0.982	1.053	48.845	0.991	0.905	1.122	49.326	0.997	0.986	1.076
	3	46.358	0.993	0.973	0.894	45.837	0.983	0.896	0.963	46.305	0.994	0.980	0.915
	4	44.112	0.988	0.961	0.784	43.592	0.973	0.887	0.856	44.087	0.991	0.973	0.789
	6	40.966	0.979	0.955	0.634	40.339	0.949	0.865	0.722	40.905	0.981	0.957	0.636
	8	38.566	0.957	0.907	0.550	38.032	0.925	0.847	0.632	38.660	0.969	0.941	0.535
	10	36.689	0.924	0.847	0.485	36.284	0.902	0.832	0.563	36.957	0.957	0.923	0.457
	12	35.118	0.888	0.792	0.444	34.832	0.880	0.813	0.507	35.600	0.943	0.904	0.398
	16	32.902	0.849	0.759	0.384	32.568	0.836	0.774	0.420	33.545	0.917	0.868	0.309
OSRX-PT-01	0	Inf	1.000	1.000	0.748	Inf	1.000	1.000	0.839	Inf	1.000	1.000	0.572
	1	57.192	1.000	0.995	0.483	55.618	0.996	0.853	0.547	57.177	1.000	0.995	0.440
	2	52.362	0.998	0.986	0.382	50.686	0.986	0.831	0.446	52.402	0.999	0.991	0.362
	3	49.390	0.997	0.987	0.326	47.557	0.973	0.810	0.405	49.386	0.997	0.988	0.315
	4	47.156	0.995	0.979	0.296	45.213	0.955	0.797	0.384	47.175	0.996	0.984	0.284
	6	44.009	0.989	0.966	0.254	41.830	0.915	0.787	0.356	44.024	0.991	0.977	0.242
	8	41.718	0.980	0.955	0.226	39.400	0.878	0.782	0.333	41.808	0.986	0.970	0.204
	10	39.984	0.971	0.946	0.201	37.539	0.851	0.779	0.313	40.110	0.980	0.963	0.175
	12	38.534	0.962	0.936	0.183	36.080	0.830	0.774	0.295	38.716	0.973	0.955	0.153
	16	36.321	0.946	0.920	0.156	33.760	0.802	0.764	0.261	36.537	0.959	0.939	0.120

Table B.6 Comparison of lossless and near lossless compression performance of the proposed method DLD and lossless benchmark algorithms, CALIC and LOCO-I while tested with medical image datasets, OSRX-CT-02, OSRX-MR-01, OSRX-MR-02 and OSRX-MR-03.

Datasets	PAE	CALIC				LOCO-I				DLD			
		PSNR	MSSIM	UQI	BPP	PSNR	MSSIM	UQI	BPP	PSNR	MSSIM	UQI	BPP
OSRX-CT-02	0	Inf	1.000	1.000	1.451	Inf	1.000	1.000	1.620	Inf	1.000	1.000	1.283
	1	52.848	0.997	0.986	0.896	51.834	0.990	0.778	1.071	52.766	0.997	0.984	0.887
	2	48.095	0.992	0.957	0.713	47.068	0.972	0.729	0.924	48.064	0.993	0.969	0.708
	3	45.146	0.983	0.922	0.603	44.010	0.945	0.691	0.830	45.163	0.987	0.952	0.579
	4	43.005	0.973	0.884	0.537	41.861	0.921	0.670	0.756	43.063	0.980	0.932	0.496
	6	39.886	0.944	0.804	0.442	38.530	0.848	0.598	0.645	40.052	0.965	0.894	0.398
	8	37.487	0.890	0.699	0.389	36.133	0.780	0.543	0.563	37.850	0.949	0.858	0.329
	10	35.675	0.845	0.633	0.353	34.287	0.722	0.507	0.501	36.086	0.933	0.825	0.282
	12	34.308	0.819	0.607	0.317	32.850	0.672	0.468	0.452	34.621	0.918	0.795	0.247
	16	32.179	0.803	0.584	0.271	30.383	0.578	0.404	0.384	32.242	0.891	0.744	0.202
OSRX-MR-01	0	Inf	1.000	1.000	1.637	Inf	1.000	1.000	1.785	Inf	1.000	1.000	1.392
	1	54.352	0.999	0.994	1.086	53.436	0.995	0.849	1.228	54.355	0.999	0.994	0.953
	2	49.588	0.997	0.988	0.852	48.546	0.984	0.824	0.996	49.584	0.997	0.988	0.769
	3	46.582	0.994	0.981	0.719	45.428	0.966	0.811	0.864	46.590	0.994	0.982	0.661
	4	44.389	0.990	0.973	0.630	43.144	0.946	0.802	0.776	44.407	0.990	0.975	0.585
	6	41.293	0.980	0.954	0.506	39.894	0.904	0.782	0.661	41.316	0.981	0.960	0.476
	8	39.062	0.965	0.933	0.433	37.562	0.865	0.763	0.587	39.140	0.971	0.944	0.402
	10	37.401	0.953	0.916	0.373	35.751	0.831	0.748	0.533	37.470	0.961	0.929	0.347
	12	36.070	0.942	0.900	0.329	34.285	0.804	0.732	0.492	36.108	0.950	0.914	0.306
	16	33.756	0.909	0.859	0.284	31.991	0.760	0.706	0.430	33.947	0.929	0.886	0.245
OSRX-MR-02	0	Inf	1.000	1.000	4.833	Inf	1.000	1.000	4.958	Inf	1.000	1.000	4.787
	1	49.889	0.996	0.987	3.303	49.889	0.996	0.987	3.411	49.882	0.996	0.986	3.296
	2	45.133	0.988	0.963	2.622	45.135	0.988	0.962	2.718	45.123	0.988	0.963	2.602
	3	42.171	0.976	0.931	2.197	42.156	0.976	0.930	2.283	42.131	0.976	0.933	2.182
	4	40.057	0.963	0.896	1.894	40.014	0.962	0.893	1.966	39.950	0.961	0.900	1.884
	6	37.130	0.933	0.821	1.493	36.971	0.929	0.818	1.557	36.862	0.927	0.832	1.471
	8	35.090	0.902	0.754	1.221	34.869	0.894	0.744	1.293	34.672	0.890	0.769	1.194
	10	33.516	0.871	0.686	1.010	33.219	0.857	0.679	1.103	33.003	0.852	0.711	0.989
	12	32.383	0.843	0.634	0.867	31.884	0.817	0.624	0.960	31.666	0.815	0.658	0.826
	16	30.317	0.780	0.534	0.650	29.676	0.734	0.532	0.752	29.574	0.746	0.565	0.590
OSRX-MR-03	0	Inf	1.000	1.000	4.145	Inf	1.000	1.000	4.325	Inf	1.000	1.000	4.069
	1	50.198	0.996	0.935	2.768	49.984	0.996	0.921	2.907	49.912	0.995	0.926	2.742
	2	45.658	0.989	0.883	2.178	45.363	0.988	0.865	2.294	45.191	0.987	0.874	2.164
	3	42.853	0.981	0.835	1.818	42.520	0.978	0.815	1.913	42.204	0.975	0.831	1.802
	4	40.834	0.972	0.790	1.561	40.506	0.967	0.771	1.647	40.042	0.960	0.793	1.551
	6	37.926	0.952	0.717	1.224	37.514	0.942	0.703	1.310	36.905	0.926	0.732	1.226
	8	35.830	0.931	0.670	1.013	35.270	0.913	0.653	1.113	34.578	0.882	0.683	1.018
	10	34.107	0.906	0.632	0.869	33.487	0.877	0.616	0.985	32.731	0.830	0.641	0.853
	12	33.019	0.890	0.592	0.735	32.063	0.841	0.582	0.889	31.251	0.775	0.603	0.724
	16	30.407	0.816	0.542	0.585	29.750	0.752	0.523	0.749	29.115	0.678	0.539	0.541

Table B.7 Comparison of lossless and near lossless compression performance of the proposed method DLD and lossless benchmark algorithms, CALIC and LOCO-I while tested with medical image datasets, OSRX-MR-04, OSRX-XA-01, OSRX-XA-02 and PHNT-MR-01.

Datsets	PAE	CALIC				LOCO-I				DLD			
		PSNR	MSSIM	UQI	BPP	PSNR	MSSIM	UQI	BPP	PSNR	MSSIM	UQI	BPP
OSRX-MR-04	0	Inf	1.000	1.000	3.775	Inf	1.000	1.000	3.950	Inf	1.000	1.000	3.716
	1	50.248	0.995	0.940	2.387	50.022	0.993	0.920	2.519	50.186	0.995	0.938	2.367
	2	45.722	0.986	0.864	1.815	45.390	0.979	0.838	1.897	45.524	0.985	0.867	1.789
	3	43.031	0.975	0.790	1.481	42.618	0.964	0.765	1.534	42.651	0.970	0.803	1.459
	4	41.141	0.964	0.730	1.260	40.637	0.948	0.703	1.308	40.582	0.951	0.748	1.224
	6	38.373	0.935	0.651	0.970	37.736	0.911	0.627	1.057	37.613	0.897	0.666	0.921
	8	36.307	0.899	0.604	0.791	35.512	0.862	0.584	0.918	35.541	0.834	0.609	0.725
	10	34.730	0.869	0.578	0.678	33.861	0.812	0.552	0.822	33.993	0.777	0.568	0.593
	12	33.505	0.859	0.549	0.588	32.513	0.771	0.525	0.749	32.770	0.735	0.537	0.498
	16	31.299	0.783	0.506	0.489	30.280	0.686	0.478	0.646	30.907	0.678	0.491	0.373
OSRX-XA-01	0	Inf	1.000	1.000	2.153	Inf	1.000	1.000	2.231	Inf	1.000	1.000	2.150
	1	51.703	0.995	0.959	1.195	51.348	0.992	0.870	1.294	51.676	0.995	0.960	1.245
	2	47.213	0.985	0.904	0.835	46.755	0.977	0.804	0.955	46.993	0.984	0.906	0.878
	3	44.684	0.975	0.847	0.626	43.981	0.954	0.743	0.758	44.211	0.971	0.853	0.654
	4	42.906	0.964	0.797	0.510	42.057	0.934	0.694	0.636	42.288	0.958	0.805	0.500
	6	40.223	0.938	0.708	0.360	39.161	0.894	0.623	0.478	39.492	0.928	0.730	0.316
	8	38.236	0.923	0.655	0.265	36.945	0.854	0.566	0.381	37.338	0.898	0.673	0.227
	10	36.442	0.901	0.605	0.222	35.000	0.807	0.508	0.319	35.536	0.869	0.631	0.174
	12	34.949	0.880	0.556	0.202	33.402	0.757	0.461	0.274	34.047	0.844	0.599	0.141
	16	32.296	0.842	0.522	0.176	31.088	0.685	0.427	0.209	31.461	0.792	0.548	0.102
OSRX-XA-02	0	Inf	1.000	1.000	2.231	Inf	1.000	1.000	2.302	Inf	1.000	1.000	2.253
	1	51.639	0.995	0.967	1.292	51.387	0.993	0.890	1.373	51.661	0.995	0.970	1.319
	2	46.941	0.985	0.921	0.936	46.755	0.980	0.855	1.072	46.967	0.985	0.936	0.932
	3	44.189	0.973	0.888	0.718	43.898	0.962	0.813	0.896	44.168	0.973	0.898	0.713
	4	42.092	0.955	0.820	0.617	41.879	0.943	0.767	0.761	42.249	0.960	0.859	0.557
	6	39.365	0.923	0.729	0.465	38.989	0.903	0.689	0.575	39.571	0.936	0.791	0.369
	8	37.238	0.873	0.628	0.408	36.913	0.868	0.626	0.458	37.516	0.913	0.735	0.269
	10	35.717	0.836	0.563	0.346	35.203	0.832	0.567	0.380	35.791	0.893	0.689	0.211
	12	34.545	0.818	0.519	0.298	33.729	0.797	0.522	0.325	34.288	0.875	0.651	0.176
	16	32.134	0.794	0.462	0.270	31.303	0.725	0.450	0.254	31.738	0.845	0.591	0.135
PHNT-MR-01	0	Inf	1.000	1.000	3.048	Inf	1.000	1.000	3.292	Inf	1.000	1.000	2.917
	1	50.134	0.993	0.971	1.783	50.029	0.993	0.956	1.968	50.155	0.994	0.976	1.760
	2	45.421	0.981	0.927	1.312	45.278	0.978	0.913	1.533	45.402	0.981	0.933	1.339
	3	42.577	0.964	0.882	1.054	42.375	0.958	0.866	1.305	42.531	0.963	0.889	1.072
	4	40.597	0.945	0.832	0.862	40.314	0.936	0.814	1.136	40.534	0.945	0.843	0.880
	6	37.874	0.902	0.720	0.632	37.412	0.886	0.705	0.884	37.759	0.902	0.747	0.616
	8	36.099	0.860	0.608	0.480	35.405	0.834	0.592	0.692	35.778	0.851	0.653	0.448
	10	34.792	0.825	0.507	0.398	33.810	0.784	0.493	0.552	34.246	0.800	0.569	0.340
	12	33.747	0.795	0.420	0.342	32.510	0.735	0.413	0.451	32.935	0.744	0.493	0.265
	16	32.079	0.745	0.300	0.277	30.521	0.651	0.303	0.322	30.860	0.633	0.375	0.177

Table B.8 Comparison of compression performance of JPEG and JPEG2000 while tested with medical image datasets, CIPR-CT-01 and CIPR-CT-02.

Datasets	Q	JPEG					JPEG2000				
		M-PAE	PSNR	MSSIM	UQI	BPP	M-PAE	PSNR	MSSIM	UQI	BPP
CIPR-CT-01	100	1	63.277	1.000	0.964	1.549	0	Inf	1.000	1.000	1.278
	99	2	60.634	0.999	0.949	1.403	3	54.034	0.994	0.760	0.604
	98	3	57.764	0.999	0.921	1.188	3	54.034	0.994	0.760	0.604
	97	4	56.385	0.999	0.908	1.090	3	54.034	0.994	0.760	0.604
	96	4	55.225	0.998	0.894	0.990	3	54.034	0.994	0.760	0.604
	95	5	54.254	0.998	0.885	0.911	3	54.034	0.994	0.760	0.604
	94	6	53.511	0.997	0.874	0.838	3	54.034	0.994	0.760	0.604
	93	6	52.881	0.997	0.868	0.781	3	54.034	0.994	0.760	0.604
	92	7	52.238	0.996	0.858	0.728	3	54.034	0.994	0.760	0.604
	90	8	51.398	0.995	0.851	0.682	3	54.034	0.994	0.760	0.604
	88	9	50.530	0.993	0.845	0.589	4	53.677	0.994	0.756	0.580
	86	9	49.916	0.992	0.839	0.554	5	53.245	0.994	0.751	0.548
	80	11	48.225	0.987	0.823	0.473	6	51.879	0.992	0.714	0.470
	60	17	45.424	0.986	0.814	0.356	10	48.970	0.986	0.670	0.353
	50	19	44.437	0.983	0.807	0.324	11	47.815	0.983	0.654	0.322
	30	27	41.998	0.974	0.790	0.260	20	45.152	0.974	0.627	0.258
	20	33	39.978	0.958	0.768	0.218	29	42.735	0.960	0.590	0.216
	10	56	36.383	0.937	0.736	0.159	45	38.754	0.927	0.513	0.157
	5	80	29.159	0.320	0.172	0.120	53	35.599	0.866	0.435	0.119
	1	116	29.108	0.796	0.124	0.099	60	33.052	0.816	0.392	0.097
CIPR-CT-02	100	1	61.719	1.000	0.977	2.391	0	Inf	1.000	1.000	2.037
	99	2	58.702	0.999	0.967	2.203	4	51.746	0.995	0.865	1.157
	98	3	55.219	0.998	0.956	1.920	4	51.746	0.995	0.865	1.157
	97	5	53.321	0.997	0.950	1.753	4	51.746	0.995	0.865	1.157
	96	6	51.829	0.996	0.945	1.594	4	51.746	0.995	0.865	1.157
	95	8	50.645	0.995	0.940	1.460	4	51.746	0.995	0.865	1.157
	94	9	49.837	0.994	0.937	1.351	4	51.746	0.995	0.865	1.157
	93	11	49.130	0.994	0.934	1.258	4	51.746	0.995	0.865	1.157
	92	11	48.499	0.993	0.930	1.174	4	51.735	0.995	0.865	1.156
	90	13	47.585	0.991	0.924	1.090	5	50.897	0.994	0.856	1.080
	88	14	46.792	0.990	0.918	0.960	5	49.680	0.991	0.835	0.953
	86	14	46.155	0.989	0.913	0.898	6	48.992	0.990	0.815	0.885
	80	17	44.565	0.984	0.894	0.747	7	47.418	0.986	0.788	0.740
	60	23	41.774	0.974	0.847	0.523	14	44.279	0.975	0.709	0.518
	50	26	40.925	0.969	0.828	0.465	18	43.389	0.972	0.696	0.463
	30	36	38.428	0.956	0.782	0.359	23	40.987	0.959	0.651	0.355
	20	42	36.447	0.940	0.749	0.292	28	39.105	0.945	0.604	0.290
	10	66	33.280	0.906	0.691	0.203	38	35.655	0.902	0.492	0.201
	5	91	28.153	0.485	0.229	0.144	55	32.026	0.826	0.360	0.141
	1	136	26.730	0.773	0.164	0.108	77	29.259	0.758	0.318	0.107

Table B.9 Comparison of compression performance of JPEG and JPEG2000 while tested with medical image datasets, CIPR-CT-03 and CIPR-CT-04

Datasets	Q	JPEG					JPEG2000				
		M-PAE	PSNR	MSSIM	UQI	BPP	M-PAE	PSNR	MSSIM	UQI	BPP
CIPR-CT-03	100	1	60.488	1.000	0.977	3.371	0	Inf	1.000	1.000	3.009
	99	2	56.783	0.999	0.966	3.161	4	50.526	0.994	0.859	1.885
	98	3	52.884	0.997	0.949	2.729	4	50.526	0.994	0.859	1.885
	97	4	50.617	0.995	0.935	2.455	4	50.526	0.994	0.859	1.885
	96	6	49.075	0.992	0.923	2.218	4	50.526	0.994	0.859	1.885
	95	7	47.814	0.990	0.910	2.011	4	50.521	0.994	0.859	1.885
	94	8	46.958	0.988	0.900	1.844	5	49.763	0.992	0.851	1.781
	93	9	46.206	0.986	0.889	1.704	5	49.010	0.991	0.840	1.656
	92	10	45.588	0.984	0.878	1.581	6	48.156	0.989	0.823	1.540
	90	12	44.662	0.981	0.862	1.450	6	47.243	0.986	0.806	1.415
	88	14	43.833	0.978	0.846	1.286	7	46.365	0.982	0.784	1.270
	86	15	43.230	0.976	0.832	1.193	8	45.798	0.980	0.766	1.183
	80	19	41.747	0.969	0.793	0.982	10	44.196	0.971	0.692	0.972
	60	29	38.799	0.953	0.692	0.667	17	41.426	0.954	0.567	0.662
	50	33	38.021	0.947	0.662	0.593	20	40.577	0.949	0.542	0.588
	30	42	35.806	0.929	0.617	0.461	28	38.340	0.933	0.505	0.457
	20	52	33.957	0.914	0.592	0.381	36	36.614	0.920	0.485	0.377
	10	76	31.032	0.882	0.544	0.270	56	33.392	0.881	0.438	0.267
	5	112	26.488	0.639	0.301	0.185	81	29.996	0.824	0.379	0.184
	1	153	24.670	0.755	0.241	0.129	115	26.791	0.749	0.324	0.127
CIPR-CT-04	100	1	61.732	1.000	0.980	2.084	0	Inf	1.000	1.000	1.774
	99	2	59.630	0.999	0.976	1.896	3	52.019	0.995	0.915	0.875
	98	3	56.545	0.999	0.969	1.641	3	52.019	0.995	0.915	0.875
	97	3	55.146	0.998	0.965	1.520	3	52.019	0.995	0.915	0.875
	96	4	53.907	0.998	0.961	1.393	3	52.019	0.995	0.915	0.875
	95	5	52.915	0.997	0.957	1.285	3	52.019	0.995	0.915	0.875
	94	6	52.221	0.996	0.954	1.187	3	52.019	0.995	0.915	0.875
	93	6	51.567	0.996	0.951	1.106	4	52.011	0.995	0.915	0.874
	92	7	50.929	0.995	0.948	1.033	4	51.989	0.995	0.915	0.872
	90	8	50.159	0.994	0.945	0.966	4	51.917	0.995	0.913	0.865
	88	10	49.343	0.993	0.941	0.852	4	51.590	0.995	0.911	0.831
	86	11	48.644	0.992	0.937	0.797	5	51.175	0.994	0.907	0.789
	80	13	46.787	0.988	0.921	0.663	6	49.399	0.991	0.887	0.651
	60	21	43.512	0.977	0.884	0.457	9	46.460	0.984	0.846	0.450
	50	24	42.244	0.972	0.866	0.401	10	45.531	0.981	0.829	0.395
	30	31	39.880	0.957	0.811	0.296	16	43.329	0.971	0.779	0.294
	20	37	37.880	0.938	0.752	0.235	20	41.361	0.957	0.715	0.229
	10	60	34.602	0.903	0.659	0.158	28	37.916	0.920	0.568	0.155
	5	76	28.985	0.465	0.189	0.118	45	34.823	0.871	0.430	0.117
	1	106	28.522	0.768	0.119	0.097	67	32.695	0.826	0.371	0.096

Table B.10 Comparison of compression performance of JPEG and JPEG2000 while tested with medical image datasets, CIPR-MR-01and CIPR- MR -02

Datasets	Q	JPEG					JPEG2000				
		M-PAE	PSNR	MSSIM	UQI	BPP	M-PAE	PSNR	MSSIM	UQI	BPP
CIPR-MR-01	100	1	59.064	0.999	0.982	3.408	0	Inf	1.000	1.000	3.039
	99	2	55.814	0.998	0.963	3.101	4	49.328	0.989	0.805	1.327
	98	3	52.649	0.996	0.928	2.604	4	49.328	0.989	0.805	1.327
	97	4	50.822	0.994	0.897	2.289	4	49.328	0.989	0.805	1.327
	96	5	49.497	0.992	0.868	2.014	4	49.328	0.989	0.805	1.327
	95	6	48.449	0.990	0.844	1.783	4	49.328	0.989	0.805	1.327
	94	7	47.759	0.988	0.824	1.593	4	49.328	0.989	0.805	1.327
	93	8	47.147	0.986	0.808	1.441	4	49.327	0.989	0.805	1.326
	92	8	46.630	0.985	0.790	1.307	5	49.143	0.989	0.802	1.294
	90	9	45.917	0.983	0.767	1.183	5	48.437	0.987	0.759	1.172
	88	10	45.272	0.980	0.743	1.012	6	47.413	0.984	0.717	0.998
	86	12	44.803	0.979	0.724	0.925	6	46.787	0.982	0.706	0.907
	80	15	43.566	0.973	0.672	0.732	8	45.530	0.977	0.662	0.725
	60	23	41.227	0.958	0.582	0.474	13	43.075	0.964	0.580	0.467
	50	26	40.360	0.942	0.558	0.414	14	42.366	0.958	0.546	0.409
	30	31	38.468	0.905	0.461	0.299	20	40.555	0.944	0.477	0.296
	20	38	36.812	0.869	0.376	0.232	24	38.980	0.927	0.411	0.230
	10	55	33.988	0.811	0.261	0.160	39	36.291	0.887	0.319	0.158
	5	91	30.390	0.666	0.167	0.116	57	33.517	0.829	0.243	0.115
	1	123	27.803	0.586	0.121	0.097	66	31.551	0.789	0.199	0.095
CIPR-MR-02	100	1	58.983	0.999	0.990	3.776	0	Inf	1.000	1.000	3.274
	99	2	55.657	0.998	0.980	3.455	4	49.121	0.992	0.900	1.579
	98	3	52.324	0.997	0.961	2.921	4	49.121	0.992	0.900	1.579
	97	4	50.544	0.995	0.948	2.598	4	49.121	0.992	0.900	1.579
	96	5	49.259	0.993	0.935	2.320	4	49.121	0.992	0.900	1.579
	95	6	48.222	0.992	0.924	2.092	4	49.121	0.992	0.900	1.579
	94	7	47.519	0.991	0.915	1.904	4	49.121	0.992	0.900	1.579
	93	8	46.904	0.990	0.907	1.752	4	49.121	0.992	0.900	1.579
	92	8	46.348	0.988	0.898	1.615	4	49.044	0.992	0.900	1.565
	90	10	45.559	0.987	0.886	1.487	5	48.519	0.991	0.890	1.478
	88	11	44.836	0.985	0.873	1.310	6	47.561	0.989	0.865	1.299
	86	13	44.275	0.983	0.861	1.213	6	47.060	0.988	0.854	1.203
	80	15	42.840	0.978	0.829	0.988	7	45.564	0.983	0.820	0.980
	60	22	40.134	0.961	0.752	0.673	13	42.836	0.973	0.762	0.663
	50	24	39.287	0.956	0.722	0.594	14	41.977	0.968	0.732	0.589
	30	31	37.149	0.931	0.644	0.440	20	39.851	0.957	0.681	0.437
	20	38	35.418	0.908	0.579	0.346	26	37.990	0.940	0.629	0.342
	10	56	32.081	0.815	0.468	0.232	38	34.935	0.906	0.564	0.228
	5	86	28.681	0.738	0.360	0.153	55	31.610	0.838	0.470	0.151
	1	115	25.664	0.620	0.262	0.111	80	29.098	0.776	0.400	0.110

Table B.11 Comparison of compression performance of JPEG and JPEG2000 while tested with medical image datasets, CIPR- MR -03 and CIPR- MR -04

Datasets	Q	JPEG					JPEG2000				
		M-PAE	PSNR	MSSIM	UQI	BPP	M-PAE	PSNR	MSSIM	UQI	BPP
CIPR-MR-03	100	1	61.473	1.000	0.978	2.895	0	Inf	1.000	1.000	2.590
	99	2	58.148	0.999	0.969	2.704	4	51.669	0.996	0.861	1.632
	98	3	54.563	0.999	0.960	2.405	4	51.669	0.996	0.861	1.632
	97	4	52.220	0.998	0.957	2.209	4	51.669	0.996	0.861	1.632
	96	6	50.524	0.997	0.954	2.036	4	51.669	0.996	0.861	1.632
	95	7	49.032	0.996	0.951	1.879	4	51.669	0.996	0.861	1.632
	94	8	48.045	0.994	0.948	1.748	4	51.669	0.996	0.861	1.632
	93	8	47.070	0.993	0.946	1.627	4	51.497	0.996	0.861	1.615
	92	9	46.295	0.992	0.943	1.526	5	50.621	0.995	0.855	1.517
	90	11	45.114	0.990	0.939	1.411	5	49.778	0.994	0.838	1.405
	88	12	44.103	0.987	0.935	1.253	7	47.871	0.991	0.806	1.241
	86	13	43.367	0.985	0.931	1.170	7	47.092	0.990	0.801	1.161
	80	17	41.629	0.979	0.920	0.974	10	44.997	0.984	0.771	0.965
	60	29	38.670	0.965	0.898	0.690	16	41.630	0.970	0.725	0.686
	50	35	37.752	0.959	0.889	0.616	18	40.655	0.964	0.712	0.612
	30	46	35.698	0.941	0.861	0.467	22	38.397	0.948	0.672	0.460
	20	56	34.073	0.921	0.829	0.372	29	36.736	0.927	0.623	0.369
	10	73	31.244	0.878	0.772	0.254	43	33.639	0.878	0.538	0.251
	5	110	27.091	0.474	0.335	0.168	76	30.255	0.799	0.477	0.165
	1	147	25.076	0.703	0.255	0.120	95	27.714	0.727	0.425	0.119
CIPR-MR-04	100	2	59.867	0.999	0.877	3.295	0	Inf	1.000	1.000	2.923
	99	2	56.157	0.998	0.813	2.991	4	50.405	0.990	0.572	1.587
	98	3	51.994	0.996	0.714	2.460	4	50.405	0.990	0.572	1.587
	97	5	49.425	0.993	0.669	2.152	4	50.405	0.990	0.572	1.587
	96	6	47.788	0.990	0.623	1.881	4	50.405	0.990	0.572	1.587
	95	8	46.517	0.988	0.596	1.662	4	50.405	0.990	0.572	1.587
	94	9	45.669	0.986	0.568	1.482	5	49.572	0.989	0.551	1.474
	93	11	44.957	0.984	0.551	1.341	6	48.597	0.987	0.532	1.334
	92	12	44.394	0.982	0.530	1.219	6	47.584	0.984	0.525	1.207
	90	14	43.558	0.980	0.518	1.102	7	46.703	0.982	0.517	1.087
	88	16	42.892	0.976	0.510	0.952	8	45.763	0.979	0.503	0.944
	86	18	42.375	0.974	0.502	0.876	10	45.165	0.977	0.493	0.870
	80	23	41.122	0.956	0.487	0.715	12	43.788	0.971	0.476	0.710
	60	34	39.239	0.958	0.451	0.483	18	41.286	0.958	0.445	0.480
	50	36	38.633	0.953	0.438	0.426	21	40.513	0.953	0.435	0.422
	30	43	37.183	0.938	0.406	0.318	29	38.718	0.937	0.409	0.313
	20	48	35.912	0.918	0.374	0.253	38	37.467	0.922	0.385	0.251
	10	62	33.473	0.882	0.302	0.169	53	35.124	0.881	0.334	0.167
	5	87	28.701	0.441	0.203	0.120	64	32.973	0.826	0.273	0.119
	1	117	27.341	0.712	0.137	0.098	72	31.259	0.767	0.233	0.096

Table B.12 Comparison of compression performance of JPEG and JPEG2000 while tested with medical image datasets, MGHD-MR-01 and MGHD -MR-02

Datasets	Q	JPEG					JPEG2000				
		M-PAE	PSNR	MSSIM	UQI	BPP	M-PAE	PSNR	MSSIM	UQI	BPP
MGH-MR-01	100	1	58.923	0.999	0.996	4.740	0	Inf	1.000	1.000	4.199
	99	2	54.796	0.998	0.989	4.456	4	48.766	0.992	0.946	2.652
	98	3	50.485	0.995	0.971	3.822	4	48.766	0.992	0.946	2.652
	97	5	47.925	0.992	0.951	3.400	4	48.766	0.992	0.946	2.652
	96	6	46.268	0.988	0.933	3.038	4	48.766	0.992	0.946	2.652
	95	8	44.925	0.984	0.914	2.727	4	48.766	0.992	0.946	2.652
	94	8	44.020	0.982	0.899	2.475	5	47.687	0.990	0.933	2.459
	93	9	43.236	0.979	0.886	2.266	6	46.663	0.987	0.907	2.246
	92	10	42.595	0.976	0.873	2.085	6	45.732	0.984	0.883	2.069
	90	12	41.617	0.972	0.854	1.890	7	44.688	0.980	0.858	1.865
	88	14	40.839	0.968	0.836	1.663	8	43.737	0.975	0.825	1.649
	86	16	40.224	0.964	0.822	1.527	9	43.046	0.972	0.805	1.516
	80	21	38.808	0.954	0.775	1.222	12	41.413	0.960	0.706	1.211
	60	31	36.392	0.931	0.671	0.795	21	38.562	0.939	0.633	0.789
	50	36	35.680	0.923	0.638	0.695	22	37.775	0.931	0.608	0.689
	30	46	34.036	0.898	0.576	0.508	30	35.814	0.910	0.567	0.502
	20	54	32.706	0.876	0.530	0.395	40	34.334	0.891	0.535	0.391
	10	70	29.947	0.761	0.449	0.262	63	31.936	0.849	0.476	0.259
	5	103	27.228	0.699	0.339	0.168	83	29.370	0.781	0.399	0.164
	1	135	24.623	0.592	0.248	0.120	98	27.288	0.715	0.331	0.118
MGH-MR-02	100	1	59.036	0.999	0.987	4.165	0	Inf	1.000	1.000	3.654
	99	2	55.296	0.998	0.969	3.846	4	48.894	0.990	0.828	1.961
	98	3	51.744	0.996	0.934	3.248	4	48.894	0.990	0.828	1.961
	97	4	49.721	0.994	0.906	2.880	4	48.894	0.990	0.828	1.961
	96	5	48.285	0.993	0.881	2.576	4	48.894	0.990	0.828	1.961
	95	7	47.063	0.991	0.860	2.321	4	48.894	0.990	0.828	1.961
	94	8	46.231	0.989	0.844	2.116	4	48.894	0.990	0.828	1.961
	93	9	45.469	0.988	0.831	1.947	5	48.648	0.990	0.818	1.922
	92	10	44.816	0.986	0.814	1.792	5	47.918	0.988	0.758	1.780
	90	12	43.810	0.984	0.794	1.639	6	47.244	0.986	0.724	1.630
	88	13	42.951	0.981	0.771	1.442	6	46.119	0.983	0.688	1.428
	86	15	42.274	0.979	0.750	1.327	7	45.404	0.981	0.674	1.318
	80	20	40.673	0.972	0.694	1.072	10	43.638	0.976	0.644	1.065
	60	28	37.819	0.949	0.611	0.729	18	40.419	0.962	0.605	0.723
	50	32	36.980	0.945	0.594	0.645	20	39.432	0.956	0.595	0.639
	30	46	34.979	0.904	0.562	0.484	27	37.166	0.937	0.562	0.478
	20	54	33.426	0.877	0.521	0.379	36	35.455	0.919	0.541	0.375
	10	71	30.706	0.775	0.449	0.250	55	32.698	0.874	0.487	0.248
	5	100	27.295	0.612	0.343	0.161	86	29.761	0.797	0.409	0.157
	1	140	24.975	0.695	0.239	0.115	103	27.721	0.732	0.340	0.114

Table B.13 Comparison of compression performance of JPEG and JPEG2000 while tested with medical image datasets, MGHD -MR-03 and MIDI-MR-01

Datasets	Q	JPEG					JPEG2000				
		M-PAE	PSNR	MSSIM	UQI	BPP	M-PAE	PSNR	MSSIM	UQI	BPP
MGH-MR-03	100	1	58.945	0.999	0.998	5.158	0	Inf	1.000	1.000	4.634
	99	2	54.721	0.999	0.995	4.903	4	49.046	0.994	0.976	3.204
	98	3	50.155	0.996	0.985	4.277	4	49.046	0.994	0.976	3.204
	97	5	47.330	0.992	0.972	3.847	4	49.046	0.994	0.976	3.204
	96	6	45.486	0.988	0.959	3.466	4	49.046	0.994	0.976	3.204
	95	8	43.983	0.983	0.944	3.134	4	48.603	0.993	0.975	3.118
	94	9	42.950	0.979	0.932	2.863	5	47.303	0.991	0.967	2.847
	93	10	42.048	0.975	0.920	2.627	7	45.757	0.987	0.949	2.602
	92	11	41.333	0.972	0.909	2.428	7	44.642	0.983	0.934	2.400
	90	14	40.218	0.965	0.890	2.197	8	43.633	0.979	0.916	2.173
	88	16	39.357	0.959	0.873	1.940	10	42.414	0.972	0.889	1.927
	86	17	38.672	0.954	0.859	1.781	11	41.544	0.966	0.854	1.766
	80	23	37.159	0.940	0.821	1.424	13	39.576	0.949	0.780	1.402
	60	35	34.676	0.909	0.726	0.913	22	36.775	0.916	0.667	0.903
	50	40	33.962	0.897	0.690	0.786	26	35.970	0.906	0.635	0.780
	30	51	32.385	0.863	0.613	0.559	35	34.118	0.880	0.587	0.555
	20	63	31.157	0.832	0.561	0.425	45	32.639	0.856	0.550	0.418
	10	81	28.893	0.763	0.470	0.269	72	30.340	0.805	0.487	0.266
	5	111	26.514	0.691	0.365	0.167	94	28.043	0.734	0.408	0.164
	1	139	23.869	0.438	0.242	0.114	112	26.084	0.659	0.329	0.113
MIDI-MR-01	100	1	59.268	0.999	0.992	3.296	0	Inf	1.000	1.000	2.942
	99	2	56.420	0.998	0.985	2.977	4	49.874	0.991	0.924	1.363
	98	3	53.088	0.996	0.969	2.523	4	49.874	0.991	0.924	1.363
	97	4	51.490	0.995	0.957	2.295	4	49.874	0.991	0.924	1.363
	96	5	50.258	0.993	0.945	2.073	4	49.874	0.991	0.924	1.363
	95	6	49.161	0.991	0.932	1.880	4	49.874	0.991	0.924	1.363
	94	7	48.365	0.989	0.921	1.701	4	49.874	0.991	0.924	1.363
	93	8	47.763	0.988	0.912	1.560	4	49.874	0.991	0.924	1.363
	92	8	47.114	0.986	0.899	1.429	4	49.790	0.991	0.923	1.350
	90	9	46.354	0.983	0.884	1.311	5	49.493	0.991	0.920	1.298
	88	10	45.633	0.980	0.867	1.139	6	48.396	0.988	0.891	1.135
	86	11	45.047	0.977	0.851	1.040	7	47.488	0.986	0.869	1.035
	80	14	43.597	0.969	0.800	0.812	8	45.611	0.978	0.818	0.804
	60	19	41.031	0.944	0.667	0.483	12	42.598	0.957	0.682	0.480
	50	21	40.284	0.936	0.614	0.402	14	41.833	0.950	0.633	0.399
	30	27	38.447	0.906	0.489	0.261	19	40.183	0.931	0.541	0.257
	20	34	37.000	0.881	0.395	0.186	24	39.138	0.915	0.459	0.184
	10	52	34.132	0.793	0.269	0.115	32	37.567	0.891	0.376	0.114
	5	79	30.310	0.703	0.163	0.080	46	36.313	0.870	0.322	0.079
	1	109	27.409	0.616	0.108	0.067	53	35.603	0.857	0.294	0.066

Table B.14 Comparison of compression performance of JPEG and JPEG2000 while tested with medical image datasets, MIDI-MR-02 and MIDI-MR-03

Datasets	Q	JPEG					JPEG2000				
		M-PAE	PSNR	MSSIM	UQI	BPP	M-PAE	PSNR	MSSIM	UQI	BPP
MIDI-MR-02	100	1	60.262	0.999	0.989	3.089	0	Inf	1.000	1.000	2.720
	99	2	57.029	0.999	0.982	2.837	4	50.933	0.994	0.932	1.490
	98	3	53.416	0.997	0.972	2.440	4	50.933	0.994	0.932	1.490
	97	5	51.486	0.996	0.964	2.211	4	50.933	0.994	0.932	1.490
	96	6	50.118	0.994	0.958	2.009	4	50.933	0.994	0.932	1.490
	95	7	48.896	0.993	0.950	1.837	4	50.933	0.994	0.932	1.490
	94	8	47.992	0.991	0.945	1.679	4	50.933	0.994	0.932	1.490
	93	9	47.279	0.989	0.939	1.554	4	50.933	0.994	0.932	1.490
	92	10	46.607	0.988	0.933	1.441	5	50.484	0.994	0.928	1.436
	90	11	45.687	0.985	0.924	1.330	6	49.712	0.993	0.922	1.326
	88	13	44.891	0.983	0.915	1.171	8	48.420	0.990	0.899	1.168
	86	14	44.228	0.980	0.906	1.084	9	47.475	0.988	0.882	1.080
	80	18	42.688	0.973	0.879	0.880	10	45.627	0.982	0.854	0.876
	60	23	40.047	0.952	0.808	0.573	16	42.028	0.961	0.747	0.569
	50	26	39.215	0.943	0.779	0.493	17	41.167	0.954	0.726	0.490
	30	33	37.295	0.918	0.697	0.337	22	39.199	0.932	0.638	0.335
	20	38	35.784	0.895	0.629	0.249	27	37.870	0.914	0.576	0.247
	10	58	32.862	0.817	0.549	0.155	40	35.911	0.883	0.488	0.153
	5	87	28.841	0.554	0.235	0.100	56	33.954	0.849	0.430	0.099
	1	132	26.872	0.674	0.151	0.073	64	32.500	0.814	0.357	0.072
MIDI-MR-03	100	1	60.021	1.000	0.993	3.810	0	Inf	1.000	1.000	3.413
	99	2	56.247	0.999	0.989	3.545	4	50.444	0.996	0.949	2.166
	98	3	52.339	0.998	0.983	3.084	4	50.444	0.996	0.949	2.166
	97	5	50.031	0.996	0.979	2.807	4	50.444	0.996	0.949	2.166
	96	6	48.405	0.995	0.975	2.563	4	50.444	0.996	0.949	2.166
	95	8	47.011	0.993	0.971	2.355	4	50.444	0.996	0.949	2.166
	94	9	46.011	0.991	0.967	2.181	4	50.408	0.996	0.949	2.161
	93	10	45.137	0.989	0.963	2.029	5	49.469	0.995	0.946	2.021
	92	11	44.397	0.987	0.960	1.894	5	48.746	0.994	0.942	1.891
	90	13	43.249	0.984	0.953	1.748	7	47.644	0.993	0.933	1.746
	88	15	42.326	0.980	0.946	1.562	9	46.065	0.989	0.918	1.559
	86	16	41.549	0.977	0.939	1.451	9	45.274	0.987	0.911	1.447
	80	20	39.833	0.967	0.921	1.201	12	43.358	0.981	0.889	1.200
	60	27	37.012	0.940	0.875	0.815	20	39.630	0.956	0.810	0.812
	50	32	36.178	0.929	0.855	0.709	21	38.514	0.943	0.764	0.706
	30	38	34.267	0.896	0.791	0.497	29	35.969	0.908	0.697	0.494
	20	45	32.780	0.861	0.722	0.362	34	34.476	0.879	0.643	0.360
	10	66	30.336	0.794	0.622	0.210	48	32.215	0.821	0.551	0.207
	5	100	27.200	0.530	0.301	0.122	70	30.322	0.763	0.465	0.121
	1	142	24.975	0.530	0.200	0.081	85	28.806	0.718	0.408	0.080

Table B.15 Comparison of compression performance of JPEG and JPEG2000 while tested with medical image datasets, MIDI-MR-04 and MIDI-MR-05

Datasets	Q	JPEG					JPEG2000				
		M-PAE	PSNR	MSSIM	UQI	BPP	M-PAE	PSNR	MSSIM	UQI	BPP
MIDI-MR-04	100	1	59.018	0.999	0.999	4.124	0	Inf	1.000	1.000	3.688
	99	2	55.781	0.999	0.997	3.783	4	49.284	0.994	0.985	2.066
	98	3	52.291	0.997	0.993	3.244	4	49.284	0.994	0.985	2.066
	97	4	50.453	0.996	0.989	2.947	4	49.284	0.994	0.985	2.066
	96	6	49.090	0.994	0.985	2.682	4	49.284	0.994	0.985	2.066
	95	6	47.942	0.992	0.981	2.456	4	49.284	0.994	0.985	2.066
	94	7	47.165	0.991	0.977	2.265	4	49.284	0.994	0.985	2.066
	93	8	46.491	0.989	0.974	2.101	4	49.282	0.994	0.985	2.065
	92	9	45.896	0.987	0.970	1.955	6	48.606	0.993	0.983	1.949
	90	10	45.027	0.985	0.964	1.807	6	47.857	0.992	0.981	1.804
	88	11	44.259	0.982	0.957	1.613	8	46.541	0.990	0.974	1.609
	86	12	43.667	0.979	0.951	1.501	9	45.655	0.987	0.966	1.494
	80	14	42.114	0.971	0.932	1.241	10	44.006	0.981	0.951	1.236
	60	20	39.152	0.946	0.875	0.838	15	40.842	0.961	0.901	0.831
	50	22	38.170	0.934	0.847	0.725	16	39.928	0.951	0.873	0.720
	30	28	35.817	0.894	0.755	0.497	22	37.827	0.924	0.794	0.494
	20	36	33.992	0.851	0.644	0.353	26	35.998	0.888	0.695	0.349
	10	55	31.126	0.764	0.443	0.196	36	33.374	0.816	0.507	0.193
	5	82	28.403	0.684	0.297	0.114	47	31.369	0.756	0.395	0.112
	1	126	25.168	0.411	0.193	0.079	63	30.018	0.719	0.331	0.078
MIDI-MR-05	100	1	59.075	0.999	0.995	4.073	0	Inf	1.000	1.000	3.637
	99	2	55.476	0.998	0.989	3.756	4	49.176	0.992	0.953	2.040
	98	3	51.729	0.996	0.977	3.217	4	49.176	0.992	0.953	2.040
	97	4	49.631	0.993	0.965	2.894	4	49.176	0.992	0.953	2.040
	96	6	48.176	0.991	0.953	2.605	4	49.176	0.992	0.953	2.040
	95	6	46.936	0.988	0.941	2.363	4	49.176	0.992	0.953	2.040
	94	7	46.047	0.985	0.930	2.152	4	49.176	0.992	0.953	2.040
	93	8	45.331	0.983	0.919	1.983	5	48.779	0.991	0.949	1.975
	92	9	44.709	0.980	0.908	1.833	6	48.033	0.990	0.943	1.829
	90	11	43.794	0.976	0.892	1.676	7	47.210	0.988	0.933	1.673
	88	11	43.046	0.973	0.876	1.479	8	45.881	0.983	0.905	1.472
	86	13	42.422	0.969	0.862	1.361	9	45.165	0.980	0.888	1.356
	80	16	40.984	0.959	0.821	1.090	10	43.542	0.973	0.857	1.087
	60	24	38.446	0.933	0.712	0.687	14	40.404	0.944	0.682	0.684
	50	27	37.662	0.923	0.664	0.585	16	39.645	0.937	0.653	0.583
	30	36	35.762	0.890	0.542	0.398	21	37.871	0.913	0.528	0.396
	20	42	34.272	0.859	0.479	0.299	25	36.594	0.897	0.493	0.297
	10	61	31.678	0.802	0.383	0.183	42	34.594	0.869	0.439	0.182
	5	96	28.775	0.731	0.286	0.114	60	32.661	0.834	0.386	0.114
	1	141	25.860	0.510	0.197	0.079	79	31.117	0.801	0.343	0.079

Table B.16 Comparison of compression performance of JPEG and JPEG2000 while tested with medical image datasets, MIDI-MR-06 and MIDI-MR-07

Datasets	Q	JPEG					JPEG2000				
		M-PAE	PSNR	MSSIM	UQI	BPP	M-PAE	PSNR	MSSIM	UQI	BPP
MIDI-MR-06	100	1	60.224	1.000	0.989	3.088	0	Inf	1.000	1.000	2.721
	99	2	57.082	0.999	0.982	2.830	4	50.954	0.995	0.934	1.486
	98	3	53.574	0.997	0.974	2.439	4	50.954	0.995	0.934	1.486
	97	4	51.671	0.996	0.967	2.222	4	50.954	0.995	0.934	1.486
	96	6	50.270	0.995	0.961	2.022	4	50.954	0.995	0.934	1.486
	95	7	49.026	0.993	0.954	1.852	4	50.954	0.995	0.934	1.486
	94	8	48.094	0.992	0.948	1.697	4	50.954	0.995	0.934	1.486
	93	9	47.366	0.990	0.943	1.572	4	50.954	0.995	0.934	1.486
	92	10	46.674	0.989	0.937	1.458	5	50.667	0.994	0.933	1.452
	90	11	45.736	0.986	0.928	1.345	6	49.856	0.994	0.928	1.341
	88	12	44.926	0.984	0.919	1.186	8	48.541	0.991	0.909	1.183
	86	13	44.258	0.981	0.910	1.099	8	47.581	0.989	0.893	1.095
	80	15	42.702	0.974	0.885	0.897	10	45.746	0.984	0.864	0.895
	60	21	40.011	0.955	0.815	0.588	16	42.128	0.963	0.753	0.584
	50	24	39.157	0.947	0.785	0.508	17	41.246	0.957	0.732	0.504
	30	30	37.144	0.921	0.705	0.351	23	39.244	0.936	0.636	0.349
	20	38	35.577	0.897	0.639	0.261	26	37.849	0.918	0.581	0.260
	10	59	32.633	0.835	0.547	0.160	39	35.543	0.885	0.489	0.157
	5	89	28.766	0.581	0.238	0.102	58	33.508	0.845	0.409	0.101
	1	127	26.601	0.645	0.156	0.073	69	31.935	0.814	0.357	0.072
MIDI-MR-07	100	1	59.233	0.999	0.991	3.285	0	Inf	1.000	1.000	2.929
	99	2	56.564	0.998	0.984	2.967	4	49.934	0.992	0.921	1.348
	98	3	53.289	0.997	0.969	2.533	4	49.934	0.992	0.921	1.348
	97	4	51.714	0.995	0.957	2.313	4	49.934	0.992	0.921	1.348
	96	5	50.468	0.994	0.945	2.091	4	49.934	0.992	0.921	1.348
	95	5	49.380	0.992	0.933	1.900	4	49.934	0.992	0.921	1.348
	94	6	48.583	0.991	0.922	1.724	4	49.934	0.992	0.921	1.348
	93	7	47.972	0.989	0.913	1.587	4	49.934	0.992	0.921	1.348
	92	8	47.319	0.988	0.901	1.456	4	49.933	0.992	0.921	1.347
	90	8	46.545	0.985	0.887	1.340	5	49.740	0.992	0.920	1.317
	88	9	45.816	0.983	0.871	1.169	6	48.744	0.990	0.895	1.166
	86	11	45.221	0.981	0.855	1.072	7	47.941	0.988	0.873	1.069
	80	13	43.734	0.973	0.806	0.846	8	46.032	0.981	0.817	0.841
	60	19	41.060	0.953	0.679	0.520	11	43.068	0.965	0.685	0.518
	50	21	40.229	0.945	0.633	0.442	12	42.208	0.958	0.637	0.438
	30	26	38.242	0.921	0.514	0.298	17	40.375	0.943	0.550	0.296
	20	35	36.628	0.900	0.430	0.220	22	39.033	0.928	0.481	0.217
	10	53	33.408	0.806	0.317	0.135	37	36.906	0.902	0.404	0.134
	5	85	29.845	0.733	0.205	0.088	55	34.995	0.872	0.339	0.087
	1	117	27.104	0.674	0.119	0.068	68	33.822	0.851	0.303	0.067

Table B.17 Comparison of compression performance of JPEG and JPEG2000 while tested with medical image datasets, OSRX-CT-01and OSRX-PT-01

Datasets	Q	JPEG					JPEG2000				
		M-PAE	PSNR	MSSIM	UQI	BPP	M-PAE	PSNR	MSSIM	UQI	BPP
OSRX-CT-01	100	1	62.868	1.000	0.975	2.579	0	Inf	1.000	1.000	2.169
	99	2	58.644	1.000	0.965	2.479	4	53.633	0.997	0.861	1.675
	98	4	53.942	0.999	0.957	2.213	4	53.633	0.997	0.861	1.675
	97	5	51.013	0.998	0.954	2.013	4	53.633	0.997	0.861	1.675
	96	7	49.110	0.996	0.952	1.840	4	53.633	0.997	0.861	1.675
	95	9	47.548	0.995	0.950	1.690	4	53.631	0.997	0.861	1.675
	94	10	46.461	0.994	0.949	1.566	4	52.277	0.996	0.848	1.561
	93	12	45.503	0.992	0.947	1.456	6	51.091	0.996	0.839	1.454
	92	14	44.745	0.991	0.946	1.367	7	49.688	0.994	0.819	1.363
	90	17	43.563	0.988	0.943	1.258	8	48.263	0.992	0.813	1.254
	88	20	42.657	0.986	0.941	1.114	10	46.685	0.990	0.803	1.111
	86	23	41.931	0.984	0.938	1.036	11	45.768	0.987	0.785	1.033
	80	30	40.354	0.978	0.932	0.866	16	43.391	0.980	0.748	0.861
	60	49	37.754	0.963	0.917	0.612	23	40.417	0.964	0.722	0.610
	50	57	36.969	0.957	0.910	0.544	26	39.472	0.957	0.711	0.542
	30	76	35.194	0.939	0.891	0.404	35	37.341	0.937	0.681	0.401
	20	89	33.770	0.919	0.867	0.313	46	35.924	0.909	0.533	0.311
	10	108	31.293	0.879	0.816	0.200	66	33.567	0.865	0.431	0.197
	5	148	27.135	0.341	0.237	0.126	99	31.370	0.806	0.352	0.125
	1	198	25.691	0.695	0.187	0.087	122	29.527	0.766	0.322	0.087
OSRX-PT-01	100	2	66.134	1.000	0.989	1.052	0	Inf	1.000	1.000	0.806
	99	2	63.826	1.000	0.987	0.980	3	57.263	0.999	0.914	0.402
	98	2	60.482	1.000	0.982	0.867	3	57.263	0.999	0.914	0.402
	97	3	58.833	1.000	0.979	0.807	3	57.263	0.999	0.914	0.402
	96	4	57.427	1.000	0.976	0.751	3	57.263	0.999	0.914	0.402
	95	4	56.324	0.999	0.975	0.704	3	57.263	0.999	0.914	0.402
	94	5	55.533	0.999	0.974	0.664	3	57.263	0.999	0.914	0.402
	93	6	54.844	0.999	0.974	0.627	3	57.263	0.999	0.914	0.402
	92	6	54.209	0.999	0.973	0.596	3	57.263	0.999	0.914	0.402
	90	7	53.304	0.999	0.973	0.566	3	57.259	0.999	0.914	0.402
	88	8	52.450	0.999	0.973	0.486	3	57.211	0.999	0.914	0.399
	86	8	51.815	0.998	0.972	0.463	3	57.175	0.999	0.914	0.398
	80	10	50.069	0.998	0.970	0.403	3	57.012	0.999	0.912	0.391
	60	15	46.723	0.995	0.971	0.309	6	54.359	0.997	0.884	0.305
	50	17	45.599	0.994	0.971	0.283	7	53.217	0.996	0.879	0.280
	30	23	42.913	0.989	0.969	0.229	11	49.734	0.992	0.838	0.224
	20	29	40.701	0.982	0.960	0.192	15	47.228	0.986	0.791	0.190
	10	46	36.910	0.966	0.951	0.139	23	42.223	0.952	0.509	0.136
	5	68	28.847	0.238	0.165	0.100	37	38.433	0.926	0.459	0.098
	1	102	29.640	0.791	0.112	0.079	54	36.176	0.883	0.382	0.078

Table B.18 Comparison of compression performance of JPEG and JPEG2000 while tested with medical image datasets, OSRX-CT-02 and OSRX-MR-01

Datasets	Q	JPEG					JPEG2000				
		M-PAE	PSNR	MSSIM	UQI	BPP	M-PAE	PSNR	MSSIM	UQI	BPP
OSRX-CT-02	100	2	61.691	1.000	0.967	2.222	0	Inf	1.000	1.000	1.799
	99	2	59.268	0.999	0.954	2.019	4	52.363	0.996	0.818	0.890
	98	3	56.199	0.999	0.942	1.722	4	52.363	0.996	0.818	0.890
	97	5	54.603	0.998	0.938	1.579	4	52.363	0.996	0.818	0.890
	96	7	53.330	0.998	0.935	1.449	4	52.363	0.996	0.818	0.890
	95	9	52.320	0.997	0.933	1.346	4	52.363	0.996	0.818	0.890
	94	10	51.553	0.997	0.932	1.251	4	52.363	0.996	0.818	0.890
	93	12	50.897	0.996	0.931	1.168	4	52.363	0.996	0.818	0.890
	92	13	50.251	0.996	0.930	1.091	4	52.363	0.996	0.818	0.890
	90	14	49.399	0.995	0.929	1.023	4	52.363	0.996	0.818	0.890
	88	15	48.604	0.994	0.928	0.900	4	52.278	0.995	0.817	0.881
	86	16	47.980	0.994	0.926	0.845	5	51.862	0.995	0.813	0.842
	80	19	46.372	0.991	0.921	0.712	7	50.507	0.993	0.781	0.710
	60	24	43.343	0.983	0.909	0.511	13	47.339	0.985	0.722	0.509
	50	27	42.331	0.979	0.902	0.456	16	46.132	0.981	0.696	0.454
	30	39	39.845	0.965	0.877	0.344	22	43.475	0.969	0.660	0.342
	20	48	37.767	0.947	0.838	0.271	28	41.405	0.955	0.624	0.269
	10	75	34.181	0.909	0.761	0.177	40	38.281	0.925	0.555	0.176
	5	100	28.724	0.479	0.290	0.117	57	35.223	0.878	0.480	0.116
	1	160	26.633	0.748	0.216	0.084	78	32.725	0.834	0.425	0.083
OSRX-MR-01	100	2	63.173	1.000	0.987	2.137	0	Inf	1.000	1.000	1.824
	99	2	59.534	1.000	0.982	1.995	4	53.148	0.998	0.922	1.197
	98	3	55.817	0.999	0.977	1.757	4	53.148	0.998	0.922	1.197
	97	5	53.629	0.999	0.975	1.613	4	53.148	0.998	0.922	1.197
	96	6	52.070	0.998	0.973	1.491	4	53.148	0.998	0.922	1.197
	95	7	50.692	0.998	0.971	1.383	4	53.148	0.998	0.922	1.197
	94	8	49.738	0.997	0.970	1.291	4	53.148	0.998	0.922	1.197
	93	9	48.896	0.996	0.969	1.213	4	52.965	0.998	0.920	1.182
	92	10	48.198	0.996	0.968	1.145	5	52.439	0.997	0.915	1.134
	90	12	47.046	0.995	0.967	1.069	6	51.664	0.997	0.909	1.065
	88	13	46.137	0.994	0.966	0.949	7	49.945	0.995	0.883	0.946
	86	14	45.360	0.993	0.964	0.891	8	49.025	0.994	0.879	0.887
	80	18	43.581	0.989	0.959	0.756	10	47.075	0.991	0.860	0.754
	60	26	40.482	0.980	0.950	0.543	17	43.481	0.980	0.797	0.541
	50	30	39.525	0.976	0.945	0.486	20	42.518	0.976	0.786	0.484
	30	39	37.361	0.963	0.930	0.366	25	40.174	0.964	0.754	0.364
	20	48	35.641	0.948	0.910	0.289	32	38.473	0.952	0.724	0.288
	10	70	32.710	0.919	0.877	0.192	49	35.850	0.920	0.542	0.190
	5	108	27.601	0.346	0.255	0.124	69	33.489	0.877	0.451	0.123
	1	159	26.393	0.749	0.193	0.086	90	31.468	0.832	0.378	0.086

Table B.19 Comparison of compression performance of JPEG and JPEG2000 while tested with medical image datasets, OSRX-MR-02 and OSRX-MR-03

Datasets	Q	JPEG					JPEG2000				
		M-PAE	PSNR	MSSIM	UQI	BPP	M-PAE	PSNR	MSSIM	UQI	BPP
OSRX-MR-02	100	1	58.853	1.000	0.998	5.359	0	Inf	1.000	1.000	5.033
	99	2	54.611	0.999	0.995	5.117	4	49.462	0.995	0.981	3.677
	98	4	49.837	0.996	0.986	4.556	4	49.462	0.995	0.981	3.677
	97	5	46.722	0.991	0.973	4.146	4	49.462	0.995	0.981	3.677
	96	7	44.618	0.986	0.958	3.758	4	49.342	0.995	0.981	3.657
	95	8	42.935	0.980	0.941	3.414	4	48.067	0.994	0.978	3.403
	94	10	41.730	0.974	0.926	3.115	6	46.526	0.991	0.962	3.104
	93	12	40.691	0.967	0.909	2.855	7	44.871	0.986	0.943	2.838
	92	13	39.887	0.961	0.895	2.633	8	43.800	0.982	0.929	2.617
	90	15	38.649	0.949	0.869	2.362	9	42.518	0.977	0.912	2.350
	88	18	37.731	0.938	0.845	2.071	12	40.859	0.965	0.864	2.059
	86	20	37.023	0.928	0.823	1.882	13	39.864	0.955	0.830	1.872
	80	24	35.580	0.903	0.769	1.470	17	37.858	0.931	0.762	1.455
	60	36	33.460	0.854	0.658	0.899	26	34.921	0.869	0.615	0.888
	50	40	32.884	0.837	0.621	0.763	29	34.190	0.852	0.583	0.752
	30	49	31.622	0.796	0.531	0.510	38	32.697	0.808	0.506	0.506
	20	57	30.620	0.759	0.461	0.366	48	31.577	0.770	0.443	0.362
	10	80	28.784	0.692	0.358	0.212	69	29.896	0.718	0.372	0.208
	5	107	26.404	0.605	0.253	0.128	95	28.299	0.659	0.293	0.126
	1	147	24.115	0.521	0.146	0.092	123	27.196	0.620	0.237	0.091
OSRX-MR-03	100	1	59.067	0.999	0.988	4.844	0	Inf	1.000	1.000	3.981
	99	2	55.015	0.999	0.980	4.565	3	50.638	0.997	0.946	2.893
	98	4	50.523	0.996	0.962	3.972	3	50.638	0.997	0.946	2.893
	97	5	47.728	0.993	0.946	3.580	3	50.638	0.997	0.946	2.893
	96	7	45.830	0.990	0.929	3.228	3	50.638	0.997	0.946	2.893
	95	8	44.308	0.986	0.911	2.932	3	50.630	0.997	0.946	2.892
	94	10	43.210	0.983	0.896	2.678	4	49.173	0.995	0.922	2.670
	93	11	42.248	0.979	0.881	2.467	5	47.960	0.994	0.905	2.461
	92	12	41.470	0.976	0.868	2.281	6	46.568	0.991	0.883	2.275
	90	14	40.249	0.970	0.847	2.072	7	45.166	0.988	0.856	2.065
	88	17	39.298	0.964	0.826	1.830	10	43.544	0.983	0.804	1.824
	86	19	38.535	0.959	0.807	1.679	12	42.516	0.978	0.762	1.675
	80	24	36.906	0.945	0.757	1.346	14	40.106	0.963	0.698	1.341
	60	34	34.438	0.912	0.651	0.860	25	36.721	0.932	0.616	0.857
	50	39	33.784	0.901	0.620	0.740	29	35.729	0.919	0.596	0.736
	30	49	32.352	0.871	0.558	0.519	36	33.982	0.893	0.558	0.516
	20	58	31.218	0.842	0.513	0.385	45	32.693	0.865	0.522	0.381
	10	77	29.107	0.779	0.441	0.232	58	30.967	0.823	0.470	0.230
	5	114	26.538	0.687	0.355	0.139	88	29.312	0.779	0.420	0.137
	1	150	23.494	0.418	0.237	0.092	110	27.879	0.735	0.366	0.091

Table B.20 Comparison of compression performance of JPEG and JPEG2000 while tested with medical image datasets, OSRX-MR-04 and OSRX-XA-01

Datasets	Q	JPEG					JPEG2000				
		M-PAE	PSNR	MSSIM	UQI	BPP	M-PAE	PSNR	MSSIM	UQI	BPP
OSRX-MR-04	100	1	59.056	0.999	0.984	4.518	0	Inf	1.000	1.000	3.794
	99	2	54.918	0.998	0.971	4.229	4	50.090	0.994	0.918	2.477
	98	3	50.599	0.995	0.941	3.596	4	50.090	0.994	0.918	2.477
	97	5	48.093	0.992	0.913	3.176	4	50.090	0.994	0.918	2.477
	96	6	46.463	0.989	0.888	2.827	4	50.090	0.994	0.918	2.477
	95	7	45.165	0.987	0.865	2.539	4	50.090	0.994	0.918	2.477
	94	9	44.263	0.984	0.848	2.304	5	48.851	0.991	0.869	2.296
	93	10	43.493	0.982	0.833	2.111	6	47.746	0.989	0.830	2.105
	92	11	42.853	0.980	0.818	1.942	7	46.678	0.987	0.801	1.935
	90	13	41.883	0.976	0.799	1.762	7	45.530	0.984	0.769	1.755
	88	14	41.120	0.973	0.780	1.549	8	44.329	0.980	0.739	1.539
	86	16	40.507	0.969	0.763	1.421	9	43.609	0.977	0.710	1.415
	80	20	39.131	0.960	0.714	1.138	13	41.731	0.968	0.646	1.131
	60	28	36.813	0.941	0.620	0.748	20	38.866	0.950	0.602	0.744
	50	32	36.101	0.932	0.598	0.654	23	38.079	0.943	0.591	0.651
	30	40	34.441	0.907	0.558	0.476	29	36.299	0.924	0.561	0.471
	20	50	33.075	0.878	0.528	0.367	38	35.046	0.910	0.543	0.364
	10	65	30.577	0.812	0.468	0.233	53	33.009	0.877	0.507	0.231
	5	95	27.634	0.689	0.379	0.146	74	31.006	0.832	0.463	0.144
	1	128	24.816	0.567	0.269	0.098	91	29.221	0.779	0.411	0.097
OSRX-XA-01	100	1	60.563	0.999	0.984	2.655	0	Inf	1.000	1.000	2.178
	99	2	56.335	0.998	0.970	2.477	4	50.280	0.992	0.881	1.185
	98	4	51.889	0.995	0.945	2.065	4	50.280	0.992	0.881	1.185
	97	5	49.746	0.991	0.921	1.742	4	50.280	0.992	0.881	1.185
	96	6	48.601	0.989	0.902	1.492	4	50.280	0.992	0.881	1.185
	95	7	47.813	0.987	0.887	1.299	4	50.280	0.992	0.881	1.185
	94	9	47.326	0.985	0.877	1.155	5	50.043	0.992	0.873	1.152
	93	11	46.925	0.984	0.869	1.041	6	49.204	0.990	0.841	1.037
	92	12	46.577	0.983	0.860	0.942	6	48.520	0.988	0.820	0.937
	90	15	46.094	0.981	0.850	0.853	7	47.967	0.986	0.798	0.848
	88	17	45.637	0.979	0.839	0.720	7	47.144	0.983	0.779	0.717
	86	19	45.271	0.978	0.830	0.656	7	46.728	0.982	0.772	0.649
	80	29	44.252	0.974	0.805	0.510	9	45.845	0.978	0.751	0.506
	60	50	42.168	0.964	0.758	0.315	13	44.453	0.970	0.683	0.313
	50	60	41.410	0.960	0.743	0.272	15	44.018	0.967	0.669	0.271
	30	85	39.618	0.948	0.697	0.191	18	42.932	0.959	0.623	0.190
	20	102	38.100	0.933	0.647	0.145	21	41.991	0.951	0.580	0.144
	10	116	35.440	0.900	0.557	0.098	35	40.398	0.934	0.498	0.098
	5	215	30.311	0.585	0.153	0.074	57	39.020	0.922	0.453	0.073
	1	243	28.351	0.717	0.092	0.065	59	38.437	0.916	0.431	0.065

Table B.21 Comparison of compression performance of JPEG and JPEG2000 while tested with medical image datasets, OSRX-XA-02 and PHNT-MR-01

Datasets	Q	JPEG					JPEG2000				
		M-PAE	PSNR	MSSIM	UQI	BPP	M-PAE	PSNR	MSSIM	UQI	BPP
OSRX-XA-02	100	1	60.544	0.999	0.985	2.899	0	Inf	1.000	1.000	2.257
	99	2	56.383	0.998	0.976	2.716	4	50.552	0.993	0.897	1.401
	98	4	51.948	0.995	0.960	2.292	4	50.552	0.993	0.897	1.401
	97	5	49.698	0.992	0.947	1.974	4	50.552	0.993	0.897	1.401
	96	6	48.443	0.989	0.937	1.724	4	50.552	0.993	0.897	1.401
	95	8	47.530	0.987	0.929	1.521	4	50.552	0.993	0.897	1.401
	94	10	46.928	0.985	0.923	1.368	5	50.262	0.992	0.890	1.365
	93	12	46.407	0.984	0.918	1.241	6	49.239	0.990	0.873	1.237
	92	14	45.937	0.982	0.913	1.141	6	48.503	0.988	0.863	1.136
	90	17	45.225	0.980	0.906	1.043	7	47.831	0.986	0.855	1.040
	88	20	44.575	0.977	0.899	0.897	7	46.886	0.983	0.843	0.894
	86	24	44.021	0.975	0.893	0.825	8	46.421	0.982	0.837	0.820
	80	33	42.582	0.970	0.875	0.655	9	45.395	0.977	0.811	0.651
	60	70	39.708	0.956	0.831	0.415	12	43.563	0.965	0.735	0.414
	50	74	38.894	0.951	0.813	0.358	13	42.874	0.960	0.717	0.355
	30	117	37.023	0.936	0.761	0.254	23	41.386	0.947	0.650	0.252
	20	124	35.627	0.920	0.706	0.191	35	39.926	0.934	0.597	0.189
	10	146	33.189	0.879	0.587	0.122	56	37.512	0.908	0.500	0.120
	5	221	29.060	0.567	0.185	0.085	84	35.558	0.884	0.434	0.084
	1	229	27.470	0.752	0.112	0.070	99	34.624	0.871	0.409	0.070
PHNT-MR-01	100	2	59.073	0.999	0.992	3.764	0	Inf	1.000	1.000	3.302
	99	2	55.183	0.998	0.987	3.455	4	49.148	0.992	0.952	1.683
	98	3	51.820	0.996	0.978	2.849	4	49.148	0.992	0.952	1.683
	97	5	50.174	0.994	0.972	2.524	4	49.148	0.992	0.952	1.683
	96	6	49.028	0.992	0.966	2.269	4	49.148	0.992	0.952	1.683
	95	7	48.052	0.990	0.961	2.059	4	49.148	0.992	0.952	1.683
	94	8	47.402	0.989	0.956	1.876	4	49.148	0.992	0.952	1.683
	93	10	46.839	0.987	0.952	1.725	4	49.147	0.992	0.952	1.683
	92	10	46.307	0.986	0.947	1.593	6	48.621	0.991	0.948	1.588
	90	12	45.590	0.984	0.940	1.469	6	47.999	0.990	0.943	1.465
	88	13	44.916	0.981	0.933	1.295	7	46.913	0.987	0.933	1.292
	86	15	44.376	0.979	0.926	1.198	8	46.186	0.984	0.926	1.193
	80	18	42.940	0.971	0.902	0.973	9	44.669	0.978	0.902	0.967
	60	25	40.167	0.946	0.835	0.621	16	41.739	0.958	0.840	0.615
	50	27	39.251	0.934	0.802	0.527	17	40.847	0.948	0.804	0.522
	30	32	37.117	0.897	0.687	0.341	24	38.687	0.919	0.690	0.339
	20	40	35.487	0.859	0.557	0.234	28	37.060	0.887	0.582	0.230
	10	58	32.810	0.784	0.343	0.125	45	34.774	0.832	0.403	0.122
	5	90	29.785	0.681	0.163	0.081	58	33.402	0.795	0.299	0.080
	1	128	26.127	0.364	0.105	0.068	64	32.835	0.780	0.261	0.067

Appendix - C : RoI Compression

Table C.1 Bit rates (bpp) obtained for image datasets CIPR-CT-01, CIPR-CT-02, CIPR-CT-03 and CIPR-CT-04. Bit rates obtained with the proposed non-resolution scalable image compression method DLD-RoI and resolution scalable image compression method RDLD-RoI with 5%, 10% and 25% area of the image marked as RoI are showed. R0 is original resolution of the image, R1 is the image resolution after first sub sampling, R2 is the image resolution after second resembling.

Datasets	B.G. PAE	DLD-RoI			RDLD-RoI								
		5%-RoI	10%-RoI	25%-RoI	5%-RoI			10%-RoI			25%-RoI		
					R0	R1	R2	R0	R1	R2	R0	R1	R2
CIPR-CT-01	1	0.653	0.660	0.699	0.860	1.460	1.796	0.876	1.485	1.833	0.917	1.561	1.953
	2	0.562	0.598	0.661	0.657	1.169	1.466	0.734	1.181	1.490	0.865	1.339	1.688
	3	0.393	0.482	0.501	0.509	0.997	1.214	0.644	1.007	1.290	0.652	1.214	1.527
	4	0.347	0.418	0.433	0.374	0.854	1.076	0.549	0.884	1.157	0.580	1.125	1.398
	6	0.213	0.278	0.342	0.274	0.680	0.884	0.281	0.724	0.911	0.493	1.012	1.270
	8	0.180	0.198	0.309	0.217	0.570	0.762	0.236	0.611	0.787	0.441	0.938	1.175
	10	0.146	0.148	0.281	0.178	0.496	0.677	0.219	0.539	0.699	0.366	0.888	1.121
	12	0.125	0.131	0.257	0.155	0.433	0.608	0.186	0.484	0.625	0.379	0.845	1.066
	16	0.089	0.110	0.215	0.136	0.355	0.521	0.167	0.401	0.538	0.360	0.794	1.016
CIPR-CT-02	1	1.132	1.325	1.327	1.387	2.273	2.770	1.632	2.509	3.045	1.636	2.624	3.215
	2	0.884	0.971	1.161	1.165	1.976	2.449	1.282	2.152	2.658	1.482	2.501	3.101
	3	0.694	0.809	1.006	0.967	1.754	2.169	1.175	1.944	2.410	1.405	2.384	2.913
	4	0.610	0.733	0.971	0.857	1.584	2.006	1.064	1.783	2.246	1.331	2.297	2.862
	6	0.507	0.621	0.776	0.640	1.358	1.756	0.943	1.583	2.030	1.062	2.180	2.693
	8	0.447	0.587	0.799	0.485	1.220	1.592	0.619	1.467	1.900	0.955	2.081	2.593
	10	0.375	0.554	0.733	0.398	1.103	1.447	0.571	1.386	1.800	0.855	2.019	2.474
	12	0.315	0.370	0.648	0.361	1.023	1.340	0.549	1.317	1.712	0.831	1.955	2.377
	16	0.199	0.290	0.521	0.316	0.909	1.192	0.504	1.233	1.600	0.782	1.927	2.325
CIPR-CT-03	1	1.749	1.948	2.002	2.050	3.006	3.429	2.291	3.215	3.637	2.245	3.336	3.821
	2	1.497	1.665	1.926	1.768	2.582	2.958	1.977	2.769	3.151	2.028	3.077	3.538
	3	1.219	1.363	1.717	1.530	2.304	2.644	1.720	2.502	2.855	1.806	2.923	3.371
	4	1.050	1.189	1.542	1.318	2.093	2.425	1.513	2.304	2.653	1.600	2.809	3.247
	6	0.846	0.990	1.413	1.026	1.788	2.104	1.288	2.018	2.359	1.425	2.630	3.060
	8	0.716	0.877	1.294	0.752	1.581	1.887	1.089	1.825	2.162	1.306	2.501	2.916
	10	0.639	0.808	1.259	0.652	1.451	1.748	0.796	1.708	2.037	1.259	2.438	2.856
	12	0.519	0.716	1.058	0.528	1.335	1.613	0.724	1.608	1.921	1.105	2.324	2.725
	16	0.331	0.451	0.803	0.472	1.208	1.463	0.670	1.489	1.781	1.069	2.279	2.661
CIPR-CT-04	1	0.998	1.175	1.186	1.373	2.279	2.656	1.587	2.516	2.929	1.243	2.151	2.513
	2	0.957	1.043	1.162	1.204	1.973	2.338	1.335	2.123	2.514	1.057	1.932	2.268
	3	0.781	0.867	1.033	1.002	1.715	2.057	1.182	1.882	2.247	0.979	1.799	2.113
	4	0.687	0.782	0.954	0.887	1.532	1.862	1.085	1.714	2.070	0.922	1.694	2.023
	6	0.554	0.662	0.870	0.720	1.290	1.604	0.940	1.495	1.838	0.843	1.563	1.917
	8	0.470	0.595	0.786	0.501	1.127	1.426	0.763	1.349	1.678	0.772	1.474	1.789
	10	0.418	0.537	0.675	0.433	1.009	1.288	0.587	1.251	1.562	0.754	1.444	1.776
	12	0.371	0.498	0.650	0.360	0.919	1.175	0.528	1.175	1.471	0.706	1.389	1.715
	16	0.221	0.305	0.479	0.301	0.779	0.979	0.483	1.066	1.337	0.646	1.359	1.678

Table C.2 Bit rates (bpp) obtained for image datasets CIPR-MR-01, CIPR-MR-02, CIPR-MR-03 and CIPR-MR-04. Bit rates obtained with the proposed non-resolution scalable image compression method DLD-RoI and resolution scalable image compression method RDLD-RoI with 5%, 10% and 25% area of the image marked as RoI are showed. R0 is original resolution of the image, R1 is the image resolution after first sub sampling, R2 is the image resolution after second resembling.

Datasets	B.G. PAE	DLD-RoI			RDLD-RoI								
		5%-RoI	10%-RoI	25%-RoI	5%-RoI			10%-RoI			25%-RoI		
					R0	R1	R2	R0	R1	R2	R0	R1	R2
CIPR-MR-01	1	1.546	1.624	1.791	1.821	2.653	3.116	1.947	2.764	3.234	2.122	3.051	3.565
	2	1.147	1.245	1.491	1.337	2.066	2.478	1.550	2.264	2.695	1.805	2.694	3.187
	3	0.859	0.968	1.254	1.005	1.684	2.077	1.279	1.975	2.383	1.577	2.483	2.962
	4	0.742	0.869	1.164	0.795	1.466	1.790	1.157	1.778	2.170	1.469	2.345	2.815
	6	0.592	0.716	1.053	0.555	1.209	1.475	0.981	1.537	1.898	1.347	2.177	2.624
	8	0.504	0.634	1.022	0.461	1.025	1.255	0.877	1.388	1.726	1.127	2.065	2.489
	10	0.446	0.583	0.949	0.388	0.882	1.096	0.589	1.281	1.600	0.911	1.978	2.378
	12	0.412	0.550	0.921	0.328	0.775	0.978	0.553	1.200	1.511	0.865	1.885	2.281
	16	0.231	0.319	0.587	0.281	0.656	0.824	0.507	1.104	1.385	0.815	1.779	2.140
CIPR-MR-02	1	1.741	1.815	1.992	2.128	3.283	3.888	2.238	3.370	3.984	2.414	3.662	4.352
	2	1.317	1.408	1.658	1.662	2.699	3.253	1.807	2.831	3.408	2.083	3.261	3.925
	3	1.035	1.133	1.448	1.353	2.341	2.866	1.525	2.505	3.060	1.846	3.019	3.667
	4	0.903	1.017	1.355	1.200	2.094	2.594	1.389	2.280	2.813	1.749	2.860	3.494
	6	0.744	0.863	1.256	0.991	1.770	2.234	1.214	1.990	2.489	1.595	2.657	3.264
	8	0.642	0.781	1.165	0.756	1.559	1.985	1.095	1.801	2.271	1.349	2.522	3.096
	10	0.577	0.723	1.123	0.659	1.397	1.796	0.827	1.664	2.112	1.233	2.409	2.975
	12	0.522	0.670	1.042	0.580	1.289	1.635	0.726	1.558	1.994	1.106	2.334	2.838
	16	0.376	0.447	0.773	0.449	1.108	1.379	0.649	1.414	1.813	1.013	2.183	2.600
CIPR-MR-03	1	1.464	1.647	1.689	1.797	2.866	3.362	2.055	3.022	3.532	2.107	3.223	3.812
	2	1.273	1.346	1.612	1.565	2.500	2.958	1.801	2.641	3.131	1.961	3.031	3.621
	3	1.080	1.174	1.465	1.369	2.216	2.617	1.565	2.384	2.821	1.827	2.873	3.396
	4	0.940	1.074	1.397	1.045	2.025	2.418	1.462	2.213	2.640	1.447	2.757	3.277
	6	0.701	0.957	1.072	0.856	1.773	2.137	1.323	1.992	2.399	1.370	2.617	3.125
	8	0.569	0.858	1.023	0.745	1.601	1.945	0.931	1.842	2.238	1.301	2.521	3.008
	10	0.518	0.795	0.975	0.674	1.468	1.772	0.836	1.721	2.104	1.213	2.447	2.890
	12	0.479	0.651	0.948	0.623	1.366	1.650	0.786	1.633	2.012	1.185	2.394	2.810
	16	0.414	0.455	0.817	0.504	1.217	1.429	0.724	1.501	1.857	1.076	2.306	2.635
CIPR-MR-04	1	1.706	1.921	1.997	1.856	2.346	2.711	2.118	2.547	2.940	2.179	2.769	3.220
	2	1.369	1.521	1.767	1.506	1.959	2.292	1.734	2.140	2.501	1.973	2.570	3.010
	3	1.073	1.212	1.571	1.241	1.714	2.027	1.457	1.918	2.259	1.781	2.443	2.873
	4	0.932	1.079	1.482	1.072	1.538	1.841	1.326	1.762	2.092	1.699	2.350	2.778
	6	0.742	0.902	1.362	0.848	1.297	1.594	1.137	1.545	1.870	1.514	2.211	2.641
	8	0.604	0.779	1.249	0.573	1.060	1.350	0.976	1.337	1.667	1.181	1.977	2.427
	10	0.499	0.714	1.070	0.500	0.913	1.158	0.667	1.238	1.509	1.118	1.854	2.203
	12	0.394	0.661	0.979	0.441	0.836	1.055	0.629	1.175	1.428	1.020	1.780	2.157
	16	0.329	0.389	0.851	0.339	0.727	0.917	0.567	1.082	1.319	0.947	1.706	2.037

Table C.3 Bit rates (bpp) obtained for image datasets MGHD-MR-01, MGHD-MR-02, MGHD-MR-03 and MIDI-MR-01. Bit rates obtained with the proposed non-resolution scalable image compression method DLD-RoI and resolution scalable image compression method RDLD-RoI with 5%, 10% and 25% area of the image marked as RoI are showed. R0 is original resolution of the image, R1 is the image resolution after first sub sampling, R2 is the image resolution after second resembling.

Datasets	B.G. PAE	DLD-RoI			RDLD-RoI								
		5%-RoI	10%-RoI	25%-RoI	5%-RoI			10%-RoI			25%-RoI		
					R0	R1	R2	R0	R1	R2	R0	R1	R2
MGH-MR-01	1	2.557	2.619	2.859	2.835	3.665	4.076	2.960	3.771	4.200	3.177	4.090	4.594
	2	1.966	2.077	2.405	2.246	3.058	3.428	2.435	3.219	3.615	2.733	3.682	4.167
	3	1.623	1.762	2.137	1.905	2.680	3.034	2.126	2.876	3.263	2.481	3.438	3.921
	4	1.370	1.510	1.910	1.634	2.412	2.749	1.855	2.633	3.008	2.254	3.262	3.731
	6	1.085	1.246	1.720	1.324	2.039	2.369	1.585	2.299	2.665	2.059	3.026	3.493
	8	0.882	1.058	1.560	1.098	1.794	2.113	1.395	2.075	2.433	1.881	2.862	3.327
	10	0.768	0.963	1.486	0.916	1.612	1.920	1.259	1.901	2.257	1.675	2.727	3.200
	12	0.639	0.880	1.301	0.770	1.464	1.760	1.040	1.773	2.127	1.485	2.598	3.057
	16	0.471	0.558	1.014	0.575	1.272	1.498	0.828	1.588	1.906	1.290	2.443	2.818
MGH-MR-02	1	2.080	2.160	2.371	2.414	3.345	3.785	2.546	3.451	3.901	2.726	3.765	4.292
	2	1.571	1.668	1.962	1.867	2.767	3.157	2.055	2.924	3.346	2.313	3.382	3.888
	3	1.242	1.366	1.700	1.533	2.406	2.787	1.745	2.603	3.017	2.068	3.144	3.648
	4	1.093	1.230	1.614	1.366	2.161	2.535	1.598	2.381	2.782	1.962	2.983	3.487
	6	0.916	1.067	1.489	1.152	1.856	2.213	1.414	2.111	2.504	1.814	2.813	3.307
	8	0.777	0.943	1.393	0.881	1.646	1.939	1.271	1.935	2.311	1.528	2.698	3.071
	10	0.694	0.870	1.357	0.748	1.454	1.705	0.949	1.800	2.164	1.357	2.494	2.886
	12	0.608	0.810	1.215	0.642	1.292	1.556	0.843	1.684	2.044	1.231	2.335	2.713
	16	0.386	0.495	0.894	0.507	1.115	1.394	0.752	1.521	1.863	1.154	2.191	2.628
MGH-MR-03	1	2.933	3.003	3.229	3.198	3.980	4.364	3.326	4.088	4.494	3.540	4.411	4.891
	2	2.333	2.437	2.783	2.593	3.352	3.698	2.778	3.515	3.896	3.089	3.983	4.450
	3	1.969	2.097	2.505	2.236	2.962	3.290	2.436	3.161	3.531	2.824	3.724	4.188
	4	1.723	1.869	2.314	1.978	2.682	2.999	2.205	2.906	3.266	2.638	3.543	4.001
	6	1.345	1.508	2.015	1.586	2.272	2.569	1.827	2.534	2.879	2.339	3.260	3.706
	8	1.122	1.294	1.822	1.344	1.987	2.282	1.623	2.276	2.617	2.150	3.060	3.506
	10	0.937	1.123	1.692	1.149	1.782	2.072	1.448	2.081	2.417	2.015	2.914	3.355
	12	0.839	1.031	1.622	0.949	1.617	1.886	1.322	1.941	2.271	1.773	2.788	3.219
	16	0.626	0.823	1.338	0.715	1.329	1.555	0.950	1.725	2.001	1.434	2.565	2.925
MIDI-MR-01	1	1.594	1.649	1.800	1.898	2.748	3.045	1.982	2.864	3.161	2.158	3.167	3.480
	2	1.233	1.322	1.480	1.476	2.187	2.462	1.607	2.360	2.632	1.842	2.801	3.102
	3	0.977	1.051	1.298	1.193	1.847	2.106	1.335	2.054	2.316	1.626	2.567	2.860
	4	0.792	0.888	1.124	0.996	1.606	1.855	1.158	1.838	2.086	1.455	2.401	2.685
	6	0.587	0.693	0.965	0.749	1.277	1.506	0.947	1.541	1.769	1.261	2.166	2.440
	8	0.462	0.573	0.856	0.535	1.053	1.274	0.775	1.335	1.553	1.021	1.975	2.268
	10	0.387	0.512	0.757	0.420	0.900	1.105	0.582	1.186	1.391	0.905	1.837	2.117
	12	0.292	0.448	0.665	0.330	0.810	0.988	0.517	1.103	1.283	0.803	1.771	2.023
	16	0.194	0.276	0.534	0.257	0.681	0.822	0.414	0.985	1.128	0.703	1.660	1.860

Table C.4 Bit rates (bpp) obtained for image datasets MIDI-MR-02, MIDI-MR-03, MIDI-MR-04 and MIDI-MR-05. Bit rates obtained with the proposed non-resolution scalable image compression method DLD-RoI and resolution scalable image compression method RDLD-RoI with 5%, 10% and 25% area of the image marked as RoI are showed. R0 is original resolution of the image, R1 is the image resolution after first sub sampling, R2 is the image resolution after second resembling.

Datasets	B.G. PAE	DLD-RoI			RDLD-RoI								
		5%-RoI	10%-RoI	25%-RoI	5%-RoI			10%-RoI			25%-RoI		
					R0	R1	R2	R0	R1	R2	R0	R1	R2
MIDI-MR-02	1	1.545	1.712	1.734	1.847	2.706	3.017	2.048	2.948	3.269	2.121	3.104	3.435
	2	1.299	1.398	1.584	1.547	2.273	2.577	1.727	2.482	2.787	1.927	2.869	3.201
	3	1.086	1.133	1.390	1.325	1.991	2.255	1.480	2.220	2.488	1.752	2.706	3.005
	4	0.907	1.008	1.243	1.130	1.773	2.044	1.328	2.017	2.289	1.615	2.579	2.890
	6	0.731	0.819	1.112	0.918	1.475	1.744	1.135	1.744	2.015	1.459	2.389	2.719
	8	0.576	0.696	0.972	0.691	1.258	1.535	0.980	1.548	1.822	1.202	2.213	2.574
	10	0.433	0.608	0.809	0.554	1.102	1.282	0.882	1.403	1.666	1.072	2.077	2.263
	12	0.355	0.553	0.772	0.460	0.937	1.125	0.597	1.306	1.538	0.976	1.832	2.072
	16	0.276	0.311	0.603	0.327	0.766	0.923	0.526	1.176	1.377	0.823	1.613	1.836
MIDI-MR-03	1	2.016	2.175	2.265	2.328	3.331	3.627	2.564	3.548	3.851	2.633	3.737	4.061
	2	1.680	1.800	2.045	1.977	2.869	3.156	2.181	3.067	3.353	2.413	3.477	3.797
	3	1.453	1.543	1.881	1.756	2.551	2.816	1.954	2.780	3.038	2.260	3.284	3.589
	4	1.282	1.404	1.713	1.578	2.315	2.570	1.781	2.555	2.805	2.106	3.143	3.437
	6	0.994	1.218	1.420	1.272	1.994	2.240	1.594	2.269	2.510	1.909	2.951	3.238
	8	0.856	1.061	1.331	1.066	1.762	2.008	1.421	2.053	2.301	1.668	2.780	3.078
	10	0.728	0.949	1.177	0.875	1.521	1.779	1.299	1.862	2.138	1.465	2.558	2.874
	12	0.612	0.855	1.100	0.761	1.371	1.599	1.112	1.726	2.009	1.379	2.429	2.760
	16	0.484	0.683	1.017	0.600	1.106	1.353	0.801	1.539	1.808	1.194	2.144	2.488
MIDI-MR-04	1	1.934	1.983	2.126	2.403	3.759	4.143	2.476	3.874	4.254	2.665	4.180	4.591
	2	1.598	1.672	1.881	2.003	3.127	3.491	2.118	3.301	3.665	2.374	3.755	4.156
	3	1.392	1.484	1.739	1.749	2.732	3.083	1.887	2.944	3.294	2.203	3.490	3.883
	4	1.229	1.331	1.566	1.556	2.452	2.790	1.720	2.691	3.027	2.032	3.303	3.686
	6	0.949	1.054	1.341	1.259	2.068	2.384	1.432	2.343	2.658	1.803	3.046	3.416
	8	0.740	0.848	1.120	1.012	1.799	2.099	1.209	2.095	2.395	1.595	2.852	3.215
	10	0.629	0.741	1.041	0.884	1.587	1.879	1.091	1.899	2.188	1.500	2.702	3.055
	12	0.528	0.645	0.955	0.746	1.421	1.703	0.986	1.745	2.027	1.341	2.580	2.930
	16	0.387	0.532	0.788	0.546	1.180	1.445	0.718	1.518	1.778	1.089	2.385	2.726
MIDI-MR-05	1	2.019	2.109	2.262	2.354	3.323	3.613	2.465	3.431	3.721	2.634	3.707	4.022
	2	1.616	1.714	1.955	1.894	2.731	3.011	2.057	2.894	3.173	2.293	3.307	3.618
	3	1.357	1.476	1.724	1.628	2.376	2.651	1.828	2.572	2.850	2.095	3.080	3.391
	4	1.164	1.251	1.513	1.416	2.122	2.394	1.596	2.351	2.622	1.904	2.918	3.232
	6	0.894	1.006	1.306	1.115	1.751	2.004	1.338	2.010	2.267	1.679	2.671	2.980
	8	0.714	0.843	1.152	0.910	1.480	1.743	1.135	1.758	2.021	1.515	2.456	2.800
	10	0.612	0.732	1.095	0.752	1.309	1.553	1.038	1.597	1.840	1.336	2.319	2.625
	12	0.534	0.671	1.024	0.603	1.180	1.400	0.886	1.478	1.704	1.140	2.226	2.491
	16	0.377	0.521	0.819	0.417	0.926	1.085	0.626	1.318	1.500	0.934	1.880	2.126

Table C.5 Bit rates (bpp) obtained for image datasets MIDI-MR-06, MIDI-MR-07, OSRX-CT-01and OSRX-PT-01. Bit rates obtained with the proposed non-resolution scalable image compression method DLD-RoI and resolution scalable image compression method RDLD-RoI with 5%, 10% and 25% area of the image marked as RoI are showed. R0 is original resolution of the image, R1 is the image resolution after first sub sampling, R2 is the image resolution after second resembling.

Datasets	B.G. PAE	DLD-RoI			RDLD-RoI								
		5%-RoI	10%-RoI	25%-RoI	5%-RoI			10%-RoI			25%-RoI		
					R0	R1	R2	R0	R1	R2	R0	R1	R2
MIDI-MR-06	1	1.537	1.673	1.749	1.838	2.745	3.064	2.051	2.995	3.331	2.129	3.162	3.509
	2	1.311	1.415	1.602	1.551	2.315	2.629	1.748	2.532	2.851	1.955	2.937	3.288
	3	1.091	1.142	1.418	1.339	2.029	2.306	1.480	2.265	2.547	1.794	2.773	3.093
	4	0.907	1.012	1.270	1.148	1.818	2.091	1.374	2.070	2.345	1.661	2.653	2.971
	6	0.734	0.862	1.137	0.919	1.525	1.786	1.170	1.805	2.068	1.459	2.481	2.800
	8	0.590	0.721	1.039	0.706	1.317	1.566	1.024	1.621	1.881	1.231	2.327	2.633
	10	0.454	0.646	0.842	0.570	1.141	1.371	0.861	1.453	1.733	1.097	2.088	2.351
	12	0.388	0.588	0.807	0.485	1.000	1.169	0.629	1.354	1.621	1.012	1.889	2.226
	16	0.296	0.339	0.651	0.347	0.787	0.950	0.560	1.221	1.441	0.851	1.666	1.925
MIDI-MR-07	1	1.545	1.613	1.747	1.884	2.843	3.183	1.967	2.958	3.298	2.153	3.258	3.623
	2	1.197	1.288	1.472	1.477	2.281	2.595	1.607	2.452	2.770	1.840	2.888	3.244
	3	0.949	1.048	1.242	1.195	1.939	2.241	1.344	2.146	2.452	1.612	2.654	3.002
	4	0.777	0.879	1.128	1.008	1.692	1.982	1.169	1.924	2.216	1.481	2.483	2.820
	6	0.599	0.705	0.976	0.782	1.357	1.627	0.965	1.628	1.893	1.283	2.239	2.556
	8	0.478	0.589	0.856	0.562	1.144	1.395	0.833	1.440	1.684	1.055	2.076	2.384
	10	0.374	0.528	0.720	0.453	1.005	1.236	0.589	1.306	1.537	0.949	1.975	2.265
	12	0.296	0.488	0.667	0.370	0.906	1.121	0.515	1.215	1.425	0.864	1.891	2.154
	16	0.231	0.274	0.574	0.282	0.771	0.926	0.448	1.082	1.283	0.751	1.776	1.997
OSRX-CT-01	1	1.551	1.697	1.776	1.687	2.311	2.577	1.945	2.416	2.688	1.962	2.622	2.928
	2	1.297	1.412	1.664	1.446	1.983	2.285	1.676	2.121	2.430	1.842	2.441	2.808
	3	1.097	1.237	1.497	1.275	1.798	2.007	1.527	1.958	2.174	1.715	2.340	2.604
	4	0.975	1.140	1.282	1.084	1.665	1.878	1.418	1.844	2.063	1.349	2.278	2.549
	6	0.609	1.008	1.023	0.763	1.493	1.698	0.936	1.698	1.913	1.226	2.211	2.481
	8	0.550	0.933	1.001	0.676	1.375	1.576	0.856	1.602	1.812	1.175	2.170	2.440
	10	0.484	0.620	0.956	0.605	1.275	1.469	0.795	1.517	1.722	1.128	2.124	2.391
	12	0.444	0.590	0.939	0.557	1.195	1.374	0.751	1.449	1.641	1.097	2.085	2.350
	16	0.382	0.538	0.885	0.477	1.066	1.213	0.680	1.339	1.516	1.022	2.021	2.287
OSRX-PT-01	1	0.299	0.460	0.377	0.811	1.342	1.606	0.988	1.426	1.701	0.882	1.496	1.760
	2	0.603	0.701	0.685	0.724	1.141	1.448	0.927	1.252	1.570	0.709	1.385	1.712
	3	0.515	0.614	0.478	0.660	1.023	1.197	0.898	1.165	1.374	0.710	1.338	1.526
	4	0.479	0.580	0.451	0.474	0.945	1.162	0.812	1.099	1.327	0.631	1.309	1.525
	6	0.307	0.385	0.418	0.387	0.727	0.840	0.552	0.977	1.046	0.594	1.284	1.393
	8	0.280	0.312	0.409	0.328	0.610	0.744	0.528	0.733	0.874	0.563	1.261	1.358
	10	0.248	0.293	0.391	0.299	0.510	0.641	0.509	0.675	0.795	0.554	1.234	1.266
	12	0.234	0.272	0.381	0.278	0.476	0.606	0.482	0.648	0.772	0.557	1.225	1.253
	16	0.194	0.254	0.360	0.243	0.446	0.562	0.477	0.623	0.742	0.534	1.216	1.228

Table C.6 Bit rates (bpp) obtained for image datasets OSRX-CT-02, OSRX-MR-01, OSRX-MR-02 and OSRX-MR-03. Bit rates obtained with the proposed non-resolution scalable image compression method DLD-RoI and resolution scalable image compression method RDLD-RoI with 5%, 10% and 25% area of the image marked as RoI are showed. R0 is original resolution of the image, R1 is the image resolution after first sub sampling, R2 is the image resolution after second resembling.

Datasets	B.G. PAE	DLD-RoI			RDLD-RoI								
		5%-RoI	10%-RoI	25%-RoI	5%-RoI			10%-RoI			25%-RoI		
					R0	R1	R2	R0	R1	R2	R0	R1	R2
OSRX-CT-02	1	0.958	1.168	1.151	1.237	2.249	2.717	1.487	2.544	3.073	1.498	2.637	3.169
	2	0.850	0.928	1.039	0.803	1.905	2.346	1.267	2.182	2.675	1.393	2.448	2.987
	3	0.730	0.813	0.957	0.700	1.695	2.118	1.143	1.967	2.422	1.310	2.301	2.815
	4	0.658	0.741	0.888	0.632	1.544	1.952	1.051	1.807	2.246	1.235	2.189	2.696
	6	0.531	0.629	0.763	0.531	1.332	1.711	0.934	1.603	2.010	1.036	2.048	2.536
	8	0.463	0.571	0.718	0.472	1.185	1.537	0.752	1.468	1.853	0.899	1.954	2.429
	10	0.385	0.551	0.664	0.426	1.076	1.390	0.592	1.362	1.723	0.843	1.875	2.332
	12	0.327	0.454	0.615	0.389	0.980	1.287	0.532	1.282	1.620	0.785	1.815	2.258
	16	0.255	0.317	0.484	0.308	0.856	1.096	0.487	1.170	1.476	0.694	1.729	2.145
OSRX-MR-01	1	1.230	1.280	1.389	1.395	2.140	2.387	1.608	2.265	2.545	1.680	2.461	2.740
	2	1.009	1.097	1.304	1.196	1.840	2.139	1.423	1.980	2.301	1.505	2.313	2.662
	3	0.844	0.966	1.109	1.060	1.631	1.827	1.318	1.815	2.038	1.409	2.188	2.454
	4	0.721	0.908	1.025	0.789	1.483	1.713	1.235	1.715	1.941	1.174	2.140	2.410
	6	0.500	0.774	0.830	0.660	1.302	1.374	1.062	1.589	1.778	1.094	2.094	2.237
	8	0.449	0.673	0.802	0.579	1.189	1.224	0.757	1.487	1.693	1.016	2.068	2.162
	10	0.399	0.444	0.778	0.527	1.040	1.105	0.726	1.409	1.582	0.993	1.967	2.043
	12	0.368	0.424	0.764	0.481	0.930	1.024	0.684	1.351	1.520	0.949	1.877	1.996
	16	0.311	0.382	0.653	0.396	0.845	0.929	0.637	1.258	1.425	0.879	1.836	1.956
OSRX-MR-02	1	3.319	3.393	3.633	3.508	4.051	4.295	3.629	4.168	4.434	3.861	4.486	4.791
	2	2.726	2.838	3.183	2.904	3.413	3.631	3.083	3.590	3.841	3.406	4.054	4.346
	3	2.318	2.458	2.874	2.511	3.014	3.219	2.712	3.228	3.475	3.111	3.785	4.070
	4	2.044	2.194	2.658	2.225	2.728	2.931	2.444	2.970	3.214	2.905	3.596	3.880
	6	1.638	1.809	2.333	1.819	2.315	2.506	2.063	2.597	2.836	2.592	3.320	3.600
	8	1.385	1.570	2.137	1.557	2.034	2.222	1.829	2.342	2.582	2.401	3.127	3.405
	10	1.179	1.376	1.972	1.356	1.830	2.017	1.643	2.155	2.393	2.238	2.989	3.265
	12	1.026	1.233	1.857	1.190	1.668	1.845	1.505	2.004	2.237	2.109	2.876	3.146
	16	0.809	1.030	1.696	0.919	1.424	1.586	1.253	1.784	2.015	1.810	2.709	2.982
OSRX-MR-03	1	2.746	2.870	3.046	2.980	3.737	3.997	3.179	3.865	4.128	3.368	4.160	4.458
	2	2.255	2.390	2.698	2.475	3.149	3.392	2.692	3.326	3.583	2.973	3.774	4.068
	3	1.915	2.067	2.461	2.130	2.783	3.022	2.380	2.997	3.250	2.715	3.538	3.830
	4	1.657	1.781	2.235	1.884	2.517	2.751	2.119	2.756	3.009	2.531	3.369	3.666
	6	1.378	1.539	2.048	1.576	2.155	2.382	1.852	2.430	2.666	2.330	3.139	3.424
	8	1.193	1.376	1.905	1.343	1.915	2.136	1.675	2.213	2.444	2.142	2.983	3.266
	10	1.045	1.230	1.785	1.122	1.742	1.958	1.521	2.057	2.282	1.885	2.871	3.147
	12	0.917	1.117	1.685	0.983	1.603	1.815	1.369	1.934	2.157	1.768	2.791	3.063
	16	0.765	0.982	1.567	0.810	1.385	1.580	1.021	1.744	1.954	1.604	2.622	2.896

Table C.7 Bit rates (bpp) obtained for image datasets OSRX-MR-04, OSRX-XA-01, OSRX-XA-02, PHNT-MR-01. Bit rates obtained with the proposed non-resolution scalable image compression method DLD-RoI and resolution scalable image compression method RDLD-RoI with 5%, 10% and 25% area of the image marked as RoI are showed. R0 is original resolution of the image, R1 is the image resolution after first sub sampling, R2 is the image resolution after second resembling.

Datasets	B.G. PAE	DLD-RoI			RDLD-RoI								
		5%-RoI	10%-RoI	25%-RoI	5%-RoI			10%-RoI			25%-RoI		
					R0	R1	R2	R0	R1	R2	R0	R1	R2
OSRX-MR-04	1	2.411	2.503	2.699	2.667	3.422	3.742	2.820	3.529	3.851	2.981	3.803	4.160
	2	1.928	2.035	2.335	2.139	2.847	3.152	2.354	3.009	3.320	2.602	3.418	3.773
	3	1.603	1.737	2.107	1.825	2.489	2.786	2.050	2.687	2.995	2.374	3.183	3.530
	4	1.333	1.474	1.886	1.560	2.227	2.517	1.810	2.452	2.752	2.178	3.018	3.368
	6	1.100	1.256	1.719	1.289	1.900	2.190	1.573	2.166	2.464	2.009	2.825	3.173
	8	0.916	1.094	1.587	1.054	1.676	1.919	1.403	1.959	2.248	1.749	2.670	2.975
	10	0.749	0.961	1.396	0.843	1.483	1.671	1.233	1.799	2.079	1.532	2.486	2.700
	12	0.624	0.883	1.287	0.722	1.294	1.503	0.928	1.675	1.932	1.384	2.283	2.538
	16	0.478	0.552	1.078	0.574	1.069	1.283	0.808	1.504	1.752	1.237	2.115	2.376
OSRX-XA-01	1	1.359	1.545	1.634	1.496	1.919	2.188	1.749	2.138	2.411	1.802	2.314	2.594
	2	1.049	1.189	1.436	1.178	1.550	1.794	1.409	1.755	2.001	1.621	2.134	2.395
	3	0.818	0.884	1.218	0.957	1.316	1.537	1.131	1.531	1.757	1.425	2.006	2.253
	4	0.639	0.766	1.137	0.770	1.148	1.367	1.008	1.377	1.597	1.347	1.918	2.171
	6	0.470	0.607	1.022	0.513	0.918	1.133	0.830	1.166	1.383	1.022	1.764	2.022
	8	0.398	0.542	0.854	0.373	0.782	0.901	0.724	1.043	1.227	0.919	1.645	1.876
	10	0.277	0.498	0.771	0.321	0.703	0.756	0.464	0.972	1.128	0.874	1.589	1.793
	12	0.254	0.387	0.756	0.257	0.652	0.690	0.442	0.926	1.068	0.762	1.559	1.754
	16	0.169	0.268	0.588	0.225	0.589	0.608	0.412	0.868	0.986	0.733	1.507	1.665
OSRX-XA-02	1	1.495	1.664	1.785	1.619	2.128	2.449	1.888	2.377	2.705	1.942	2.531	2.867
	2	1.150	1.273	1.562	1.288	1.762	2.064	1.517	1.976	2.277	1.748	2.358	2.689
	3	0.899	1.037	1.376	1.062	1.522	1.786	1.292	1.745	2.014	1.600	2.227	2.528
	4	0.709	0.845	1.225	0.870	1.342	1.605	1.099	1.577	1.839	1.461	2.128	2.433
	6	0.529	0.675	1.099	0.670	1.105	1.350	0.917	1.361	1.605	1.335	1.996	2.289
	8	0.444	0.598	1.063	0.560	0.952	1.182	0.823	1.228	1.454	1.275	1.911	2.188
	10	0.389	0.550	1.016	0.470	0.852	1.058	0.756	1.138	1.341	1.092	1.854	2.113
	12	0.354	0.516	0.897	0.321	0.780	0.968	0.510	1.075	1.259	0.874	1.811	2.057
	16	0.185	0.285	0.597	0.257	0.691	0.849	0.448	0.993	1.149	0.817	1.753	1.979
PHNT-MR-01	1	1.820	1.925	2.082	2.157	3.149	3.490	2.280	3.281	3.629	2.466	3.585	3.963
	2	1.430	1.538	1.785	1.725	2.558	2.878	1.872	2.743	3.069	2.150	3.209	3.579
	3	1.180	1.296	1.607	1.441	2.202	2.504	1.620	2.419	2.728	1.950	2.981	3.340
	4	0.952	1.070	1.395	1.208	1.953	2.242	1.390	2.194	2.490	1.758	2.822	3.174
	6	0.716	0.843	1.212	0.935	1.605	1.874	1.135	1.876	2.150	1.565	2.582	2.923
	8	0.574	0.709	1.106	0.756	1.358	1.611	0.998	1.650	1.911	1.402	2.412	2.736
	10	0.479	0.630	1.048	0.573	1.173	1.412	0.910	1.480	1.726	1.214	2.278	2.588
	12	0.424	0.583	0.992	0.474	1.033	1.253	0.614	1.349	1.576	1.082	2.172	2.469
	16	0.272	0.372	0.694	0.313	0.841	1.031	0.522	1.164	1.369	0.880	1.973	2.263

Appendix - D: Resolution Scalable Compression

Table D.1 Compression performance of the proposed resolution scalable image compression algorithm for different PAE criteria (PAE=1,2,3,4,6,8,10,12,16) in terms of PSNR, MSSIM and UQI. R0 is original resolution of the image, R1 is the image resolution after first sub sampling, R2 is the image resolution after second resembling. Datasets shown are: CIPR-CT-01, CIPR-CT-02, CIPR-CT-03, CIPR-CT-04, CIPR-MR-01, CIPR-MR-02, CIPR-MR-03 and CIPR-MR-04.

Datasets	PAE	RDLD						Datasets	PAE	RDLD					
		PSNR	MSSIM	UQI	BPP (R0)	BPP (R1)	BPP (R2)			PSNR	MSSIM	QI	BPP (R0)	BPP (R1)	BPP (R2)
CIPR-CT-01	0	Inf	1.000	1.000	1.269	1.939	2.419	CIPR-MR-01	0	Inf	1.000	1.000	3.069	4.027	4.628
	1	54.870	0.997	0.892	0.779	1.213	1.614		1	49.978	0.991	0.884	1.740	2.456	2.939
	2	50.698	0.993	0.847	0.590	0.964	1.322		2	45.618	0.966	0.745	1.205	1.798	2.231
	3	48.036	0.989	0.829	0.489	0.826	1.158		3	43.149	0.938	0.644	0.912	1.428	1.837
	4	46.013	0.984	0.808	0.422	0.729	1.043		4	41.397	0.914	0.577	0.733	1.193	1.575
	6	43.053	0.973	0.779	0.338	0.597	0.881		6	38.833	0.855	0.470	0.520	0.886	1.228
	8	40.886	0.960	0.754	0.283	0.512	0.771		8	36.993	0.799	0.391	0.399	0.699	1.004
	10	39.213	0.948	0.733	0.245	0.451	0.693		10	35.522	0.744	0.331	0.327	0.577	0.850
	12	37.766	0.933	0.714	0.214	0.398	0.624		12	34.356	0.700	0.289	0.274	0.493	0.742
	16	35.529	0.912	0.686	0.173	0.325	0.519		16	32.548	0.628	0.232	0.207	0.383	0.594
CIPR-CT-02	0	Inf	1.000	1.000	1.866	2.810	3.469	CIPR-MR-02	0	Inf	1.000	1.000	3.405	4.690	5.537
	1	52.758	0.997	0.970	1.201	1.927	2.501		1	49.938	0.994	0.936	2.032	3.054	3.735
	2	48.106	0.990	0.932	0.911	1.543	2.058		2	45.341	0.980	0.865	1.504	2.395	3.018
	3	45.323	0.983	0.896	0.743	1.310	1.790		3	42.572	0.957	0.799	1.214	1.989	2.578
	4	43.346	0.974	0.856	0.625	1.140	1.598		4	40.618	0.931	0.743	1.017	1.705	2.265
	6	40.559	0.959	0.790	0.478	0.903	1.325		6	37.858	0.878	0.653	0.774	1.341	1.851
	8	38.449	0.943	0.737	0.392	0.757	1.155		8	35.877	0.831	0.588	0.628	1.106	1.577
	10	36.697	0.927	0.697	0.339	0.661	1.033		10	34.342	0.791	0.539	0.527	0.945	1.381
	12	35.332	0.918	0.669	0.294	0.578	0.926		12	33.077	0.759	0.500	0.455	0.825	1.228
	16	33.051	0.894	0.616	0.243	0.470	0.777		16	31.111	0.708	0.444	0.360	0.660	1.012
CIPR-CT-03	0	Inf	1.000	1.000	2.898	3.885	4.453	CIPR-MR-03	0	Inf	1.000	1.000	2.312	3.477	4.148
	1	51.569	0.996	0.947	1.993	2.696	3.190		1	52.542	0.998	0.984	1.632	2.523	3.083
	2	46.831	0.988	0.899	1.563	2.188	2.638		2	47.778	0.994	0.967	1.326	2.088	2.594
	3	43.896	0.978	0.852	1.321	1.888	2.311		3	44.795	0.988	0.949	1.139	1.820	2.295
	4	41.770	0.966	0.803	1.134	1.678	2.086		4	42.641	0.981	0.928	1.005	1.627	2.081
	6	38.917	0.943	0.716	0.869	1.354	1.746		6	39.604	0.964	0.889	0.815	1.350	1.776
	8	36.959	0.926	0.642	0.703	1.128	1.510		8	37.451	0.946	0.852	0.691	1.161	1.564
	10	35.070	0.905	0.598	0.605	0.995	1.359		10	35.795	0.927	0.817	0.595	1.018	1.403
	12	34.097	0.905	0.557	0.508	0.868	1.215		12	34.420	0.910	0.789	0.526	0.907	1.272
	16	31.494	0.875	0.510	0.413	0.736	1.047		16	32.224	0.871	0.724	0.425	0.744	1.079
CIPR-CT-04	0	Inf	1.000	1.000	1.767	2.788	3.289	CIPR-MR-04	0	Inf	1.000	1.000	2.813	3.316	3.772
	1	52.563	0.996	0.964	1.205	1.928	2.398		1	52.095	0.996	0.755	1.611	2.024	2.432
	2	47.884	0.989	0.928	0.939	1.524	1.945		2	47.715	0.989	0.596	1.208	1.581	1.948
	3	45.038	0.980	0.892	0.767	1.280	1.669		3	44.989	0.981	0.524	0.964	1.310	1.650
	4	43.007	0.970	0.855	0.656	1.106	1.472		4	43.016	0.971	0.487	0.809	1.134	1.456
	6	40.128	0.947	0.784	0.490	0.864	1.196		6	40.205	0.951	0.442	0.608	0.901	1.191
	8	38.136	0.926	0.717	0.393	0.695	0.999		8	38.157	0.929	0.405	0.489	0.750	1.018
	10	36.360	0.900	0.658	0.330	0.586	0.863		10	36.496	0.906	0.374	0.408	0.643	0.892
	12	35.017	0.883	0.620	0.279	0.500	0.753		12	35.122	0.883	0.346	0.348	0.563	0.795
	16	32.832	0.842	0.532	0.212	0.384	0.596		16	32.887	0.839	0.298	0.266	0.450	0.653

Table D.2 Compression performance of the proposed resolution scalable image compression algorithm for different PAE criteria (PAE=1,2,3,4,6,8,10,12,16) in terms of PSNR, MSSIM and UQI. R0 is original resolution of the image, R1 is the image resolution after first sub sampling, R2 is the image resolution after second resembling. Datasets shown are: MGHD-MR-01, MGHD-MR-02, MGHD-MR-03, MIDI-MR-01, MIDI-MR-02, MIDI-MR-03, MIDI-MR-04 and MIDI-MR-05.

Datasets	PAE	RDLD						Datasets	PAE	RDLD					
		PSNR	MSSIM	UQI	BPP (R0)	BPP (R1)	BPP (R2)			PSNR	MSSIM	QI	BPP (R0)	BPP (R1)	BPP (R2)
MGH-MR-01	0	Inf	1.000	1.000	4.268	5.185	5.747	MIDI-MR-02	0	Inf	1.000	1.000	2.682	3.731	4.123
	1	50.012	0.994	0.968	2.710	3.484	3.905		1	51.151	0.995	0.972	1.727	2.509	2.862
	2	45.325	0.984	0.918	2.090	2.786	3.171		2	46.466	0.986	0.936	1.359	1.970	2.297
	3	42.441	0.969	0.863	1.715	2.355	2.725		3	43.575	0.973	0.898	1.124	1.641	1.948
	4	40.408	0.949	0.808	1.446	2.037	2.400		4	41.521	0.957	0.854	0.950	1.407	1.699
	6	37.560	0.887	0.703	1.092	1.611	1.959		6	38.702	0.918	0.776	0.703	1.089	1.361
	8	35.632	0.811	0.620	0.867	1.330	1.665		8	36.778	0.875	0.702	0.537	0.864	1.119
	10	34.216	0.749	0.562	0.717	1.134	1.454		10	35.338	0.837	0.646	0.426	0.707	0.946
	12	33.103	0.715	0.522	0.611	0.991	1.302		12	34.176	0.808	0.603	0.346	0.591	0.812
	16	31.306	0.675	0.463	0.476	0.795	1.079		16	32.285	0.771	0.541	0.250	0.445	0.636
MGH-MR-02	0	Inf	1.000	1.000	3.752	4.807	5.400	MIDI-MR-03	0	Inf	1.000	1.000	3.252	4.388	4.760
	1	50.023	0.993	0.914	2.277	3.153	3.616		1	51.030	0.997	0.985	2.213	3.134	3.471
	2	45.515	0.978	0.816	1.694	2.466	2.898		2	46.289	0.991	0.968	1.795	2.561	2.873
	3	42.852	0.948	0.723	1.352	2.034	2.451		3	43.316	0.983	0.950	1.543	2.201	2.500
	4	41.030	0.913	0.654	1.133	1.746	2.154		4	41.138	0.972	0.926	1.368	1.942	2.230
	6	38.503	0.869	0.586	0.879	1.402	1.785		6	38.039	0.944	0.879	1.101	1.583	1.849
	8	36.641	0.849	0.553	0.728	1.188	1.549		8	35.889	0.914	0.831	0.907	1.331	1.580
	10	35.140	0.832	0.526	0.622	1.036	1.378		10	34.270	0.881	0.786	0.761	1.141	1.380
	12	33.843	0.816	0.501	0.543	0.918	1.238		12	32.969	0.847	0.745	0.650	0.995	1.223
	16	31.767	0.784	0.455	0.428	0.745	1.029		16	30.976	0.773	0.672	0.482	0.775	0.988
MGH-MR-03	0	Inf	1.000	1.000	4.655	5.525	6.035	MIDI-MR-04	0	Inf	1.000	1.000	3.569	5.207	5.658
	1	49.987	0.995	0.984	3.084	3.815	4.190		1	49.934	0.995	0.988	2.334	3.600	3.995
	2	45.243	0.987	0.956	2.441	3.090	3.430		2	45.184	0.986	0.968	1.882	2.886	3.261
	3	42.289	0.974	0.921	2.047	2.646	2.973		3	42.214	0.973	0.941	1.601	2.437	2.798
	4	40.162	0.959	0.882	1.764	2.325	2.639		4	40.081	0.957	0.910	1.382	2.116	2.465
	6	37.200	0.922	0.803	1.367	1.869	2.169		6	37.115	0.917	0.841	1.059	1.681	2.003
	8	35.150	0.872	0.725	1.092	1.547	1.840		8	35.104	0.874	0.769	0.834	1.377	1.684
	10	33.609	0.812	0.655	0.899	1.305	1.589		10	33.591	0.828	0.697	0.669	1.146	1.442
	12	32.400	0.756	0.602	0.760	1.135	1.412		12	32.388	0.784	0.629	0.548	0.962	1.246
	16	30.555	0.680	0.526	0.576	0.900	1.157		16	30.455	0.690	0.512	0.389	0.707	0.966
MIDI-MR-01	0	Inf	1.000	1.000	2.970	4.143	4.510	MIDI-MR-05	0	Inf	1.000	1.000	3.586	4.723	5.088
	1	50.018	0.992	0.941	1.810	2.583	2.912		1	50.057	0.994	0.968	2.259	3.170	3.483
	2	45.436	0.976	0.864	1.350	1.946	2.249		2	45.341	0.982	0.920	1.781	2.502	2.799
	3	42.702	0.954	0.783	1.058	1.560	1.843		3	42.443	0.965	0.865	1.483	2.096	2.387
	4	40.809	0.929	0.703	0.846	1.282	1.548		4	40.405	0.945	0.811	1.252	1.806	2.087
	6	38.216	0.873	0.564	0.571	0.910	1.151		6	37.620	0.901	0.707	0.922	1.386	1.661
	8	36.389	0.828	0.459	0.411	0.679	0.898		8	35.650	0.844	0.614	0.715	1.100	1.360
	10	34.872	0.791	0.383	0.315	0.530	0.720		10	34.090	0.767	0.535	0.573	0.905	1.150
	12	33.566	0.759	0.325	0.248	0.427	0.599		12	32.837	0.682	0.471	0.465	0.758	0.988
	16	31.422	0.705	0.244	0.171	0.299	0.436		16	31.128	0.574	0.391	0.332	0.566	0.773

Table D.3 Compression performance of the proposed resolution scalable image compression algorithm for different PAE criteria (PAE=1,2,3,4,6,8,10,12,16) in terms of PSNR, MSSIM and UQI. R0 is original resolution of the image, R1 is the image resolution after first sub sampling, R2 is the image resolution after second resembling. Datasets shown are: MIDI-MR-06, MIDI-MR-07, OSRX-CT-01, OSRX-PT-01, OSRX-CT-02, OSRX-MR-01, OSRX-MR-02 and OSRX-MR-03.

Datasets	PAE	RDLD						Datasets	PAE	RDLD					
		PSNR	MSSIM	UQI	BPP (R0)	BPP (R1)	BPP (R2)			PSNR	MSSIM	QI	BPP (R0)	BPP (R1)	BPP (R2)
MIDI-MR-06	0	Inf	1.000	1.000	2.658	3.759	4.156	OSRX-CT-02	0	Inf	1.000	1.000	1.710	2.854	3.470
	1	51.104	0.996	0.972	1.741	2.545	2.905		1	52.748	0.997	0.976	1.167	2.003	2.608
	2	46.395	0.987	0.935	1.377	2.007	2.338		2	48.043	0.992	0.953	0.938	1.611	2.168
	3	43.494	0.974	0.897	1.142	1.679	1.991		3	45.148	0.986	0.931	0.782	1.373	1.893
	4	41.432	0.958	0.853	0.971	1.447	1.746		4	43.060	0.978	0.902	0.682	1.205	1.694
	6	38.571	0.918	0.775	0.724	1.124	1.401		6	40.083	0.961	0.852	0.536	0.974	1.415
	8	36.585	0.872	0.705	0.560	0.899	1.157		8	37.956	0.942	0.803	0.447	0.816	1.217
	10	35.081	0.826	0.648	0.447	0.738	0.977		10	36.285	0.924	0.759	0.385	0.700	1.066
	12	33.896	0.789	0.605	0.367	0.622	0.844		12	34.903	0.906	0.720	0.331	0.612	0.947
	16	32.045	0.746	0.547	0.267	0.471	0.664		16	32.746	0.874	0.651	0.263	0.489	0.779
MIDI-MR-07	0	Inf	1.000	1.000	2.924	4.216	4.659	OSRX-MR-01	0	Inf	1.000	1.000	1.687	2.456	2.806
	1	49.975	0.992	0.936	1.802	2.665	3.059		1	54.333	0.999	0.990	1.179	1.820	2.133
	2	45.392	0.977	0.857	1.354	2.034	2.396		2	49.559	0.997	0.981	0.966	1.520	1.811
	3	42.642	0.955	0.778	1.069	1.648	1.988		3	46.559	0.994	0.973	0.841	1.330	1.608
	4	40.708	0.928	0.702	0.868	1.369	1.696		4	44.364	0.989	0.961	0.746	1.192	1.459
	6	38.017	0.866	0.573	0.607	0.995	1.290		6	41.248	0.979	0.942	0.613	0.997	1.247
	8	36.130	0.818	0.481	0.453	0.761	1.024		8	39.045	0.967	0.922	0.524	0.861	1.099
	10	34.625	0.787	0.417	0.360	0.617	0.856		10	37.369	0.955	0.904	0.456	0.756	0.985
	12	33.341	0.764	0.370	0.296	0.515	0.729		12	36.000	0.942	0.886	0.402	0.674	0.891
	16	31.179	0.730	0.301	0.216	0.385	0.563		16	33.859	0.917	0.851	0.322	0.552	0.754
OSRX-CT-01	0	Inf	1.000	1.000	2.069	2.576	2.917	OSRX-MR-02	0	Inf	1.000	1.000	4.998	5.572	5.952
	1	54.066	0.999	0.986	1.513	1.975	2.294		1	49.884	0.996	0.986	3.452	3.892	4.163
	2	49.294	0.997	0.974	1.217	1.660	1.955		2	45.123	0.988	0.963	2.757	3.165	3.409
	3	46.296	0.994	0.965	1.051	1.461	1.741		3	42.117	0.976	0.932	2.323	2.714	2.942
	4	44.086	0.990	0.951	0.923	1.316	1.584		4	39.947	0.961	0.899	2.018	2.389	2.612
	6	40.907	0.979	0.929	0.757	1.110	1.361		6	36.870	0.928	0.829	1.590	1.929	2.141
	8	38.646	0.965	0.906	0.646	0.966	1.205		8	34.684	0.892	0.763	1.305	1.618	1.822
	10	36.925	0.950	0.884	0.560	0.858	1.086		10	33.008	0.855	0.702	1.090	1.386	1.590
	12	35.544	0.934	0.862	0.496	0.768	0.987		12	31.665	0.820	0.647	0.924	1.203	1.395
	16	33.468	0.902	0.817	0.389	0.625	0.830		16	29.593	0.754	0.550	0.677	0.934	1.117
OSRX-PT-01	0	Inf	1.000	1.000	0.786	1.366	1.636	OSRX-MR-03	0	Inf	1.000	1.000	4.357	5.124	5.493
	1	57.156	1.000	0.991	0.576	0.993	1.233		1	49.911	0.995	0.926	2.947	3.554	3.843
	2	52.366	0.999	0.983	0.483	0.823	1.042		2	45.190	0.987	0.875	2.337	2.886	3.155
	3	49.358	0.997	0.978	0.424	0.716	0.923		3	42.233	0.975	0.830	1.967	2.469	2.728
	4	47.139	0.995	0.970	0.378	0.639	0.837		4	40.079	0.962	0.792	1.704	2.170	2.426
	6	43.992	0.990	0.959	0.313	0.530	0.713		6	36.955	0.930	0.728	1.357	1.765	2.002
	8	41.761	0.983	0.947	0.264	0.457	0.628		8	34.660	0.890	0.676	1.130	1.491	1.717
	10	40.056	0.976	0.937	0.228	0.403	0.563		10	32.854	0.844	0.632	0.959	1.288	1.506
	12	38.670	0.967	0.927	0.200	0.361	0.512		12	31.411	0.795	0.594	0.826	1.129	1.339
	16	36.467	0.950	0.905	0.159	0.300	0.437		16	29.318	0.713	0.532	0.629	0.905	1.101

Table D.4 Compression performance of the proposed resolution scalable image compression algorithm for different PAE criteria (PAE=1,2,3,4,6,8,10,12,16) in terms of PSNR, MSSIM and UQI. R0 is original resolution of the image, R1 is the image resolution after first sub sampling, R2 is the image resolution after second resembling. Datasets shown are: OSRX-MR-04, OSRX-XA-01, OSRX-XA-02 and PHNT-MR-01.

Datasets	PAE	RDLD					
		PSNR	MSSIM	UQI	BPP (R0)	BPP (R1)	BPP (R2)
OSRX-MR-04	0	Inf	1.000	1.000	4.025	4.820	5.245
	1	50.181	0.995	0.938	2.589	3.234	3.585
	2	45.532	0.985	0.867	2.003	2.582	2.911
	3	42.673	0.971	0.801	1.631	2.171	2.497
	4	40.613	0.952	0.744	1.381	1.878	2.194
	6	37.632	0.899	0.659	1.070	1.508	1.807
	8	35.536	0.837	0.602	0.861	1.254	1.539
	10	33.975	0.785	0.563	0.717	1.076	1.351
	12	32.756	0.747	0.533	0.608	0.940	1.204
	16	30.893	0.693	0.487	0.465	0.756	0.999
OSRX-XA-01	0	Inf	1.000	1.000	2.309	2.703	3.035
	1	51.670	0.995	0.957	1.360	1.671	1.966
	2	46.975	0.984	0.898	0.965	1.228	1.494
	3	44.190	0.971	0.842	0.729	0.965	1.210
	4	42.261	0.957	0.785	0.562	0.783	1.017
	6	39.553	0.928	0.697	0.365	0.552	0.758
	8	37.586	0.902	0.629	0.255	0.412	0.595
	10	35.999	0.880	0.581	0.195	0.325	0.485
	12	34.662	0.862	0.541	0.159	0.268	0.408
	16	32.329	0.824	0.477	0.114	0.200	0.309
OSRX-XA-02	0	Inf	1.000	1.000	2.445	2.932	3.304
	1	51.656	0.995	0.968	1.458	1.854	2.214
	2	46.947	0.985	0.931	1.057	1.414	1.741
	3	44.116	0.973	0.889	0.824	1.154	1.456
	4	42.168	0.959	0.845	0.660	0.968	1.253
	6	39.519	0.934	0.766	0.447	0.715	0.980
	8	37.586	0.911	0.696	0.330	0.557	0.798
	10	35.996	0.892	0.638	0.258	0.451	0.669
	12	34.620	0.877	0.593	0.212	0.378	0.573
	16	32.294	0.851	0.515	0.158	0.290	0.448
PHNT-MR-01	0	Inf	1.000	1.000	3.359	4.482	4.927
	1	50.151	0.994	0.973	2.068	2.968	3.356
	2	45.398	0.981	0.929	1.584	2.300	2.658
	3	42.507	0.963	0.882	1.280	1.898	2.228
	4	40.480	0.944	0.832	1.063	1.619	1.928
	6	37.678	0.899	0.728	0.762	1.228	1.508
	8	35.739	0.850	0.625	0.563	0.950	1.211
	10	34.294	0.805	0.532	0.430	0.746	0.988
	12	33.098	0.758	0.449	0.334	0.593	0.812
	16	31.219	0.671	0.327	0.219	0.399	0.572